Universidade de Évora - Instituto de Investigação e Formação Avançada

Programa de Doutoramento em Ciências da Terra e do Espaço

Área de especialização | Física da Atmosfera e do Clima

Tese de Doutoramento

Short-term Forecasting for Direct Normal Irradiance with Numerical Weather Prediction Models in Alentejo (Southern Portugal): Implications for Concentration Solar Energy Technologies

Francisco Manuel Tavares Lopes

Orientador(es) | Hugo M. G. Silva
Manuel Collares Pereira
Rui Paulo Salgado

Évora 2020

Universidade de Évora - Instituto de Investigação e Formação Avançada

Programa de Doutoramento em Ciências da Terra e do Espaço

Área de especialização | Física da Atmosfera e do Clima

Tese de Doutoramento

Short-term Forecasting for Direct Normal Irradiance with Numerical Weather Prediction Models in Alentejo (Southern Portugal): Implications for Concentration Solar Energy Technologies

Francisco Manuel Tavares Lopes

Orientador(es) | Hugo M. G. Silva
Manuel Collares Pereira
Rui Paulo Salgado

Évora 2020

O tese de doutoramento foi objeto de apreciação e discussão pública pelo seguinte júri nomeado pelo Diretor do Instituto de Investigação e Formação Avançada:

Presidente | Mourad Bezzeghoud (Universidade de Évora)

Vogais | Hugo M. G. Silva (Universidade de Évora) (Orientador)
María Aránzazu Revuelta Menéndez (Agência Estatal de Meteorologia)
Margarida da Conceição Rasteiro Magano Lopes Rodrigues Liberato (Universidade de Trás-os-Montes e Alto Douro)
Marion Schroedter-Homscheidt (Deutsches Zentrum Fuer Luft)
Pedro Miguel Matos Soares (Instituto Dom Luís)

Évora 2020

UNIVERSIDADE DE ÉVORA

Science and Technology School

Physics Department

Short-term Forecasting for Direct Normal Irradiance with Numerical Weather Prediction Models in Alentejo (Southern Portugal)

Francisco Manuel Tavares Lopes

Supervisors *Hugo Manuel Gonçalves Silva*
Manuel Pedro Ivens Collares Pereira
Rui Paulo Vasco Salgado

Earth and Space Sciences

Thesis

January 6, 2021

"The best way to predict the future is to create it."

***Lincon, A.**, 1809-1865*

Acknowledgments

I have been fortunate enough to have an extraordinary group of friends, family and colleagues, who helped me in each step towards the end of my doctoral programme, which is concluded, in part, with the writing of this thesis. These people deserve a profound acknowledgement and my deepest appreciation. Therefore, I express my gratitude to everyone of them, without exception, for supporting (putting up with) me during these last few years. As expected, during this period several obstacles and challenges were faced, however each barrier revealed itself as a lesson, an opportunity for improvement.

This research work would not be possible without the leadership, help and support of my advisor, and good friend, Hugo Silva. Your profound knowledge combined a strong desire for new ideas has provided me invaluable experience during my research, giving me the opportunity to improve myself as a researcher in the best possible way. I deeply appreciate the freedom and trust you have given me since our first meeting, as well as the guidance and support you offered when needed. I already miss those long brainstorm sessions.

It was through my supervisor that I had the opportunity to met and work with my co-advisors, Professor Rui Salgado at the Institute of Earth Sciences and Professor Manuel Collares Pereira at the Renewable Energies Chair. With his vast knowledge in Atmospheric Sciences, Professor Rui Salgado was a constant source of inspiration during my research, helping me to learn many valuable things on a routine basis. My sincere thanks to you Professor, I will never forget the trust you gave me and the opportunity to develop my research work at the University of Évora. With his wide expertise in Solar Radiation, among other fields of Science, Professor Collares Pereira was also an important support during this thesis, allowing me to extend my research work at the University. I am forever thankful to you Professor, for your wisdom and guidance during these years.

My research work would not be complete without the invaluable help and support of my colleagues, which became good close friends. I believe that in order for a work group to function well there has to be free will of speech, a healthy exchange of ideas, share and support. I fell lucky to have been part of such group and I will miss our coffee breaks and interesting conversations about interesting things. I want to particularly say thanks to my colleague and friend Ricardo Conceição, which, with his numerical skills and

experience in Solar Radiation, helped me to improve my studies over the years. To my other colleagues, Ailton Tavares and Daniel Lopes, thank you for your kind friendship and the every day well disposition. I wish the best of luck to all of you whether professionally or personally. I also have to acknowledge the important support given by Thomas Fasquelle, which, aside from being very comprehensive and helpful, shared valuable information for the center piece of this thesis.

I want to give a word of appreciation to Professor Paulo Canhoto for his help and important recommendations during my thesis, to Samuel Bárias and Afonso Cavaco for their technical support, and to the ECMWF and Jorge Neto (IPMA) for their availability in providing the needed data. Of course, I do not forget those that helped me at the beginning of my academic path prior to the start of my PhD. Rita Cardoso and Pedro Soares, you both gave me important support, thank you. A special acknowledgment to Susana Barbosa and Reik Donner, for believing in my skills as a researcher and for providing me opportunities and valuable teachings for the tasks that would follow. I am deeply appreciated.

I would also like to thank my host institutions, the Institute of Earth Sciences, as well as the Renewable Energies Chair, both renown research laboratories from the University of Évora, which allowed me to exercise my functions in their facilities. All this work would not be possible without the PhD grant from the DNI-A project (ALT20-03-0145-FEDER-000011) from the University of Évora, which would latter be replaced by the PhD scholarship grant (SFRH/BD/129580/2017) awarded to me by the Portuguese Foundation for Science and Technology. I am truly grateful to have been in such position.

Finally, and most importantly, none of this could have happened without my family. Mother (Fátima Tavares) and Father (Fernando Lopes), I love you. In the midst of my research work I have found a beacon, an endless source of joy and happiness. Susy, my heart is yours from the moment I met you.

Contents

List of Figures

List of Tables

Acronyms

AE *Absolute Error*

AERONET *AErosol RObotic NETwork*

ALC *ALCoutim measuring station*

APREN *Associação Portuguesa de Energias Renováveis*

ARIMA *Autoregressive Integrated Moving Average*

ASI *All-Sky Imager*

BSRN *Baseline Surface Radiation Network*

CAISO *California Independent System Operator*

CAMS *Copernicus Atmosphere Monitoring Service*

CER *Cátedra Energias Renováveis*

CR *Central Receiver*

CPV *Concentrating Solar Photovoltaic*

CSP *Concentrating Solar Power*

CZA *Cosine of the solar Zenith Angle*

DHI *Diffuse Horizontal Irradiance*

DLR *Deutsches Zentrum für Luft- und Raumfahrt*

DNI *Direct Normal Irradiance*

ECMWF *European Centre for Medium-Range Weather Forecasts*

EMSP *Évora Molten Salt Platform*

ENIAC *Electronic Numerical Integrator And Computer*

ETS *Equitable Threat Score*

EVO *ÉVOra measuring station*

GHI *Global Horizontal Irradiance*

HTF *Heat Transfer Fluid*

ICT *Instituto de Ciências da Terra*

IFS *Integrated Forecasting System*

IPMA *Instituto Português do Mar e da Atmosfera*

MAE *Mean Absolute Error*

MBE *Mean Bias Error*

MIT *MITra measuring station*

MSE *Mean Square Error*

McICA *Monte-Carlo Independent Column Approximation*

MODIS *Moderate Resolution Imaging Spectroradiometer*

MOS *Model Output Statistics*

MRM1 *Multivariate Regression Model 1*

MRM2 *Multivariate Regression Model 2*

nMAE *normalized Mean Absolute Error*

nRMSE *normalized Root Mean Square Error*

NREL *National Renewable Energy Laboratory*

NWP *Numerical Weather prediction*

SAM *System Advisor Model*

SCA *Solar Collector Assembly*

SE *Standard Error*

SRM *Simple Regression Model*

SS *Skill Score*

STD *STandard Deviation*

RMSE *Root Mean Square Error*

PDF *Probability Density Function*

PECS *Plataforma de Ensaios de Coletores Solares*

PRT *PoRTalegre measuring station*

PT *Parabolic-Trough*

PV *PhotoVoltaic*

TES *Thermal Energy Storage*

TOA *Top-Of-Atmosphere*

TMY *Typical Meteorological Year*

TRNSYS *TRaNsient SYStem*

UÉ *University of Évora*

UTC *Coordinated Universal Time*

Nomenclature

DNI_{mod} Direct normal irradiance forecasted at surface

DNI_{obs} Direct normal irradiance measured at surface

DNI_{per} Persisted direct normal irradiance

DNI_{TOA} Direct normal irradiance calculated at Earth's top-of-atmosphere

d2m Dew point temperature forecasted at 2 m height

dsrp Forecasted direct solar radiation on a plane perpendicular to the direct sun beam

E_{G} Andasol 3 produced electrical energy

E_{P} Gemasolar produced electrical energy

$E_{\mathrm{b}}^{\mathrm{mod}}$ *Forecasted DNI availability at surface*

$E_{\mathrm{b}}^{\mathrm{obs}}$ *Measured DNI availability at surface*

$E_{\mathrm{b}}^{\mathrm{TOA}}$ *Calculated DNI availability at Earth's top-of-atmosphere*

$E_{\mathrm{t}}^{\mathrm{obs}}$ *Measured GHI availability at surface*

$E_{\mathrm{t}}^{\mathrm{TOA}}$ *Calculated GHI availability at top-of-atmosphere*

fdir Total sky direct solar irradiance forecasted at surface

GHI_{mod} Forecasted Global horizontal irradiance at surface

GHI_{obs} Measured global horizontal irradiance at surface

GHI_{per} Persisted global horizontal irradiance

GHI_{TOA} Calculated global horizontal irradiance at top-of-atmosphere

GW Gigawatt

GWh Gigawatt per hour

I_0 Total solar power from the Sun at the average Earth-Sun distance

J/m^2 Joule per square meter

k_b DNI hourly clearness index

K_b DNI daily clearness index

k_t GHI hourly clearness index

K_t GHI daily clearness index

kW_e Kilowatt-electric

kWh Kilowatt-hour

kWh/m^2 Kilowatt-hour per square meter

MSE_for Mean square error from the forecast model

MSE_per Mean square error from the persisted time series

MW Megawatt

MW_e Megawatt-electric

MW_p Megawatt-peak

MW_th Megawatt-thermal

MWh_e Megawatt-electric-hour

MWh_t Megawatt-thermal-hour

r Pearson correlation coefficient

R^2 Coefficient of determination

rh2m Calculated relative humidity at 2 m height

sp Forecasted atmospheric pressure at surface

t2m Forecasted air temperature at 2 m height

tcc Forecasted total cloud cover

TES Thermal energy storage

TES_charge Thermal storage charge energy

$TES_\mathrm{discharge}$ Thermal storage discharge energy

TES_ecmwf Predicted based thermal energy storage energy

TES_{obs} *Measured based thermal energy storage energy*

tp Forecasted total accumulated precipitation

u Forecasted wind velocity horizontal component at 10 m height

v Forecasted wind velocity vertical component at 10 m height

W/m^2 *Watt per square meter*

$cos(\theta)$ *Angle between beam irradiance and the surface normal*

ΔE_{b} *Relative difference of the total DNI availability*

ΔE_{t} *Relative difference of the total GHI availability*

Abstract

With the potential to sustain the world's energy needs, solar energy plays a major role for the renewable energy transition. However, inherent problems exist in solar energy forecasting, a very important tool for power plant operators that allows an efficient energy management and dispatch operations in the electric grid. In particular, concentrating solar power (CSP) systems, which rely on direct normal irradiance (DNI) and its high variability, which links uncertainty to the electrical energy outputs of CSP plants. The main atmospheric factors that influence DNI variation at surface are clouds and aerosols, which are misrepresented by current numerical weather prediction models. To provide accurate predictions of DNI for efficient CSP operations, particularly during periods of direct solar intermittency, the solar resource needs to be well characterized. Solution to this problem is still one of today's challenges in solar forecasting. This thesis makes use of short-term forecasts of DNI from the Integrated Forecasting System (IFS), the global model of the European Centre for Medium-Range Weather Forecasts (ECMWF), together with ground-based measurements in Alentejo region (southern Portugal). The evaluation of the solar resource in the region is based on the IFS predictions, as well as the prediction of energy production outputs from different CSP systems through the System Advisor Model (SAM) power plant simulator, in which the results are compared with local measured data. To improve the role that DNI forecasting has in CSP power plants, several post-processing techniques are used for the correction of hour and day-ahead values of DNI. Different operational strategies are discussed and proposed according to the obtained results.

Keywords: Numerical Weather Prediction Modelling, Direct Normal Irradiance, ECMWF, Short-term Forecasts, Concentrating Solar Power

Resumo

Previsão de Curto Tempo de Radiação Normal Directa Através de Modelos Numéricos de Previsão do Tempo no Alentejo (Sul de Portugal): Implicações para as Tecnologias de Concentração Solar

Com potencial para assegurar as necessidades energéticas do mundo, a energia solar desempenha um papel importante na transição energética renovável. Contudo, existem problemas inerentes na previsão de energia solar, uma ferramenta muito importante para os operadores de centrais eléctricas que permite uma gestão energética mais eficiente e operações de distribuição da mesma na rede eléctrica. Em particular, os sistemas de concentração de energia solar (CSP), que dependem da radiação normal directa (DNI) e da sua elevada variabilidade, atribuindo incerteza à geração de energia eléctrica resultantes de centrais CSP. Para fornecer previsões precisas para operações CSP eficientes, particularmente durante períodos de intermitência solar directa, o DNI precisa de ser bem caracterizado. Os principais factores atmosféricos que influenciam a variação de DNI à superfície são as nuvens e os aerossóis, que não são representados realisticamente pelos actuais modelos numéricos de previsão do tempo. A solução para este problema é ainda hoje em dia um desafio em previsão solar. Esta tese faz uso das previsões de curto-período de DNI do Integrated Forecasting System (IFS), modelo global do European Centre for Medium-Range Weather Forecasts (ECMWF), em conjunto com medidas à superfície na região do Alentejo (sul de Portugal). A avaliação do recurso solar na região é efectuada com base em previsões do IFS, tal como a previsão de outputs de produção energética de diferentes sistemas CSP através do simulador de centrais eléctricas System Advisor Model (SAM), onde os resultados são comparados com os obtidos com medidas meteorológicas locais. Para melhorar o papel que a previsão de DNI tem em centrais CSP, várias técnicas de pós-processamento são efectuadas para a correção de valores de DNI para a hora e dia seguinte. Diferentes estratégias de operação são discutidas e propostas de acordo com resultados obtidos.

Palavras chave: Modelação Numérica de Previsão do Tempo, Radiação Normal Directa, ECMWF, Previsões de Curto Tempo, Concentração Solar

1

Introduction

The first chapter includes fundamental historical references and state of art regarding numerical weather prediction modelling, solar forecasting and concentrating solar power systems. Having into consideration the current state of Solar Energy in the renewable energies sector, concerns about the future of the solar resource are discussed. Then, as an important part of this thesis, the motivation for this work, as well as its sctructure, are presented. As an end note, the dessimination work carried out by the author, including all publications, is also provided.

1.1 Historical background

The Sun, source of life and energy, sits at a mean distance from the Earth of 149.60 million km, usually referenced as one astronomical unit (abbreviated AU). With a surface temperature (photosphere) of about 5.500 °C and an equatorial radius of 695.500 km, this massive sphere of hot gaseous matter (92.1 % hydrogen, 7.8 % helium and 0.1 % of other elements) releases tremendous amounts of heat due to the combination between hydrogen atoms, allowing the occurrence of fusion processes [1]. The resulting heat energy is then carried by electromagnetic waves through the vacuum of space until it reaches the Earth's top-of-atmosphere (TOA) with the mean value of 1361 W/m^2 [2], also known as the solar constant, I_0. Once there, the resulting interaction processes between the incoming radiation, atmosphere, land surface, cryosphere and oceans, are responsible for meteorological phenomena, including the ocean currents, winds, weather and climate, contributing to the global radiation balance (e.g. [3]).

Out of all available sources of renewable energy, whether ocean currents, wind, geothermal, bio, or hydro, solar radiation is the most desirable one due to its abundance, high quality, and high potential for electricity generation or for direct heating. However, like all renewable sources, the process of harvesting solar radiation is challenging, requiring the understanding of the causes for its variability, as well as the ability to predict the resulting complex processes that occur in the atmosphere over a wide range of scales [4]. The atmospheric and oceanic circulations can be modulated and predicted through a series of partial differential equations, known in literature as the Navier-Stokes equations. Together with the conservation of mass and energy, these equations establish the fundamentals of numerical weather prediction (NWP) modelling, which is "among the greatest of any area of physical science" [5], creating an impact in human society on a daily basis since its debut at the turn of the twentieth century.

In 1904, Vilhelm Bjerknes (**Fig. 1.1a**) published his work [6] detailing for the first time the use of physical laws to forecast the weather. Bjerknes research proposed that a set of seven partial differential equations (also known as primitive equations) could be used to predict the state of the atmosphere, starting from measurements of the current weather. His work would later inspired other renown scientists in the field of NWP, namely Carl-Gustav Arvid Rossby and Vagn Walfrid Ekman, which applied Bjerknes's equations in their studies concerning large-scale motions in the atmosphere [7] and oceans ([8]), respectively. After the end of World War I, at a time when surface weather maps would be produced through the use of empirical and analog-based processes, the skill in performing weather forecasting started to experience a continuous increase. Particularly, it was with the published work of Lewis Fry Richardson (**Fig. 1.1b**), entitled "Weather Prediction by Numerical Process" in 1922 (available online from https://archive.org/details/weatherpredictio00richrich), that NWP procedures started to be outlined. In this case, the well-known Bulk Richardson Number, a dimensionless ratio that allows to quantify the dynamic stability and the formation of turbulence in the atmosphere, such as the characterization of convective-storm types in different environments [9]. However, the technological means for the application of such procedures were still insufficient at the time.

(a) Norwegian physicist and meteorologist Vilhelm Friman Koren Bjerknes (1862-1951).

(b) English mathematician and physicist, Lewis Fry Richardson (1881-1953).

Figure 1.1: Bjerknes and Richardson pioneered modern physics and mathematical techniques fundamental in today's numerical weather forecasting. Photographs taken circa 1920 (a) and 1931 (b), being publicly available.

It was only after World War II, that the first computer simulations started to be produced by the electronic numerical integrator and computer (ENIAC), at the Institute for Advanced Study in the University of Princeton, New Jersey. The ENIAC (**Fig. 1.2a**), which weighted thirty tons and fully occupied a room of 10 x 15 meters, had been previous used under the supervision of John Von Neumann (**Fig. 1.2b**) to compute military tactical trajectories for World War II and to study the effects of a nuclear bomb explosion, particularly to assess the viability in using the Hydrogen bomb (codename Fat Man) over Nagasaki and Hiroshima. In 1948, Neumann gathered a team of scientists to implement Richardson ideas in the ENIAC. The procedure enabled the production of the first weather forecasts build on very simple approximations to the atmospheric governing equations, allowing to substantially reduce the time needed to perform a forecast, which had been made by-hand until then. The following years were marked by the introduction of higher resolution simulations, which included cloud physics and radiative transfer effects [10], being latter associated to the development of the first limited area models (early 1970s). The evolution of such models was closely related with the crucial information provided by ground-based observations through the use measuring equipment. The recordings of the atmospheric state not only allowed to study the variability of all atmospheric, oceanic and surface variables, but also to predict their behaviour by including measured values in the initial state (i.e. initial conditions) of NWP models. By including the spatial distribution of a set of variables (e.g. temperature, wind, pressure, moisture, amongst others) in the initial state of a NWP model, a complex process, posteriorly known as data assimilation [11], would bring a constant presence of forecast

uncertainty in NWP. Such uncertainty, being related to a shortage in the number of available observations to fulfill the degrees of freedom of the system, started to decrease with the constant increase of measuring equipment accuracy and the number of available ground-based stations. Moreover, measurements, which had been perform only at the Earth's surface, could also be carried out above through the use of meteorological balloons and weather satellites, allowing to improve data assimilation. For instance, satellite images were able to help the description from 12 to 72 hours of different weather patterns in NWP [12], allowing to estimate irradiance values at the Earth's surface. It was only until the mid-eighties, when researchers began to assemble the "network of networks", which became the modern Internet, that noticeable technological efforts started to be made to improve weather forecasts, particularly throughout the following decades with the tremendous increase of computer technology and sophisticated numerical methods. These efforts were carried out by different groups of scientists and technicians, many as independent intergovernmental organizations. The resulting synergy between these enabled modern NWP models to perform high-quality forecasts, by which mesoscale and global circulations could be resolved (i.e. regional and global models, respectively) under three different categories: short-, medium- and long-term. Short-term forecasts can be carried out to predict the weather over the next day or two. Medium-term are related to predictions from three days to about two weeks ahead, while long-term can go up several months ahead in predicting the weather. One example is the European Centre for Medium-Range Weather Forecasts (ECMWF), funded by the European Cooperation in Science and Technology (COST), in partnership with several European countries, being hosted in the United Kingdom (1975). The ECMWF first global operational forecasts started to be performed in 1979, where these would be made five days a week, increasing to seven days a week in the following year. As part of the operational forecasting system at a global scale, the first ensemble predictions were produced by the ECMWF in 1992. The ECMWF objective was to provide different possible future states of the atmosphere and, at the same time, to account for the forecast uncertainty in NWP models, in which errors resulted from incorrect initial conditions and from the models themselves. Focus to this subject will be given further on.

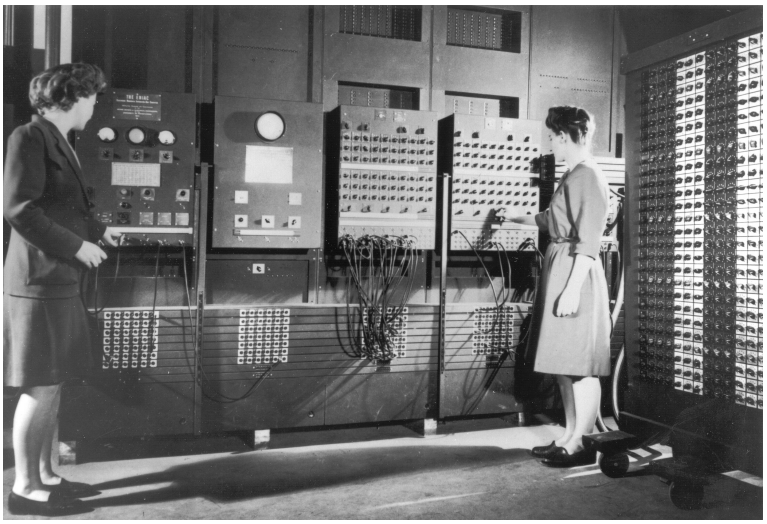

(a) Two women operating the main control panel of the electronic numerical integrator and computer (ENIAC), the first computer build for weather forecasting.

(b) Hungarian-American mathematician and physicist John Von Neumann (1903-1957).

Figure 1.2: Together with a group of scientists, Neumann initiated the implementation of Richardson's numerical applications in the ENIAC. Photographs taken: (a) from an unknown date (publicly available by the U.S. Army); (b) from Los Alamos publication (Los Alamos Beginning of an Era, 1943-1945), Los Alamos National Scientific Laboratory (1986).

In addition to the need of understanding solar radiation variability, the process of harvesting, generate energy (thermal or electrical) and then dispatch it into the electrical grid (if the latter), a process also known as energy dispatchability, is often costly [13], requiring the use of solar collecting systems that need to be installed at the Earth's surface. The first modern technological developments to harvest solar energy go way back into the eighteenth century, since the invention of the first solar collector in 1767 by Horace de Saussure (**Fig. 1.3a**). Saussure designed and constructed a three-layer glass box to magnify and absorb heat energy that could reach temperatures in excess of 110 °C (**Fig. 1.3b**). More than a century later, in 1887, Heinrich Hertz helped establish the photoelectric effect (later explained by Albert Einstein, in 1916), where a charged object experiences charge losses when illuminated by ultraviolet radiation, initiating a spark upon the detection of electromagnetic waves. This breakthrough lead to the production of the first solar heater in 1891 and the introduction of the first solar cell in 1893, a complete different way of harvesting solar energy, by the so called photovoltaic (PV) effect. Moreover, the solar heater experiment would serve as an inspiration to other research works, such as the innovative Pyreheliophoro [14] constructed by Manuel António Gomes (nicknamed Father Himalaya) in 1904 (**Fig. 1.4**). The Pyreheliophoro, which went through several phases of development, could reach temperatures up to 3800 °C in its final version, allowing to melt rocks and metals.

It was only after the beginning of the Cold War (in 1947) that solar energy was officially introduced to the commercial sector. In 1954, the production of the first practical PV-cell was carried out by Daryl Chaplin,

Gerald Pearson and Calvin Souther Fuller at the Bell Labs in Berkeley (New Jersey). Few years later, the first solar PV systems started to be implemented for space exploration (e.g. satellites and space stations). In 1963, studies about Global Warming started to hit the press, point out to the need for investment in the renewable energy sector. Since then, technological advances in the energy sector, being perpetually associated with the fast increase in computer technology, allowed the improvement of solar cells and solar concentrators efficiency with respect to their effects on energy costs. Since most of the materials used for the assembly of PV panels were already being used in the electrical industry, PV systems became considerably cheaper to manufacture in 1970. In addition to that, several incentives were made for the installation of PV technology in different countries (e.g. Germany and Japan), including remote areas where grid connected renewable energy systems could not be economically sustained. At the beginning of the next decade, the first PV powered machines, such as the first solar powered aircraft and car, started to be produced. At the same time that PV technology was growing in the electrical market (particularly in China with its mass production of PV panels at the turn of the twentieth century), concentrating solar power (CSP), also known as solar thermal electricity, systems had a slower growth in comparison with PV, since these were (and still remain) more costly to be produced.

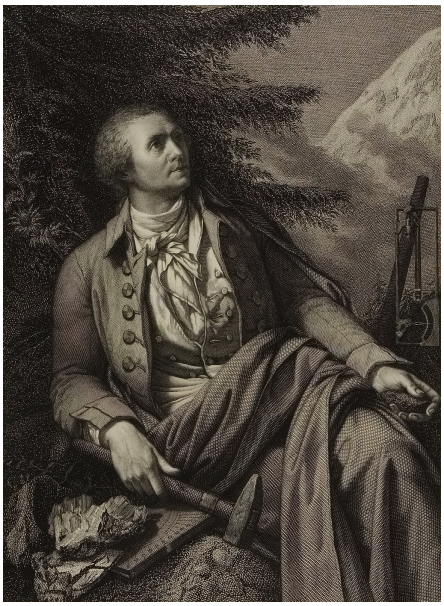

(a) Swiss physicist and meteorologist Horace Bénédict de Saussure (1740-1799).

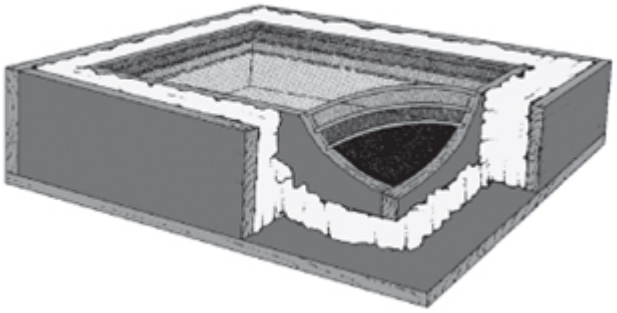

(b) Saussure's concept model for the first "solar collector cell" (1767).

Figure 1.3: Saussure created the first solar collector, which became later known as solar oven. Saussure's engraving (a) was created in the nineteen century and is credited to the Harvard Art Museums/Fogg Museum, Gift of Belinda L. Randall from the collection of John Witt Randall (© President and Fellows of Harvard College, R11017). The concept model design (b) of Saussure's solar hoven drawing is from an unknown date, being publicly available.

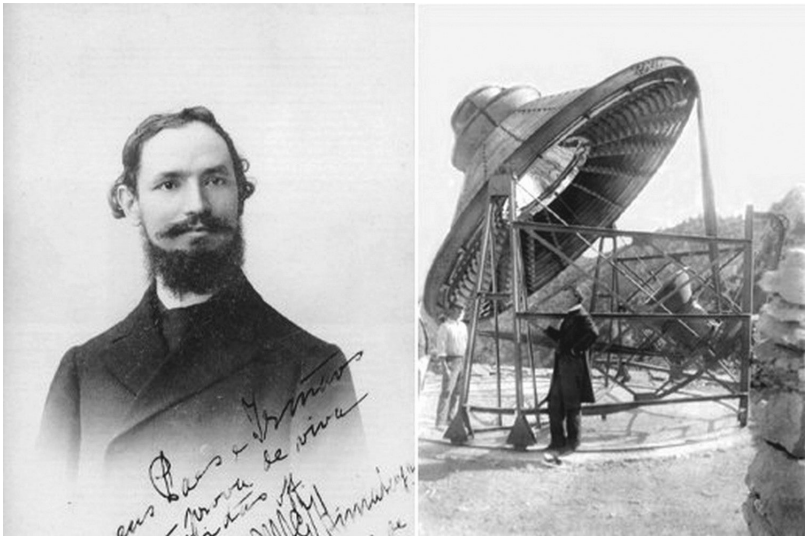

Figure 1.4: Portuguese Catholic priest, inventor and physicist, Manuel António Gomes (1868-1933), nicknamed Father Himalaya (left picture). At the turn of the nineteenth century, Father Himalaya presented the Pyreheliophoro (right picture), a high temperature and concentration solar optical system that could reach temperatures up to 3800 °C. Picture publicly available, photos taken at unknown date.

By the end of the twentieth century, as technology and energy demand grown, solar parks started being build with the installation of PV systems with a high power capacity. Consequently, the increase number of PV stations lead to the introduction of payments made to households generating their own electricity (i.e. feed-in tariffs) in 2008, in which Spain played a major role with more than sixty solar parks that had a power capacity higher than 10 MW_p [15]. However, with the worldwide increase of awareness towards the impact of fossil fuel emissions and the desire for an energy transition in face of different climate change scenarios (with a record in 2012), the prevalence of Spain would soon be withdrawn by other countries that have currently a predominant market (e.g. China, India and U.S.A). All of these countries possess power plants that have the capacity to produce hundreds of MW, in which a selected few are able to reach more than one GW. In comparison, as published by the Portuguese Renewable Energy Association (APREN), the installed power capacity in Portugal has been having a gradual increase since the beginning of the twentieth century (retrieved online from https://www.apren.pt/en/renewable-energies/power/). It was only after 2005, when only 3 MW of installed power capacity were accomplished, that efforts were made to increase the national solar power capacity, resulting in an annual growth of 7 % with the attainment of 828 MW by the end of 2019. Currently, there are two main solar parks in Portugal: the Amareleja ≈46.4 MW_p station, operational in the municipality of Amareleja since 2008; and the Ourika ≈46 MW_p station, recently installed (2018) in the municipality of Ourique. Other small sized solar parks exist distributed in the country, including Madeira and Azores islands.

1.2 State of the art

In order to perform forecasts, a combination of numerical models and weather observations is used to simulate the atmospheric state and its evolution through the integration in the time domain of the constitutive and state equations that describe the physical phenomena in the atmosphere. At the turn of the twenty first century, technological advances and continuous improvements in the quality of numerical models and solar radiation measuring equipment at ground-level were attained, including the methods used for weather forecasting [16]. In this context, forecasts of environmental energy fluxes, such as solar irradiance, for time-scales spanning from 1 to 2 days (hourly resolutions) are one fundamental approach for an efficient integration of renewable energy resources into existing energy supply structures. In particular, PV and non-concentrating solar thermal systems, which use both the direct and diffuse components, need primarily global horizontal irradiance (GHI) forecasts, while concentrating solar photovoltaic (CPV) and CSP technologies require direct normal irradiance (DNI) forecasts [17]. PV, CPV and CSP systems demand high GHI and DNI forecasting accuracy for an efficient management of solar energy harvesting, which occurs ideally under clear sky conditions (e.g. [18, 19, 20, 21, 22, 23]).

The GHI consists in the direct and diffuse irradiances on a horizontal plane at the Earth's surface. The former component is defined as the solar direct irradiance that is received on a plane normal to the Sun's rays over the total solar spectrum [24], i.e. DNI, and is typically measured as the incoming beam from the Sun's disc and circumsolar irradiance within a 2.5° cone around the Sun's center [25]. The latter component is commonly defined as diffuse horizontal irradiance (DHI), i.e. the radiation received on a horizontal plane at the Earth's surface after being scattered by molecules and particles present the atmosphere (e.g. clouds and aerosols). For PV systems, the knowledge of GHI resource and prediction of solar energy generation allows to provide a higher power output under cloudy and clear sky conditions. Additionally, information about GHI availability is important to predict the energy output of PV systems and to help the mitigation of possible power fluctuations that can occur in electrical grid injections [26]. In the case of CSP systems, which have the advantage of having a higher energy storage capacity [27], knowledge of DNI is fundamental if clear sky conditions occur. Forecasting DNI is important mainly for CSP plants operation in order to reduce the uncertainty of solar power plant outputs due to solar irradiance intermittency [28] and to optimize the necessary CSP electrical energy generation (on time scales of few minutes to few hours) and maximize the energy output for a given day. In other words, there is the utility side where DNI predictions are important to project the impact of a possible sudden interruption in the grid and also to predict the total electricity needed in the grid. In fact, for medium and long-term periods such predictions are important for the power plant's operation and its energy dispatchability, i.e. the capability of a power plant to carry out energy outputs in the grid to increase economic return by delivering electricity during the more demanding and valuable periods [19].

In recent years, a remarkable increase has been observed regarding the global capacity of solar energy conversion technologies installed worldwide (**Fig. 1.5a** and **Fig. 1.5b**, respectively). The installation of PV systems has been growing exponentially over the last decades, with approximately 402.5 GW of

cumulative worldwide installed capacity by the end of 2017 [29]. On the other hand, approximately 5.7 GW of cumulative worldwide installed capacity regarding CSP technology was available by the end of 2017 [30], as a consequence of a much smaller growth rate than PV. However, the fact that CSP has the advantage of providing high-quality dispatchable power at lower prices when compared to PV electrical storage, is one of the strongest reasons [31] for investing in such technology. Additionally, CSP storage materials, such as molten salts, are a more affordable, safer and locally available way of storing energy than conventional technologies such as lithium batteries. Discerning by region, as shown in **Fig. 1.5c**, Spain and the U.S. have been playing a major role in the CSP market since 2006, being followed by the rest of the world, including Morocco (in 2015), South Africa and China (in 2016).

With the installed capacity increase for both PV and CSP systems, an improvement in solar forecasting is also expected to occur, since information provided to the power plant operator, for instance, regarding day-ahead (i.e. up to 48-hours) irradiance values, can have a key role not only in the production of energy but also in its distribution and management towards the electricity grid market. In particular, predictions of DNI are essential for CSP technologies [17, 32], since these can provide the operator the capacity of improving the plant's energy management. For instance, during the most demanding and valuable periods [19], in which higher levels of profitability can be achieved [33]. In this context, accurate forecasts of DNI are demanded for clear sky periods and, particularly, for partly cloudy skies [22, 23], where a reduction of the uncertainty related to the solar power plant outputs due to solar intermittency [28] is essential. Solar intermittency is characterized by a very high variability over space and time, which partially depends on the local weather conditions. Consequently, the spatial and temporal variability of solar radiation impacts the economic market, as described by the "duck curve" [34], named after the California Independent System Operator (CAISO). The "duck curve" simply shows a large portion of the electrical energy demand during the day that is being modulated by renewable energy production (including solar power). As described by [35], current challenges to mitigate the effect of the "duck curve" in the operation of power plants consist in the ability of: i) conventional power generation fleet to meet the downward and upward net load ramping needs that occur during sunrise and sunset hours, respectively; ii) conventional power plants to substantially decrease the generation levels or cease the energy output during a few hours at mid-day, i.e. during the period of lowest net demand in the day. To reduce the uncertainty of such challenges, and to reach a minimum generation (during mid-day) and ramping requirements (during sunrise and sunset), these authors give emphasis to the use of accurate solar power forecasts, a more stable and economic approach that embraces better unit commitment and financial choices.

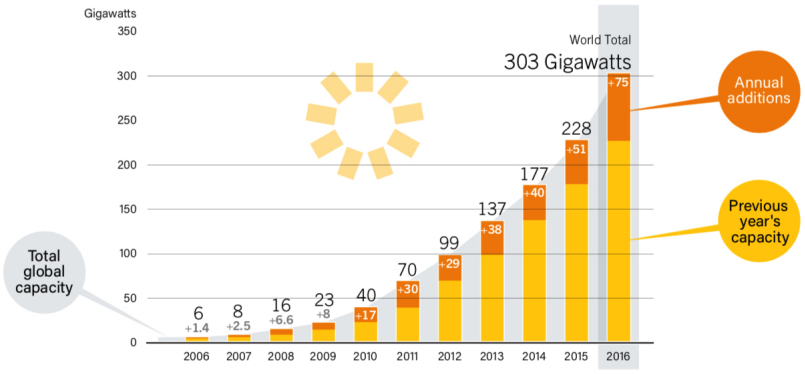

(a) PV global capacity (in GW) with annual additions (from 2006 to 2016).

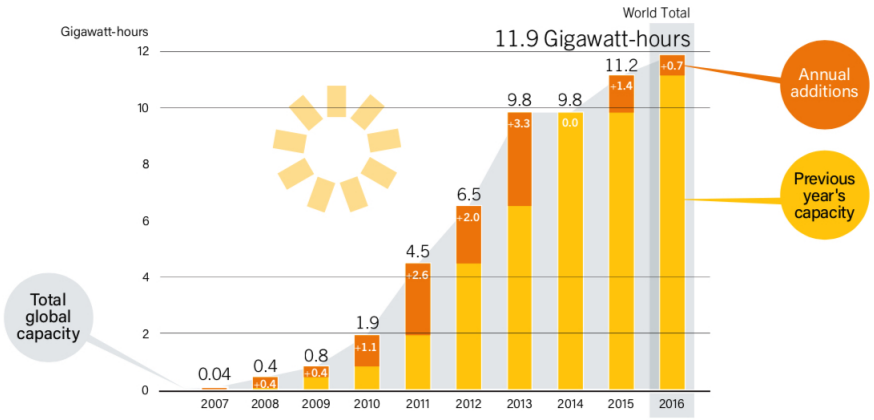

(b) CSP global capacity (in GWh) with annual additions (from 2007 to 2016).

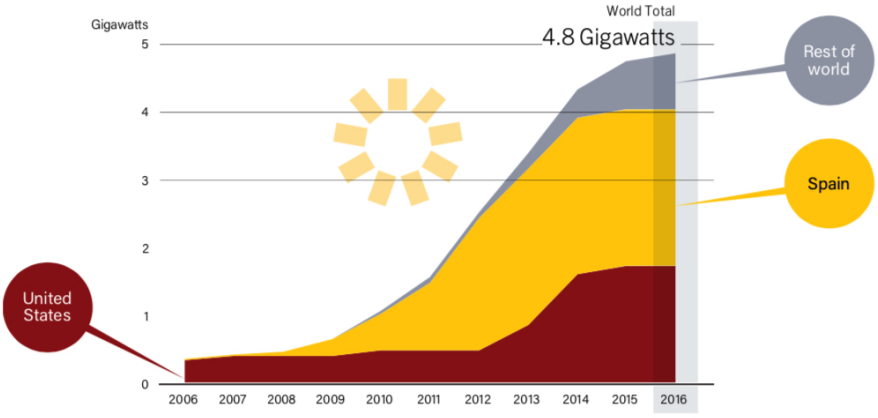

(c) CSP global capacity (in GW), by country and region (from 2006 to 2016).

Figure 1.5: Global statistics on PV and CSP installations: adapted from [29].

With the growth of the solar energy sector, in particular CSP technologies, there has been a simultaneous increased interest in the use of NWP models in order to perform short-term predictions of DNI (e.g. [20, 21]). DNI predictions depend on many factors, which can influence the energy output of a solar power plant. Such dependency is predominantly related to atmospheric conditions, e.g. air temperature, air moisture,

wind speed/direction and, more significantly, clouds (type and dynamic coverage) and aerosol load. To characterize accuratly these parameters, a combination of state-of-the-art monitoring and assessment techniques for solar radiation, together with advanced NWP modelling, can be performed. Particularly, with short-term forecasts ($<$ 48 hours), which are known to be useful for energy resource planning and scheduling [36], allowing an increase of management effectiveness of CSP plants and higher-penetration of commercial solar power into the electricity grid market. The accuracy of DNI predictions depends on the forecast horizon, since forecasting uncertainty tends to be smaller with the reduction of the projection period. Smaller forecast horizons can be performed at higher resolutions with very expensive computational costs [37].

Currently, there is a wide range of DNI forecast horizons performed with different methods (**Table 1.1**). As described by [36], forecasts within the nowcasting range ($<$ 30 minutes), can be performed through the use of ground-based sky imagers and persistence models. Stochastic-learning techniques, such as autoregressive integrated moving averages (ARIMA) and artificial neural networks (ANN), can be suitable for short-term forecasts ($<$ 2 hours). For a temporal horizon between 2 and 6 hours, a combination of techniques is usually adopted through NWP models and satellite data. Ahead of the 6-hour horizon, forecasts are mainly carried out through physics-based models, which are able to produce week-ahead forecasts.

A factor that contributes to inaccurate forecasts of DNI is the generation of the initial state of the atmosphere, the oceans and the surfaces. As previously mentioned, uncertainties in the initial conditions of NWP models are always present due to a shortage of observations and, thus, observational errors. NWP models represent and describe the dynamics of the atmosphere and the physical processes that take place (e.g. cloud-radiation interaction), however, despite the great developments attained in the last three decades, current state-of-the-art NWP models are still limited in certain aspects. This is mainly due to the fact that the atmosphere is a very complex and non-linear system, in which many relevant phenomena occur on model non-resolvable scales. Thus, in one hand, the physical modelling of some phenomena can still be improved, particularly in the case of the radiation transfer in both solar and infrared spectral ranges. On the other hand, numerical representation of clouds and aerosols are usually hindered by the complexity of cloud microphysics [22] and aerosol [38] modelling, two key parameters that significantly affect the DNI, due to the radiation scattering and absorption phenomena and its interaction with cloud microphysical and dynamical processes [39]. At such small scales, nonlinear and turbulent motions contribute to a chaotic and stochastic behaviours, as oppose to a deterministic (i.e. single-valued) solution carried out by NWP models [4]. For instance, during partly cloudy days, NWP models are typically able to predict clouds, however the exact location and timing of cloud formation and dissipation (i.e. cloud life cycle) are difficult to predict. This occurs especially for mesoscale clouds (i.e. below a horizontal resolution of several km). Additionally, the generalized use of monthly climatology of aerosol types and concentrations in the NWP models, increases the errors of the predicted radiation, especially for clear sky conditions. For instance, variations in DNI can reach a reduction of 80–90 % in extreme events such as desert dusts [40]. As a matter of fact, [41] has recently shown that extreme dust events depicting large DNI mean bias overpredictions are found to be 4.6 times higher than background results. Under clear sky conditions, NWP models also reveal

that aerosol component is essential to obtain accurate estimations of surface irradiance, with improvements of the forecasts up to 58 and 76 % in GHI and DNI, respectively, as described by [42]. An important improvement in NWP models would be the use of coupled modules for aerosol and chemistry, as those developed within the Copernicus Atmosphere Monitoring Service (CAMS), allowing to use a prognostic aerosol scheme initiated by an aerosol data assimilation system. However, the use of such prognostic aerosol schemes can have a high impact in a model's efficiency, with the computational cost increasing more than 50 % [43]. For such reason, a monthly climatological description of the aerosol component is currently the most viable approach to be considered. Additionally, the radiative effects of clouds tend to be underestimated by the models, while the radiative effects of the aerosols tend to be overestimated under very clear atmospheric conditions and underestimated under dusty conditions, namely desert dust events. Solutions for these problems have been pursued more intensely in the recent years with the development of advanced NWP methods. One example of such improvement is the radiation scheme used by the Integrated Forecasting System (IFS), the global NWP model of the ECMWF, which has been upgraded over the years to provide more accurate forecasts of solar radiation, particularly DNI.

Table 1.1: Some examples of different methods used for DNI forecasting.

Time-scale	Methods	Scale
Intra-hour (1 min - 2 hours)	Persistence models [44, 45, 46] Sky Imagers [47, 48, 49, 50]	Microscale (≈0 m - 1 km)
Intra-day (< 2 hours)	ARIMA models [51] ANN [52, 53, 54]	Microscale (≈0 m - 1.3 km)
Intra-day (2-6 hours)	NWP models [55] Satellite-based models [56]	Mesoscale (≈1 m - 10 km)
hour, day and week-ahead (> 6 hours to several days)	NWP models [57]	Mesoscale and synoptic (>10 km)

Statistical post-processing of dynamical NWP outputs can be of practical use for weather forecasting [58], in which two main categories of classification for statistical downscaling methods exist [59]: perfect prognosis and model output statistics (MOS). Perfect prognosis [60] is related to the finding of empirical relationships associated to large-scale atmospheric predictors and small-scale predictands, in which both sets of data are originated from historical or actual observations. While in MOS [61], the output from NWP models are post-processed using statistics of local historical or actual observations. Each method has its own advantages and disadvantages, but, essentially, MOS accounts for systematic model errors (e.g. dry bias) with the use of multiple predictors, allowing for a better fit to the predictand data and higher accuracy. Such accuracy, is generally better than pure statistical models, which have a high performance at very short time resolutions ($<$ 30 minutes) within the nowcasting range (i.e. from 0 to 6 hours), or pure NWP models, which go beyond the 6-hour range. After combining observations with NWP model outputs, statistical techniques, such as the use of statistical regression models (the most basic form of MOS), can be applied to derive forecast equations, allowing to improve the original forecasts [62]. To reduce NWP uncertainty and improve the systematic error correction of DNI forecasts, several statistical methods have been used. For instance, [21] implemented a simple post-processing correction over three-hour average values of predicted DNI, leading to satisfactory results with correlations in the order of 0.9. In their work, the authors concluded that clouds were the main source of numerical bias. In [63], a third-degree polynomial fit was performed over monthly mean hourly values, providing a high correlation coefficient of about 0.96 between the clearness index and historical DNI data. Depending on the forecast horizon, several other more complex approaches have been used to evaluate the systematic errors. For instance: Multi-Model [64]; Multi-Parameterization [65]; Stochastic Parameterization [66]; Multi-Parameter [67]; Stochastic Kinetic Energy Backscatter methods [68]; artificial neural networks [69]; autoregressive integrated moving average (ARIMA) models [70, 51]; assemble MOS [71], amongst others. Besides statistical downscaling methods, the nesting of high-resolution limited-area models in global models (i.e. dynamic downscaling) can also be used to improve NWP outputs. As described by [72], the method has the advantage of not requiring local observations and the potential to provide better results than statistical methods, particularly the prediction of extreme events. However, the desavantage lies in the fact that systematic errors present in the global models are propagated to the mesoscale ones, and the higher computational cost needed for implementing a high-resolution model.

In the context of forecasting inaccuracies, to quantify the forecast error and compare the performance of different forecasts, it is important to compute the forecasting accuracy. As described in [36], although several conventional metrics exist, to determine the most appropriate ones depends on the user. For instance, CSP plant operators can be sanctioned per kilowatt-hour (kWh) deviation from the expected production [73]. In such cases, error metrics, which allow operators to perform an accurate estimation of the costs related to forecasting errors, are crucial. Particularly, for the application of electrical grid management, the root mean square error (RMSE) has been widely used, due to the importance that large errors have for the safety of an electrical grid system [17]. Considering the mean square error (MSE) of both forecast and persistence (i.e.

persistence of the previous measured 24-hour values) models with respect to measurements, forecasting ability can be performed using the skill score (SS). The SS allows to evaluate the global performance of the forecast model towards measurements, being a forecasting metric suitable to measure forecasting performance and should be considered regarding forecast inaccuracies. Other conventional metrics that can be used to assess the forecast error are the mean bias error (MBE), mean absolute error (MAE), Pearson correlation coefficient (r) and coefficient of determination (R^2). More detailed information concerning the use of these, and other error metrics, in solar forecasting is available in [36].

It is also important that solar power plant models accurately convert predicted irradiation values, which are found by integrating irradiance values over time, to energy output forecasts. Most of the available software for the simulation of power plants, such as the System Advisor Model (SAM, [74]), use by default satellite-based data with the generation of a typical meteorological year (TMY), particularly for specific locations outside national territory, in which the software is developed. An alternative approach to satellite data, is the use of local measurements for generating TMY, which should be considered together with a priori quality control of the data and an analysis of different typical periods [75]. Although using TMY data is suitable for solar power plants design, since it can provide an estimation of the amount and variability of energy generation in a specific location, it is still essential to know the predicted DNI availability for the day-ahead. The combined use of high-quality local measurements, NWP models and power plant modelling can generate useful information for the energy management and operation of a CSP power plant.

1.3 Future perspectives

With the world population increase in the next decades (9.7 billion by 2050, and near 11 billion by 2100, as reported by [76]), an inevitable increase in the energy demand is expected. Such demand will be even more evident in the renewable sector, particularly in Solar Energy, not only because an energy independent state is economically important but also due to the energy transition as a response to fossil fuel emissions and different climate change scenarios. For instance, for continental Portugal, a recent electrical production balance (**Fig. 1.6**) shows the contribution that the different renewable energy sources have in the total electricity generated for the month of May 2020, corresponding to about 71.6 %. During this month, Hydro power generated ≈1085 GWh, Wind power ≈679 GWh, Natural Gas ≈598 GWh, Fossil Cogeneration ≈348 GWh, Bio-energy ≈253 GWh, Solar ≈127 GWh, and Coal ≈10 GWh. With the country's high potential for solar energy harvesting, increasing the number of solar stations in the southern region will bring higher energy security, a reduction of the fossil fuel dependency, and a higher contribution in the overall energy mix, which is currently dominated by Hydro and Wind power in the northern region of the country. In particular, due to the desertification of this part of the country in the next decades, as a consequence of Climate Change, it is expected a higher number of CSP than PV systems in the region, since PV is less efficient than CSP under very high temperatures. Such aspects reflect the importance that solar energy systems will have in the future, particularly for countries committed to a renewable energy transition.

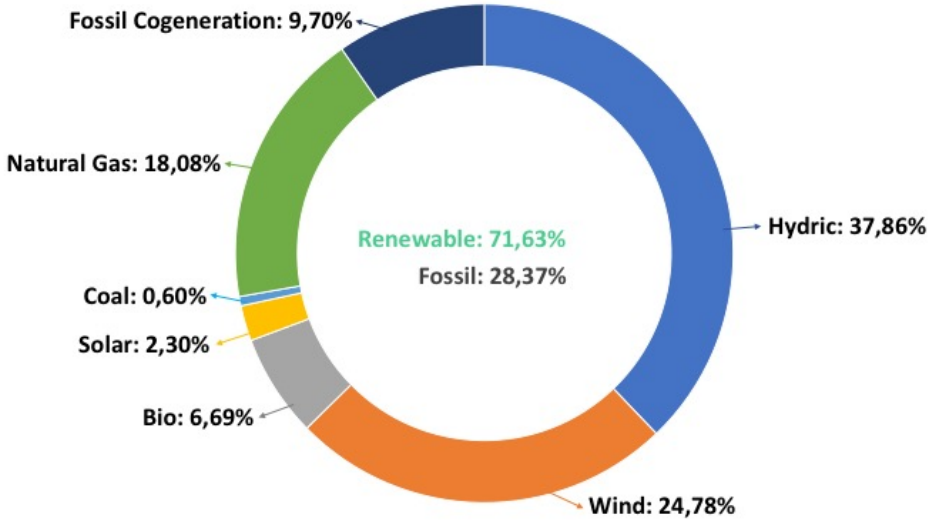

Figure 1.6: Electrical production balance from the different renewable energy sources in continental Portugal (May 2020). Adapted from https://www.apren.pt/en/renewable-energies/production/.

To improve the Solar Energy sector, increasing the number of power stations is fundamental. In fact, as part of the Portuguese National Plan of Energy and Climate for 2021-2030 [77], a substantial increase of installed capacity for electrical production is expected to occur. This commitment is in line with the established milestones for the 2030 horizon, where, at national level, a future with neutral carbon is planned. As a consequence of the improvement in the renewable sector, about 80 % of the Portuguese electrical production is expected to be reached by 2030 (**Fig. 1.7**). Of all the renewable resources, Solar is the one that will have the highest growth, with a contribution of about 31 % in in the next decade.

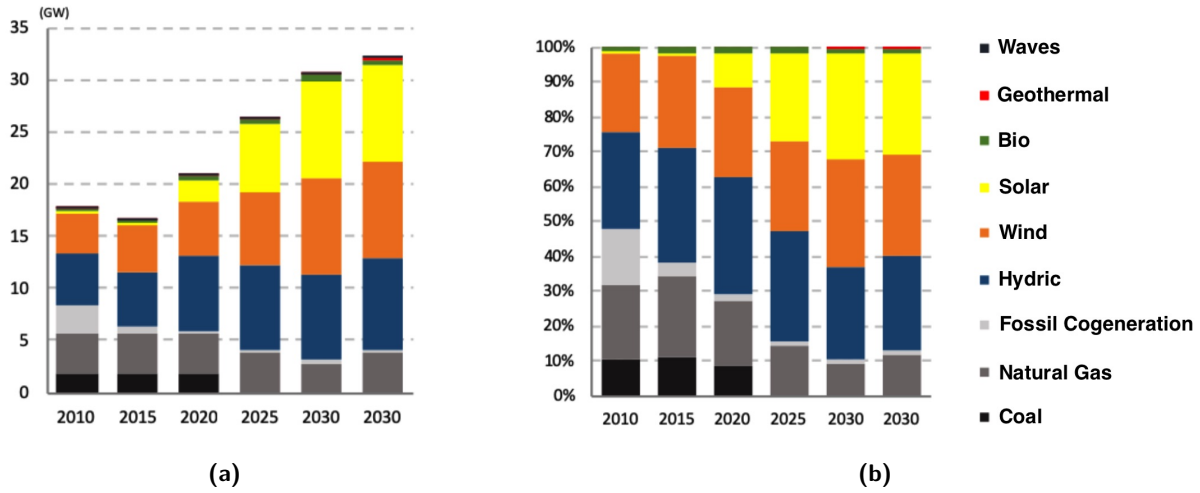

(a) **(b)**

Figure 1.7: Estimates of installed capacity, in (a) GW and in (b) %, for the electrical production obtained from different sources of renewable energy, as part of the 2021-2030 horizon in Portugal. Adapted from: [77].

Aside from the increase number of power stations, an efficient operation of such systems is also important. In the context of CSP plants management, information regarding the next-hour or next-day of DNI is fundamental for the plant operator, particularly if accurate forecasts of DNI are available. However, several issues must be fixed in the next years to improve current forecasts from NWP models and the sub consequent energy output predictions from power plants models.

An inherent problem in NWP is the existence of errors in the initial state of a model, which are directly linked to the number of available ground observations. Therefore, increasing the number and data acquisition quality of measuring stations in the future will allow to reduce such errors in NWP. This effort is not only restricted to ground based stations but also to airborne (e.g. airplanes) and extra-terrestrial (e.g. satellites) measurements. In the context of using DNI forecasts for CSP operations, an increased number of observations will also contribute to improve the solar assessment, a crucial step prior to the deployment of such solar systems, which are an emerging technology, as showed by **Fig. 1.5b**.

An overall difficulty still exists in NWP to provide accurate forecasts of DNI due to cloud and aerosol misrepresentation from the models. With the constant developments towards computer technology and sophisticated numerical methods (for instance, in the field of artificial neural networks), it is expected in the next decades (possibly in the following years) the achievement of a higher level of accuracy concerning this solar resource. On the short-term, aside from the continuous release of new operational radiation schemes for NWP models, some techniques can already be implemented to improve DNI forecasts from NWP models. For instance, the use of hybrid nowcasting systems composed by higher resolution models and all-sky imager (ASI) systems [78], which allows to track cloud movements. Such methods can allow to generate more refined short-term forecasts of solar radiation for energy applications than the previous state-of-the-art (e.g. [79, 50, 80]. Additionally, including a prognostic aerosol scheme and an aerosol data assimilation system, which can be carried out by the CAMS system (ECMWF), instead of climatological aerosol monthly mean values, will also contribute to increase forecast accuracy, particularly during clear sky days (i.e. maximum rentability periods for CSP plants).

1.4 Motivation and previous work

1.4.1 Synopsis

The work that led to the writing of this thesis was conducted entirely at the University of Évora (UÉ) in Portugal, in between the Institute of Earth Sciences (ICT- *Instituto de Ciências da Terra*) and the Renewable Energies Chair (CER- *Cátedra Energias Renováveis*) facilities. Several reasons guided the author to perform his research work at this university: i) the opportunity of pursuing an academic career in Atmospheric Sciences after obtaining his Master Degree in Geophysical Sciences (with the specialization in Meteorology) at the Faculty of Sciences, from the University of Lisbon; ii) after his graduation, and before starting the doctoral programme in Earth and Space Sciences (with the specialization in Atmospheric and Climate Physics) at the UÉ, the author participated in other research works, such as in the field of Atmospheric Electricity at the ICT. During his research, the author started to be more acquainted with the renewable energy topic and the implications that solar radiation forecasts have in CSP technologies. Particulary, the use of the nebulosity index for the determination of fair-weather (i.e. clear sky) days, which was performed using solar radiation data (more details are given below); iii) the fact that both the ICT and CER provide high-quality resources for the study of solar radiation, including state-of-the-art measuring equipment and historical data for solar radiation assessment, maintaining a national network of 13 operational stations scattered across Portugal. Moreover, leading research regarding CSP technology is being conducted at UÉ with two experimental platforms outside Évora city, namely the Évora Molten Salt Platform (EMSP) and the *Plataforma de Ensaios de Coletores Solares* (PECS); iv) the fact that this research work could be carried out in the Alentejo, a region with one of the highest solar potential in Europe; and the v) already existing collaborations with several national and international top institutions, such as the Portuguese Meteorological Service (IPMA- *Instituto Português do Mar e da Atmosfera*) and the German Aerospace Center (DLR- *Deutsches Zentrum für Luft- und Raumfahrt*).

With the available tools, and considering that CSP is an emerging technology, this thesis is a contribution for the improvement of future CSP deployments, operational strategies and energy dispatchability procedures, particularly in southern Portugal, an optimal region for solar prospects. Attention to this subjects will be given in the following chapters.

1.4.2 Knowledge acquired prior to this thesis

After accomplishing his Master Degree, the author had gained experience in other fields of Atmospheric Sciences, such as in Atmospheric Electricity. As a result, several first-author publications were accomplished [81, 82], in which the former was published already during the author's first academic year as PhD student. In fact, these research works allowed the author to be acquainted with meteorological and, particularly, solar radiation measurements (DNI, GHI and DHI), as well as the required data quality treatment. Moreover, the nebulosity index K_n was used as means to characterize the diurnal variability of solar irradiance, allowing

the selection of fair-weather (i.e. clear sky) days. Likewise, the clearness index would be latter used for GHI and DNI (k_t and k_b, respectively) characterization in the assessment of solar radiation in the Alentejo region (Chapter 3).

The determination of fair-weather days in Graciosa Island of the Azores Archipelago allowed to analysed measurements of the atmospheric electric field under different K_n values for the study of the Globlal Electric Circuit variability (**Fig. 1.7**). The results showed that under these conditions the Island's electrical Potential Gradient was locally affected by the marine air, inflicting diurnal variations from the classic Carnegie Curve. It was also found that, on a global scale, seasonal changes in the Island's Potential Gradient depicted signatures of large scale systems such as the El Niño Southern Oscillation (ENSO).

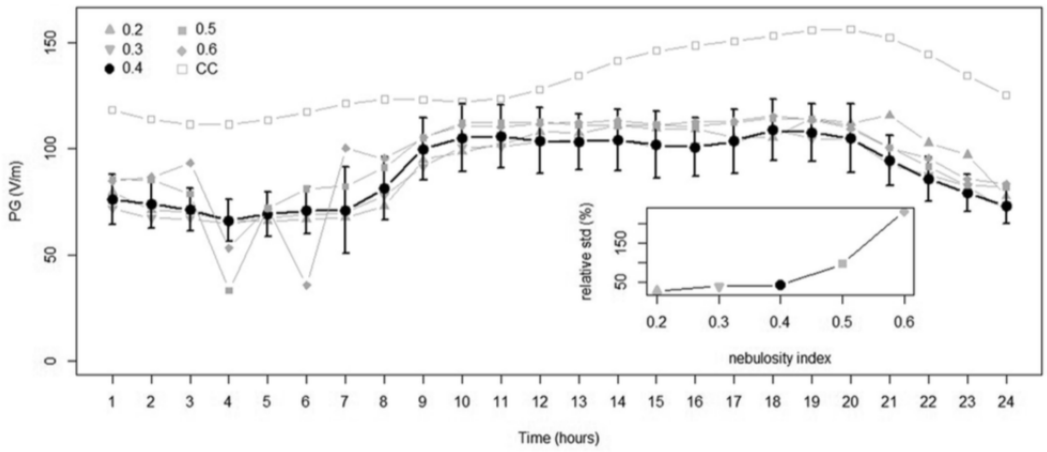

Figure 1.8: Daily averaged Potential Gradient (PG, in V/m) for each daily average K_n below 0.2, 0.3, 0.4, 0.5 and 0.6, together with the general Carnegie curve (empty squares time series). Error bars were added to the Potential Gradient (PG) curve corresponding to $K_n < 0.4$, whilst the inset plot shows the relative standard deviation (%) for each curve.

1.5 Thesis structure

After the introductory chapter, the remainder of this thesis is structured as follows: Chapter 2 describes the data and methodology used in the subsequent chapters, which correspond to different stages of development regarding this thesis; Chapter 3 concerns the use of short-term forecasts of solar radiation from the ECMWF in the Alentejo region, as well as important forecasting skill and error metrics considering different locations; since forecast uncertainty is inherent in DNI predictions due to cloud and aerosol representations in NWP models, Chapter 4 presents several approaches to improve hourly and daily predictions of DNI; the use of DNI forecasts for operational purposes of CSP systems is presented in Chapter 5, in which predictions of electrical and thermal energy values from different CSP simulations are carried out with a power plant model simulator; discussion and final conclusions regarding all the research topics presented in this thesis are given in Chapter 6; extra material from chapters 4 and 5 are accordingly summarized in appendices C and A, while appendix B comprises research work carried out by the author prior to the thesis.

All the work that was led to the writing of this thesis resulted in several publications as first author and as co-author through other research collaborations. This includes peer-review journals, conferences and other types of communications (listed below). As part of the main structure of this thesis, several first-author publications are presented in a non-chronological order, in which Chapter 2 sums up the methodology adopted in the following chapters: the majority of Chapter 3 is based in the first publication [83] with all the performed measured and predicted data analysis, where the last section is part of a third publication [84], in which a comparative analysis between the McRad and the ecRad is shown; Chapter 4 is entirely based in the fourth research work [85], except the subsection regarding CSP operations with improved forecasts, which are presented in the following chapter; Chapter 5 comprises several research studies performed over the course of this thesis, including the regional evaluation of the solar resource from the first publication, the Gemasolar and Andasol 3 simulations, from the second [86] and third [84] publications, and also a preliminary analysis, from the economical point of view, regarding the used of adjusted rpedictions in the simulation of Andasol 3, as demonstrated in the last part of the fourth publication. With this in mind, it should be noted that the selected order of chapters does not follow chronologically the publication dates of the published articles. The reason for this choice was to create a thesis written with unity and scientific coherence in face of the initial proposed milestones of the author's doctoral programme (as discussed in the final conclusions section in Chapter 6). In this context, text changes were performed over the original content from the publications in order to consolidate the reading between chapters, allowing a clear understanding of the presented topics. For instance, small introductory paragraphs were added at the beginning of each chapter, as well as few minor language corrections to enrich the overall presented analysis.

1.6 Research dissemination

The following publication lists are presented in the chronological order, i.e. from the most recent to the oldest one.

Peer-review journals:

- Francis M. Lopes, Ricardo Conceição, Hugo G. Silva, Rui Salgado and Manuel Collares-Pereira. Improved ECMWF forecasts of direct normal irradiance: a tool for better operational strategies in concentrating solar power plants. Renewable Energy 2020, 163, 755-771. https://doi.org/10.1016/j.renene.2020.08.140
- Francis M. Lopes, Ricardo Conceição, Thomas Fasquelle, Hugo G. Silva, Rui Salgado, Paulo Canhoto, Manuel Collares-Pereira. Predicted direct solar radiation (ECMWF) for optimized operational strategies of linear focus parabolic-trough systems. Renewable Energy 2019, 151, 378-391. https://doi.org/10.1016/j.renene.2019.11.020
- Francis M. Lopes, Ricardo Conceição, Thomas Fasquelle, Hugo G. Silva, Rui Salgado, Paulo Canhoto, Manuel Collares-Pereira. Short-term Forecasts of DNI from the Integrated Forecasting System (ECMWF) for Optimized Operational Strategies of a Central Receiver System. Energies 2019, 12, 1368. https://doi.org/10.3390/en12071368
- Francis M. Lopes, Hugo G. Silva, Rui Salgado, Afonso Cavaco, Paulo Canhoto, Manuel Collares-Pereira. Short-term Forecasts of GHI and DNI for Solar Energy Systems Operation: assessment of the ECMWF Integrated Forecasting System in Southern Portugal. Solar Energy 2019, 170, 14-30. https://doi.org/10.1016/j.solener.2018.05.039

Conferences:

- Francis M. Lopes, Ricardo Conceição, Hugo G. Silva, Rui Salgado, Paulo Canhoto, Manuel Collares-Pereira. Predictive Value of Short-term Forecasts of DNI for Solar Energy Systems Operation. SolarPACES 2018, AIP Proceedings 2126, 190010(2019). https://doi.org/10.1063/1.5117707

Collaborations:

- Ailton Tavares, Ricardo Conceição, Francis M. Lopes, Hugo G. Silva. Direct Normal Irradiance assessment based on Global Horizontal Irradicance ground measurements: case study for Portugal (Southern Europe). (in development)
- Ricardo Conceição, Francis M. Lopes, Daniel Lopes, Ailton Tavares. Soiling effect in second-surface CSP mirror and improved cleaning strategies. Renewable Energy 2020, 158, 103-113. https://doi.org/10.1016/j.renene.2020.05.054

- Bijan Nouri, Stefan Wilbert, Niklas Blum, Pascal Kuhn, Thomas Schmidt, Zeyad Yasser, Thomas Schmidt, Luis F. Zarzalejo, Francisco M. Lopes, Hugo G. Silva, Marion Schroedter-Homscheidt, Andreas Kazantzidis, Christian Raeder, Philippe Blanc and Robert Pitz-Paal. Evaluation of an all sky imager based nowcasting system for distinct conditions and five sites. AIP Conference Proceedings 2020, 2303, 180006. https://doi.org/10.1063/5.0028670
- H.G. Silva, Edgar F.M. Abreu, Francis M. Lopes, A. Cavaco, P. Canhoto, J. Neto, M. Collares-Pereira. Solar Irradiation Data Processing using Estimator Matrices (SIMS) validated for Portugal (Southern Europe). Renewable Energy 2019, 147, Part I, 515-528. https://doi.org/10.1016/j.renene.2019.09.009
- Ricardo Conceição, Francis M. Lopes, Hugo G. Silva, Manuel Collares-Pereira, 2019. PV system design with the effect of soiling on optimum tilt angle. Renewable Energy 2019, 133, 787-796. https://doi.org/10.1016/j.renene.2018.10.080
- H.G. Silva, F. Lopes, S.M. Barbosa, K. Nicoll, S.N. Pereira, R.G. Harrison, M. Collares-Pereira. Saharan dust electrification perceived by a triangle of atmospheric electricity stations in Southern Portugal. Electrostatics 2016, 84, 106-120. https://doi.org/10.1016/j.elstat.2016.10.002

Communications:

- Francis M. Lopes, Hugo G. Silva, Rui Salgado, Manuel Collares-Pereira, 2019. Utilidade das previsões do ECMWF de radiação normal directa na produção eléctrica de centrais de concentração solar térmica. III Congresso Luso- Extremadurense de Ciências e Tecnologia, Évora, Portugal, November 25-26, 2019. (Poster)
- Francis M. Lopes, Hugo G. Silva, Rui Salgado, Manuel Collares-Pereira, 2019. Assessment and forecast of direct normal irradiance in Alentejo region for CSP systems. 11° Simpósio da APMG 2019, Cascais, Portugal, March 25-27, 2019. (Poster)
- Francis M. Lopes, Hugo G. Silva, Rui Salgado, Manuel Collares-Pereira, 2018. Short-term Forecasting for Direct Normal Irradiance with Numerical Weather Prediction Models in Alentejo (Southern Portugal): Implications for Concentration Solar Energy Technologies. IPMA Workshop, A Previsão Numérica do Tempo em Portugal: Estado da Arte e Novos Desafios. Lisbon, Portugal, November 26-27, 2018. (Presentation)
- Francis M. Lopes, Ricardo Conceição, Hugo G. Silva, Rui Salgado, Paulo Canhoto,Manuel Collares-Pereira, 2018. Predictive Value of Short-term Forecasts of DNI for Solar Energy Systems Operation. SolarPACES 2018. Casablanca, Morocco, October 02-05, 2018. (Poster)
- Francis M. Lopes, Hugo G. Silva, Afonso Cavaco, Ricardo Conceição, Rui Salgado, Paulo Canhoto, Manuel Collares-Pereira, 2018. ECMWF Forecasts of DNI Towards a more Efficient Management of Concentrated Solar Thermal Plants. 4° Simpósio IPES: A Concentração Solar e o Futuro. Évora, Portugal, September 24-25, 2018. (Presentation)

- Francis M. Lopes, E.F.M. Abreu, A. Cavaco, R. Salgado, H.G. Silva, P. Canhoto, M.J. Costa, C. Lac and Q. Libois. Simulation of Direct Normal Irradiance (DNI) in Portugal with the Meso-NH Model. Several Case Studies. 9th meeting of Meso-NH Users, CNRM, Toulouse, France, 12-13 October 2017. (Presentation)
- Salgado, R. Lopes, FM, et al., 2017 DNI Meso-NH in Alentejo (Southern Portugal). 10 Simpósio da Associação Portuguesa de Meteorologia e Geofísica APMG 2017. Fundação Calouste Gulbenkian, Lisboa, 20-22 March 2017. (Poster)
- Lopes, FM, Silva, HG, Salgado, R, 2016. Determination of Fair-Weather Days from Solar Radiation Data: Application to Atmospheric Electricity. Workshop on Earth Sciences WES 2016, Évora, Portugal, December 8-10, 2016. (Presentation)

Other publications prior to this thesis:

- Francis M. Lopes, Hugo Gonçalves Silva, Alec J. Bennett, A. Heitor Reis. Global Electric Circuit research at Graciosa Island (ENA-ARM facility): first year of measurements and ENSO influences. Electrostatics 2017, 87, 203-211. https://doi.org/10.1016/j.elstat.2017.05.001
- Francisco Lopes, Hugo Gonçalves Silva, Rui Salgado, Miguel Potes, Keri A. Nicoll, R. Giles Harrison. Atmospheric Electric Field measurements near a Fresh Water Reservoir and the formation of the Lake Breeze. Tellus 2016, 68:31592. https://doi.org/10.3402/tellusa.v68.31592
- Francis M. Lopes, Hugo Gonçalves Silva, Kim Nitschke, and Eduardo Azevedo. Atmospheric Electric Field Measurements at Eastern North Atlantic ARM Climate Research Facility. Global Electric Circuit Evolution. EGU General Assembly 2016, 18, EGU2016-8552. https://meetingorganizer.copernicus.org/EGU2016/EGU2016-8552.pdf
- Salgado, R., Potes, M., Albino, A., Apolinário, J., Barbosa, S., Lopes, F. et al. Interactions Lake- Atmosphere: The ALEX 2014 Field Campaign and Numerical Simulations. Conference: LAKE 2015: 4th Workshop on Parameterization of Lakes in Numerical Weather Prediction and Climate Modelling. https://doi.org/10.13140/RG.2.1.4624.7842
- Lopes, F. Silva, H.G., Bárias, S., Barbosa, S.M. Preliminary results on soil-emitted gamma radiation and its relation with the local atmospheric electric field at Amieira (Portugal). Journal of Physics 2015: Conference Series 646, 012015. https://doi.org/10.1088/1742-6596/646/1/012015
- Barbosa, S.M., Lopes, F., Pereira, A., Neves, L. Temporal variability of radon in a remediated tailing of uranium ore processing – the case of Urgeiriça (central Portugal). Journal of Environmental Radioactivity 2015, 142, 14-23. https://doi.org/10.1016/j.jenvrad.2014.12.015

2

Methodology

The second chapter presents the adopted methodology and instrumentation used for solar radiation, including measurements, forecasts, and the power plant model used to simulate two CSP plants currently operational.

2.1 Observational data

2.1.1 Measurements

It is important to highlight the fact that the results obtained in this work are not restricted to one region only, since the obtained conclusions can be adapted to other similar regions that possess high solar potential, allowing better management of solar electrical power plants that demand high accuracy forecasts. For instance, regions that are located in arid climates away from major sources of pollution, such as south of the Iberian Peninsula, northern and southern Africa, Australia, South and North America. The work carried out during this thesis is focused in southern Portugal, also known as the Alentejo region, which has exceptional conditions for the installation and development of solar technologies, covering an area of ≈27,272 km^2 (i.e. ≈29.6 % of the country).

The climate in the southern region of Portugal, particularly in Alentejo, is mostly of the Mediterranean type (Csa, according to the Köppen classification), with a small area within the mid-latitude steppe (Bsk) category [82]. Maximum temperatures can reach between 31-35 °C on average during July and August, often reaching values close to 40 °C, or even higher. In this semi-arid region, the synoptic circulation during the summer months is dominated by the frequent development of the shallow Iberian low-pressure system inside a larger scale high-pressure system, the Azores anticyclone [87]. With a clean atmosphere, the region has exceptional conditions for solar irradiance harvesting, holding one of the highest solar resource potentials measured in Europe, with ≈1900 kWh/m^2/year in GHI and over 2100 kWh/m^2/year in DNI annual availabilities [88]. Usually, very low inter-annual variabilities for solar irradiance are observed in the region, with values reaching down to ≈1.4 % [89].

For these reasons, an operational network of 14 radiometric ground-based measuring stations was installed in Alentejo, as part of the DNI-ALENTEJO project (ALT20-03-0145-FEDER-000011). All stations were designed and implemented for the study of direct, global and diffuse irradiances, as well as their relation with meteorological variables (see [89]). The objective of this network was the mapping of solar irradiance, particularly DNI, as well as defining strategies for an improved regional operation of CSP plants. Amongst all available ground-measuring stations, four were selected as the most suitable for this analysis, particularly for the regional evaluation of solar radiation predictions: Évora (EVO), Mitra (MIT), Portalegre (PRT) and Alcoutim (ALC), while only EVO station was further used for the application of DNI forecasts in the operation of CSP systems. Besides providing coverage for the southern part of Portugal, some of these stations are relatively close from each other (**Fig. 2.1**). The EVO station (38.567686°N, 7.91172°W) is located within Évora city, on the top of the ICT research facility. In the countryside, at ≈13 km of the city, the closest station from EVO is the MIT station (38.530522°N, 8.011221°W) located in the PECS facility, while to the north is the PRT station (39.269221°N, 7.442716°W), located in Portalegre city (≈340 m). More into the south remains the ALC station (37.441844°N, 7.744901°W), in an open area in the outskirts of Alcoutim city (≈30 km from the seashore). These two last stations are located in regions where the orography is characterized by mountains, allowing the frequent occurrence of small scale fogs.

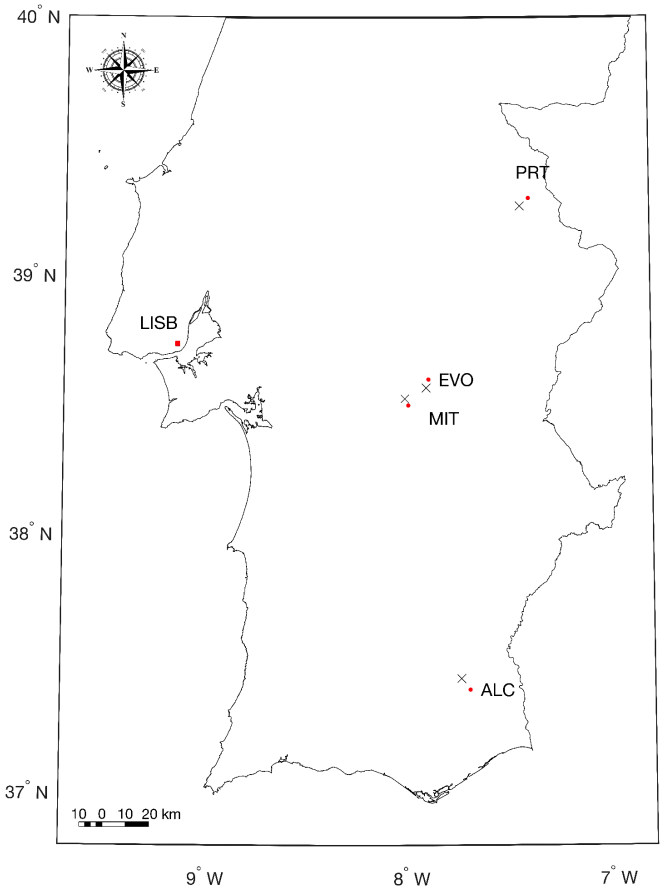

Figure 2.1: Geographic locations of the measuring sites at Évora (EVO), Mitra (MIT), Portalegre (PRT) and Alcoutim (ALC) in southern Portugal. A depiction is shown of the nearest IFS locations (red dots) to the measuring stations (black crosses). Geographical reference to the capital, Lisbon (LISB), is also made (red square).

Maintenance protocols were established during the operation of these stations, which consisted typically in a daily cleaning (i.e. using a microfiber cleaning cloth and, if necessary, distilled water to clean each sensor), together with a daily calibration checkup of the instruments. For this thesis, one station stands as a reference station (EVO) to the remaining ones, due to a close proximity to the measuring location. In this station, a regular maintenance of the instruments was performed continuously to ensure the quality of the data used. In this context, soiling effects [90], or any significant periods of missing data, are not present in EVO. Since the MIT station is relatively close to EVO station, a regular maintenance was also performed. This allowed the possible use of MIT as a neighbour station to EVO, in order to fill any eventual missing period of data due to equipment malfunction (e.g. sudden power shutdowns).

Measured data was acquired with a sampling rate of 5 seconds and then averaged and recorded every

1-minute, with an exception for the ALC station, in which only 15-minute records were available. Hourly data was calculated through hourly backward means, i.e. by considering the previous sixty 1-minute records of measured data, whereas hourly mean values in ALC were based on the 15-minute records. State-of-the-art measurements for solar radiation were performed through the use of Kipp & Zonen instruments (https://www.kippzonen.com). The DNI was measured with pyrheliometers (model CHP1), World Meteorological Organization (WMO) First Class instrument, with an aperture angle of 2.5 ° and an associated estimated uncertainty on a daily basis of < 1 %. The pyrheliometers are calibrated every 2 years following the International Organization for Standardization (ISO) 9059:1990 standard. Both GHI and DHI were measured with pyranometers (model CMP11), following the ISO 9060 Secondary Standard with an associated estimated uncertainty at daily basis of < 2 %. The pyranometers were also calibrated every 2 years following the ISO 9847:1992 standard. Regarding the ISO standards used, a detail description for each one is available online (https://www.iso.org/obp/ui). All instruments were mounted on a SOLYS2 Sun-Tracker (**Fig. 2.2**), which had a Sun sensor, in the case of EVO and MIT stations, for a more accurate solar tracking.

(a) One pyrheliometer is used for DNI measurements (MIT station).

(b) Two pyranometers are used for GHI and DHI measurements (MIT station).

Figure 2.2: Solar monitoring stations include a SOLYS2 Sun-Tracker, which provides a mounting for a pyrheliometer and two pyranometers. The station moves horizontally (azimuth) and vertically (zenith) to follow the solar arc.

Local meteorological measurements are also considered in this thesis, particularly for the simulation of CSP systems with EVO data, being acquired with standard meteorological measuring equipment. These included air temperature and relative humidity through the use of a hygro-thermo transmitter from Thies Clima (https://www.thiesclima.com), model 1.1005.50.512, installed near the SOLYS2 Sun-Tracker. Following these, wind speed and atmospheric pressure at ground level were also recorded using an anemometer from Vector Instruments (https://www.windspeed.co.uk), model A100R, and a barometric pressure sensor from Campbell Scientific (https://www.campbellsci.com), model PTB101B-CS105, respectively. It should be noted that, in the case of EVO station, atmospheric pressure is not available and the wind is not representative, since the flow is disturbed by nearby buildings. For these reasons, hourly data from IPMA station, located at Évora aerodrome (38.53654°N, 7.88795°W), i.e. ≈4 km from EVO station (**Fig. 2.3**), was used as representative of the wind speed and atmospheric pressure in EVO station.

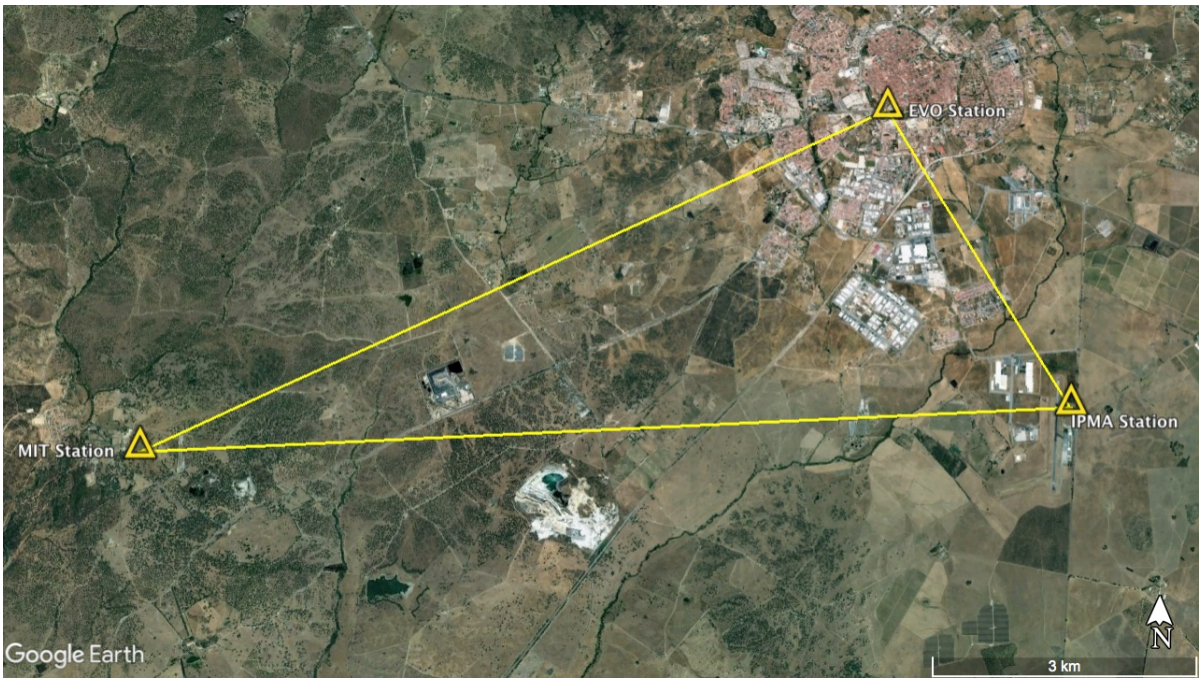

Figure 2.3: Geographic location of the ground-based station used as a reference in this study, Évora (EVO), and two other stations, Mitra (MIT) and Évora Aerodrome (IPMA), that were used for EVO data quality control. All rights reserved (© Google Earth 2019).

2.1.2 Clearness Index

Several models have demonstrated an important role in the development of new forecasting methods [91]. For instance, linear models techniques that make usage of forecasted time series, providing successful predictions. One example are techniques based on the clearness index, which allows to define the type of irradiance reaching the Earth's surface, and further assess the forecasts towards measurements, such as in [92]. Being a fundamental tool in solar radiation analysis [21], hourly clearness indices (k) are used in this thesis considering GHI (k_t) and DNI (k_b). This dimensionless parameter is defined as the ratio between terrestrial (i.e. observed at the Earth's surface) and extraterrestrial (i.e. calculated at TOA) irradiances on a horizontal and normal surface, respectively for GHI and DNI, as described by [31]:

$$k_t = \frac{GHI_{obs}}{GHI_{TOA}}, \tag{2.1}$$

$$k_b = \frac{DNI_{obs}}{DNI_{TOA}}. \tag{2.2}$$

The approach in using irradiance values at TOA has been documented in literature [93, 94]. To this end, in this thesis the considered total solar irradiance value at TOA, i.e. the total power from the Sun at the average Earth-Sun distance, has the value of I_0=1361 W/m^2, as referenced by [95]. The GHI and DNI calculations at TOA are described in **Eq. 2.77** by [31], as follow:

$$GHI_{TOA} = I_0 \left[1 + 0.033 \cos\left(\frac{360N}{365}\right)\right] \times CZA, \tag{2.3}$$

$$DNI_{TOA} = I_0 \left[1 + 0.033 \cos\left(\frac{360N}{365}\right)\right], \tag{2.4}$$

where CZA is the cosine of the solar zenith angle and N is the day number in the year.

Moreover, daily clearness indices (K) can also be expressed through daily values of GHI (K_t) and DNI (K_b), as follow:

$$K_t = \frac{E_t^{obs}}{E_t^{TOA}}, \quad \text{with} \quad E_t = \sum_1^{24} GHI, \tag{2.5}$$

$$K_b = \frac{E_b^{obs}}{E_b^{TOA}}, \quad \text{with} \quad E_b = \sum_1^{24} DNI, \tag{2.6}$$

where E_t and E_b are the irradiation availabilities (kWh/m^2), respectively for hourly GHI and DNI, which were simply calculated by considering the integration of daily irradiances values. Typical values of K_t can range from ≈0.1 to 0.9, while values of K_b are between ≈0 and 0.8, in which minimum and maximum values are found during overcast and clear (and very clean aerosol) sky conditions, respectively. The relative differences (%) of the total energy availability (i.e. considering the daily values) between measurements and

forecast model can be given by:

$$\Delta E_t = \left(\frac{\sum E_t^{\mathrm{mod}}}{\sum E_t^{\mathrm{obs}}} - 1 \right) \times 100\%, \tag{2.7}$$

$$\Delta E_b = \left(\frac{\sum E_b^{\mathrm{mod}}}{\sum E_b^{\mathrm{obs}}} - 1 \right) \times 100\%, \tag{2.8}$$

where the summations are expressed by the sum of the daily availabilities obtained in **Eq. 2.5** and **Eq. 2.6**.

2.1.3 Quality-control

As described by [96], there is no definitive procedure for data processing, however the application of proper filters to the measured data is important to perform a correct analysis of surface solar radiation. In this context, to ensure a high confidence level in the measurements, and to compare these with forecasted data, quality control procedures were carried out prior to the analysis. For consistency reasons, the same missing periods found in measurements were set equally in the forecast model output.

Since the measured data is site-dependent, it is important to know the context of the measuring location. Several factors can contribute to the variation of solar radiation at the surface (as described in [97]. For instance, geographical coordinates (latitude, longitude), astronomical factors (solar declination, daylight hours), geometric factors (solar azimuth angle), physical factors (scattering and absorption effects due to aerosol content present in the atmosphere), terrain topography, surface albedo, nearby structures (trees, buildings) and meteorological variables (clouds, air temperature, wind speed, air relative humidity, precipitation). For instance, in the MIT station, measurements of solar irradiance are influenced by local shadows due to the orographic unevenness of the terrain, since this station is situated in a small valley. Consequently, when using data from this station, a solar altitude threshold of 10° should be used, corresponding to nearly 1-hour after sunrise and 1-hour before sunset. This threshold was found to be the proper value to be considered in this station, allowing to avoid shadow and horizon interference near the morning and evening. Additionally, a relative closure function can also be considered to remove existing deviations related to calibration issues during experimental periods:

$$\left| 1 - \frac{(DHI + DNI \times CZA)}{GHI} \right| \times 100\% < 10\% \tag{2.9}$$

Moreover, remote locations of difficult man-made access often show large missing periods of recorded data (from a few days to several weeks), whether due to equipment malfunction or to sudden power supply shutdowns, which can last up to several hours. Thus, other filters should be applied in accordance to the characteristics of the selected region and specific location of the measuring equipment. The following quality control filters were taken into account in this work for all GHI and DNI measurements in southern Portugal:

1. Positive GHI and zero or positive DNI values, i.e. daylight hours were considered.

2. Days that have more than two hours of missing records, between sunrise and sunset, are rejected, while days with less than two hours of missing records have the corresponding gaps linearly interpolated from the values of the neighbouring hours.

3. Baseline Surface Radiation Network (BSRN) Global Network maximum and minimum physically possible limits [98].

2.2 Integrated Forecasting System

To simulate atmospheric processes, NWP models make use of equations based (as much as possible) in the fundamental principles of physics, requiring a large computational effort. Amongst a wide range of current operational models, the IFS, i.e. the global atmospheric model and data assimilation system from the ECMWF, stands as one of the highest scored NWP models in terms of medium range global weather forecasting capacity [99]. Several radiation schemes [100] have been used throughout the past decades to perform deterministic predictions of solar radiation in the IFS, in which major changes were accomplished. As described by [101], the first significant development started with the implementation of the Morcrette scheme in 1991. In the following years, improvements were made, culminating with the introduction of the Rapid Radiative Transfer Model [102], which allowed the simulation of clear sky irradiances with higher accuracy. In 2007, the radiation scheme was upgraded to the McRad version. This new version included an improved description of the land-surface albedo from observations carried out by Moderate Resolution Imaging Spectroradiometer (MODIS), which, being based on the Rapid Radiative Transfer Model, allowed the calculation of radiation fluxes (longwave and shortwave). Further information regarding this scheme can be consulted in [103]. The McRad experienced several improvements through the following years (cycles 32R2, 35R3, 41R1, 41R2 and 43R1) until recently (July 2017), with the replacement of the current (up to the present date) operational ecRad radiation scheme. Until such period, the IFS had used the Tegen aerosol climatology [104], which ended up being replaced by a more realistic monthly mean aerosol climatology from the CAMS system. The radiation transfer under cloudy periods is represented in the model through the Monte-Carlo Independent Column Approximation (McICA), which has been enhanced in the ecRad radiation scheme to reduce numerical noise.

The CAMS is able to predict aerosol concentrations, using a set of coupled modules for aerosol and chemistry, and an aerosol data assimilation system. A full coupled IFS-CAMS system is expected to be fully operational in future versions. However, an increase of more than 50 % towards the computational cost of the IFS [43] is delaying its implementation.

In this thesis, operational forecast data for the next 24 hours is provided by the IFS model with a forecast issue time set to start at 0 UTC using an average spatial resolution of $\approx$9 km ($0.125^\circ \times 0.125^\circ$). The acquisition procedure comprised several available parameters due to their influence in solar radiation, in particular, over DNI and the operational strategies of CSP plants. In addition to GHI and DNI, meteorological

variables, such as air temperature, dew point temperature, wind velocity components, total precipitation and total cloud cover, were also retrieved. Over the course of this thesis, two IFS radiation schemes were used for analysis. The first, i.e. the McRad, was used at an early stage of this thesis, particularly in most of Chapter 3 for the solar radiation assessment in Alentejo. At the end of this chapter, the second radiation scheme, i.e. the ecRad, was used to show the obtained improvements in comparison to its predecessor. Then, in the following chapters, towards the improvement of DNI predictions (Chapter 4) and their use in the operations of different CSP systems (Chapter 5), only the ecRad is considered. This change results naturally from the fact that during the time of this thesis the former radiation scheme from the IFS was replaced by the ecRad version (cycle 43R3) on July 2017. The irradiation parameters given by the McRad and the ecRad for the predicted direct irradiation are the total sky direct solar irradiance at surface (*fdir*) and the direct solar radiation incident on a plane perpendicular to the direct sun beam (*dsrp*). This means that, in order to obtain the predicted DNI, *fdir* needs to be divided by the deterministic hourly CZA parameter (in accordance to the selected location). Consequently, the predicted DNI from the McRad can be subjected to additional source of errors. A performance analysis was made in this thesis using EVO data at the end of Chapter 3, whilst a detailed description concerning the McRad and ecRad schemes is available in [100]. Moreover, GHI forecasts were also acquired from the IFS, through the surface solar radiation downwards (*ssrd*) parameter.

To compare predictions with actual measurements, hourly accumulated irradiation values (J/m^2) from the IFS were divided by 3600, being converted to mean energy flux values (W/m^2). The comparative analysis between predicted and measured data was carried out with the use of daily energy availabilities for GHI and DNI, i.e. E_t and E_b (kWh/m^2), respectively, considering the integration of hourly mean values, which were also used for the monthly availabilities. Corresponding relative differences, i.e. ΔE_t and ΔE_b (%), for the total energy availability between observations and model for a given period of days were also calculated.

Regarding meteorologic variables, following variables were considered: air and dew point temperatures at 2 m height (respectively *t2m* and *d2m*, in K); horizontal components of wind velocity at 10 m height (*u* and *v*, in m/s); total accumulated precipitation (*tp*, in m), i.e. the sum of convective and large scale precipitation; surface pressure (*sp*, in Pa); total cloud cover (*tcc*, in %), i.e. the percentage of the sky hidden by all visible clouds; and air relative humidity at 2m height. The latter was computed having into consideration *t2m* and *d2m*, as described by [105]:

$$rh2m = \frac{6.11 \times 10^{\frac{7.5\times \mathrm{d2m}}{237.7+\mathrm{d2m}}}}{6.11 \times 10^{\frac{7.5\times \mathrm{t2m}}{237.7+\mathrm{t2m}}}}. \tag{2.10}$$

2.3 Forecasting metrics

Due to forecasting inaccuracies in NWP, characteristic deviations from measurements exist, particularly in hourly predictions of DNI. For instance, overestimation is frequent under an overcast sky due to underestimation of the radiative effects of clouds. On the other hand, under a very clean (dirty) atmosphere, hourly predictions of DNI underestimate (overestimate) measurements due to the use of monthly aerosol climatology instead of actual values.

In order to quantify the forecast error and compare the performance of different forecasts, it is important to compute the forecasting accuracy. Although several conventional metrics exist, to determine the most appropriate ones will depend on the end user [36]. For instance, evaluation metrics can allow CSP plant operators to perform an accurate estimation of the costs related to forecasting errors. A very particular important evaluation metric recommended for the application of electrical grid management is the RMSE, **Eq. 2.11**, due to the importance that large errors have for the safety of an electrical grid system [17]. Other conventional metrics can be used to assess the forecast error: the MBE, **Eq. 2.12**, allows to characterize the performance of the model in comparison to the measurements by establishing a balance between over- and underprediction [36]; the MAE, **Eq. 2.13**, which is a global error measure metric that allows to average the magnitude of the error without the account for extreme forecast events, as opposed to the RMSE which gives more weight to large errors [106]. These relations can be expressed as follows:

$$RMSE = \sqrt{MSE} = \sqrt{\frac{1}{n} \times \sum_{j=1}^{n} \left[I(j) - \hat{I}(j) \right]^2}, \tag{2.11}$$

$$MBE = \frac{1}{n} \times \sum_{j=1}^{n} \left[I(j) - \hat{I}(j) \right], \tag{2.12}$$

$$MAE = \frac{1}{n} \times \sum_{j=1}^{n} \left| I(j) - \hat{I}(j) \right|, \tag{2.13}$$

where I(j) and $\hat{I}$(j) are the measured and the predicted value at time j, respectively, while n is the number of assessed pairs. A perfect prediction would yield a RMSE or a MAE of null value, while a MBE equal to zero would correspond to an unbiased prediction. In the latter, if negative or positive values are to be obtained, then an over- or underestimation by the model will be depict, respectively. Together with these metrics, Pearson correlation coefficient, r, and coefficient of determination, R^2, are also used in the analysis.

To assess the overall level of agreement between the forecast model and measurements, forecasting skill can be taken into account through appropriated forecasting metric, such as the mean square error Skill Score (SS). The SS is computed considering the MSE of both forecast and persistence (i.e. persistence of

the previous measured 24-hour values) models with respect to measurements, as given by [107]:

$$SS = 1 - \frac{MSE_{\text{for}}}{MSE_{\text{per}}}, \tag{2.14}$$

where MSE_{for} and MSE_{per} are error metrics respectively for the forecast model and persistence calculated through **Eq. 2.11**. The latter is a simple forecast method obtained by persisting the previously measured values over the forecast range. If the obtained SS is equal to one, then a perfect forecast is achieved, while negative SS values correspond to worse performances by the model than the persistence. Null values indicate no improvement over the reference. Additionally, probability density functions (PDF's) were used, allowing to determine the probability distribution (i.e. the frequency of occurrence) of forecasted and measured values.

2.4 CSP plant model

In general, a CSP system consists in the harvesting of solar energy through the conversion of solar radiation into thermal energy and then into electrical energy. The conversion from solar radiation into thermal energy can be achieved through four commercial types of concentrating solar systems: linear parabolic-trough collector, linear Fresnel reflector, central receiver and parabolic dish (**Fig. 2.4**, adapted from [108]). These can be classified according to the focus type (line or point), the receiver type (fixed or movable) or the concentration level (medium or high), as described in [109] and [110]. Apart from the fact that these systems have different characteristics, they share the same operating principle, which consists in the concentration of solar radiation from reflector elements to receivers. Within these, a transfer medium, denominated as a heat transfer fluid (HTF), is heated, reaching temperatures up to 393 °C in the case of parabolic-trough commercial CSP systems. A thermodynamic power cycle equipped with a turbine is then used to convert thermal energy into electric energy, most commonly a Rankine cycle, in which steam is generated by receiving heat from the HTF at an appropriate heat exchanger. Then, a fraction of the thermal energy generated during the day can be stored in a liquid or solid medium (e.g. molten salt), allowing the energy use at night and during cloudy periods in order to maintain the power plant operational. More details concerning the complexities of the Rankine cycle in CSP are available in literature [111, 112].

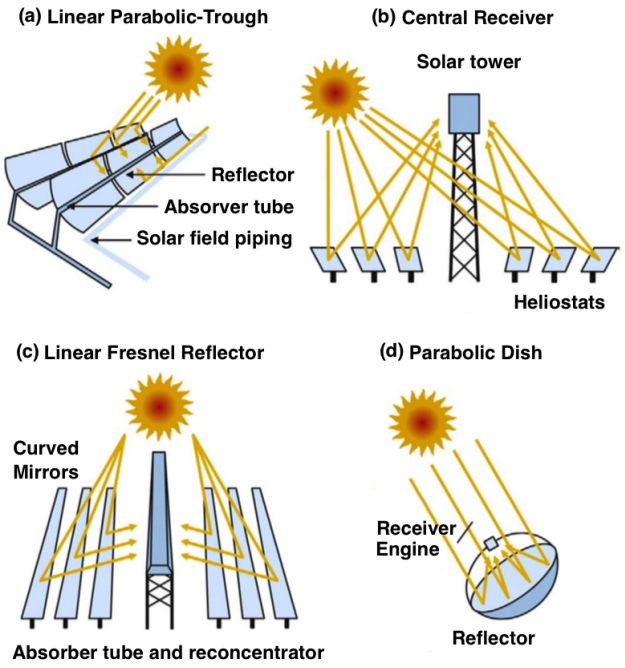

Figure 2.4: Four commercial types of solar concentrators: (a) linear parabolic-trough collector; (b) central receiver concentrator; (c) linear Fresnel reflector; (d) parabolic dish reflector. Adapted from [107]

Power plant models exist to simulate these systems and obtain to the corresponding performance outputs. One example is the SAM model [74], developed by the National Renewable Energy Laboratory (NREL) from the U.S. Department of Energy, being a freely available modelling software for renewable energy systems. The model has implemented the transient system (TRNSYS) simulation tool (available online from https://www.trnsys.com/index.html) for the modelling of concentrating solar thermal power plants, being built around three components: a user-friendly interface, calculation engine and programming interface. All input and design variables, simulation controls, as well as a summary of the results in the form of data tables and graphs, are provided in the user interface. The calculation engine (run by the SAM simulation core), performs a step-by-step simulation of the power plant operation, calculating hourly values through a performance module, thus allowing to compute the respective annual performance metrics of CSP systems. Since the source code for the SAM simulation and calculation modules is not available to the public, detailed information concerning the use of the software is available online (https://sam.nrel.gov/). The SAM (version 2017.9.5) was used in this thesis (Chapter 5) to validate the use of day-ahead forecasts of DNI from the IFS for the operational management of CSP plants, namely central receiver (CR) and linear focus parabolic-trough (PT) systems.

The simulation of a power plant with the configuration of a CR system requires information regarding all the design and control parameters characteristic of such systems. A CR system, also known as a solar power tower, uses sun-tracking mirrors (heliostats) to focus the Sun's direct beam onto a receiver installed at the top of the tower. Within the receiver, the HTF is then heated, reaching temperatures up

to 565 °C, allowing the generation of water steam, through a heat exchanger. The latter is then used by conventional turbine-generators, to produce electricity (Rankine cycle). CR systems have several advantages in comparison to PT systems, such as higher temperatures of use, superior heat transfer and energy storage capabilities, making use of molten salt as HTF. Moreover, in comparison to PT, CR systems have the capability to operate with direct circulation, allowing the power plant to store and produce electricity at the same time. One example of this kind of power system is the 19.9 MW_e Gemasolar thermosolar plant located in the Sevilla province (Spain), which has been operational since April 2011. The power plant possesses a 15-h storage capacity and is surrounded by 2650 heliostats (**Fig. 2.5**), within an area less than 200 hectares. The Gemasolar was intended to produce 110,000 MW_eh/year [113], however, probably due to technical issues created by the new challenges that were addressed during the operation of the plant, an annual generation of 80,000 MW_eh/year is reached. More information concerning design configurations of the Gemasolar power plant is available online (https://solarpaces.nrel.gov/gemasolar-thermosolar-plant). It should be noted that, full access to the actual information regarding the Gemasolar configuration is not possible, due to privacy reasons. For this reason, the Gemasolar plant simulation in the SAM uses a few design and control input parameters that are SAM's standard values for CR systems, while others are research-based assumptions (see **Table A.1**, Appendix A).

Figure 2.5: Gemasolar thermosolar power plant located in the province of Sevilla, Spain (37.560613°N, 5.331508°W). All rights reserved (© Google Earth 2019).

Similarly, to simulate a PT system with the same configurations as the Andasol 3 CSP (37.228644°N, 3.051147°W), an upgraded installation of Andasol 1 and 2 (**Fig. 2.6**), located in the Spanish municipalities of Aldeire/La Calahorra (Granada, Spain), is considered. Being operational since August 2011, this 50 MW_e commercial power plant uses a linear focus PT system that runs with thermal oil (Downtherm A) as HTF, with a 7.5-hour indirect molten salt storage capacity at full load. The system, which was designed to reach a net annual energy generation of 165,000 MW_eh/year at typical meteorological conditions [114], currently has an estimated annual energy generation of 175,000 MW_eh/year. Since the simulation is centred in Évora, instead of Granada, a direct comparison between simulated outputs and real operational values will not be the focus of the analysis. Concerning the available information, details on the Andasol 3 CSP project can be consulted online (https://solarpaces.nrel.gov/andasol-3). Like in the Gemasolar simulation, full access to the actual information of Andasol 3 was not possible due to privacy reasons, thus few design and control input parameters are SAM's standard values for PT systems and others are research-based assumptions (see **Table A.2**, Appendix A).

Figure 2.6: Andasol 1, 2 and 3 CSP located in Aldeire, Spain (37.228644°N, 3.051147°W). All rights reserved (© Google Earth 2019).

It should be noted that intermittent generation technologies, such as CSP, depend on the weather conditions to produce electricity. In this context, to run each SAM simulation, solar radiation resource and meteorological parameters are needed as input data. User data can be applied to force the model, which can be based on measurements or predictions. The resulting hourly performance outputs are part of a full year of annual electricity production of the considered power plant. Details concerning results from these two simulations are presented in Chapter 5, where operational strategies are given accordingly.

3

Solar Radiation Forecasts in Alentejo

The third chapter comprises two first-author publications. From the first [83], where an evaluation of solar radiation forecasts in the Alentejo region is carried out, the entire scientific content (i.e. analysis, tables and original figures) is maintained. Similarly, from the second [84], a preliminary analysis between two IFS radiation schemes is presented in the final section. These publications are listed at the end of this chapter.

3.1 Introduction

Solar assessment is a fundamental step that should be carried out prior to the deployment of solar radiation harvesting systems. This is of particular relevance when financial support for future solar harvesting projects is pursued. This includes the knowledge of the regional annual availabilities values, as well as the interannual variability, of the solar resource. Inaccurate (or an absence of) solar assessment procedures implies a higher risk of insufficient revenue for the contractor upon a low solar harvesting year, threatening financial reliability of financial institutions [115]. In this context, a good characterization of GHI and DNI will contribute to an efficient operation of PV and CSP plants, respectively. This is of particular relevance for DNI due to the fact that there is still the need for development in the prediction of this resource, since it has the potential to enhance the profit and investment in the energy and environmental sectors.

This chapter is focused on the plant operator's point of view for the day-ahead (i.e. the next 24 hours) horizon of available GHI and DNI. To this end, forecasts from the ECMWF global model are analysed and compared with different ground-based measuring stations in the Alentejo region. These stations are part of the DNI-A network, which was designed and installed for the operationalization of solar power plants rather than using BSRN records [116], which are typically used for solar assessment only. As a first step for the operationalization of existing and future solar energy applications in semi-arid and arid regions, this study aims to provide advice and optimization through the use of GHI and DNI forecasts for regional irradiation maps performed by the IFS model.

3.2 Preliminary analysis

Since the number of measured days in each station was not the same, a systematic and robust statistical assessment of the model 24-hour predictions against measurements in each site was performed. To this end, one year of ground-based measurements (from April 1st 2016 to March 31st 2017) was used for the four selected stations, corresponding to the operational period of the McRad (cycle 41R2). As it was previously mentioned, data quality control was performed prior to the analysis of the available data considering the characteristics of each station. Besides only taking into account irradiance values above a 10° solar altitude, a closer function (**Eq. 2.7**) was used, in which a threshold of 10 % was found to be the appropriated limit. This function was applied in all stations with the exception of ALC, where no local DHI measurements were available (a requirement for the use of such filter). Moreover, the same missing periods of measuring data were placed in the forecast model to allow a fair comparison between measured and predicted data sets and to correctly assess the model performance. After applying the proposed filters, the number of solar hours (*N hours*) found for GHI were of 4325, 4313, 4299 and 4316 respectively for EVO, MIT, PRT and ALC. For the case of DNI, the number of hours found were 4358, 4043, 3711 and 4355 respectively for EVO, MIT, PRT and ALC. The measured hourly data (**Fig. 3.1**) depicts the general tendency that solar irradiance values should have during the period of analysis. As expected, higher values of GHI take place in spring

and summer, while lower values occur in winter. Likewise, the daily maximum DNI has a more constant behaviour throughout the year, with higher values occurring under clear sky days, which are more frequent to occur in the summer. This results from the fact that summer months have lower solar zenith angles (i.e. lower air masses around the solar noon) and more sunshine hours, which increases the solar daily availability. Overall, measured data yield higher mean values and standard deviation (STD) of DNI when compared with GHI in all stations, as expected. Further statistical details are shown in **Table 3.1**.

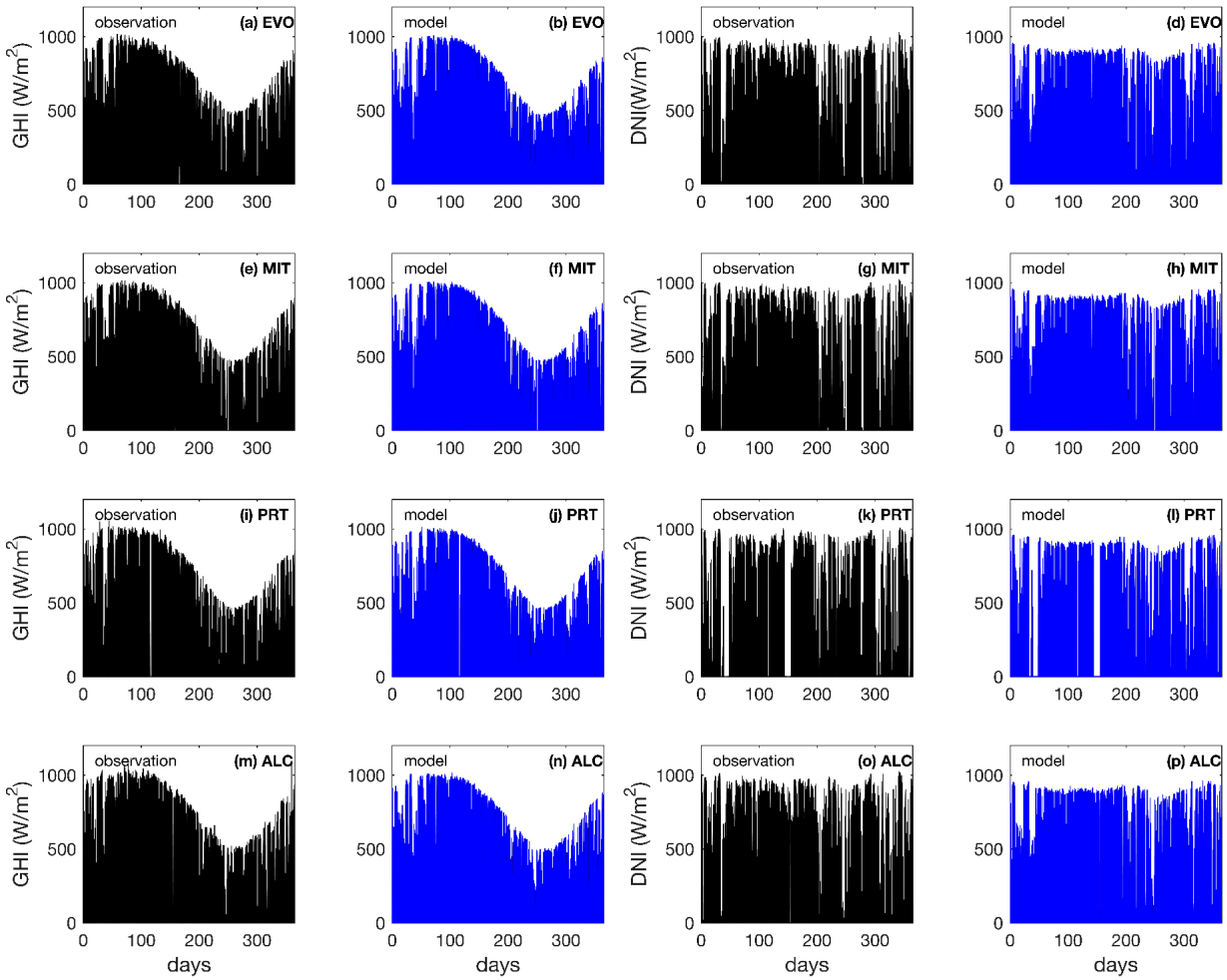

Figure 3.1: Hourly means for ground measurements and IFS model predictions of solar irradiance (W/m^2) in EVO (a, b, c, d), MIT (e, f, g, h), PRT (i, j, k, l) and ALC (m, n, o, p). Global horizontal irradiance (GHI) and direct normal irradiance (DNI) are analysed for a period of 365 days (from April 1^{st} 2016 to March 31^{st} 2017.

Table 3.1: Statistical and descriptive analysis for measurements and IFS model predictions of global horizontal and direct normal irradiances (GHI and DNI, respectively) in Évora (EVO), Mitra (MIT), Portalegre (PRT) and Alcoutim (ALC) stations. One year of data is considered (from April 1st 2016 to March 31st 2017). Results take into account a solar altitude threshold of 10° in all sites.

	EVO		**MIT**		**PRT**		**ALC**	
	Measurements	**IFS**	**Measurements**	**IFS**	**Measurements**	**IFS**	**Measurements**	**IFS**
Longitude (°)	7.91172°W	7.9°W	8.011221°W	8.0°W	7.442716°W	7.4°W	7.744901°W	7.7°W
Latitude (°)	38.567686°N	38.6°N	38.530522°N	38.5°N	39.269221°N	39.3°N	37.441844°N	37.4°N
Distance (km)	3.73		3.53		5.02		6.11	
Mean DNI (W/m^2)	548.85	587.15	566.19	611.19	559.27	617.79	547.80	611.29
Mean GHI (W/m^2)	474.53	475.41	467.52	477.40	462.40	466.23	489.21	489.72
Median DNI (W/m^2)	651.37	668.12	652.41	682.91	668.18	697.20	629.84	684.84
Median GHI (W/m^2)	452.55	448.96	441.71	453.25	421.34	439.33	468.26	469.83
STD DNI (W/m^2)	335.05	283.75	325.80	267.66	336.35	272.23	333.04	269.71
STD GHI (W/m^2)	258.31	255.53	261.91	255.85	268.63	255.62	270.28	255.50
Skewness DNI	-0.46	-0.69	-0.50	-0.78	-0.49	-0.81	-0.43	-0.82
Skewness GHI	0.22	0.29	0.27	0.28	0.31	0.30	0.23	0.25
Kurtosis DNI	1.73	2.22	1.82	2.44	1.73	2.44	1.74	2.51
Kurtosis GHI	1.98	2.03	1.97	2.02	1.97	2.03	1.96	2.01
N hours DNI	4358	4358	4043	4043	3711	3711	4355	4355
N hours GHI	4325	4325	4313	4313	4299	4299	4316	4316
E_b ($kWh/m^2/year$)	2020	2162	1961	2101	1769	1943	2009	2243
E_t ($kWh/m^2/year$)	1750	1753	1707	1743	1685	1699	1797	1799
ΔE_b (%)	7.02		7.15		9.78		11.65	
ΔE_t (%)	0.20		2.12		0.85		0.16	
R^2_b	0.77		0.73		0.65		0.69	
R^2_t	0.95		0.95		0.94		0.95	

3.3 The McRad radiation scheme

In this study, the IFS radiation scheme (the McRad) was used considering deterministic predictions of GHI and DNI for the assessment of solar radiation in the Alentejo region using four ground-measuring stations. The McRad provides a flexible radiation grid, which is more suitable for more coarse applications, when several modules are used. Since the irradiation outputs of the IFS model are hourly accumulated values (i.e. time step values integrated in an hourly basis), the direct irradiance in a horizontal surface implemented by the model (defined by the *fdir* parameter) was divided by the previously averaged CZA [31], taking also into account the nearest model grid point to the corresponding station.

Previous studies have shown that NWP models have an inferior performance when forecasting DNI as compared to GHI under clear and cloudy conditions [107]. This is highlighted by the fact that the main difficulties and challenges in weather forecasting are the representation of clouds and aerosols, i.e. two of the most important factors when predicting solar radiation, along with its partition between direct and diffuse components. It should be noted that a correct representation of clouds is highly dependable on the accuracy of several environmental variables, namely temperature, moisture, wind and respective vertical profiles, which in turn are highly dependable on data assimilation quality and on the representation of surface processes. Also, the impact of an incorrect estimation of the aerosols distribution is higher in DNI than in GHI, as the decrease in direct radiation due to aerosols is partially compensated by the increase in diffuse radiation.

In order to perform data quality control between both time series, an assessment regarding the forecast model (GHI_{mod}, DNI_{mod}) and measurements (GHI_{obs}, DNI_{obs}) was firstly carried out for two case studies. To illustrate this exercise, one day with clear sky conditions (July 14^{th} 2016) recorded in all stations is depicted in **Fig. 3.2**, while in **Fig. 3.3** a cloudy day (July 8^{th} 2016) is presented. During clear sky, results show good agreement between model and measurements, being well represented by very similar daily amplitudes in all stations, particularly for GHI. DNI deviations that take place in the early hours of the day between 6-7 UTC (**Fig. 3.2b**, **3.2c** and **3.2d**) and in the early evening between 20-21 UTC (**Fig. 3.2c**) may be a consequence of local horizon interference (e.g. orographic unevenness of the terrain and nearby trees), justifying the use of a proper filter for such type of obstacles. The filter used considered a 10° threshold for the solar altitude (as described in the previous chapter). Moreover, during this particular day, all stations show different amplitudes of DNI between measurements and forecast model. This is probably related to the representation of aerosols in the CAMS system, which currently provides to the IFS a mean monthly aerosol climatology instead of an actual representation of the aerosol content in the atmosphere. In this context, under very clean atmosphere (such as the one depicted during this day), the aerosol load introduced in the model is higher than what is expected in reality, consequently the aerosol radiative effects (i.e. absorption and scattering of radiation as function of aerosol type and dimension) are overestimated by the model, as the predicted DNI values tend to be lower than the measured ones. Based on these results, average differences between model and measurements of $\approx$31, 47, 11 and 45 W/m^2 were respectively found for this day in EVO, MIT, PRT and ALC stations, being related to the effects of an aerosol climatology instead

of measured values. Moreover, during aerosol events, which are common in the region during this period, namely due to airborne pollen from nearby trees [117], ashes casted by wildfires [118] and atmospheric transport of Saharan dusts [119], the actual aerosols present in the atmosphere are underestimated by the model. In turn, this leads to an overestimation in the predicted DNI and, to a lesser extent, in the predicted GHI, even under cloudless sky conditions.

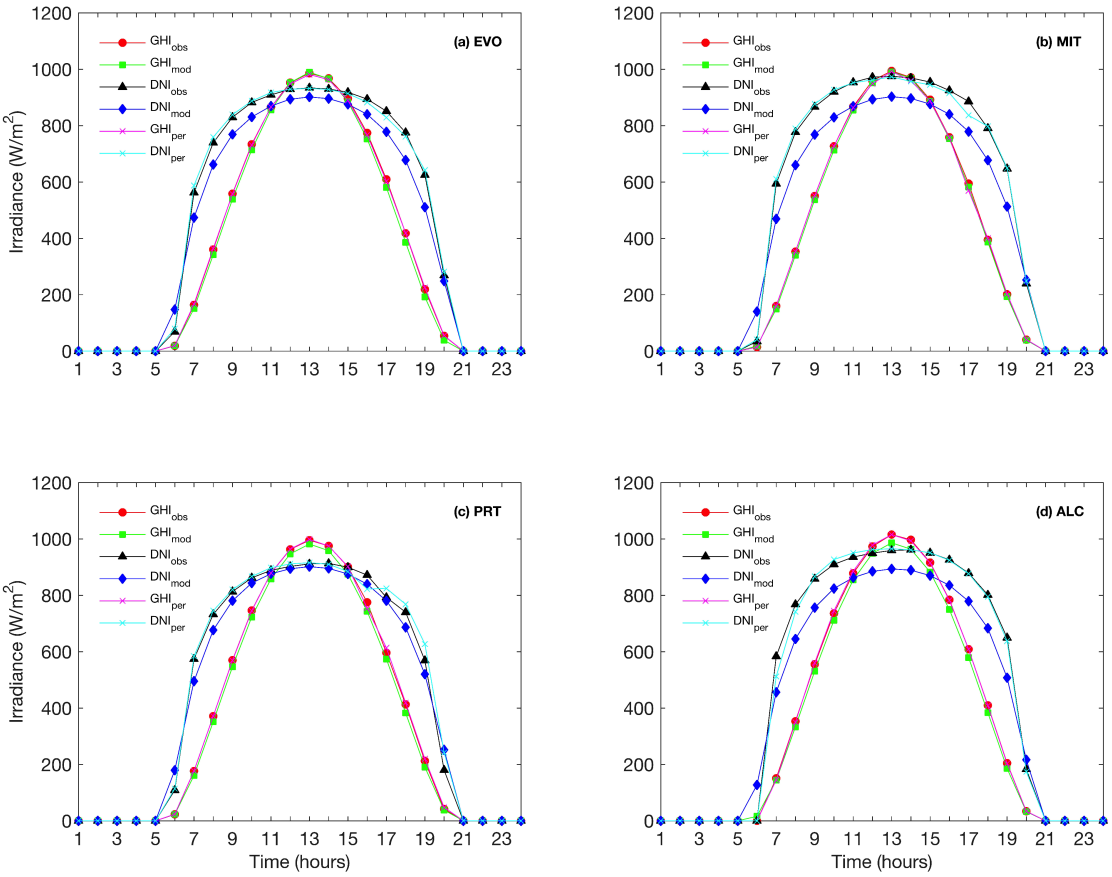

Figure 3.2: Observed (obs) and IFS predicted (mod) solar irradiance (W/m^2) hourly means of global horizontal and direct normal irradiance (GHI and DNI, respectively) for EVO (a), MIT (b), PRT (c) and ALC (d). Persistence (per) forecast hourly means are also depicted. An example of one day with very clear sky conditions was selected (July 14^{th} 2016).

During cloudy days (**Fig. 3.3**) the forecast model shows a general underestimation of cloud radiative effects. During these periods, there are commonly low measured values, as opposed to those produced by the model (which tend to be higher). This is evident in all plots, particularly during the early hours of the day. The underestimation (overestimation) of the radiative effects of clouds (aerosols under very clean atmosphere) carried out by the IFS will be further discussed in this analysis. Additionally, a persistence test for the IFS (GHI_{per} and DNI_{per}) is also included in these sets of figures, showing how the persistence forecasts perform well in comparison to the IFS predictions during the summer. This is a consequence of a higher frequency of occurrence of clear sky days during this period.

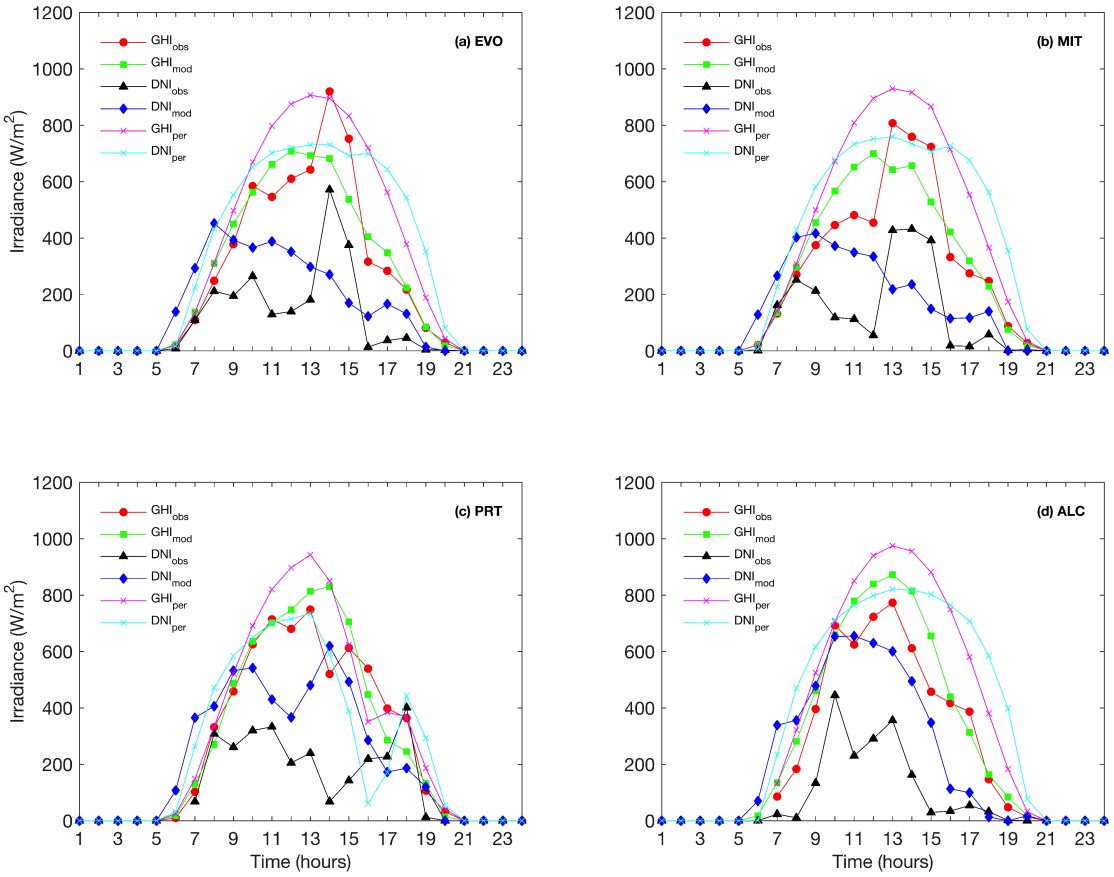

Figure 3.3: Observed (obs) and IFS predicted (mod) solar irradiance (W/m^2) hourly means of global horizontal and direct normal irradiance (GHI and DNI, respectively) for EVO (a), MIT (b), PRT (c) and ALC (d). Persistence (per) forecast hourly means are also depicted. An example of one day with cloudy conditions was selected (July 8th 2016).

3.3.1 Statistical analysis

In all measuring stations, mean annual values between measurements and IFS results show a very similar behaviour for both GHI and DNI. Having into consideration the same missing periods as the experimental data, the hourly values for the 24-hour predictions (**Fig. 3.1**) yield good agreement with measurements. The small differences that exist between predictions and measurements are linked to a general overestimation carried out by the IFS in all stations, particularly for predicted DNI (**Table 3.1**). For instance, considering the mean annual values, a GHI maximum overestimation of 9.9 W/m^2 (≈2.1 %) in MIT station was obtained, while ALC station shows the highest DNI model overestimation with 63.5 W/m^2 (≈11.6 %). As opposed to these, the lowest deviations occur in the same stations with small overestimations of 0.5 W/m^2 (≈0.1 %) in ALC station for GHI and 38.3 W/m^2 (≈7 %) in EVO station for DNI. This shows how the

GHI is better predicted by the model than DNI, since the latter is highly dependable in the representation of clouds and fogs, as well as to their respective intrinsic spatiotemporal inhomogeneity [120], as they are key parameters that strongly impact on DNI variation. For instance, while GHI can be reduced to only 10 %, DNI can be suppressed to almost zero as result of thin high-altitude clouds composed by ice crystals, such as cirrus [49]. This happens because GHI is balanced by the diffuse irradiance that results from light scattering in the clouds. The use of global and diffuse irradiances as a mean to measure cloud thickness and discriminate different cloud types has been determined (e.g. [121]).

Hourly clearness indices (**Fig. 3.4**), k_t for GHI and k_b for DNI, Eqs. (2.1) and (2.2), respectively, generally yield good correlations between IFS and measurements in each station, in particular for GHI. A high density of k_t values occurs around 0.75 (as expected), while for k_b, values are more likely to be in the range between 0.60 and 0.75. The RMSE, as calculate in **Eq. 2.11**, demonstrates that GHI is being better predicted as compared with DNI, where minimum values of RMSE in k_t are observed in MIT (0.11) and the highest in PRT (0.13). In the case of DNI, the RMSE in k_b is higher in PRT station (0.17), while the lowest error is found in MIT station (0.15). Moreover, the obtained MBE, as calculated in **Eq. 2.12**, for the hourly clearness indices is generally negative, corresponding to the model overestimation, with the exception for k_t values in EVO. It should be noted that, a few common features are observed amongst all stations: There is a tendency for the existence of higher dispersion of k_b towards lower values of the index, while close to zero there are clusters of k_b values, probably depicting the model overestimation of DNI under cloudy conditions, i.e. non-zero modelled values instead of the null observations; and the model seems to underestimate the measurements for high values of both k_t and k_b (i.e. for clear sky conditions). This underestimation of the model should be related to the use of the previously mentioned mean monthly aerosol climatology from CAMS instead of a continuous updated aerosol content based on aerosol analysis (and eventually on the integration of a prognostic equation) inside the atmospheric model. One interesting application for such approach would be for the case study of a very clear sky day during the summer, after a rainy day, in which the aerosol load in the atmosphere is significantly lower than the climatological value used in the IFS and where, as a consequence, the measured DNI is substantially higher than the predicted one.

The stated differences between k_t and k_b tend to agree with the fact that the hourly clearness indices are shaped by the sub-daily variability of GHI and DNI, as these are led by clouds and fogs. In turn, the latter depend on sub-scale features (from the point of view of global NWP models) that can affect irradiances within a short time-frame. This is particularly depicted in the obtained k_b values in **Fig. 3.4**, which showed higher RMSE values of $\approx$0.15, 0.15, 0.17 and 0.16 respectively in MIT, EVO, PRT and ALC stations. On the other hand, the lower RMSE values found for k_t were of $\approx$0.11, 0.11, 0.13 and 0.12 respectively in MIT, EVO, PRT and ALC stations. Such sub-scale features are difficult to be simulated by global NWP models, showing the need of performing dynamical downscaling post-processing through high-resolution models.

One example is the use of the non-hydrostatic mesoscale atmospheric model [122, 123], which would allow such improvement. The use of this limited area model for hourly predictions of DNI was tested in a preliminary study to this analysis. In that study (included here as Appendix B), an assessment of the Meso-NH model was carried out for a three-day case study, comprising July 21st-July 24th 2014, over

the southern region of Portugal. This period corresponded to the intensive observational period of an meteorological experiment performed in the region, namely the Alqueva hydro-meteorological experiment 2014 (ALEX2014) campaign [124, 125, 82]. The Meso-NH model run over a 3 x 3 km^2 horizontal grid, forced by ECMW 6-hourly analysis. The comparison of the model outputs was conducted by using 6 in-situ stations and data from radiosondes. Hourly predictions were analysed. Results showed that simulated profiles of meteorological components were close to the measured data. However, the radiation results have shown that the radiation scheme of the Meso-NH model, version V5-3-0, did not represent properly the hourly variation of the solar resource when clouds were present. Some of the founded issues were linked to the implementation of the radiation scheme, which were addressed latter by the Meso-NH development team. In the Appendix B, some of the results are shown and analysed.

Nevertheless, results from the IFS confirm the difficulties that the model has in simulating accurately the DNI irradiance under partly cloudy conditions. This is not so evident in the k_t values, since in cloudy periods the decrease in GHI is partially compensated by the increase in DHI.

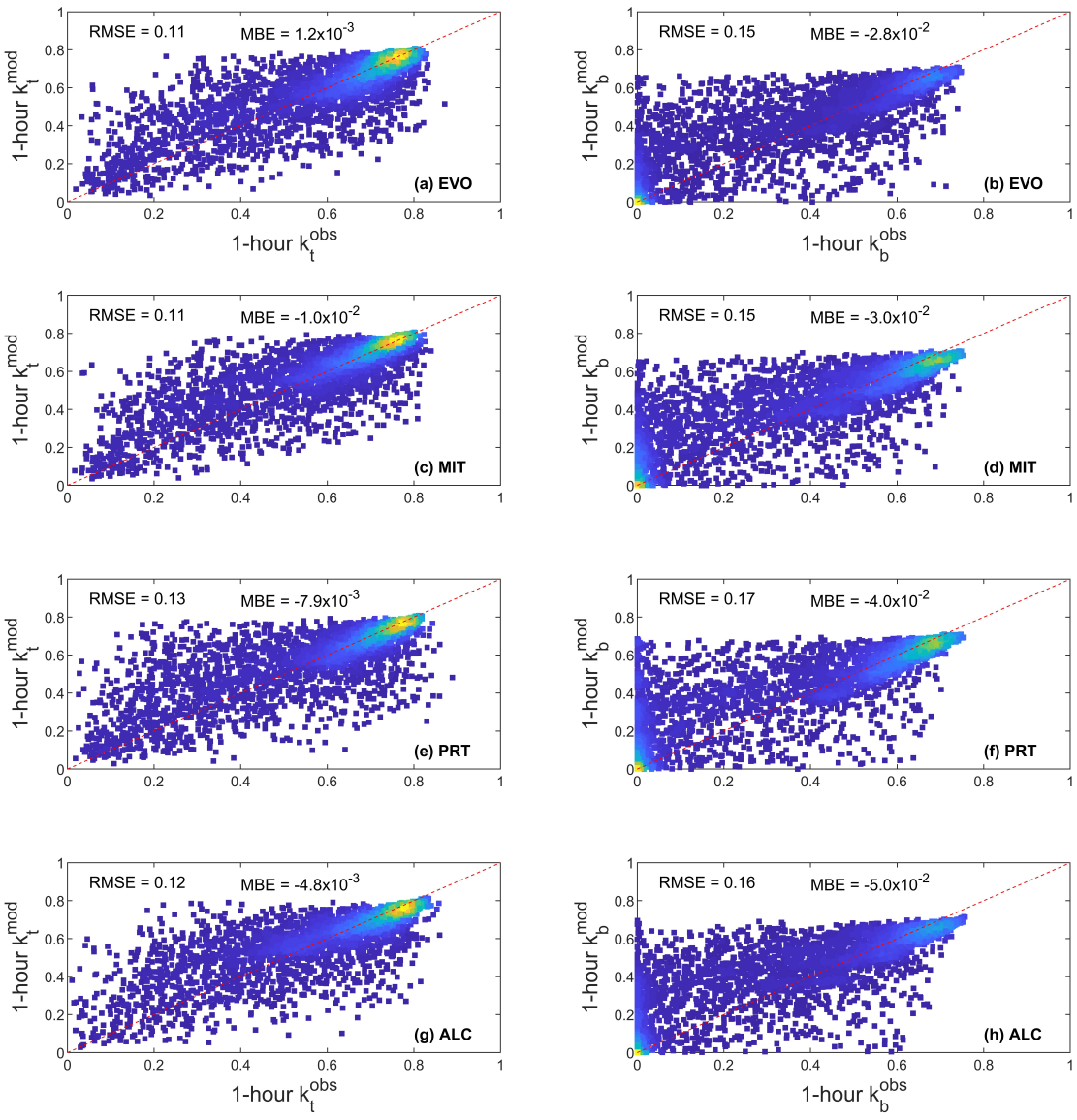

Figure 3.4: Hourly clearness indices for GHI (k_t) and DNI (k_b) in EVO (a, b), MIT (c, d), PRT (e, f) and ALC (g, h) during one year of measurements (from April 1st 2016 to March 31st 2017). Root mean square error (RMSE) and mean bias error (MBE) are depicted together with a normal regression (dashed red line) between observation and model.

The PDFs for each k_t and k_b index, as well as the respective correlations coefficients (r and p-value), are depicted in **Fig. 3.5**. As previously stated, good correlation values between measurements and forecast model occur for the k_t indices. Correlations show higher values in MIT with ≈0.82 for k_t and ≈0.79 for k_b, while PRT depicts the lowest correlation of k_t (≈0.79) and k_b (≈0.76) values. Although some of the differences between stations may be related to the quality of the measurements (e.g. the PRT station has

more days of missing periods), another possible reason for the deviations should be the presence of local surface heterogeneities, since PRT and ALC are located in regions of more complex orography, close to mountains. The result of a global model, such as the IFS, are representative, at best, for a grid of 9 x 9 km^2. Thus, the greater the heterogeneity in the interior of a grid box, the greater will be the deviation between local and mean grid box values. Regarding GHI, for both measurements and model, the curve peaks are very close with k_t values around 0.75. For DNI, there are more substantial differences for low and high values of k_b. In particular, for lower values, measurements always show a higher peak of probability density (related to cloud representation during overcast periods), while for higher values (≈0.65), the model always overestimates measurements (related to aerosol representation during very clear sky days).

Additionally, a two sample Kolmogorov-Smirnov statistical test D* (**Table 3.2**) is performed, indicating that in all stations k_b has higher values, as compared to the ones found for k_t. It is evident that the null hypothesis H_0 is rejected in all cases, revealing a certain degree of relation between measurements and model for both k_t and k_b, respectively.

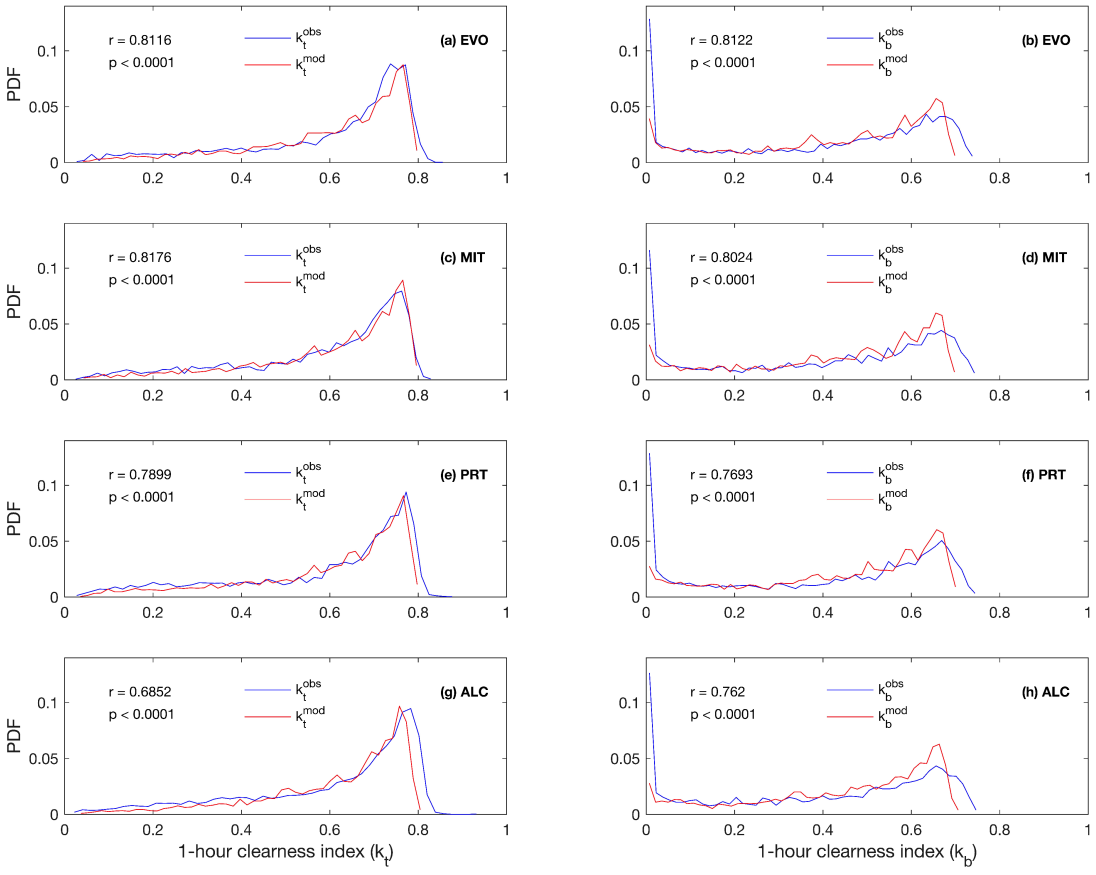

Figure 3.5: Probability density functions (PDFs) and respective correlations coefficients (r and p-value) for the 1-hour clearness indices for GHI (k_t) and DNI (k_b) in EVO (a, b), MIT (c, d), PRT (e, f) and ALC (g, h) during one year of measurements (from April 1st 2016 to March 31st 2017).

Table 3.2: Kolmogorov-Smirnov statistical test between two samples (observation, model) for GHI (k_t) and DNI (k_b) hourly indices in Évora (EVO), Mitra (MIT), Portalegre (PRT) and Alcoutim (ALC) stations. One year of measurements is considered in the study (from April 1st 2016 to March 31st 2017). Results are obtained taking in consideration a solar altitude angle above 10° in all stations.

Kolmogorov-Smirnov test	**EVO**	**MIT**	**PRT**	**ALC**
k_t H_0	1	1	1	1
D*	0.06	0.05	0.07	0.11
k_b H_0	1	1	1	1
D*	0.09	0.10	0.11	0.12

Daily clearness indices (**Fig. 3.6**) where also calculated, considering the hourly values of GHI and DNI during each day, i.e. K_t and K_b, as given respectively by Eqs. (2.5) and (2.6). Lower values of absolute error (AE), calculated through the difference between the measured and the predicted value, are found for GHI, as expected. Moreover, higher frequencies of K_t values occur around 0.75 in all stations, with EVO and MIT having correspondingly ≈20 and 30 % of the total number of days with the RMSE below the threshold error of 0.01. A similar distribution is observed in the remaining stations for the same criteria, where K_t values are observed to occur ≈21 and 17 % in PRT and ALC, respectively. The daily clearness indices based on DNI, show high frequency around 0.60 in all stations. Larger dispersion of errors between K_b values of each day occur during overcast and partly cloudy periods. Values of RMSE lower than 0.01 are ≈10 % of the total number of days in EVO, while ≈12, 9 and 11 % are observed in the case of MIT, PRT and ALC stations, respectively. In the case of K_b values, as previously observed for the hourly values in **Fig. 3.4**, there is a higher dispersion close to zero, with deviations being related to the difficulties that the IFS has in cloud representation (i.e. the model tendency to overestimate observations during cloudy periods). The AE depicts higher occurrences of negative values close to zero, which are represented by the non-zero values of modelled DNI when in fact the observation considered near null values due to clouds. Moreover, a small increase of AE for $K_b > 0.6$ is observed, where these values correspond to very clean sky days, as this error should be related to the aerosol representation only (no clouds are present).

Under very clean atmosphere, the model demonstrates a tendency to overestimate the aerosol load, predicting lower DNI values. As previously mentioned, this is probably related to the use of mean monthly aerosols climatology instead of actual aerosol forecasts, as proposed by [126], but also due to an incomplete representation of the radiative effects of aerosols. Recent efforts have been developed towards the improvement of the aerosol representation with the inclusion of aerosol indirect effects in high-resolution global NWP models in order to improve the accuracy of short-range weather forecasts [38]. As described by [43], it is still possible and advantageous to improve aerosol climatology and reduce its induced errors, as these have a strong dependence on surface measurements, through the improvement of transport models and the quality of observations. Aerosol measurements can be assimilated, enabling the filling of gaps

that exist in sparse network of measurement sites [127] and by the use of empirical methods (e.g. [128]), merging model fields, satellite and surface observational data.

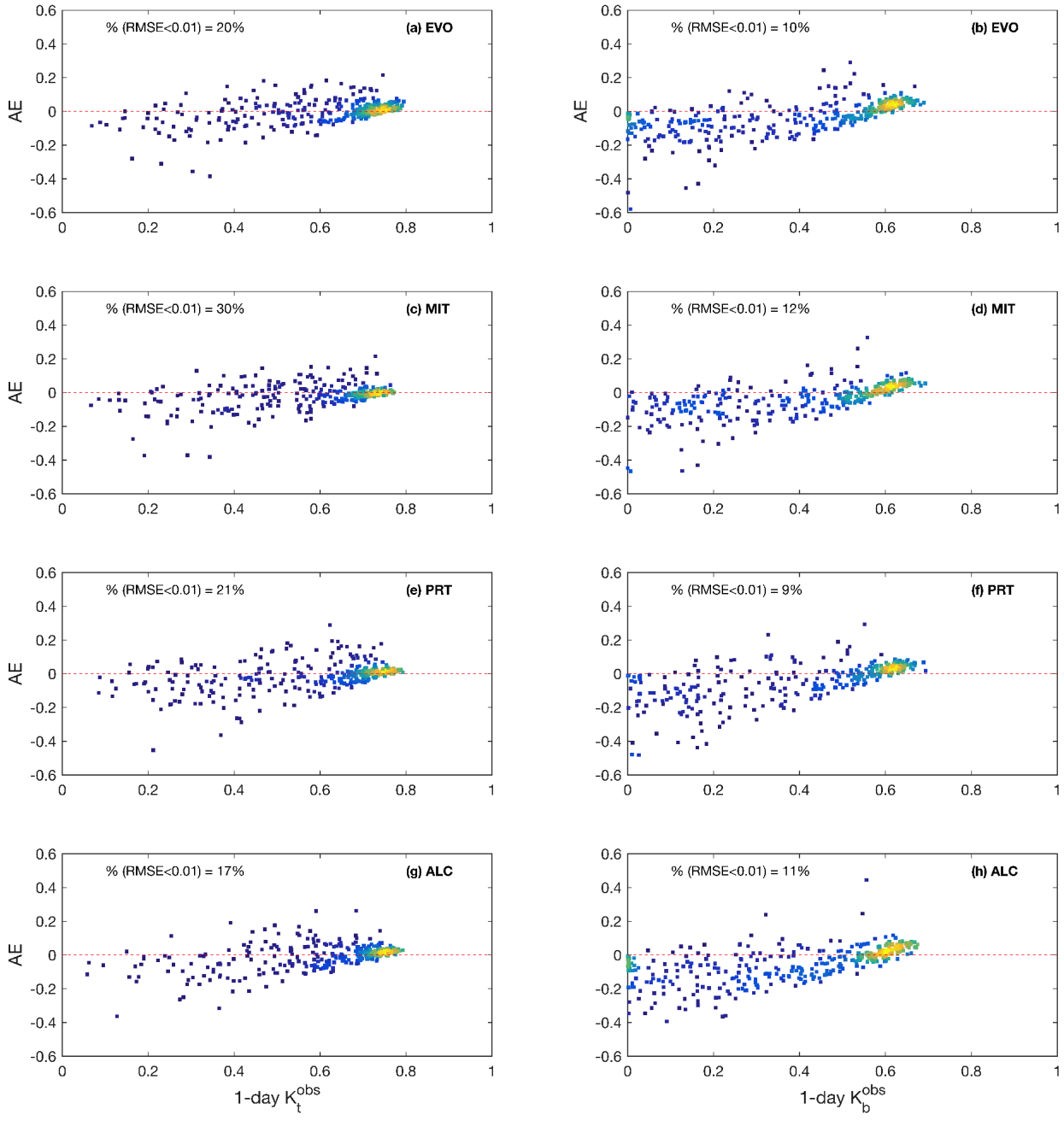

Figure 3.6: Absolute error (AE) between 1-day clearness indices from measurements and model for GHI (K_t) and DNI (K_b) in EVO (a, b), MIT (c, d), PRT (e, f) and ALC (g, h) during one year of measurements (from April 1st 2016 to March 31st 2017). The red dashed line represents the threshold between positive and negative AE values.

Daily irradiation availability (i.e. daily accumulated values) of GHI and DNI for both hourly measurements and predictions were also calculated for the considered 1-year period (**Fig. 3.7**). The restriction of solar altitudes above 10° is maintained here. As previously stated, the IFS performs well in simulating GHI, showing higher correlations than DNI. These high correlations take place under clear sky conditions in the summer period, where daily irradiations of GHI (E_t) and DNI (E_b) reach ≈9 kWh/m^2 and more than 11 kWh/m^2, respectively. For instance, there is an evident correspondence with the E_t fitting curve (dashed line) than for E_b values, in which for high values the model demonstrates a tendency to significantly underestimate DNI. As previously discussed, this should be related to climatological values of aerosol load introduced in the IFS, which appear to be higher than the real ones in all stations for the case of high DNI, corresponding to cloudless periods with a very clean atmosphere. In EVO, the relative difference between model and measurements show deviations of ≈0.20 and 7.02 %, correspondingly for GHI and DNI, while for MIT these were ≈2.12 and 7.15 %. In PRT the relative difference found was ≈0.85 % for E_t and 9.78 % for E_b. The ALC station show differences of ≈0.16 % for E_t with the highest being found for E_b, i.e. ≈11.65 %. These results confirm that in this analysis, in comparison with the obtained results in EVO and MIT, the predictions are less valuable in PRT and ALC, partially due to the location in regions with a more pronounced relief, which enhance the formation of near surface sub-scale clouds.

Nevertheless, taking in consideration the assumptions previously described for the adopted methodology, these results show that the total energy irradiation availability obtained from the measurements and predictions (for both GHI and DNI) are found to be close to the reference annual values in the region, with ≈1900 kWh/m^2/year for GHI and more than 2100 kWh/m^2/year for DNI, respectively [88]. The differences that are stated between reference and predicted values result mainly from: i) missing periods of data; ii) the 10° threshold for solar altitude; iii) the closure function; and iv) the model tendency to overestimate daily irradiation availabilities under cloudy sky conditions, partially due to small sub-scale fogs and clouds unresolved by a global model at 9 km^2 horizontal resolution.

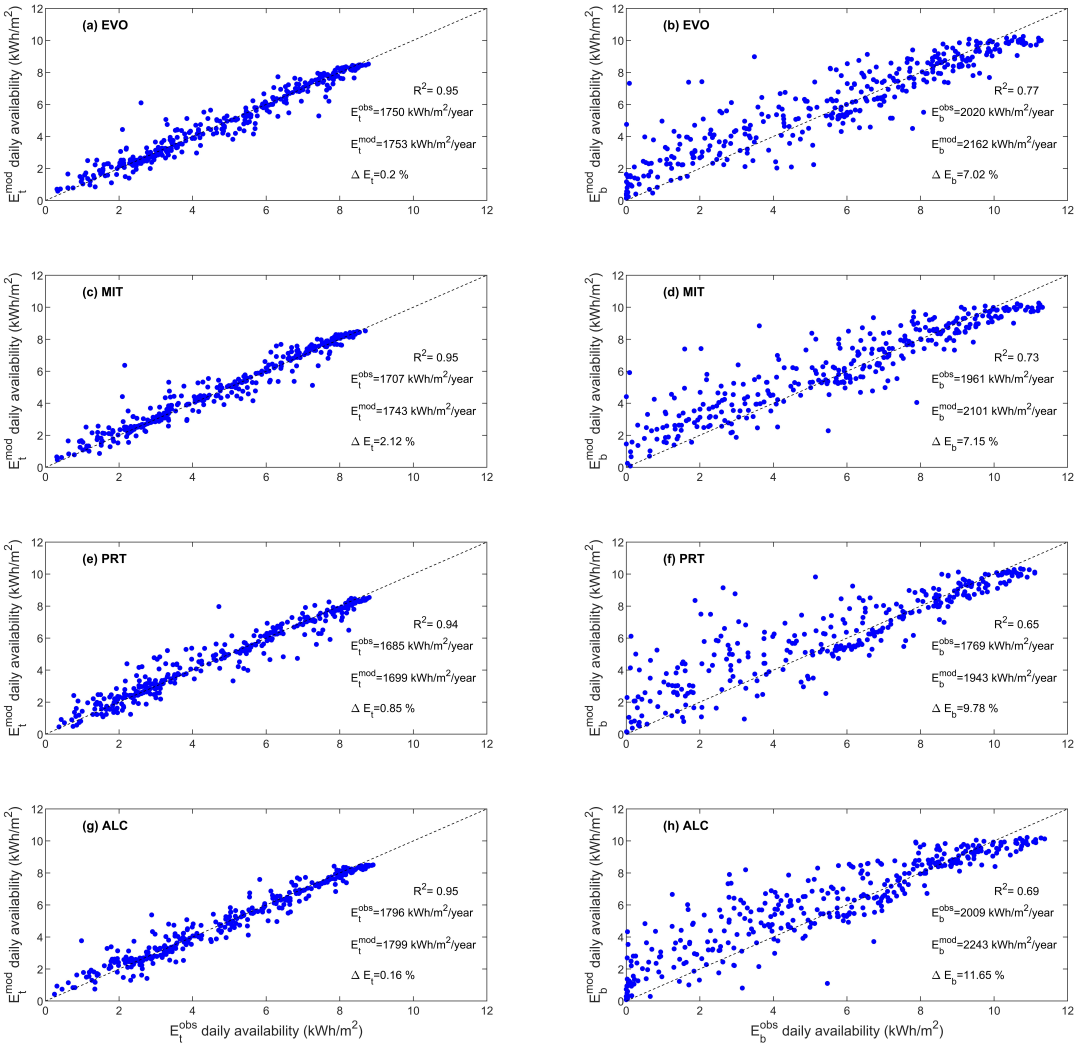

Figure 3.7: Daily availabilities (kWh/m^2) for GHI (E_t) and DNI (E_b) in EVO (a, b), MIT (c, d), PRT (e, f) and ALC (g, h) during one year of measurements (from April 1st 2016 to March 31st 2017). Reference annual values ($E_{t,b}$), relative differences ($\Delta E_{t,b}$) and coefficient of determination (R^2) between model and measurements are also presented. Equal values for measurements and model is depicted by the dashed line.

3.3.2 Forecasting skill

Since solar forecast accuracy depends on a number of factors such as region, weather conditions, forecast horizon and the model itself, it is important to compare quantitatively the IFS hourly predictions with a reference forecast. To this end, an exercise of forecasting skill is taken into consideration by calculating the SS, **Eq. 2.14**, between values of clearness index (i.e. k_t and k_b) of the forecast model and a persistence model. the latter is calculated through a 24-hour shift ahead of the local measured values for the entire

period of analysis. The statistical k_t and k_b results between the IFS predictions and measurements are summarized in **Table 3.3**, respectively for GHI and DNI. Similarly, but for results between the persistence model and measurements are shown in **Table 3.4**. Then, in **Table 3.5**, the obtained SS between IFS and persistence in all stations is presented.

A forecast improvement is seen with the IFS in comparison with the persistence for both GHI and DNI. **Tables 3.3** and **3.4** show that, in all stations, there are higher correlations and lower errors between k_t and k_b for the IFS than the ones found for the persistence in relation to the measurements. The obtained SS results (**Table 3.5**) are generally above 0.5 with higher values being found in both EVO and MIT stations, with ≈0.70 for k_t and 0.61 for k_b, as these are relatively close to each other. On the other hand, lower scores occur in PRT and ALC stations, respectively with ≈0.58 and 0.64 for k_t, and ≈0.57 and 0.56 for k_b. Such contrast indicates well how the IFS is better in predicting GHI than DNI, in which the highest performance is achieved by the IFS in EVO station, especially for GHI. Ultimately, these results are also an indication that, for the 24-hour horizon, the predictions of the ECMWF global model have significant predictive value.

Table 3.3: Statistical results between the hourly clearness indices for GHI (k_t) and DNI (k_b) obtained from the ECMWF global model and measurements for the period of one year. Pearson correlation (r), root mean square error (RMSE), mean bias error (MBE) and mean absolute error (MAE) are shown.

k_t	EVO	MIT	PRT	ALC
r	0.81	0.82	0.79	0.79
RMSE	0.11	0.11	0.13	0.12
MBE	1.2×10^{-3}	-0.01	-7.9×10^{-3}	-4.8×10^{-3}
MAE	0.07	0.07	0.08	0.08

k_b	EVO	MIT	PRT	ALC
r	0.81	0.79	0.76	0.79
RMSE	0.15	0.15	0.17	0.16
MBE	-2.8×10^{-2}	-0.03	-0.04	-0.05
MAE	0.10	0.11	0.11	0.11

Table 3.4: Statistical results between the hourly clearness indices for GHI (k_t) and DNI (k_b) obtained from the persistence forecast and measurements for the period of one year. Pearson correlation (r), root mean square error (RMSE), mean bias error (MBE) and mean absolute error (MAE) are shown.

k_t	EVO	MIT	PRT	ALC
r	0.43	0.45	0.51	0.48
RMSE	0.20	0.20	0.20	0.20
MBE	-8.12×10^{-4}	-3.43×10^{-4}	-8.57×10^{-4}	-4.23×10^{-5}
MAE	0.13	0.13	0.13	0.13

k_b	EVO	MIT	PRT	ALC
r	0.52	0.50	0.46	0.54
RMSE	0.24	0.24	0.26	0.24
MBE	-2.24×10^{-4}	-1.81×10^{-4}	-4.00×10^{-3}	3.06×10^{-4}
MAE	0.17	0.17	0.17	0.16

Table 3.5: Skill score (SS) based in the mean square error (MSE) of hourly clearness indices for GHI (k_t) and DNI (k_b) between the ECMWF global model and persistence forecast considering the period of one year.

k_t	EVO	MIT	PRT	ALC
SS	0.6975	0.6975	0.5775	0.6400

k_b	EVO	MIT	PRT	ALC
SS	0.6094	0.6094	0.5725	0.5556

3.3.3 Monthly analysis

Annual cycles of GHI and DNI are depicted in **Fig. 3.8** for EVO, MIT, PRT and ALC stations. As expected, the annual variations are characterized by high availabilities (both for GHI and DNI) in the summer period (from June to August), with maximum values reaching ≈250 kWh/m^2/month for GHI and between 280-300 kWh/m^2/month for DNI. On the other hand, in the winter period (from December to February), low availabilities occur with minimum values of ≈70 kWh/m^2/month for GHI and between 80-150 kWh/m^2/month in the case of DNI. The higher values in the summer are mainly related to a higher irradiance at the surface due to lower solar zenith angles at noon and to longer periods of day light. In the winter, low values are the result of overcast periods, which are more frequent during this period of the year, and also to higher solar zenith angles and a shorter duration of day light. Higher correlations throughout the year are found for GHI with very similar curve trends between forecast model and measurements. The annual cycle of the forecasted DNI depicts larger deviations of the IFS towards measurements when compared with the predicted GHI. These deviations are expected to occur (being smaller during the summer months), since the main source of uncertainty of DNI predictions is the representation of clouds in the model, and the fact that longer cloudless periods are more frequent during this period of the year. As previously discussed, spring and summer can also experience aerosol events, which can diminish the DNI measured at surface, while the predicted one does not have these fully into account. Besides the regional airborne pollens and wildfires smoke, dusts events can also occur, such as from the Saharan desert dust (e.g. [119]), which can be transported by the synoptic circulation that is, in the summer, dominated by the frequent development of the shallow Iberian low-pressure system. On the other hand, during the winter period the DNI deviations are much larger mainly due to cloud representation together with the assimilation of strong wind and its direct effect in clouds, as these are more frequent to occur during such months. Particularly, significant deviations are found in February in all stations, since this month was characterized by strong winds and heavy rain.

It should be noted that between June and September, in the PRT station, there were missing periods of data, particularly a group of eleven consecutive days, which is suppressed the monthly availabilities for GHI and DNI.

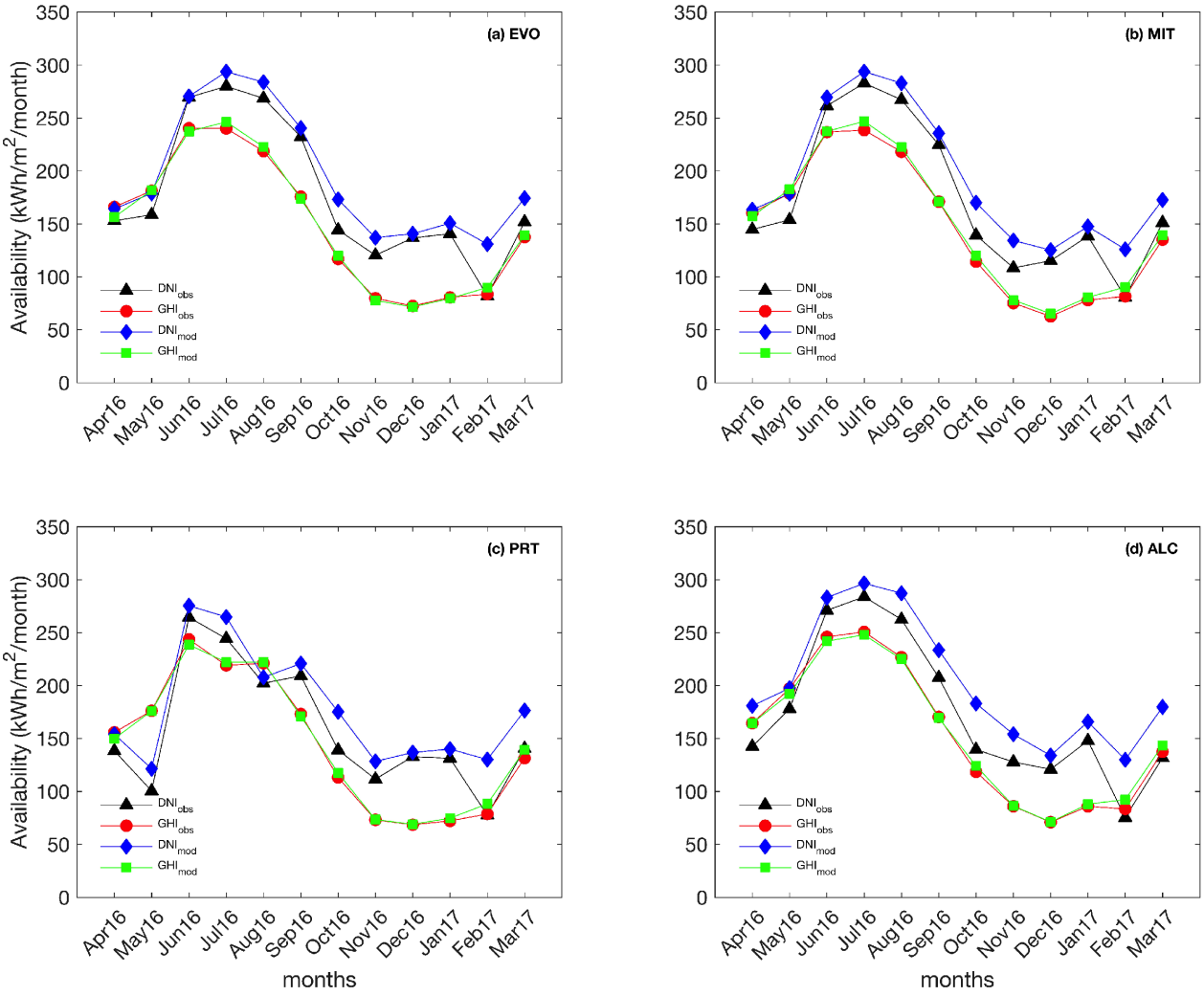

Figure 3.8: Monthly values for GHI and DNI availability (kWh/m^2/month) in EVO (a), MIT (b), PRT (c) and ALC (d) during one year of measurements (from April 1st 2016 to March 31st 2017).

3.4 The ecRad radiation scheme

In the previous section, a statistical analysis for the assessment of hourly forecasts regarding GHI and DNI against measured data in four ground-measuring stations showed the McRad capabilities in representing these two parameters for the day-ahead. For CSP systems, DNI is the most important solar resource to be used for the production of electricity. Thus, accurate forecasts of DNI are fundamental in order to improve the operational decisions that the power plant operator has to make. In this context, and with the implementation of a new radiation scheme from the ECMWF, i.e. the ecRad, a performance analysis between the McRad (cycle 41R2) and the ecRad (cycle 43R3) was carried out having into account measured data from EVO station. The results showed a general improvement of DNI predictions from the previous to the new scheme, as shown in **Table 3.6**. Since the ecRad started to be operational in July 2017, the following preliminary analysis consists in using two consecutive periods of data: the first year (July 1st 2016 to June 30th 2017), comprising the McRad operational version; and the second year (July 1st 2017 to June 30th 2018), comprising the ecRad operational version. For each of the considered years, a total number of 4747 hours of daylight, i.e. the total number of daylight hours available, were used for the hourly analysis. As mentioned in the previous chapter, small data gaps can exist in the measured time series at EVO, being related to sudden electrical shutdowns. In EVO station, throughout an entire year of continuous measurements, ≈0.05 and 0.003 % of missing data were found respectively for the established McRad and ecRad periods. Considering the MIT station, solely used here for the gap-filling procedure, ≈5.24 and 0.14 % of gaps were also found for the McRad and ecRad periods, respectively. This demonstrates how-well maintained the EVO station has been and why it is used as a reference for the assessment of DNI predictions.

Overall, overestimations of ≈10.6 and 0.12 % were obtained regarding the predicted annual mean values of DNI in comparison to the measured ones, respectively for the McRad and ecRad schemes. The predicted values from the ecRad showed to be much closer to the measurements (i.e. with lower deviations), as opposed to the previous version. This behaviour is also represented by the obtained hourly correlation coefficients of ≈0.86 and 0.87, and RMSE of ≈188.60 and 180.44 W/m^2, for the McRad and ecRad, respectively. The corresponding obtained MAE were ≈126.06 and 125.93 W/m^2, showing the decreasing tendency for lower errors from one version to the other.

Table 3.6: Statistical and descriptive analysis of the McRad (cycle 41R2) and ecRad (cycle 43R3) radiation schemes from the IFS global model. Several statistical parameters between measured and predicted hourly mean values of irradiance were calculated considering only the daylight period (i.e. a total of 4747 hours) during an entire year of data: mean, median, standard deviation (STD), root mean square error (RMSE), mean absolute error (MAE), correlation coefficient (r), skewness, kurtosis, total energy availability (E_b), relative difference of E_b (ΔE_b) and the skill score (SS), with their respective units for power values (in W/m^2) and for energy values (kWh/m^2). In reference to the measuring station in Évora city, the periods used go from July 1st 2016 to June 30th 2017 (McRad) and from July 1st 2017 to June 30th 2018 (ecRad).

	McRad		**ecRad**	
	Measurements	**IFS**	**Measurements**	**IFS**
Mean (W/m^2)	463.61	512.76	444.24	444.76
Median (W/m^2)	501.74	563.31	452.32	457.80
STD (W/m^2)	351.71	310.67	361.87	310.72
r_{hourly}		0.86		0.87
r_{daily}		0.88		0.91
RMSE (W/m^2)		188.60		180.44
MAE (W/m^2)		126.06		125.93
Skewness DNI	-0.07	-0.31	0.03	-0.07
Kurtosis DNI	1.44	1.66	1.40	1.50
E_b (kWh/m^2/year)	2192	2424	2096	2100
ΔE_b (%)		10.62		0.19
r_{E_b}		0.90		0.91
SS_{hourly}		0.60		0.67
SS_{daily}		0.70		0.77

Hourly and mean daily values of measured and predicted DNI are compared in **Fig. 3.9**. Higher correlations were observed for high DNI values ($>$ 900 W/m^2), which occurred during clear sky periods. On the other hand, lower correlations were obtained for inferior values, being characterized by higher dispersion, corresponding to cloudy periods, as a consequence of the difficulties that the model has in representing cloud microphysics. This is well shown by the model tendency to overestimate measurements for overcast and partly cloudy periods (depicted by a cluster of values for $x=0$), and the model tendency to underestimate measurements during clear sky periods, particularly under a very clean atmosphere (depicted by high DNI values), as previously observed. As expected, daily values showed higher correlations coefficients of $\approx$0.88 and 0.91, respectively for the McRad and ecRad, in comparison with the hourly correlations. This increase was higher for the correlation between measurements and predictions provided by the ecRad, with a value of almost 4.6 %, as opposed to 2.3 % for the McRad correlations. The reduction of error from the hourly to the daily results is well represented in **Fig. 3.10**, where a decrease in the absolute error (AE) of DNI was observed with the approximation of AE values towards zero, particularly in the case for the daily

values. Additionally, the total annual energy availability obtained from the predicted DNI of the ecRad (E_b) is closer to the regional measured values, which can range from ≈1841 to 2073 kWh/m^2/year [89]. The obtained relative differences (ΔE_b) in **Table 3.6**, were ≈10.6 and 0.19 % for the McRad and ecRad schemes, respectively. The monthly energy availability, shown in **Fig. 3.11** provides an overview of the IFS performance in predicting the DNI through the McRad and ecRad schemes. Relative differences of ≈10.6 and 0.1 % were found between predicted and measured monthly values for the McRad and the ecRad periods, respectively.

In the context of forecasting skill assessment of the 24-hour predictions provided by the IFS, the obtained SS showed an improvement of the model in performing DNI forecasts. From **Table 3.6**, hourly SS showed an increase from ≈0.60 to 0.67, and ≈0.70 to 0.77 for the hourly and daily SS, respectively for McRad and ecRad schemes.

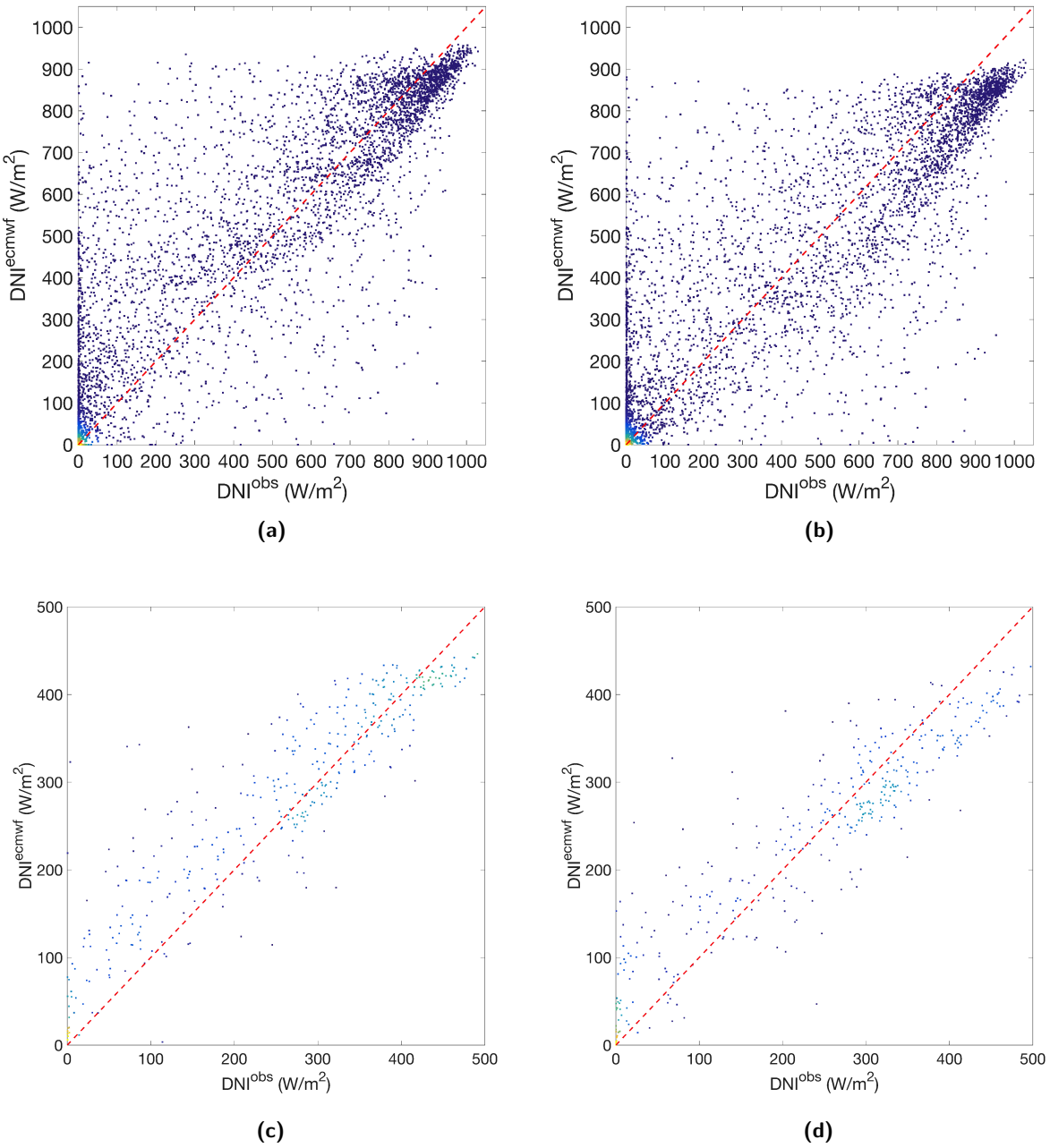

Figure 3.9: Comparison of hourly (a, b) and daily (c, d) mean DNI values (W/m^2) between IFS predictions (ecmwf) and measurements (obs), for the McRad (a, c) and ecRad (b, d) radiation schemes, considering only daylight hours during an entire year of data. The corresponding periods are centred in the measuring station located in Évora city, going from July 1st 2016 to June 30th 2017 (McRad, cycle 41R2) and from July 1st 2017 to June 30th 2018 (ecRad, cycle 43R3). The red dashed line represents the identity line $y{=}x$ between measurements and forecasts.

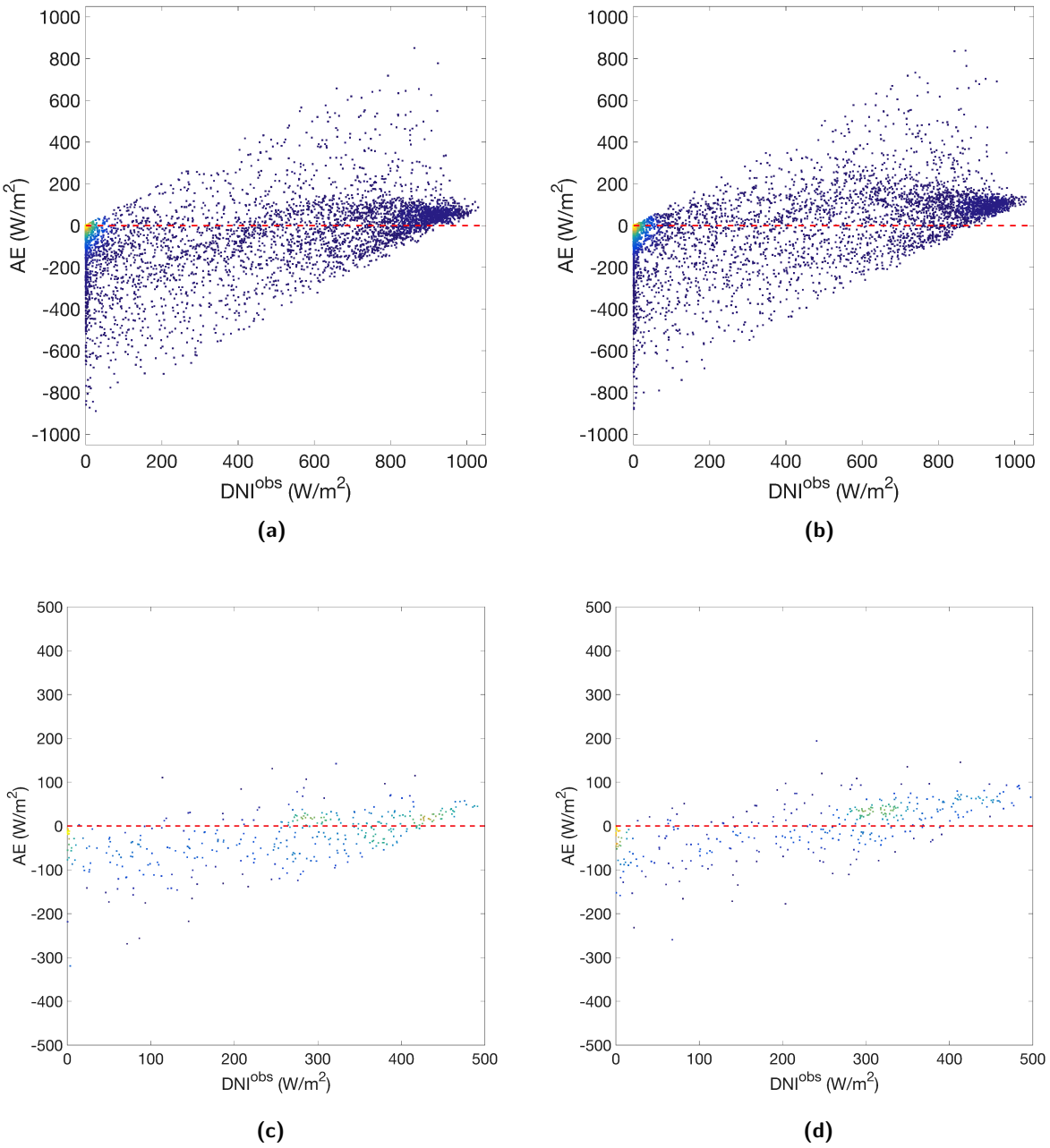

Figure 3.10: Absolute error (AE) between hourly (a, b) and daily (c, d) mean DNI values (W/m^2), considering only daylight hours during an entire year of data. The corresponding periods are centred in the measuring station located in Évora city, going from July 1st 2016 to June 30th 2017 (McRad, cycle 41R2) (a, c) and from July 1st 2017 to June 30th 2018 (ecRad, cycle 43R3) (b, d). The horizontal line *y=0*, represented by a red dashed line, establishes a threshold between positive and negative AE values.

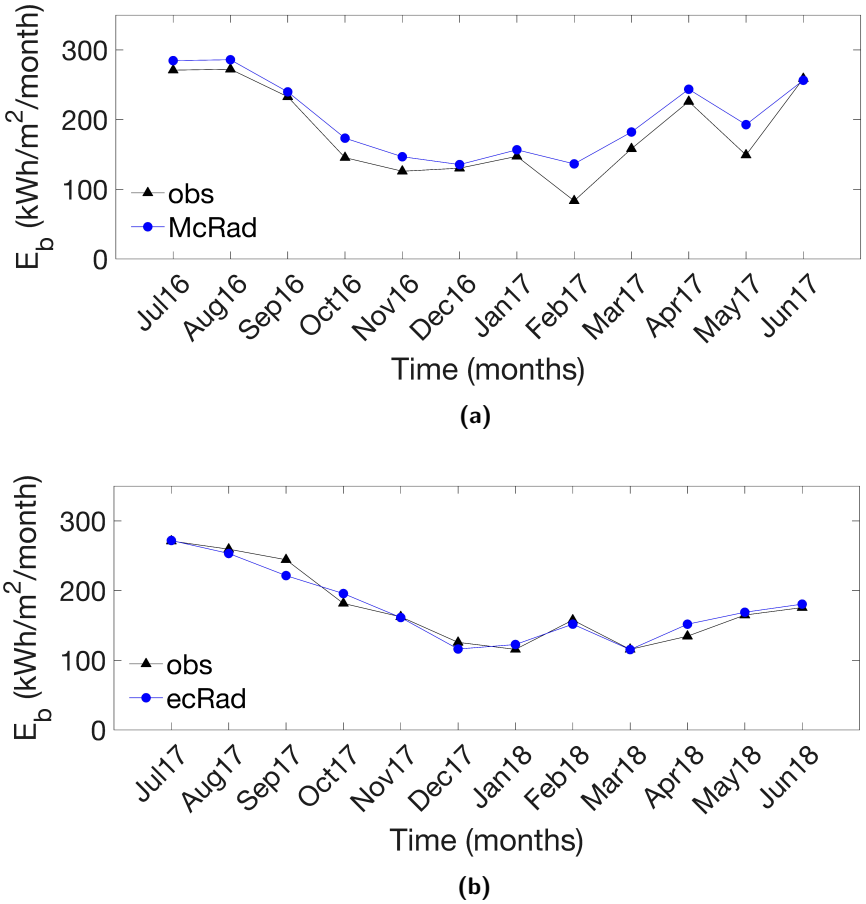

Figure 3.11: Measured (obs) and predicted (ecmwf) monthly energy availability, E_b (kWh/m^2/month), considering only daylight hours during an entire year of data. The corresponding periods are centred in the measuring station located in Évora city, going from: a) July 1st 2016 to June 30th 2017 (McRad, cycle 41R2) and b) from July 1st 2017 to June 30th 2018 (ecRad, cycle 43R3).

This analysis indicates that, for the day-ahead horizon, DNI predictions from the IFS have been significantly improved with the new radiation scheme ecRad. This is a result of recent developments towards a better representation of cloud microphysics and the implementation of a more realistic aerosol climatology [101]. Having into account the previous results, it is therefore possible to conclude that the ecRad (cycle 43R3) is best suited to provide DNI forecasts and to be used as an input parameter for CSP plant simulations, as it will be discussed in the following chapters.

3.5 Conclusions

In this chapter, the IFS global model from the ECMWF was used for the first time to assess 24-hour predictions of GHI and DNI for solar energy applications in the Alentejo region (southern Portugal) during a period of 365 days (from April 1st 2016 to March 31st 2017). Results showed that the IFS radiation scheme McRad (cycle 41R2) performed well in predicting GHI, whilst DNI forecasts were particularly hindered by cloud and aerosol representations. During overcast periods, the measured DNI was overestimated by the model mainly due to cloud representation, since cloud 3D distribution and cloud microphysics are still difficult to be predicted in NWP. Under these conditions, such effect is not so important in GHI predictions due to a compensation through an increase in the predicted DHI. On the other hand, for clear sky conditions and a very clean atmosphere, the IFS demonstrated a tendency to underestimate measurements of both GHI and DNI, as consequence of using climatological aerosol monthly means. This is of particular relevance, since during such periods, accurate forecasts of DNI are essential for an efficient operation of a CSP power plant. Ultimately, cloud and aerosol representation can affect both GHI and DNI, although with more emphasis in the latter, as showed in this study. Nevertheless, taking into account the aforementioned aspects of the forecast model and the assumptions considered for this analysis during one year of data, results yield satisfactory values between IFS and measurements. Amongst the four selected locations, relative differences of annual availabilities for GHI were found between ≈0.16 to 2.12 %, whilst for DNI, values ranging from ≈7 to 12 % were found. The respective obtained correlations were around 0.95 for GHI and between 0.65 and 0.77 for DNI. Moreover, considering the importance that accurate DNI forecasts have in CSP, a performance analysis between the McRad and the new operational ecRad was carried out for EVO station only, showing an overall improvement in the day-ahead predictions of DNI. The corresponding relative differences were found, showing values of ≈10.6 and 0.19 % for the total annual energy availabilities between forecasts and measurements for one year. Despite the improvements, it is evident that further developments for the representation of clouds and aerosols in NWP, two fundamental parameters that hinder DNI forecasting, are still required. Nevertheless, these results are a good indication that GHI and DNI forecasts can be of valuable use to the implementation and efficient operations of PV, CPV and CSP systems in the region. More details regarding the use of DNI forecasts in CSP operations are presented in Chapter 5.

The work presented in this chapter resulted from the following publications:

- Francis M. Lopes, Hugo G. Silva, Rui Salgado, Afonso Cavaco, Paulo Canhoto, Manuel Collares-Pereira, 2018. Short-term Forecasts of GHI and DNI for Solar Energy Systems Operation: assessment of the ECMWF Integrated Forecasting System in Southern Portugal. Solar Energy (2018), 170, 14-30.
- Francis M. Lopes, Ricardo Conceição, Thomas Fasquelle, Hugo G. Silva, Rui Salgado, Paulo Canhoto, Manuel Collares-Pereira. Predicted direct solar radiation (ECMWF) for optimized operational strategies of linear focus parabolic-trough systems. Renewable Energy (2019), 151, 378-391.

4

Improvement of DNI Forecasts: Implications for CSP

The fourth chapter includes all the scientific content (i.e. analysis, tables and original figures) presented in one publication [85]. An exception is made regarding the use of improved forecasts in the SAM simulation of the Andasol 3 CSP plant, which will be discussed in the next sections. This publication is listed at the end of this chapter.

4.1 Introduction

As previously discussed, solar forecast uncertainty is inherent in NWP models, particularly in hourly predictions of DNI. Moreover, cloud and aerosol misrepresentation by the models increase the prediction error from actual measurements during cloudy days. In turn, when these predictions are implemented in power plant models, the predicted energy output of a simulated power plant will also have an associated error. Therefore, as an objective of this study, the adjustment of short-term forecasts of DNI is carried out.

Post-processing techniques of easy application to the plant operator are to be applied in the IFS forecasts (ecRad, cycle 43R3), having into account measurements in the EVO station during a period of two years (from July 1st 2017 to June 30th 2018 and from July 1st 2018 to June 30th 2019). To this end, several regression models are created, where a compound model that uses previous measured hour of irradiance values to forecast the next-hour values (i.e. within the nowcasting range) is proposed. Daily adjustments can also be used to improve daily operational strategies, which can then be refined by the hourly predictions from the proposed models throughout the day.

4.2 Regression models

Statistical models can be used to adjust predictions of DNI, such as the case of regression models, in which the dependent variable (predictand) is studied, i.e. the measured DNI, considering a set of independent variables (predictors), i.e. measured and forecasted data, that influence and have impact over the former. Each regression coefficient obtained represents the effect that a predictor has in the predictand over time (at the same time that all other predictors remain constant). These basic regression models can be refined using complex multivariate and non-linear relationships between several predictors and the predictand, providing better estimations.

In this analysis, three regression models are used to adjust hourly predicted DNI. The first model consists in a simple regression model (SRM), based on a third-degree polynomial fitting. The fitting method is based on the use of regression coefficients obtained between measured DNI (i.e. the predictand) and the predicted DNI (i.e. the predictor) from the first year as input to adjust the second year of predicted DNI. The second model is a linear multivariate regression model (MRM1), which uses an interactive stepwise function with an adjusted r-squared criterion. This function performs all possible combinations between predictors to find the best fitting option, in this case a second-degree polynomial is considered. The atmospheric predictors in the MRM1 are: GHI^{IFS}, DNI^{IFS}, GHI^{TOA}, DNI^{TOA}, air temperature (T^{IFS}), relative humidity (RH^{IFS}), wind velocity (W^{IFS}), total precipitation (Pr^{IFS}) and total cloud cover (Tcc^{IFS}). To obtain the improved predictions of DNI from the MRM1, the following relation is considered:

$$DNI_i^{MRM1} = F(GHI_i^{IFS}, DNI_i^{IFS}, GHI_i^{TOA}, DNI_i^{TOA}, T_i^{IFS}, RH_i^{IFS}, W_i^{IFS}, Pr_i^{IFS}, Tcc_i^{IFS}). \quad (4.1)$$

Then, by including the previous hour (*i*-1) of measured DNI and GHI as predictors to the MRM1 setup, a compound multivariate regression model (MRM2) is created to perform next-hour (*i*) predictions of DNI accordingly to the following relation:

$$DNI_i^{MRM2} = F(GHI_{i-1}^{OBS}, DNI_{i-1}^{OBS}, GHI_i^{IFS}, DNI_i^{IFS}, GHI_i^{TOA}, DNI_i^{TOA}, T_i^{IFS}, RH_i^{IFS}, W_i^{IFS}, Pr_i^{IFS}, Tcc_i^{IFS}), \quad (4.2)$$

where function *F* is adjusted so that the DNI predictions (DNI_i^{MRM1}, DNI_i^{MRM2}) of the first year are closer to the predictand (DNI_i^{OBS}) for the same year. For the case of the MRM2, the previous hour of measured GHI and DNI (GHI_{i-1}^{OBS} and DNI_{i-1}^{OBS}, respectively) are included as predictors. The function *F* is then applied to the second year of data for validation of the forecast improvement for both MRM1 and MRM2. Regarding the use of previous hour from measured data, only DNI and GHI are considered in the MRM2, since using other available measured variables would require a higher computational cost, with no significant improvement in the forecast. That is, increasing the number of predictors would lead to more complex polynomials, where the adjustments obtained would not improve significantly the hourly DNI, as compared with the use of measured irradiances.

A similar procedure is performed for the daily adjustments of the MRM1 and MRM2 using as predictors: DNI and GHI daily availabilities (E_b^{IFS} and E_t^{IFS}, respectively), daily averages of air temperature ($\overline{T}^{IFS}$), relative humidity ($\overline{RH}^{IFS}$), wind velocity ($\overline{W}^{IFS}$), total precipitation ($\overline{Pr}^{IFS}$) and total cloud cover ($\overline{Tcc}^{IFS}$). The obtained improved daily predictions of DNI from the MRM1 and MRM2 are then given by the following relations:

$$E_{b,j}^{MRM1} = F(E_{t,j}^{IFS}, E_{b,j}^{IFS}, E_{t,j}^{TOA}, E_{b,j}^{TOA}, \overline{T}_j^{IFS}, \overline{RH}_j^{IFS}, \overline{W}_j^{IFS}, \overline{Pr}_j^{IFS}, \overline{Tcc}_j^{IFS}), \quad (4.3)$$

$$E_{b,j}^{MRM2} = F(E_{t,j-1}^{OBS}, E_{b,j-1}^{OBS}, E_{t,j}^{IFS}, E_{b,j}^{IFS}, E_{t,j}^{TOA}, E_{b,j}^{TOA}, \overline{T}_j^{IFS}, \overline{RH}_j^{IFS}, \overline{W}_j^{IFS}, \overline{Pr}_j^{IFS}, \overline{Tcc}_j^{IFS}), \quad (4.4)$$

where the MRM2 includes the previous day (*j*-1) of measured GHI and DNI availabilities ($E_{t,j-1}^{OBS}$ and $E_{b,j-1}^{OBS}$, respectively) as predictors to the MRM1 daily adjustments.

It should be noted that several polynomial terms, and respective metrics, are obtained after applying linear multivariate regression for hourly and daily adjustments of MRM1 (**Tables C.1** and **C.2**, respectively) and MRM2 (**Tables C.3** and **C.4**, respectively) using the stepwise function. More detail information regarding these can be seen in the Appendix C, including all possible iterations between predictors and predictand. After running the stepwise function, for the hourly adjustments of MRM1, nine predictors were considered, while for the daily adjustments, only five predictors were used. In the case of the MRM2 adjustments, in which two more predictors were added (i.e. DNI_{i-1}^{OBS} and GHI_{i-1}^{OBS}) to the previous MRM1 setup, hourly adjustments considered ten predictors, while for the daily adjustments, five predictors were used.

4.3 Results

4.3.1 IFS predictions

A first analysis was carried out between measured and predicted DNI over the two consecutive years, i.e. from July 1st 2017 to June 30th 2018 and from July 1st 2018 to June 30th 2019. The respective statistical and descriptive results are presented and summarized in **Table 4.1**, showing how the IFS predictions behave in comparison with the EVO measured data. During the considered periods, the annual predicted DNI obtained was remarkably close to the observed one, with very slight overestimation (first year) and underestimation (second year) of the measured values. For instance, mean annual values of ≈480.38 and 502.04 W/m^2 predicted by the IFS corresponded to an overestimation of ≈0.09 W/m^2 and an underestimation of ≈0.01 W/m^2 for the first and second year, respectively. Moreover, these small differences were respectively attended with a MBE of ≈-0.05 and 0.01 W/m^2. The overall good performed of the IFS is also shown by the annual availability obtained values, which were close to the expected regional ones (i.e. above 2100 kWh/m^2/year). This is evident in the very small relative differences obtained between annual measured and predicted availabilities (ΔE_b), particularly in the second year, where a value of ≈0.002 % was found. Regarding the obtained annual STD, a smaller deviation was registered for the IFS in the second year (≈288.77 W/m^2), i.e. ≈8.01 W/m^2 less than the measured one. Despite the close approximation between the annual values, the RMSE found between hourly values shows the difference that exists between hourly predicted and measured DNI, mainly due to cloud and aerosol misrepresentation. Nevertheless, such values are found to be consistent with the ones obtained in solar radiation forecasting, e.g. [17, 107], reinforcing the need to improve DNI predictions, as this chapter aims at. A smaller RMSE (≈186.20 W/m^2) was also obtained in the second year, in comparison to the error associated with measurements. For the hourly r, values of ≈0.85 and 0.84 were found in the first and second year, respectively, corresponding to an R^2 of ≈0.72 and 0.71. Considering the daily availabilities correlations, values of ≈0.91 and 0.83 were found for r and R^2, respectively, in both years. High correlations are expected to be found on the daily scale, since the daily summations filter the hourly variability, in which cloud misrepresentations are most noticed.

From the first to the second year of data, an overall decrease in the deviations was observed. This may be related to different intra-annual atmospheric variability. In fact, both measured and predicted data showed less variability in the second year. This can also be associated to the occurrence of less clouds, resulting in a higher annual availability (2200 kWh/m^2/year), i.e. ≈95 W/m^2 more than in the first year.

Table 4.1: Statistical and descriptive analysis summary between measured and IFS predicted DNI over two consecutive years in Évora (southern Portugal), from July 1st 2017 to June 30th 2018 and from July 1st 2018 to June 30th 2019. Several annual statistical and error metrics are presented: the standard deviation (STD), root mean square error (RMSE), mean absolute error (MAE), mean bias error (MBE), annual DNI availability (E), correlation coefficient (r), coefficient of determination (R^2). Hourly results are presented considering only the daylight period. Daily values of r and R^2 (r_{daily} and R^2_{daily}, respectively) are also shown.

	Year 1		**Year 2**	
	Measurements	**IFS**	**Measurements**	**IFS**
Mean (W/m^2)	480.29	480.38	502.05	502.04
Median (W/m^2)	528.33	506.80	557.52	552.47
STD (W/m^2)	353.42	296.78	347.05	288.77
RMSE (W/m^2)		187.80		186.20
MAE (W/m^2)		135.38		135.94
MBE (W/m^2)		-0.05		0.01
Skewness	-0.113	-0.198	-0.180	-0.311
Kurtosis	1.459	1.597	1.527	1.690
E (kWh/m^2/year)	2104.6	2105.0	2200.0	2199.9
ΔE (%)		0.019		0.002
r_{hourly}		0.847		0.844
R^2_{hourly}		0.718		0.712
r_{daily}		0.910		0.912
R^2_{daily}		0.829		0.832

In the context of assessing the error associated to the IFS original predictions in comparison to local measurements of DNI, hourly clearness indices (k_b) and respective PDF's were also calculated for each year, as shown in **Fig. 4.1**. As expected, close to null-values of k_b, a cluster of values was obtained, as a consequence of the prediction overestimation (due to the misrepresentation of clouds) towards measurements during overcast periods. For instance, during a cloudy period, measurements yield k_b values close to zero while the IFS predictions consider values up to 0.6. As opposed to this, close to high values of k_b, another cluster of hourly values was found, corresponding to clear sky conditions (particularly, very clean atmospheric days), in which an underestimation of the predictions towards measurements occurs. This underestimation is most likely to result from a sub-estimation of the radiative effects towards sub-grid clouds and, most

importantly, to the use of an aerosol climatology, which overestimates the actual aerosol load under such conditions. For instance, close to k_b values above 0.7, e.g. during a sunny day that occurs after a rainy day, the actual aerosol concentration in the atmosphere is very low, as opposed to the climatologic aerosol value implemented in the model. During very clean atmosphere conditions, the relation between predicted and measured data was depicted by a smaller dispersion of k_b values in comparison with the ones obtained under overcast and partly cloudy conditions. Particularly, between both extremities (i.e. during partly cloudy periods), there was a high distribution of hourly values that resulted from clouds passing over the measuring equipment, in which the forecast model had difficulties in representing these at the hourly scale. A similar behaviour was observed in both years, as previously discussed. Moreover, the obtained PDF's allowed to observe the frequency of occurrence of k_b values and both of the previous discussed clusters (i.e. for low and high values of k_b). A summary of the statistical results between IFS and measured based k_b values during the second year is presented in **Table 4.2**. During this preliminary analysis, an hourly SS of ≈0.66 was found for the second year, being similar to the value obtained for the previous year (not shown here).

Table 4.2: Statistical summary of hourly clearness indices for DNI (k_b) between measurements and predictions (IFS, SRM, MRM1 and MRM2) for a one year (July 1st 2018 to June 30th 2019) in Évora. Correlation coefficient (r), coefficient of determination (R^2), root mean square error (RMSE), mean bias error (MBE), mean absolute error (MAE) and skill score (SS) are presented. The SS is calculated towards a referenced persistence model (i.e. measurements time series displaced 24 hours ahead).

	IFS	**SRM**	**MRM1**	**MRM2**
r	0.846	0.849	0.866	0.929
R^2	0.716	0.720	0.750	0.864
RMSE	0.137	0.136	0.129	0.095
MAE	0.100	0.099	0.092	0.062
MBE	1.855×10^{-4}	5.091×10^{-4}	0.003	7.834×10^{-4}
SS	0.656	0.661	0.697	0.835

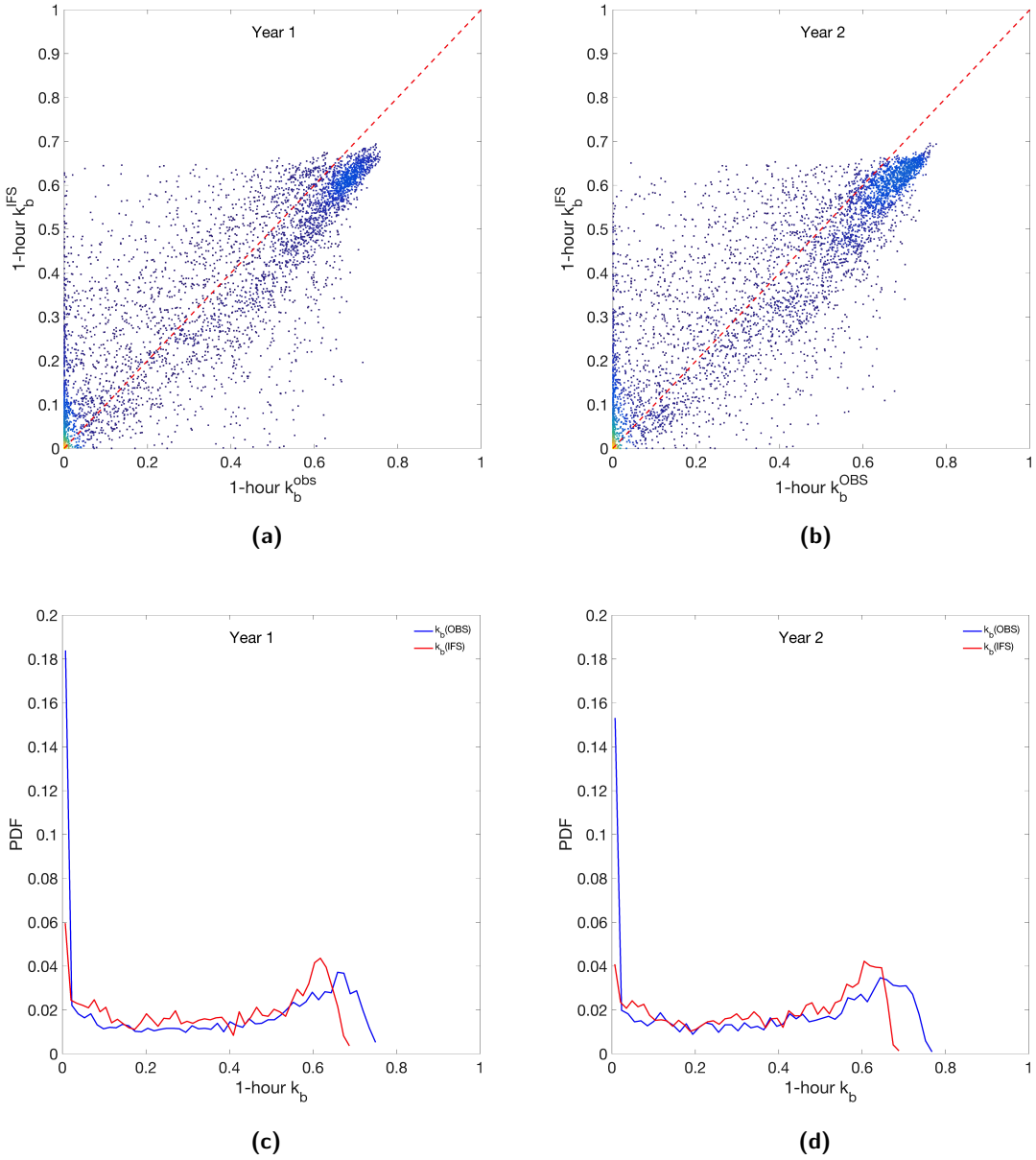

Figure 4.1: Hourly (a, b) clearness indices for DNI (k_b) between measurements (obs) and predictions (IFS) considering two consecutive years of data in Évora, from July 1st 2017 to June 30th 2018 (year 1) and from July 1st 2018 to June 30th 2019 (year 2), with the identity line y=x being also represented (red-dashed line). The respective probability hourly density functions (PDF's) are also shown (c, d).

When considering daily values, a general improvement of the deviation between predicted and measured values of K_b was found for both years, as shown in **Fig. 4.2**. The results, based on the daily availabilities of DNI, showed that the previous overestimation of the model close to null K_b values was significantly reduced, leading to higher correlations and lower errors. As previously discussed, at this scale, such effect is expected in NWP, since the IFS, like most NWP models, has difficulties in predicting the precise location and moment

when a variation of DNI occurs, particularly from one hour to the next. However, despite such inability, the forecast model is relatively good in predicting cloud occurrences. For instance, cloud formation, advection and dissipation, result from complex microphysics process that can occur at sub-grid and sub-hourly scales, and therefore the model will not be able to represent them precisely. When considering daily values of DNI, temporal phase errors are filtered, allowing the IFS to provide satisfactory results when compared with local daily measured based values. This was shown by the narrowing of K_b values towards the identity line in **Fig. 4.2**, which depicted a closer behaviour between predicted and measured daily data, although the underestimation of the model during clear sky conditions still prevails. The respective daily PDF's, besides showing a reduction of the error in comparison with the hourly results, shows an apparent high variability. However, it should be considered the fact that a smaller range of frequency (i.e. *yy* axis) is being depicted and the reduced number of samples in this case. The statistical results obtained are summarized in **Table 4.3**, where a daily SS of ≈0.73 was attained between measurements and predictions for the second year. The daily values, which consider predicted daily availabilities, also allowed to visualize the potential of the IFS regarding the definition of operational strategies of a CSP plant. Such information is particularly important to the plant operator concerning the expected DNI availability and the distribution of energy dispatchability for the next day.

Table 4.3: Statistical summary of daily clearness indices for DNI (K_b) between measurements and predictions (IFS, SRM, MRM1 and MRM2, for a one year period (July 1st 2018 to June 30th 2019) in Évora. Correlation coefficient (r), coefficient of determination (R^2), root mean square error (RMSE), mean bias error (MBE), mean absolute error (MAE) and skill score (SS) are presented. The SS is calculated towards a referenced persistence model (i.e. measurements time series displaced 24 hours ahead).

	IFS	**SRM**	**MRM1**	**MRM2**
r	0.892	0.897	0.911	0.899
R^2	0.795	0.804	0.831	0.809
RMSE	0.090	0.084	0.077	0.082
MAE	0.071	0.063	0.056	0.058
MBE	-0.002	-0.002	0.006	0.005
SS	0.734	0.772	0.805	0.779

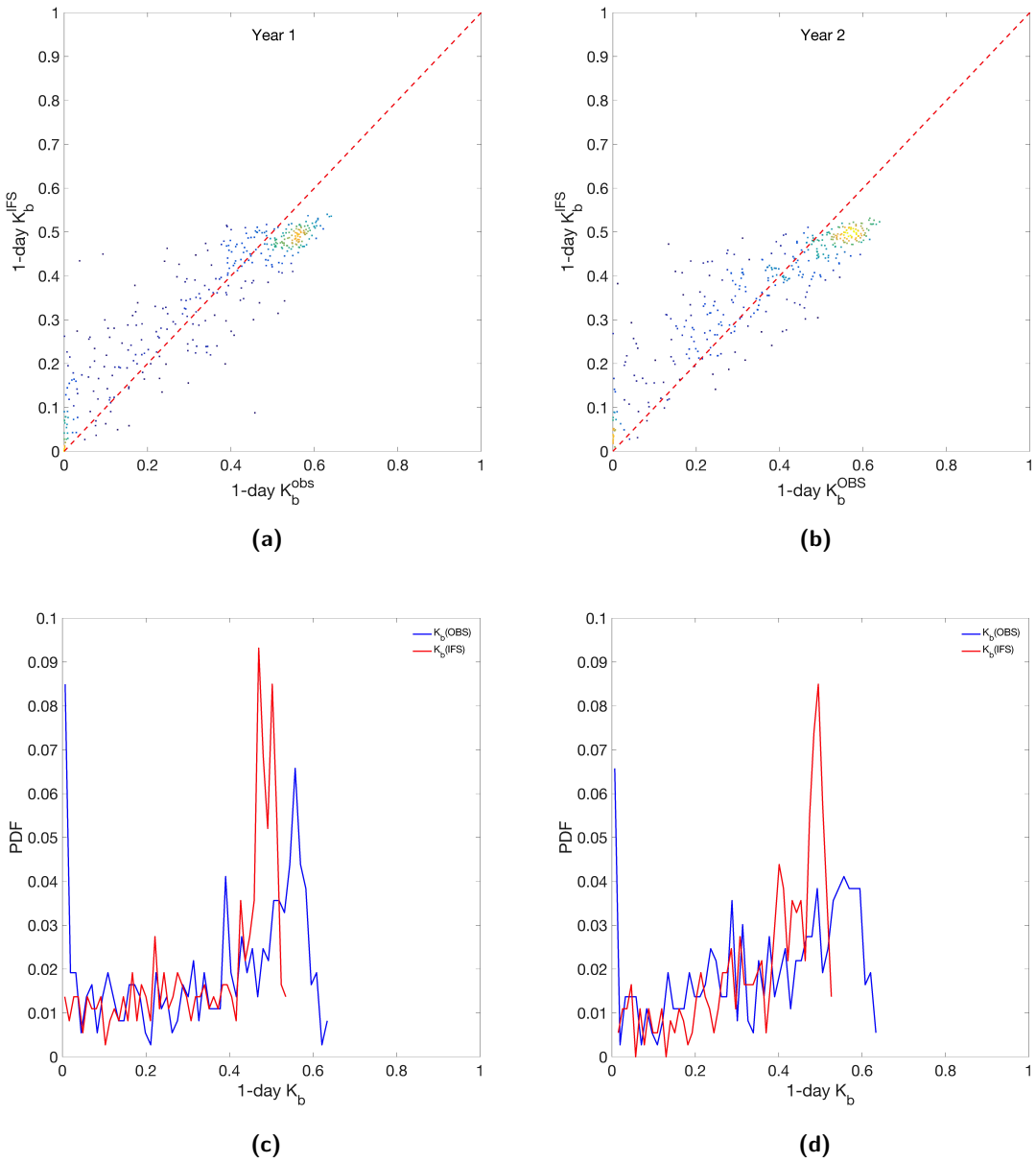

Figure 4.2: Daily (a, b) clearness indices for DNI (K_b) between measurements (obs) and predictions (IFS) for two consecutive years in Évora, from July 1st 2017 to June 30th 2018 (year 1) and from July 1st 2018 to June 30th 2019 (year 2), with the identity line $y{=}x$ being also represented (red-dashed line). Respective probability daily density functions (PDF's) are also shown (c, d). Daily values were calculated through DNI availabilities (kWh/m^2), i.e. the sum of each 24-hour period.

To improve hourly predictions of DNI, post-processing methods can be applied. Since the ecRad (cycle 43R3) was implemented in July 2017, this work only considers the period of two years. This can be seen as a limitation regarding statistical downscaling methods (e.g. the application of perfect prognosis) for the adjustment of DNI, particularly towards daily adjustments. However, MOS techniques are suitable for the

present analysis, which considers the use of the first year to improve hourly predictions in the second year. Moreover, these methods can be further enhanced if longer time series are to be considered, allowing to statistically validate the coefficients from multivariate regression adjustments.

4.3.2 Spatial average

Prior to the application of regression analysis, a simple error adjustment was performed by implementing a spatial average that considers the closest grid points to the actual measuring location, instead of using the nearest global model grid point. The method has some benefits [129], in which small improvements can be attained when considering hourly predictions of DNI from the IFS. This was the case when performing an average from a 3 x 3 grid points (corresponding to an area of about 18 km x 18 km), centred in the nearest grid point to the EVO geographic coordinates. The spatial average, which was separately applied for both years, yield very similar results. Overall, when compared with the nearest point to the measuring location, results from the second year showed an hourly correlation increase of ≈0.51 % and a decrease of ≈1.20 % in the RMSE.

It should be noted that an increase in the number of available grid points used for averaging could be an option, however the resulting average DNI would be unrepresentative of the exact location of study. Moreover, performing the spatial average considering daily availabilities did not provide any improvement, since intra-day variability is already reduced by the daily summation. For this matter, to further improve hourly DNI predictions, different techniques should be pursued to significantly reduce the associated error.

4.3.3 Simple regression model (SRM)

Regression coefficients obtained from a polynomial adjustment in first year, between measured and predicted values of DNI, can be used to adjust the IFS predictions in the second year. To this end, several polynomials were tested, in which a third-degree polynomial was found to provide the best results with the IFS for the application of the SRM. Results showed small improvements and the presence of a non-linear relation, as shown by the k_b obtained values (**Fig. 4.3a**). Comparing these results with the ones previously obtained between the IFS original predictions and measurements (**Table 4.2**), an increase of ≈0.35 % and a decrease of ≈0.73 % were found for the r and RMSE, respectively. An hourly SS of ≈0.66 was attained using the SRM, corresponding to an increase of ≈0.76 %. When comparing the respective PDF's (**Fig. 4.3b**), the improvement is evident, particularly for higher values of k_b (i.e. in the absence of clouds) where hourly SRM values are closer to the observed behaviour than the ones obtained with the IFS (**Fig. 4.1c**).

A similar procedure, but for the daily availabilities (**Fig. 4.4a**), showed correlations of ≈0.90 and a SS of ≈0.77 (**Table 4.3**), i.e. an increase of ≈0.56 and 5.05 % (respectively) towards the IFS daily K_b's.

These results, besides showing improvements using simple regression methods, evidence the need of using more complex approaches that can lead to a more substantial reduction of the error associated to hourly predicted DNI. One example is to include other variables related to DNI modulation for the polynomial adjustment, as discussed in the following sections.

4.3.4 Multivariate regression model (MRM1)

As it was shown in the previous section, adjusting only DNI forecast to the DNI observations, does not improve substantially the forecasts. This is a result of the complex nature of the DNI related physical processes. Thus, in this subsection, other forecasted meteorological variables along with predicted DNI are considered to match the observed DNI, using a multivariate regression technique. This technique uses the observed DNI as the objective function and determines the optimal combination of coefficients and input variables (in this case, the forecasted variables) to approximate the predictions to the observations. The method has the advantage of simulating some of the physical phenomena that actual occur, allowing to consider interaction terms between variables (e.g. predicted DNI with predicted temperature). In this context, like in the previous section, regression coefficients, which resulted from the adjustment made between predictions and measurements for the first year, were used to adjust the IFS predictions in the second year with the inclusion of eight new predictors. These include the same hour predicted variables, i.e. GHI, irradiances calculated at TOA (GHI^{TOA}, DNI^{TOA}), air temperature, relative humidity, wind velocity, total precipitation and total cloud cover. Due to the large number of predictors, the resulting model MRM1 was found to best perform through a second-degree polynomial fitting with the stepwise function. It should be noted that when running the stepwise function, negative values can result from the multivariate adjustment of the original IFS data; especially for low observed and predicted DNI values. With this method, a total of 121 negative values were found to occur. In such cases, the original IFS predicted values of the second year of data were maintained. The application of the stepwise function for MRM1 was based on the best fitting found through an iterative process that tested 43 different formulations between predictand and all predictors (**Table C.1**, Appendix C).

When performing an analogous method of multivariate regression but to daily DNI availabilities, daily mean values of air temperature, relative humidity, wind velocity, precipitation and cloud cover, were considered. In the case of solar radiation variables, availability values (i.e. the sum of each 24-hour periods) were used. The resulting daily adjustment considered 11 different formulations between daily predictand and predictors (**Table C.2**, Appendix C). After performing the adjustment to the originally predicted availabilities, 7 negative values were found, being the corresponding IFS daily predictions maintained instead.

Results showed that the hourly k_b values obtained, presented in **Fig. 4.3b** and **5.3e**, illustrate further improvements attained through the MRM1, in comparison to simple linear regression methods. Particularly, during cloudy conditions, i.e. close to null-values of k_b, there is a reduction in the previous overestimation

of the predictions in comparison to the measurements. It is also observed that for clear sky conditions, there is also a compensation in the underestimation of the predictions. From its original value (i.e. from the IFS) to the value obtained with MRM1, an increase of ≈2.36 % in the correlation was attained, together with an overall decrease in the errors, such as ≈5.84 % in the RMSE (**Table 4.2**). Regarding the hourly SS, a value of ≈0.70 was found, corresponding to an increase of ≈6.25 % from the original value. Daily availabilities (**Fig. 4.4b** and **5.4e**), which resulted from the polynomial adjustment expressed in **Table C.2** (Appendix C), showed K_b values with correlations of ≈0.91 and RMSE of ≈0.08 (**Table 4.3**). Moreover, daily values showed that the best results were obtained with the MRM1 (highlighted in gray), in which an increase of ≈9.55 % in the daily SS was obtained in relation to the original value found when using the IFS daily predictions.

In the next section, a new addition to MRM1 is carried out by including the previous hour of measured GHI and DNI as predictors in the case of the hourly analysis. While for the daily analysis, the previous day of measured availability is used to improve the IFS day-ahead predictions.

4.3.5 Compound multivariate regression model (MRM2)

As means to optimize the MRM1 outputs, the proposed MRM2 was created using the same setup as in MRM1, but with the inclusion of the previous hour of measured GHI and DNI to the former MRM1 predictors. The resulting iterative process tested 50 different formulations between predictand and all predictors (i.e. a total of 11 predictors), as shown in **Table C.3** (Appendix C). As before with the MRM1, negative values (a total of 84) were obtained for the MRM2 during the regression procedure. Likewise, these values were maintained by the original IFS predicted values, as well as for the first forecast of the day (right after sunrise).

When compared with the IFS hourly values, the MRM2 significantly improves DNI predictions, as shown by the obtained k_b values (**Fig. 4.3c** and **5.3d**). The results depict a narrowing towards the identity line $y=x$, i.e. closer to a linear relation than the previous results obtained. In addition to a lower occurrence of overestimated k_b values close to zero, a smaller dispersion of values was also attained for partly cloudy conditions, as well as less underestimated k_b values during clear sky conditions. As shown in the statistical summary (**Table 4.2**), the best hourly improvements were obtained with the MRM2 (highlighted in gray), with an hourly correlation of ≈0.93 and a SS of ≈0.84 were found, corresponding to increases of ≈9.81 and 27.29 %, together with a general decrease of the errors.

For the daily availability analysis, the IFS predicted availability of the first day was preserved. Moreover, daily DNI availabilities (**Table C.3**), in which the previous day availability value was used to forecast the next day, resulted from the polynomial adjustment presented in **Table C.4** (Appendix C). After 23 different formulations, the best fitting found produced 8 negative values, in which the IFS forecasted values were maintained. The K_b values found with this method are showed in **Fig. 4.4c** and **4.4f**, where high correlations and low errors between adjusted predictions and measurements are found. A daily correlation (**Table 4.3**) of ≈0.90 and an SS of ≈0.78 were obtained for the second year of data. In comparison with

the original IFS predicted values, these correspond to increases of ≈0.78 and 6.13 %, respectively.

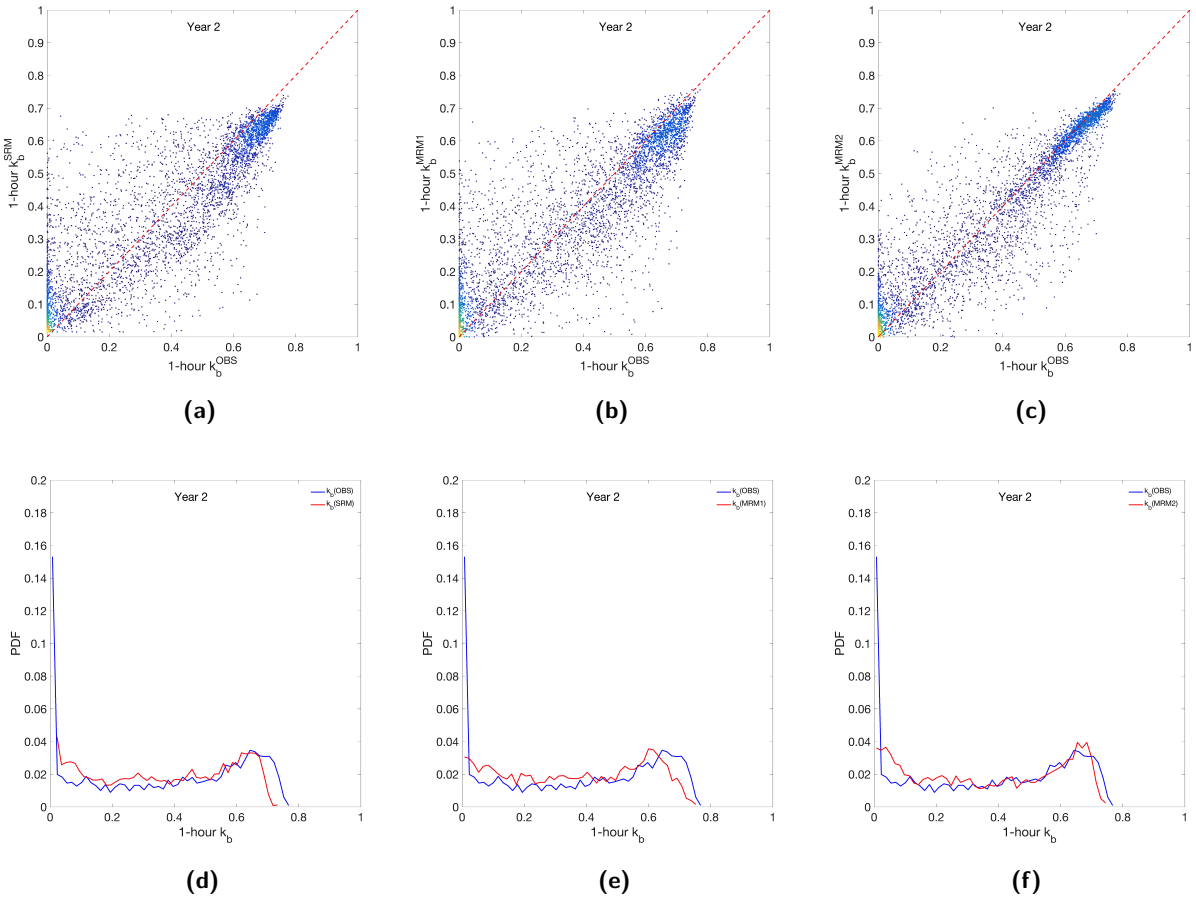

Figure 4.3: Hourly clearness indices for DNI (k_b) between measurements (obs) and improved DNI predictions with (a) SRM, (b) MRM1 and (c) MRM2, where the identity line $y=x$ is represented as a red-dashed line. Analysis is performed over one year of data in Évora, from July 1st 2018 to June 30th 2019. The respective probability hourly density functions (PDF's) are also depicted (d, e and f).

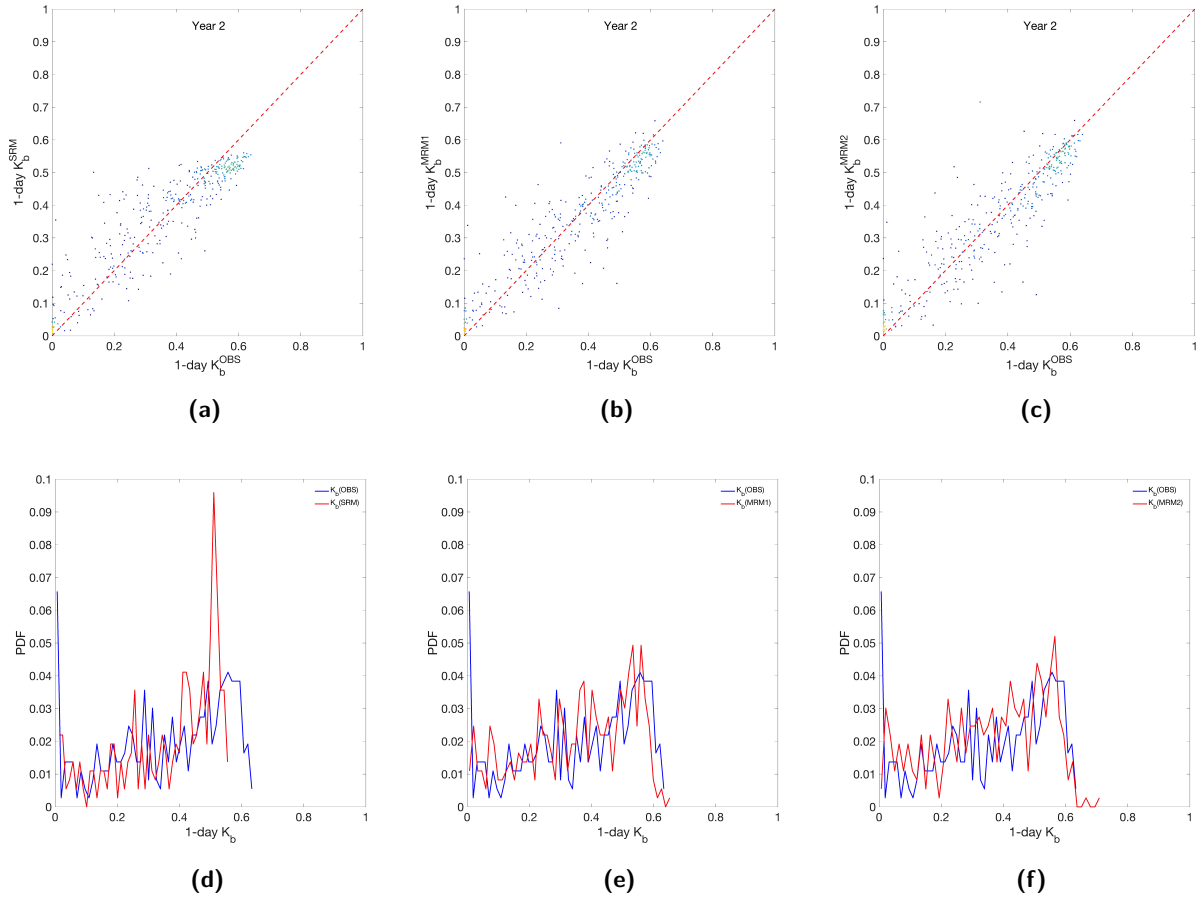

Figure 4.4: Daily clearness indices for DNI (K_b) between measurements (obs) and improved DNI predictions with (a) simple regression model (SRM), (b) multivariate regression model (MRM1) and (c) compound multivariate regression model (MRM2), with identity line $y=x$ represented as a red-dashed line. Analysis is performed over one year of data in Évora, from July 1st 2018 to June 30th 2019. The respective probability hourly density functions (PDF's) are also being depicted (d, e and f). Daily values are calculated through DNI availabilities (kWh/m^2), i.e. the sum of each 24-hour period.

Despite a dependency on measurements taken in the previous hour or previous day (depending on the case of study), the MRM2 method presents itself as the best fitting found when using multivariate analysis. Through the use of the previous hour of measured DNI and GHI, the model allowed to achieve the best results with significant improvements for the hourly values in comparison with the other presented methods. Moreover, it is possible to observe that for daily availabilities, the improvements obtained are not as significant as the ones obtained on the hourly basis. This is due, in part, to the fact that the IFS daily predictions are already satisfactory, making it more difficult to achieve further improvements. Another important reason is the fact that only one year of data is being used to adjust predicted DNI. This affects particularly the daily adjustment, in which the daily data can be nearly twelve times less than the data used for the hourly adjustment. For this matter, in the context of MRM2 daily predictions, more statistical

information is required than the one used for this analysis. Thus, with more data (i.e. with an increased number of years) to perform the MRM2 daily adjustments, better predictions with less dispersion of values in comparison to the measured ones from one day to the next should occur.

4.3.6 Application to CSP operation

After applying different methodologies to improved IFS forecasts, the following two-steps methodology is proposed for their implementation as a tool in CSP operations: i) the use of daily MRM1 improved DNI availabilities to define the generic operation strategy for each day (as suggested in the next chapter); and ii) the application of the hourly MRM2 improved DNI predictions to refine hour-by-hour the operation strategy throughout each day, similarly to nowcasting techniques [130]. In summary, using this information for the optimization of CSP plants is fundamental, since precise day-ahead forecasts of DNI allow to predict the day-ahead CSP plant's electricity generation. In addition to the improved daily strategies based on different estimates of DNI availability, these can then be further refined with the use of hourly adjustment, particularly from the MRM2. Focus to these subjects will be given in the next section.

4.4 CSP daily strategies

Considering the previous results, improved forecasts can now be used to improve operational strategies regarding CSP plant's energy management. These strategies can be implemented on the hourly basis, to optimize energy use throughout the day (being related to short periods of solar intermittency), and, particularly, on the daily basis. This allows the plant operator to decide on how and when to sell the predicted electrical energy generated by the plant at a premium tariff in the electrical market.

This section focuses the use of contingency tables with daily measured and predicted (IFS, SRM, MRM1 and MRM2) availabilities separated by different ranges, according to the previously defined strategies. Such tables aim to evidence the improved accuracy of daily availability range predictions with the use of the adjustment methods discussed previously. An improved prediction implies a better day-ahead planning regarding a plant operation strategy. This has the potential to lead, if properly articulated with the improved hourly predictions, to an overall enhancement of the solar to electricity conversion procedure. In turn, this will be reflected in an increase of the plant's efficiency (e.g. by enabling higher temperatures of the superheated steam in the power block), as well as its dispatchability (e.g. by smoothing temperature variations at the solar field outlet of the heat transfer fluid). The improved hourly predictions will be based on the MRM2, which was shown to be the best adjustment method. Thus, this analysis has the objective of combining improved daily availability predictions with improved hourly forecasts of DNI to increase a power plant operation reliability. Using such combined strategy would certainly improve the electrical energy production and its value, reducing the final levelized cost of electricity, i.e. the ratio between the sum of the discounted total cost during the lifetime of a plant and the sum of the discounted total amount of electrical

energy delivered. Consequently, the client's electricity bill would also be reduced, (another strong reason to optimize CSP plants). Although such life cycle analysis is out of scope of the present study, it can certainly be carried out in future research works.

Results for the daily availabilities from the IFS, SRM, MRM1 and MRM2, respectively in **Tables 4.4, 4.5, 4.6** and **4.7**, were obtained for a period of one year (from July 1st 2018 to June 30th 2019). In these tables, the number of occurrences when predictions coincide with measurements correspond to the "Hits", whereas the corresponding success rate (%) is calculated considering the total number of measured availabilities values. The range by which this evaluation was carried out is divided in four intervals, which go from overcast to clear sky conditions, corresponding to different strategies defined for the corresponding atmospheric conditions that have distinct effects over a CSP plant electrical production (as it will be discussed in the next chapter). As expected, all day-ahead adjustment models provide satisfactory results, with prediction accuracies generally above 50 %, mainly due to the reduction of the intra-day variability, as a consequence of the daily summation. This includes the original IFS day-ahead predictions, which depict the highest daily success rates of "Hits" between 3-6 and 6-9 kWh/m^2/day (≈68.48 and 88.14 %, respectively). The daily adjustments were able to significantly increase the day-ahead estimations accuracy during overcast and very clean atmospheric periods. Success rates of "Hits" between ≈70.89 and 73.42 % were respectively found for the MRM2 and for both SRM and MRM1, corresponding to cloudy days (from 0 to 3 kWh/m^2/day). Considering clear sky days (from 9 to 13 kWh/m^2/day), success rates of ≈75 and 77.63 % were respectively found for the MRM1 and for both SRM and MRM2.

Table 4.4: Contingency table for availability values of DNI (kWh/m^2/day) between observations (OBS) and IFS predictions. A range divided in four intervals defines different weather conditions during a one year period (from July 1st 2018 to June 30th 2019) in Évora. Corresponding values between the IFS and observations within each interval are highlighted in grey. The total number of measurements (Total OBS) is also presented.

		IFS				
		0-3	**3-6**	**6-9**	**9-13**	**Total OBS**
OBS	**0-3**	47 (59.49 %)	28 (35.44 %)	4 (5.06 %)	0	79
	3-6	2 (2.17 %)	63 (68.48 %)	27 (29.35 %)	0	92
	6-9	0	12 (10.17 %)	104 (88.14 %)	2 (1.70 %)	118
	9-13	0	1 (1.32 %)	37 (48.68 %)	38 (50.00 %)	76

Table 4.5: Contingency table for availability values of DNI (kWh/m^2/day) between observations (OBS) and SRM predictions. A range divided in four intervals defines different weather conditions during a one year period (from July 1st 2018 to June 30th 2019) in Évora. Corresponding values between the IFS and observations within each interval are highlighted in grey. The total number of measurements (Total OBS) is also presented.

		SRM				
		0-3	**3-6**	**6-9**	**9-13**	**Total OBS**
OBS	**0-3**	58 (73.42 %)	17 (21.52 %)	3 (3.80 %)	1 (1.27 %)	79
	3-6	10 (10.87 %)	55 (59.78 %)	26 (28.26 %)	1 (1.09 %)	92
	6-9	0	16 (13.56 %)	97 (82.20 %)	5 (4.24 %)	118
	9-13	0	1 (1.32 %)	16 (21.05 %)	59 (77.63 %)	76

Table 4.6: Contingency table for availability values of DNI (kWh/m^2/day) between observations (OBS) and MRM1 predictions. A range divided in four intervals defines different weather conditions during a one year period (from July 1st 2018 to June 30th 2019) in Évora. Corresponding values between the IFS and observations within each interval are highlighted in grey. The total number of measurements (Total OBS) is also presented.

		MRM1				
		0-3	**3-6**	**6-9**	**9-13**	**Total OBS**
OBS	**0-3**	58 (73.42 %)	19 (24.05 %)	2 (2.53 %)	0	79
	3-6	14 (15.22 %)	57 (61.96 %)	20 (21.74 %)	1 (1.09 %)	92
	6-9	1 (0.85 %)	15 (12.71 %)	98 (83.05 %)	4 (3.39 %)	118
	9-13	0	1 (1.32 %)	18 (23.68 %)	57 (75.00 %)	76

Table 4.7: Contingency table for availability values of DNI (kWh/m^2/day) between observations (OBS) and MRM2 predictions. A range divided in four intervals defines different weather conditions during a one year period (from July 1st 2018 to June 30th 2019) in Évora. Corresponding values between the IFS and observations within each interval are highlighted in grey. The total number of measurements (Total OBS) is also presented.

		MRM2				
		0-3	**3-6**	**6-9**	**9-13**	**Total OBS**
OBS	**0-3**	56 (70.89 %)	21 (26.58 %)	2 (2.53 %)	0	79
	3-6	15 (16.30%)	62 (67.40 %)	14 (15.22 %)	1 (1.09 %)	92
	6-9	1 (0.85 %)	11 (9.32 %)	97 (82.20 %)	9 (7.63 %)	118
	9-13	0	1 (1.32 %)	16 (21.05 %)	59 (77.63 %)	76

Overall, when planning CSP daily operational strategies, the plant operator can rely on the improved daily availabilities, particularly the MRM2 if longer time series are available, to define general operation strategies for the day, as it will be discussed in the following chapter. This is a tremendous advantage for solar energy applications, allowing a considerable reduction of operation uncertainties.

4.5 Conclusions

In order to improve hourly and daily predictions of DNI from the ECMWF global model, statistical post-processing methods were applied to the provided 24-hour forecasts of the IFS. Considering two consecutive years of both predicted and measured data in Évora, the attained adjusted predictions resulted from the use of simple techniques, suitable to be used from the operational point of view, including linear and multivariate regression analysis. It was observed that best results were achieved with the use of the MRM2 adjustment model. Through the use of hourly clearness indices, the MRM2 showed a high correlation ($\approx$0.93), representing an increase of $\approx$9.81 % in comparison with the IFS original value. Moreover, the MRM2 demonstrated a skill score (SS) of $\approx$0.84, i.e. $\approx$27.29 % higher than the one obtained with the IFS. As expected, on the daily scale, the proposed adjustment models showed satisfactory results due to the reduction of the cloud overestimation characteristic of the hourly predictions, as a consequence to the daily summation. Lower daily errors and higher correlations were found using the daily adjustment models, particularly with the MRM1, where a daily SS of $\approx$0.81 was obtained. Using the MRM2 daily adjustments, a daily SS of $\approx$0.78 was found. Differences between the daily adjustments of the MRM1 and the MRM2 are due to the high inter-daily variability of DNI, which are highlighted in the daily MRM2 with the use of previous day measured availability to adjust the next day value. Nevertheless, to further improve the MRM2 daily predictions more than one year of data should be used, certainly allowing a better daily performance than the MRM1. Moreover, the analysis made use of daily contingency tables, created to provide generic strategies to the plant operator under different atmospheric conditions. On a daily basis, predictions can be used with the adjusted values, particularly for overcast and clear sky days, while during partly cloudy periods the original IFS daily availabilities from the IFS are maintained. Operational strategies based on day-ahead predictions can also be refined throughout the day using the MRM2, which was shown to be the most suitable model to be used on the hourly time scale.

The work presented in this chapter resulted from the following publication:

- Francis M. Lopes, Ricardo Conceição, Hugo G. Silva, Rui Salgado, Manuel Collares-Pereira. Improved ECMWF forecasts of direct normal irradiance: a tool for better operational strategies in concentrating solar power plants, Renewable Energy (2020), 163, 755-771.

5

DNI Forecasts for CSP Operational Strategies

The fifth chapter comprises all first-author publications, including the respective scientific content (i.e. analysis, tables and original figures). The first part concerns the regional evaluation of the solar resource in the Alentejo region with the production of availability maps, being retrieved from [83]. In the second part, simulations and operational strategies of the Gemasolar [86] and Andasol 3 [131, 84] power plants are carried out. The final part focus the use of improved DNI forecasts in the Andasol 3 simulation to improve daily strategies, as shown in the last section of another work [85]. These publications are listed at the end of this chapter.

5.1 Introduction

Solar power forecasts play a critical role in the power-system management, scheduling and dispatch operations of solar energy harvesting systems. In particular, accurate forecasts of DNI are required for efficient operations of CSP plants during periods of high energy demand, which are characterized by high values of DNI at the surface (clear sky days) and during solar intermittency periods, which are characterized by high DNI intra-day variability (partly cloudy days) [17, 23]. Such information has the potential to help the power plant operator to improve hour and day-ahead operational strategies related to control operations, energy saving procedures, and the anticipation of the plant's energy output for the day-ahead electricity market. In the case of the latter, an estimation of the electricity generated in advance allows the operator to sell it at the premium tariff [73], i.e. the operator can have a direct role on the electricity market, instead of being subjected to flat-rate prices (i.e. the fixed tariff option).

This chapter focus the use of day-ahead (24 hours) forecasts of solar radiation for CSP operational purposes in southern Portugal. First, GHI and DNI predictions are used to produce availability maps to characterize the solar resource of the region. Then, DNI and other relevant meteorological variables from the IFS are used as inputs parameters for the simulation of different types of CSP plants. To this end, the forecasts are used in a power plant model, known as the SAM, to simulate a CR and a PT system, as described in Chapter 2. The simulated power plants were selected according to their relevance in the electrical industry: i) CR units are seen as the future of CSP systems, due to their efficiency in solar harvesting; and ii) PT is currently the most commercial viable technology. The objective of these simulations will help to assess the potential that accurate forecasts of DNI can have in these systems, which differ in design and control procedures, allowing to evaluate the usage of solar radiation predictions in each system. The predicted energy outputs obtained from each simulated system are then assessed by comparing the predicted results with the ones obtained using local ground-based measurements for the same period and location, namely EVO station. Moreover, regarding control strategy, operational strategies are proposed for different weather scenarios to handle the energy management of the simulated CSP plants, including the effect of thermal energy storage capacity.

5.2 Solar irradiance availability maps

Accurate forecasts of GHI and DNI are required in order to provide information for an efficient operation of solar energy applications. In particular, CSP power plants, which are known to have a higher energy storage capacity than other systems, are in a current need for precise predictions of DNI (mainly for partly cloudy conditions). Such predictions will allow to reduce the uncertainty concerning solar power plants outputs and to optimize the necessary electrical energy generation and, consequently, to maximize the energy output for a given day. In this context, **Fig. 5.1** depicts the annual GHI and DNI availability maps obtained with the IFS data considering a complete set of 365 days. For this purpose, and without the application

of filters, solar assessment is made for solar altitude angles above 0° considering the solar irradiation time series from the 24-hour predictions. It should be noted that, in this section, the obtained results consider solar radiation forecasts from the McRad radiation scheme, since the improved version (i.e. the ecRad) was not operational at the start of this thesis. As previously mentioned in Chapter 3, the McRad was replaced by the ecRad (cycle 43R3) around July 2017, which became the main source of solar radiation forecasts in the following research works, and thus in the following sections.

In the southern region of Portugal, predicted GHI availability (**Fig. 5.1a**) was found to be between 1700-2000 kWh/m^2/year, while the predicted DNI availability (**Fig. 5.1b**) was higher, between 2000-2500 kWh/m^2/year. It should be mentioned that higher irradiation availability values of DNI were found outside the unmasked area, corresponding to southern Spain and Atlantic Ocean. Taking in consideration the IFS overestimation, particularly for DNI, the values found for southern Portugal had an overall good agreement with the regional ones established in the past for GHI (1900 kWh/m^2/year) and DNI (over 2100 kWh/m^2/year), as documented in literature [88]. As expected, both GHI and DNI annual availabilities increase from northwest to southeast, as consequence of the latitude effect and the lower average of cloudiness occurrences in the central and southern region of Portugal. This behaviour has been previously observed in other research works (e.g. [89]).

Despite the available different time periods considered in this analysis, the DNI annual availability values, obtained between 2015-2017 (EVO, MIT and PRT) and 2014-2017 (ALC) from the DNI national network [89], allow to give a sense of comparison with the global model results (**Table 5.1**). Results show a general overestimation by the IFS, with a significant difference for PRT (≈19.3 % more than the measured). This is likely to be attributed to the frequent occurrence of small scale fogs in the area, but overall differences are mainly related to the use of larger sets of measured data than that of the model output, since annual means of more than one year are being referenced here.

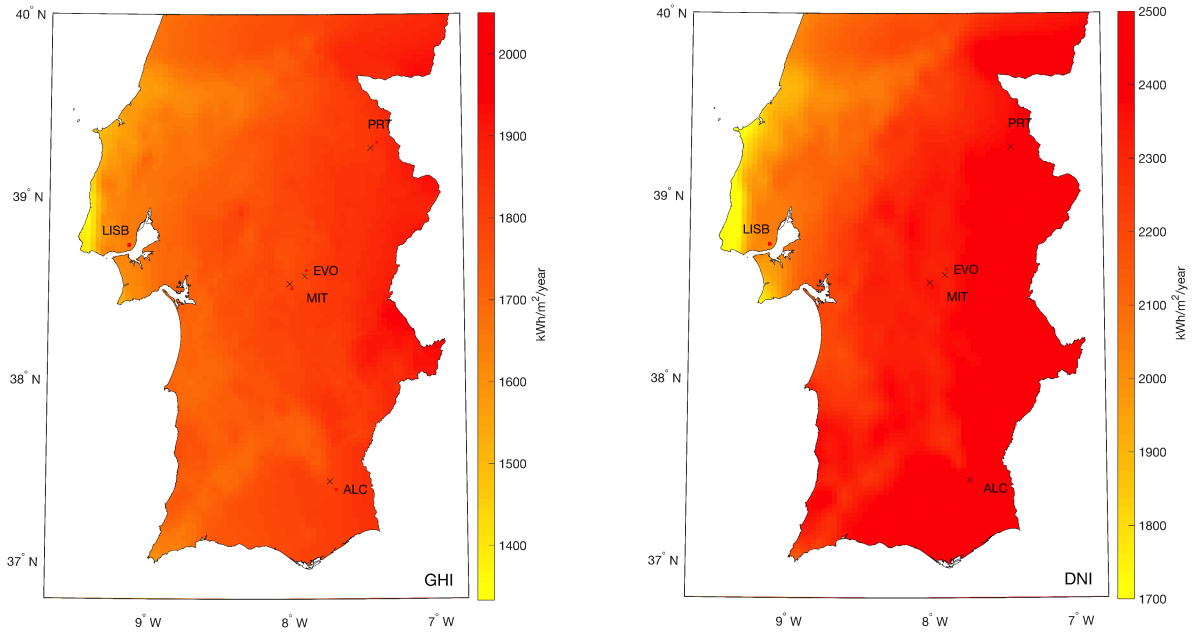

(a) Predicted annual GHI.

(b) Predicted annual DNI.

Figure 5.1: Spatial distribution of predicted annual availability (kWh/m^2/year) maps for solar irradiance in southern Portugal, comprising four measuring locations: Évora (EVO), Mitra (MIT), Portalegre (PRT) and Alcoutim (ALC), during one year of measurements (April 1st 2016 to March 31st 2017). The represented values were obtained through the use of day-ahead predictions from the IFS (McRad).

Table 5.1: Comparison of annual DNI availability (kWh/m^2/year) between measurements [88] and IFS (McRad) predictions. One year (from April 1st 2016 to March 31st 2017) of simulations is considered, while the measured data comprises longer periods: 2015-2017 for Évora (EVO), Mitra (MIT), and Portalegre (PRT), and 2014-2017 for Alcoutim (ALC).

DNI (kWh/m^2)	EVO	MIT	PRT	ALC
Measurements	2073	1989	1841	2015
IFS	2155	2142	2197	2235

Regarding the use of GHI and DNI predicted availability maps for efficient day-ahead operations of solar power plants, **Fig. 5.2** depicts an example on how solar radiation forecasts can have such benefit by considering two case studies. The first example shows one day with clear sky conditions (July 12th 2016) over all stations, in which predictions show higher values occurring uniformly in the southern part of the country (**Fig. 5.2a** and **5.2b**). In the case of predicted GHI availability, only PRT station show higher values (≈8.4 kWh/m^2/day) as compared with the remaining stations, which had ≈8.32, 8.33 and 8.35 kWh/m^2/day for EVO, MIT and ALC, respectively. For the predicted DNI availability,

a general increase of irradiation is to be expected with ≈10.12, 10.16, 10.63 and 10.35 kWh/m^2/day, respectively for EVO, MIT, PRT and ALC stations. It is also observed that during this day cloud formation occurred in the northern part of the considered domain, near PRT (a common local feature due to the orography of the terrain). The second example depicts one day with cloudy conditions (May 8th 2016), in which predictions show a more uneven spatial distribution of irradiation in the region (**Fig. 5.2c** and **5.2d**). Here, GHI daily values are higher (≈5.23 kWh/m^2/day) in the area that covers PRT station. Likewise, high values of DNI (≈4.68 kWh/m^2/day) should be foreseen to occur more in the northern part of the region, above PRT station. More to the southeast the presence of clouds affect the daily irradiation at surface with lower values that range between 1-4 kWh/m^2/day. In the context of an efficient management of the solar power plants, this means that during one clear day all hypothetical power plants in southern Portugal would be able to operate at high power outputs, and thus optimizing the local harvesting of incoming DNI and GHI irradiances. In the case of one cloudy day, all southeast stations should be at medium power output level, while at north (in particular for DNI) CSP power plants should be more focused for a higher power output level.

These results show that, for day-ahead procedures, this information can be economically valuable from an electrical grid operation management point of view, and further efforts for the implementation of such practice for a regional (or even national) level in the future should be carried out.

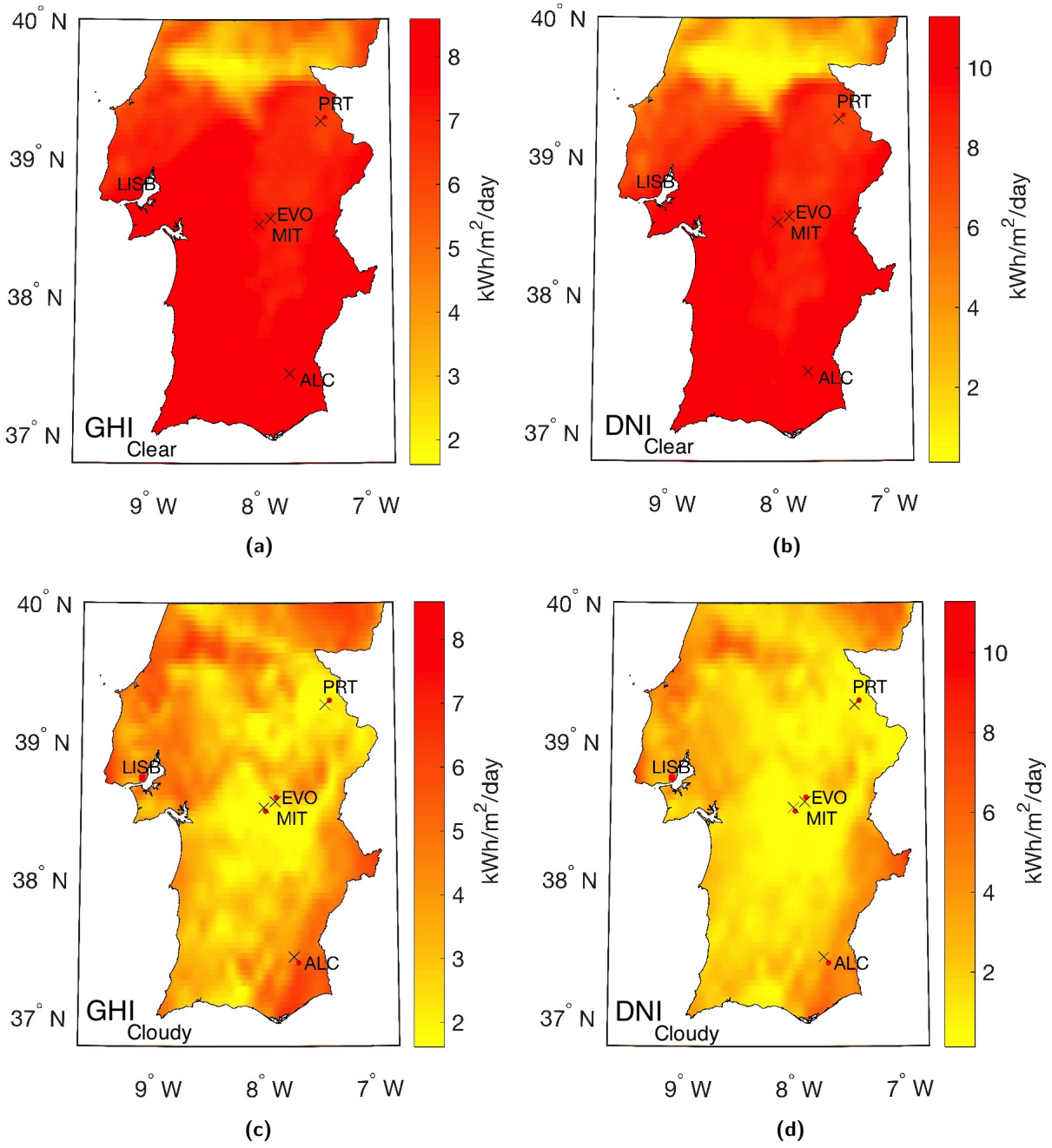

Figure 5.2: Spatial distribution of predicted daily irradiation availability (kWh/m^2/day) from the ECMWF model for two test cases in southern Portugal: one clear sky day (July 12th 2016) and one cloudy day (May 8th 2016). Irradiation maps are portrayed as: GHI_{clear} (a), DNI_{clear} (b), GHI_{cloudy} (c) and DNI_{cloudy} (d). The depicted measuring stations are Évora (EVO), Mitra (MIT), Portalegre (PRT) and Alcoutim (ALC).

5.3 CSP simulations

As it was demonstrated in the previous section, solar radiation forecasts can have potential value for the power plant operator. In particular, to provide energy production outputs from a CSP system, DNI data is required. In this section, a 365 day-period is considered, in which the study location is centred in EVO station, i.e. the reference measuring station for DNI in this thesis. In order to run the SAM simulations and to obtain annual performance outputs, the input parameters (i.e. DNI and meteorological data) need to start at the beginning of the year. Thus, the initial time series were reconstructed in order to start in January and end in December by considering two time windows: from January to June 2018 and from July to December 2017. As it was shown in a previous analysis (Chapter 3, section 3.4), forecasts of DNI provided by the IFS are best represented using the ecRad (cycle 43R3), being suitable to be used for the improvement of energy management regarding operational CSP systems. In this context, an important output parameter that needs to be predicted is the daily power generation, i.e. a crucial information that the plant operator can use for day-ahead operations involving the plant's own energy maintenance and its distribution in the electrical market. For this matter, through the SAM simulations, hourly mean values of electricity generated by two different CSP plants are analysed having into account both measured and predicted data as input parameters. In addition to electrical energy outputs from the CR and PT simulations, thermal stored energy values are also subject of analysis.

It should be noted that for the case of CR and PT systems, both electrical and thermal energy outputs are provided differently in the SAM simulations. For the solar tower, the total electric power to grid (MW_eh) is the direct output, while for the parabolic-trough it is defined as the electricity to grid (kW_eh), being latter converted to MW_eh (i.e. dividing the hourly outputs by 1000) for the following analysis. In this thesis, to differentiate one system from another, the produced electrical energy parameter is defined as E_P and E_G for the CR and PT systems, respectively. Regarding the thermal energy storage (TES, MW_th), the SAM provides the same definition for the TES, however different outputs are provided. This results from the fact that both systems have different operation procedures regarding the TES. In the PT system, there is no direct circulation of the molten salts in the storage, unlike the CR, which can charge or discharge the thermal energy stored at the same time. Instead, for the PT, the heat is transferred from the thermal oil, which circulates the solar field, to the molten salts inside the storage tanks through a heat exchanger. Thus, the PT TES output from the SAM is not presented separately in charge and discharge quantities, as these can not occur at the same moment. For this reason, for the PT simulation, the total TES is considered, while the TES charge and discharge energies are considered for the CR case.

Moreover, as proposed in Chapter 4, improved DNI predictions are a suitable tool for CSP operations. However, since the implementation of improved forecasts in CSP simulations was only made possible at the end of this thesis, in the last part of this chapter (i.e. section 5.4) the role of improved DNI predictions in a simulated CSP plant is discussed.

5.3.1 Central receiver production results

The first simulation focus the case of a system with similar configurations as Gemasolar thermosolar plant, since the Gemasolar is seen as a typical CR system (**Fig. 2.5**, Chapter 2). It should be mentioned that substantial information regarding the Gemasolar configuration is not available, due to privacy reasons. For this matter, full access to the complete configuration of the Gemasolar was not possible. Consequently, several design and control input parameters needed for the simulation are not provided by NREL, creating a limitation in this exercise. However, in order to obtain the best performance results that correspond close to the actual Gemasolar's performance outputs, some input parameters needed for the simulation result from research-based assumptions regarding the operation of the CR systems (**Table A.1**, Appendix A).

As previously mentioned, electrical and thermal output parameters based on forecasted and measured hourly values are analysed, in which DNI and meteorological data from EVO station are considered. In this context, the produced electrical energy, E_P (MW_eh), and the stored thermal energy, TES (MW_th), charge and discharge energies, were analysed for a 365 day-period, i.e. from July 1^{st} 2017 to June 30^{th} 2018.

In **Table 5.2**, the statistical summary for the obtained E_P, and respective TES charge and discharge energies, based on forecasts and measurements of DNI, as well as meteorological variables, are shown. It should be noted that night periods are considered in this analysis since non-production hours are characterized by energy loss in order to maintain the power plant running. This includes parasitic power consumption and a constant derating. The former takes into account losses that tend to reduce temperature differentials, such as for the cooling systems, affecting the plant efficiency. These losses increase throughout the day, achieving higher values during periods of high energy production [132]. The latter is usually used to prevent decreases in the power plant output induced by unusual local weather conditions (e.g. higher ambient temperature than design set point) or excess power within the electrical grid.

As expected, due to the IFS underestimation of cloud cover, the results obtained using simulated hourly values show a general overestimation of the IFS forecasts in comparison to the measurements. A total of ≈115,992 and 121,668 MW_eh/year is obtained, respectively, for the E_P based in DNI measurements and forecasts, with a correlation of ≈0.78, between both outputs. The representation of clouds performed by the IFS, significantly influenced the forecasted values of DNI at the surface and, consequently, the respective E_P output from the simulated Gemasolar. Taking into account the parasitic power consumption during non-production hours and a constant derating value of 4 %, the SAM results show an annual energy generation of ≈111,353 and 116,801 MW_eh/year, regarding measurements and predictions, respectively, i.e. a relative difference of ≈4.9 %. Despite the fact that the objective of this simulation is not a direct comparison with the Gemasolar's actual production values, the obtained annual values through the SAM simulations differed from the values that would certainly be obtained if an actual Gemasolar was operating in Évora. Several reasons can be pointed out for such deviations: (i) DNI and meteorological data from Évora was used considering a different time period, comprising different intra-annual variations; (ii) lack of data regarding design and control parameters for the simulation of Gemasolar; (iii) start-up time (0.5 h) and stop operations of the simulated plant together with the internal temporal discretization, considered by the

SAM; and (iv) actual daily operational strategies adopted for the Gemasolar power management in Sevilla.

Moreover, charge and discharge powers also show an overestimation when using the forecasted inputs, in comparison with those obtained when using measurements, although with higher correlations. Simulation results show annual charge and discharge energies of ≈151,104 and 148,399 MW_t/year, based on measurements, while ≈153,187 and 150,465 MW_t/year are obtained for the forecast-based outputs. Although the discharge energy has a lower r than the charge-hourly values (≈0.83), it shows less deviations between the measured and forecasted outputs.

Table 5.2: Statistical and descriptive analyses for the hourly values of produced electrical energy, E_P ($MW_e h$), and stored thermal energy, TES ($MW_t h$), charge and discharge energies based on measurements (obs) and forecasts (ecmwf). The sum of the hourly values (Total) of E_P and TES (charge and discharge) corresponded to one year of data (from July 1st 2017 to June 30th 2018), produced by a central receiver power plant similarly configured as the Gemasolar thermal power plant (Sevilla province, Spain), simulated through the System Advisor Model (SAM). Hourly error metrics for the correlation coefficient (r), root mean square error (RMSE), and mean absolute error (MAE) are also presented.

Energy	$Total_{obs}$ ($MW_{e,t}h$)	$Total_{ecmwf}$ ($MW_{e,t}h$)	r	RMSE ($MW_{e,t}h$)	MAE ($MW_{e,t}h$)
E_P	115,992	121,668	0.78	6.30	2.31
TES_{charge}	151,104	153,187	0.88	16.46	5.97
$TES_{discharge}$	148,399	150,465	0.83	12.32	4.09

Hourly and daily outputs generated by the SAM, based on the forecasted and measured DNI values, are presented in the scatter plots of **Fig. 5.3** and **5.4**, respectively for the E_P and for the TES charge and discharge energies. As commonly used, in these plots, the red dashed line represents the identity line ($y=x$), in which the dots that are closer to the line depict higher correlations than the ones that deviate from it. In **Fig. 5.3**, two green dashed–dotted lines bound an interval, in which the predicted and measured E_P values had an AE less than the obtained MAE (≈2.31 $MW_e h$). For the hourly E_P results, the total number values within the established high and low thresholds corresponded to ≈85.94 %.

These results also show a few features that are characteristic of CSP systems. Most of the values are centred on high values of E_P, i.e. between 18 and 21 $MW_e h$, which is due to clear sky conditions. Outside this range, E_P values (including the negative ones) correspond to the non-production hours, in which electricity for parasitic power consumption needs to be purchased from the grid. During these periods, deviations between the forecasted and measured E_P occurs, in particular for E_P (obs) > 0 and E_P (IFS) ≤ 0; E_P (obs) ≤ 0 and E_P (IFS) > 0. During cloudy days with short periods of unobstructed solar beam radiation, the predicted and measured E_P also have deviations. If only non-negative hourly values of E_P were considered, the correlation between the forecasted and measured values would drop significantly to 0.37, showing the importance that non-production hours have in the correlations, since these periods correspond to shut-down and start-up operations carried out by the power plant. This means that predictions have a good correspondence with measurements for such periods. Other particular features

are shown in this figure, corresponding deviations between predictions and measurements under clear sky conditions: i) E_P (obs) $\approx$20 MW_eh and 0 $<$ E_P (IFS) $\leq$20 MW_eh; ii) 0 $<$ E_P (obs) $\leq$20 MW_eh and E_P (IFS) $\approx$20 MW_eh. The former corresponds to periods in which the IFS predicts clouds passing over the solar field when the observations show the presence of none, while the opposite behaviour is shown in the latter situation, where the IFS predicts a cloudless sky but the observations show the presence of clouds. The respective PDF (**Fig. 5.3b**) depicts well two observed features, as highlighted by the two peaks: the higher frequency of occurrence around the non-production hours (i.e. zero values), particularly by the E_P based in measurements; and the high frequency of occurrence for the higher values of E_P. TES charge and discharge values are related to the power plant electrical energy values, as shown in **Fig. 5.4**. As previously observed in the hourly E_P values (**Fig. 5.3a**), hourly TES charge and discharge values depict similar features during clear sky periods due to deviations between predicted and measured values, as a consequence of the misrepresentation of clouds in the IFS. Nevertheless, for the case of hourly TES charge and discharge energies (**Fig. 5.4a** and **5.4b**), a slight improvement is observed in the correlation for the charge periods ($\approx$0.88), in comparison to the discharge ones ($\approx$0.83). These correlations are closely linked to the non-production (close to zero) and the high production periods ($\approx$100 MW_th). Relative differences of $\approx$1.38 and 1.39 % are found for the charge and discharge outputs, respectively. On the other hand, hourly TES charge values depict a tendency pattern below the identity line, demonstrating that less storage was gained with the forecasted based output, in comparison to the measured one. This is a consequence of the IFS underestimation towards measurements during days with very clean atmospheric conditions, in which the actual aerosol load was less than that in the prescribed climatology.

As expected, daily values (i.e. calculated through the 24-hour sum of each day) are characterized by higher correlations (**Table 5.3**), despite overestimations from the forecasts, as depicted by the obtained negative MBE values. An r $\approx$0.89 is obtained for the daily E_P values (**Fig. 5.3c**), with $\approx$70.14 % of the total number of daily values having an AE below an MAE of $\approx$46.88 MW_eh. The corresponding PDF (**Fig. 5.3d**) shows the same pattern as that for the hourly results, but, naturally, with less frequency of occurrence, with two similar peaks, i.e. one for the non-production hours and another for the high values of E_P. Regarding the daily TES charge and discharge energies correlations, values of $\approx$0.89 and 0.88 are respectively found (**Fig. 5.4c** and **5.4d**).

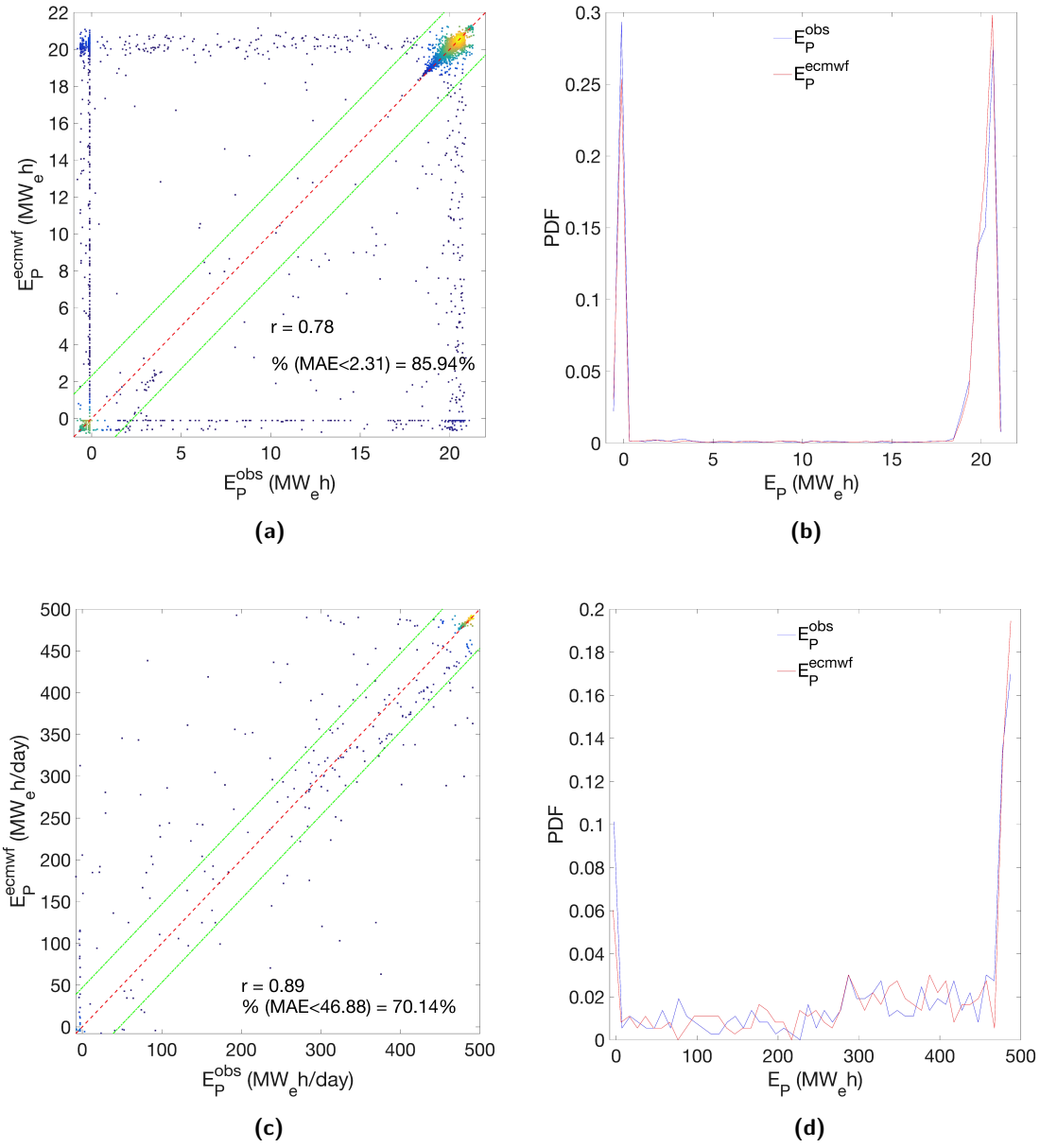

Figure 5.3: Estimated hourly (a, b) and daily (c, d) values of produced electrical energies, E_P ($MW_e h$), and respective probability density functions (PDF), computed from forecasted (ecmwf) and measured (obs) data at Évora. Hourly values of direct normal irradiance (DNI) were used in the SAM to simulate the E_P from a central receiver power plant with configuration similar to the Gemasolar plant (Sevilla, Spain). In the scatter plots, identity lines (red dashed lines), corresponding correlation coefficients, r, and an interval defined by the calculated MAE (≈2.31 $MW_e h$), given by two green dashed–dotted lines, are shown. The period of study corresponds to one year, from July 1st 2017 to June 30th 2018.

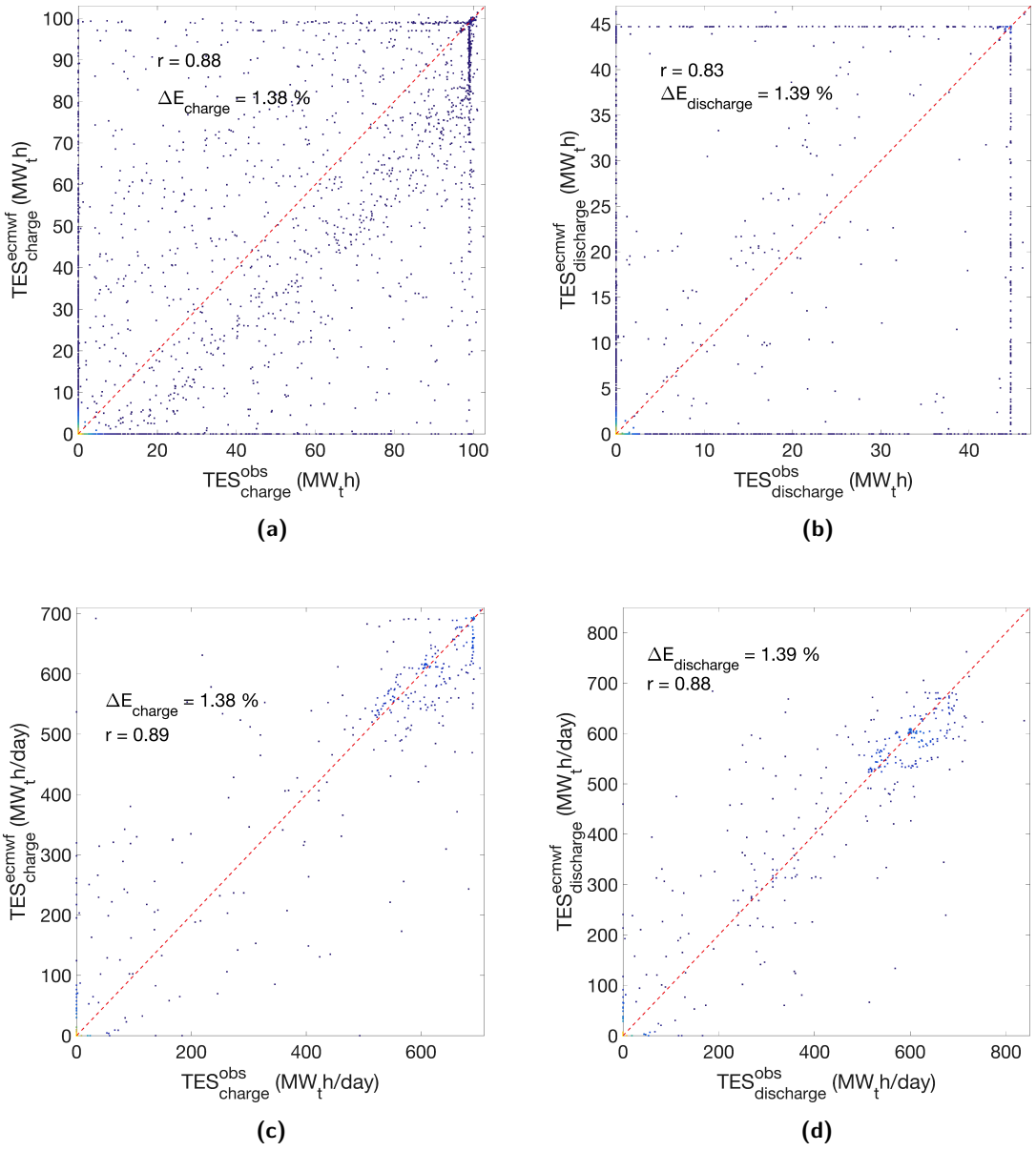

Figure 5.4: Estimated hourly values of thermal energy storage, TES ($MW_t h$): (a) charge and (b) discharge energies, computed from forecasted (ecmwf) and measured (obs) data at Évora, while corresponding daily values are presented in (c) and (d). Hourly values of DNI were used in the SAM to simulate the TES from a CR power plant, with a configuration similar to the Gemasolar plant (Sevilla, Spain). Identity lines (red dashed lines), the corresponding correlation coefficients, r, and relative differences, ΔE, are shown. The period of study corresponded to one year, from July 1st 2017 to June 30th 2018.

Table 5.3: Statistical analysis of the daily values (i.e., the sum of each 24-hour values) of the estimated electrical energy to the grid, E_P (MW_eh), and stored thermal energy, TES (MW_th) charge and discharge energies computed from measurements (obs) and forecasts (ecmwf). Values of E_P and TES correspond to one year of data (from July 1st 2017 to June 30th 2018) produced by a CR power plant with a configuration similar to the Gemasolar plant (Sevilla, Spain) simulated through the SAM. Daily statistical error metrics such as the correlation coefficient (r), root mean square error (RMSE), mean absolute error (MAE), and mean bias error (MBE) are presented.

Energy	r	RMSE ($MW_{e,t}h$)	MAE ($MW_{e,t}h$)	MBE ($MW_{e,t}h$)
E_P	0.89	79.43	46.88	-15.55
TES_{charge}	0.89	119.96	74.25	-5.70
$TES_{discharge}$	0.88	111.66	71.37	-5.66

Having into account the previous Gemasolar production results, particular attention will be given in the next subsection regarding the use of E_P, and TES, using forecasted and measured data in the operational strategies of CR power plants considering different weather conditions.

5.3.2 Central receiver strategies for typical days

An accurate solar resource prediction model has two advantages for the power plant operator: i) it allows the estimation of electricity production from the power plant, helping the power grid management and enabling to sell electricity before production at a good price, i.e. the premium tariff option [73]; and ii) it gives the opportunity to choose appropriate control strategies to maximize the power plant energy efficiency. However, such strategies have to be in accordance to the different weather scenarios (i.e. clear sky, partly cloudy, and overcast days), which can affect differently the power plant performance. Moreover, the versatility of control strategies is deeply tight to TES capacity. Without a storage system, electricity production is constricted to solar resource availability.

It is important to have into account the fact that the SAM software does not incorporate high-level strategy algorithm. Consequently, the power block is started when sufficient power is available, without considering neither the energy stored in the TES system or the evaluation of the DNI variability within previous instants. In this sense, and since multiple starts and stops of the power block should be avoided (in order to increase its lifespan and efficiency) and nominal point operation should be targeted, the following proposed strategies are different from SAM's.

As demonstrated in the previous results, performance outputs from a power plant are generally affected by local meteorological variables, whether on the hourly or daily timescales. Since these interactions can affect the power plant efficiency, several different operational strategies should be considered. An example of the implemented global strategy is to avoid power block start-up and shutdown, allowing to maintain the plant at a nominal power and a maximum efficiency. Another aspect is the possible full state of charge of

the storage tank, during the day. In this scenario, the operator is advised to perform a partial charge in the early morning to handle a possible cloud passing over, except for predicted clear sky days, in which production is to be started as soon as possible. For the case of a 19.9 MW_e CR power plant, the high storage capacity (i.e. a 15-hour TES system) allows the easing of the operator decision algorithm considering different weather scenarios.

Strategy I: high irradiance prediction, no clouds

Full charge for a 15-hour storage system can only be encountered during days that have very high solar irradiation levels. For such days, the best strategy is to maximize electricity production by starting the power block at the earliest moment. An example of this scenario is shown in **Fig. 5.5**, where a constant power production is observed, due to the huge storage capacity and high availability. Here, defocusing of the solar field is also shown, leading to a lower receiver output power after 14 hours (production with predicted DNI) or 15 hours (production with measured DNI).

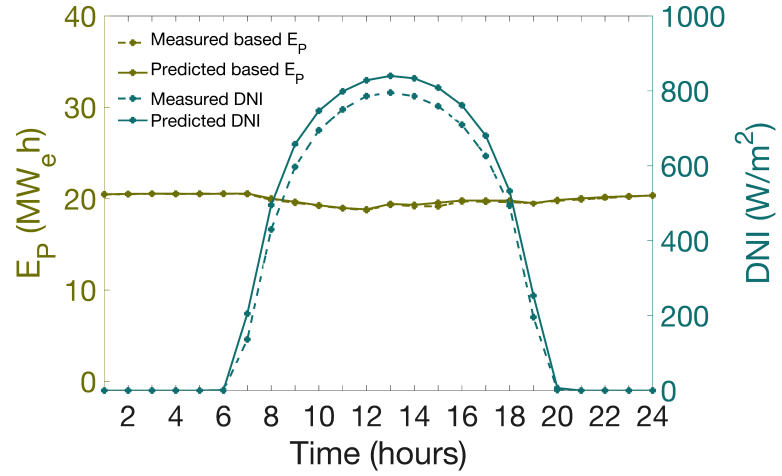

(a)

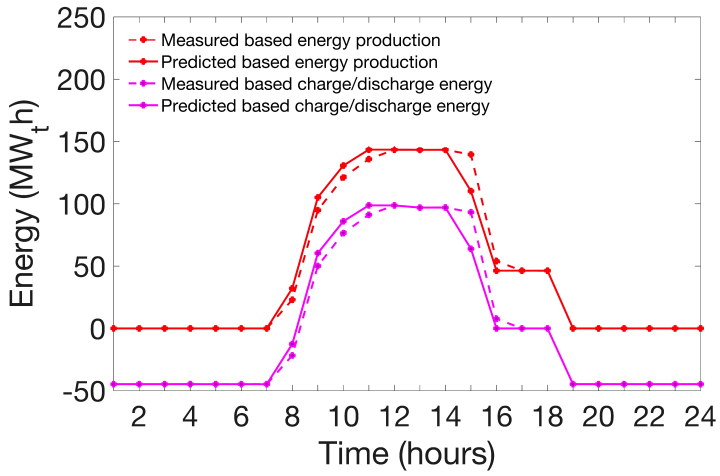

(b)

Figure 5.5: Comparison between the results of the SAM simulation for August 21st 2017, with predicted and measured (a) hourly mean DNI (W/m^2) values (in blue) and produced electrical energy E_P ($MW_e h$) values (in green); and (b) thermal energy ($MW_t h$) of charge/discharge values (in purple) and produced solar energy (in red).

Strategy II: low irradiance prediction, with foreseen clouds

On partly cloudy days, different types of strategies can be applied, e.g. full shifting of the solar production to the evening, constant power generation during the entire day, among others. Since solar power generation is easily higher than what the power block requires, this leads to a high amount of energy surplus in the system, even during the early morning periods. Under such conditions, in order to increase the safety of the power block continuous production, a small partial charge can be performed in the early morning. This partial charge does not lead to potential defocusing because the available energy is not sufficient to reach a 100 % state of charge, during the day. **Fig. 5.6** shows an example of such operation scenario, for a day,

with low irradiation levels due to passing clouds. Since the power block production can be started with a DNI higher than 300 W/m^2, a high amount of energy is charged during the morning hours. For the case of observed DNI, it drops to 300 W/m^2 after 12 hours, due to the presence of clouds, leading to a stop of the charging process. After 16 hours, since DNI drops below 300 W/m^2 due to a second cloud, discharge is performed to maintain electricity production to a constant value.

In this example, the forecast model predicted only one long period of cloud obstruction, during the afternoon, with both forecasted and measured systems responding well, in terms of power production. It should be noted that this type of scenario tends to degrade the correlation between the forecasted and measured based E_P, particularly under the hourly horizon, although for larger time scales, the differences between both outputs estimates are not so significant.

Other particular strategies can be given for the receiver protection of a CR system regarding thermal stress. For instance, avoiding periodic or sudden strong increases and decreases of the receiver temperature, due to a passing cloud. In such cases, the forecast model is by itself sufficient to warn the power plant operator that variations will take place but with a lower accuracy in the time of occurrence. Nonetheless, the available predicted information is already useful to apply thermal protection strategies on the receiver, or to strategize the energy management of the power plant for one day.

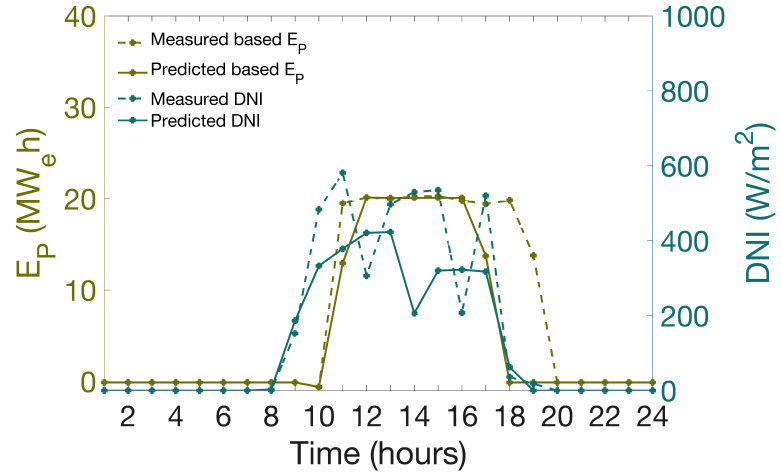

(a)

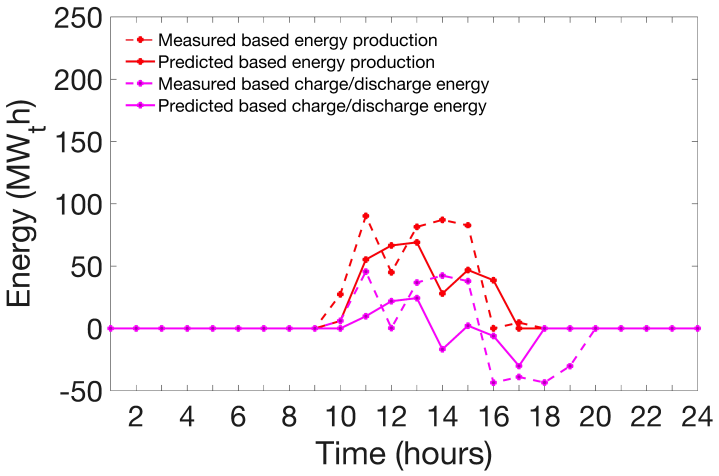

(b)

Figure 5.6: Comparison between results of the SAM simulation results for January 11th, with predicted and measured (a) hourly mean DNI (W/m^2) values (in blue) and produced electrical energy E_P (MW_eh) values (in green); and (b) thermal energy (MW_th) of charge/discharge values (in purple) and produced solar energy (in red).

Strategy III: very low irradiance prediction, with foreseen clouds

For operational purposes, the analysis of a specific day without any, or near null, DNI income is also relevant, simply because when there is no DNI to be collected, then there is no production, particularly when such periods can last for several days. Consequently, the power plant should be running at the lowest power generation possible (or in stand-by mode to keep the equipment warm and the salt in liquid state), depending on the available storage. In this sense, it is important to anticipate such long periods of no production, and the impact that these have on the energy management, and to accordingly implement the necessary strategies. During such periods, and in the case of no available storage, the power plant has negative

production values, since the system needs to consume energy, in order to maintain the continuous function of basic equipment. For that reason, the success that the IFS has in predicting periods of negative production, using the simulated values, is analysed. In such scenario, a dichotomous analysis can be performed with the use of a contingency table created to evaluate the forecasts of E_P values. Moreover, an equitable threat score (ETS) can be used to measure the fraction of the forecasted and observed E_P events that were accurately predicted (information retrieved online from https://cawcr.gov.au/projects/verification). The ETS is usually used in NWP models to evaluate other meteorological variables, such as rainfall [133], since it allows to equitably compare the obtained scores across different regimes. In this context, the following equation is used to calculate the ETS:

$$\mathrm{ETS} = \frac{\mathrm{Hits} - \mathrm{Hits}_{\mathrm{random}}}{\mathrm{Hits} + \mathrm{Misses} + \mathrm{False\,alarms} - \mathrm{Hits}_{\mathrm{random}}}, \tag{5.1}$$

with,

$$\mathrm{Hits}_{\mathrm{random}} = \frac{(\mathrm{Hits} + \mathrm{False\,alarms}) \times (\mathrm{Hits} + \mathrm{Misses})}{\mathrm{Total}}, \tag{5.2}$$

where: "Hits" represents the number of occurrences (i.e. the number of days) with forecasted and observed negative E_P values; "Misses" represents the number of days in which the forecast model did not predict the E_P values when these were actually observed; "False alarms" corresponds to the predicted occurrences of E_P values that were not observed; and "Total" is the total number of occurrences, which took into account the number of days of "correct rejections", i.e. when the forecast model did not predict the E_P negative values that were not actually observed. A perfect forecast (i.e. a perfect score of 1) would be characterized only by "Hits" and "correct rejections", without "Misses" and "False alarms".

Considering together the daily values of forecasted or measured production values, it is found that there are 41 days (in a total of 365 days) with partial or complete cloudy (overcast) conditions, i.e. depicting negative production values (consumption). Results (**Table 5.4**) show that the forecast model predicts a total of 16 days (≈4.4 % of the total number of days) with negative production, which coincided with the measurements, following the condition E_P (ecmwf) < 0 and E_P (obs) < 0, which designates the "Hits". For cloudy days with short periods of no production, where the model predicted overcast (but which was not observed), i.e. when E_P (ecmwf) < 0 and E_P (obs) > 0 (which designates the "False alarms"), 6 days are found, corresponding to just ≈1.6 % of all days. The opposite occurs when the IFS does not predict overcast (but which was observed), i.e. when E_P (ecmwf) > 0 and E_P (obs) < 0 (which designates the "Misses"), with 19 days being found, i.e. ≈5.2 % of the total number of days. The latter is an evident result of the IFS general overestimation, due to cloud misrepresentation, as previously discussed. Moreover, the number of days in which the IFS and measurements do not show the occurrence of negative production values is 324 (i.e. ≈88.8 %), designating the "correct rejections". Thus, the obtained ETS, **Eq. 5.1**, for

the occurrence of negative production forecasted by the IFS is ≈36 %. Under these conditions, i.e. when the forecast model predicts negative production (E_P (ecmwf) < 0), the power plant operator is advised to not proceed with the electrical energy generation. In the case of a wrong prediction, if solar energy is available for collection during the day, then production is to be started but without spending any storage. If a success rate of ≈90 % is to be found, then the operator is simply advised not to produce during such day.

Table 5.4: Dichotomous analysis for the total number of forecasted (ecmwf) and measured (obs) occurrences and non-occurrences of daily negative electrical production values (E_P) for the Gemasolar power plant simulation through the SAM. The obtained E_P simulated values were based on hourly DNI and meteorological data (forecasted and measured) input parameters acquired for Évora for the same period of study (from July 1st 2017 to June 30th 2018). Four different events of negative E_P values occurrences and non-occurrences are depicted: "Hits" (E_P (ecmwf) < 0 and E_P (obs) < 0); "False alarms" (E_P (ecmwf) < 0 and E_P (obs) > 0); "Misses" (E_P (ecmwf) > 0 and E_P (obs) < 0) and the "correct rejections" (E_P (ecmwf) > 0 and E_P (obs) > 0).

Electrical production occurrences	E_P(obs) <0	E_P(obs) >0
E_P(ecmwf) <0	16 (4.38 %)	6 (1.64 %)
E_P(ecmwf) >0	19 (5.21 %)	324 (88.77 %)

5.3.3 Parabolic-trough production results

Power stations that implement PT technology for solar harvesting are currently the most commercial viable option for the electricity market. Consequently, PT deployments have a global predominance over CR systems. In this context, in the following sections, focus is given to the use of solar radiation forecasts for the operation strategies of a PT system with similar configuration as the Andasol 3 CSP plant (**Fig. 2.6**, Chapter 2).

Like in the previous simulated 19.9 MW_e CR system, the case study for a conventional PT power plant is carried out under Évora's conditions, i.e. with the same database (DNI and meteorological data from EVO station) and time period (from July 1st 2017 to June 30th 2018), for the SAM setup. Similarly to the previous CR simulation, for the PT configuration, full access to the configuration of the actual 50 MW_e Andasol 3 was not possible due to privacy reasons. Thus, several configuration parameters were set as SAM's standard values for such systems, while others were research-based assumptions (**Table A.2**, Appendix A). The estimated hourly electrical and thermal outputs, E_G ($MW_e h$) and TES ($MW_t h$) respectively, based on measured and forecasted data are presented in **Table 5.5** and **Fig. 5.7**.

After running the Andasol 3 simulations, the annual performance hourly outputs (**Fig. 5.7**) show, as expected, that during the summer there is more electrical energy being generated and higher thermal energy

being stored, as represented by both measured and forecasted outputs. This is a consequence of: i) the higher frequency of clear sky days occurrences when DNI values are the highest; ii) the increase in the number of sunlight hours during the day (an important feature for the total energy production); and iii) the smaller solar zenith angle. On the other hand, during the winter, the E_G generation tends to be lower and, in some cases, null due to a higher frequency of overcast occurrences (which can prevail during several consecutive days). It is during such periods that the IFS predictions are hindered by the representation of clouds, leading to lower values of predicted E_G and TES than the ones obtained with measurements. This is evident during December, where a significant decrease of E_G is observed for the predicted data, while CSP energy generation based on measured data depicts a smaller decrease. The Andasol 3 simulation also shows that the total annual electricity generated based on forecasted data (≈159,795 MW_eh/year) has an overestimation of almost 6,140 MW_eh/year of the total annual energy against results based on DNI measurements (≈153,655 MW_eh/year), corresponding to a relative difference of nearly 3.99 %. The obtained bias is an evident consequence of the annual DNI overestimation depicted by the IFS, which is here transferred to the energy output of a CSP plant through a non-linear transfer function (thermo-electric model), including the effect of local meteorological variables that can affect the system efficiency. Moreover, similarly to the simulation of Gemasolar, parasitic power consumption and a constant derating value of 4 % are also taken into consideration, contributing to deviations in the outputs. Particularly, in PT systems, the main parasitic load contributors are the HTF pumps, with small inputs also being incremented by the feed water pumps and solar collectors tracking units during the hours of maximum production [132].

As summarized in **Table 5.5**, the total estimated E_G for the measured and forecasted data showed values of 158,836 and ≈163,337 MW_eh/year, respectively, with a correlation coefficient of ≈0.87 between the hourly values, together with a RMSE of 11.93 MW_eh and a MAE of 4.31 MW_eh. As expected, measured and predicted based results showed very small quantities (close to null-values) of total TES values, being very close to one other, i.e. 4.75 and 3.91 MW_th, respectively. Moreover, the total TES results yield an hourly correlation of 0.83 between measured and predicted based outputs, together with a RMSE and a MAE of 33.99 and 14.69 MW_th, respectively. As a consequence of using monthly mean aerosol climatology in the IFS, measured values of DNI are underestimated, particularly in days of very clean atmospheric conditions, leading to lower predicted values of stored energy. For instance, it can be observed that, during the summer (**Fig. 5.7**), measured based TES reaches a maximum of 200,000 MW_th, in comparison with 170,000 MW_th obtained with the IFS based output.

Table 5.5: Statistical and descriptive analyses for hourly values of produced electrical energies, E_G (MW_eh), and stored thermal energy, TES (MW_th), based on measurements (obs) and forecasts (ecmwf). The sum of (Total) E_G and TES hourly values corresponded to one year (from July 1st 2017 to June 30th 2018), produced by a linear focus parabolic-trough power plant similarly configured as the Andasol 3 CSP plant (Granada, Spain), simulated through the System Advisor Model (SAM). Statistical error metrics for the correlation coefficient (r), root mean square error (RMSE), and mean absolute error (MAE) are presented.

Energy	$Total_{obs}$ ($MW_{e,t}h$)	$Total_{ecmwf}$ ($MW_{e,t}h$)	r	RMSE ($MW_{e,t}h$)	MAE ($MW_{e,t}h$)
E_G	158,836	163,337	0.87	11.93	4.31
TES	4.75	3.91	0.83	33.99	14.69

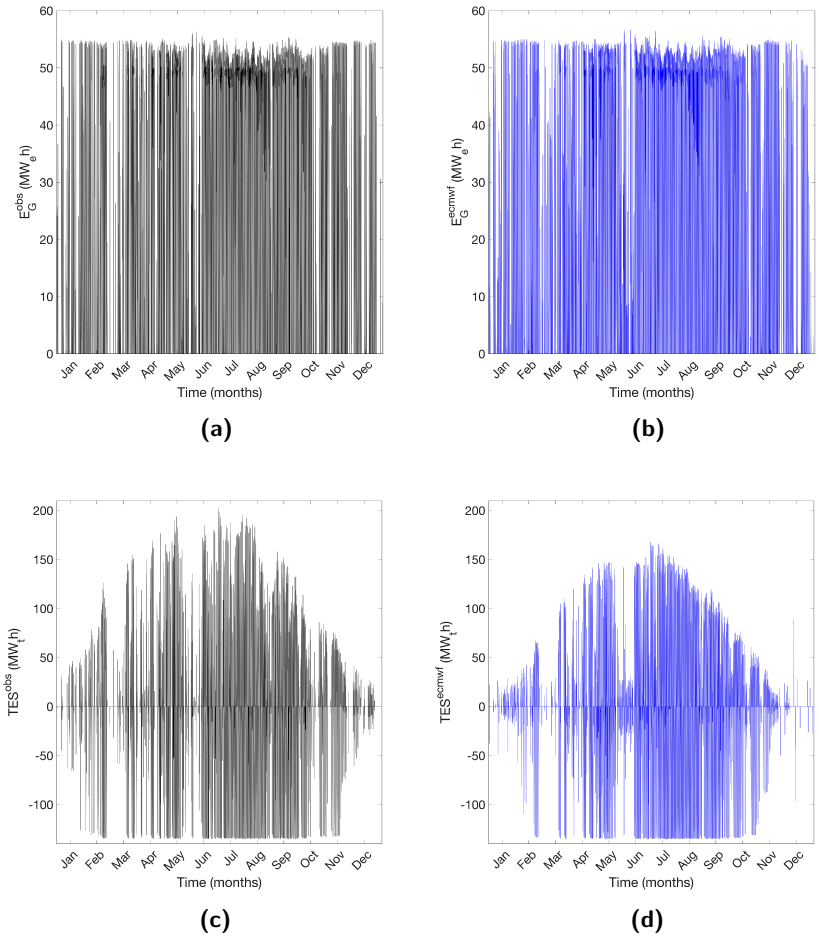

Figure 5.7: Estimated hourly values of electricity to grid E_G (MW_eh), based on (a) measured (obs) and (b) forecast (ecmwf) data through the simulation of the Andasol 3 CSP plant, and thermal energy into storage TES (MW_th), based on (c) measured and (d) forecast data. The period of study is from July 1st 2017 to June 30t 2018 and considers data from the measuring reference station in Évora, southern Portugal.

A closer comparison between measurements and IFS predictions regarding hourly mean values of E_G and TES obtained through the SAM simulation is shown in **Fig. 5.8a** and **5.8b**. Higher correlations between measurements and predictions are given by values that are closer to the identity line $y=x$, where the predicted values meet the measured ones. On the other hand, values that are more dispersed from this line are related to lower correlations. Considering the obtained hourly values of E_G (**Fig. 5.8a**), a MAE of $\approx$4.31 $MW_e h$ was obtained and defined as the upper and lower limit for the establishment of a confidence interval (i.e. depicted by two green dashed-dotted lines), with nearly 83.9 % of the total number of hourly values that have an AE less than the obtained MAE. Moreover, two common features can be observed in the obtained E_G outputs: i) a small cluster of E_G values around 25 $MW_e h$ (half the nominal value), being related to the plant start-up time (0.5 hours) and stop operations, as well as the temporal discretization implemented internally, considered by the SAM; ii) a better correspondence during clear sky hours (leading to production values around 48-55 $MW_e h$), as shown by a large cluster of E_G values. Significant dispersions are found outside of this threshold, being linked to overcast and shutdown periods. Particular attention should be given to the latter, since these correspond to null E_G values, which are found in both *xx* and *yy* axis, being related to the stored energy. A higher amount of stored energy during the day means smaller shutdown periods during the nigth and, consequently, fewer null E_G values. The correlation between E_G measured and forecasted values is then strongly related to deviations regarding such periods. For instance, if all null E_G values are removed from the analysis, the correlation between measured and forecasted values decreases significantly to $\approx$0.58. This highlights the importance that shutdown periods have in the overall performance of the simulated power plant.

Discrepancies between estimated stored energy based on measured and predicted DNI (**Fig. 5.8b**) show discharge and charge energy being represented by negative and positive values, respectively. The obtained hourly values of TES show an overall correlation coefficient of $\approx$0.83 between simulated results based on DNI predictions and measurements. Relative differences of $\approx$8.62 % for the charge and $\approx$8.29 % for the discharge energies were found. Since DNI input values are hardly identical between prediction and measured, very few points will be located on the $y=x$ line, i.e. excess and lack of energy for a specific period is always different. However, a cluster of points can be observed below the $y=x$ line for charged energies ($TES_{ecmwf} > 0$ and $TES_{obs} > 0$). This is a result of good perfomance regarding DNI prediction, although with lower absolute values, leading to lower excess energy and therefore lower charged energy when compared with results based on measured DNI.

Moreover, a "cross-like" pattern representing very strong discrepancies can also be observed. These points represent all the periods in which simulations predict any charge or discharge for the forecasted DNI, while the contrary is obtained from measured DNI (i.e. $TES_{ecmwf} \neq 0$ and $TES_{obs} \approx 0$ or $TES_{ecmwf} \approx 0$ and $TES_{obs} \neq 0$). As previously stated, this is due to differences in the predicted and measured solar resource, leading to different states of charge and discharge of the TES system. Thus, one simulation might charge the TES for a longer duration than the other (top and right parts of the "cross"), or one simulation can show an earlier or longer discharge (left and bottom parts of the "cross"). These differences are also attributed to delays or advances between predicted clouds and their actual occurrence, leading to out of sync charges and

discharges between predicted and measured data. Lower prediction values are found when one simulation is performing a charge while the other is performing a discharge (top left corner and bottom right corner, i.e. $TES_{ecmwf} > 0$ and $TES_{obs} < 0$ or $TES_{ecmwf} < 0$ and $TES_{obs} > 0$). Fortunately, these situations are not frequent and only occur upon the use of DNI data that demonstrates a strong decrease during a part of the day for one simulation, while the other simulation shows a constant and higher DNI value, for instance, when a cloud is predicted but not observed. Additionally, a cluster of points is found when full nominal power discharge is performed in both cases (bottom left corner, i.e. $TES_{ecmwf} = TES_{obs}$, ≈-135 $MW_t h$). However, it is not uncommon that one simulation is performing discharge at full rate, while the other gives a partial discharge (due to residual power coming from the solar field), leading to the two "lines of points" (horizontal and vertical) that can be observed at the bottom left corner (i.e. TES_{ecmwf} ≈-135 $MW_t h$ and $TES_{obs} < 0$ or $TES_{ecmwf} < 0$ and TES_{obs} ≈-135 $MW_t h$).

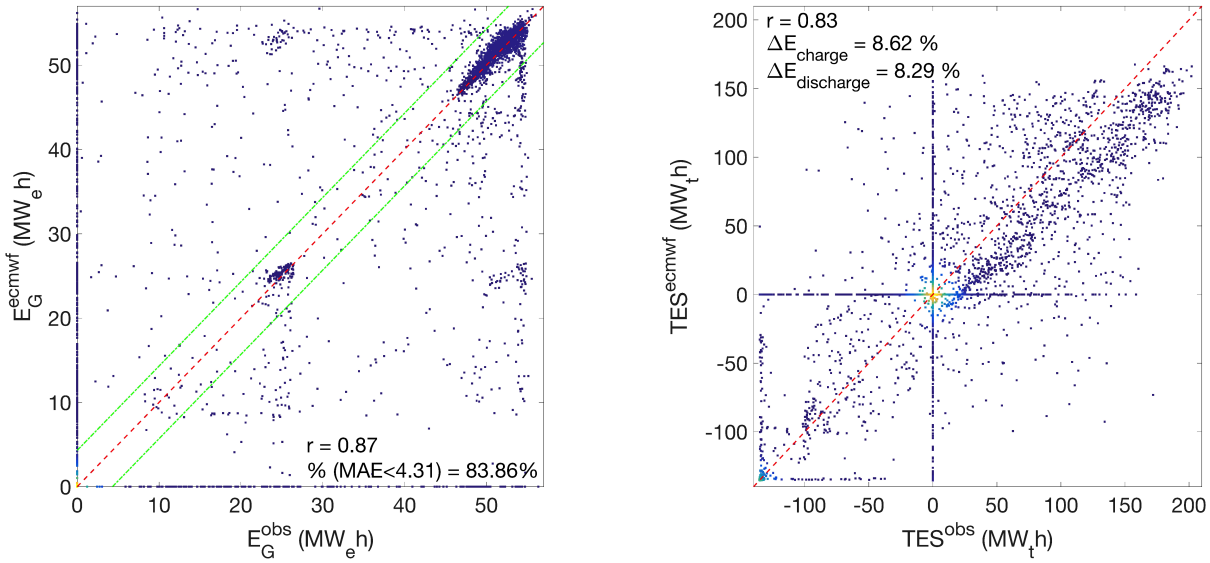

(a) Produced electrical energy, E_G ($MW_e h$). **(b)** Thermal energy into storage, TES ($MW_t h$).

Figure 5.8: Estimated hourly values of E_G and TES ($MW_e h$ and $MW_t h$, respectively) obtained through the SAM simulation with the use of measurements (obs) and the IFS forecasts (ecmwf) for the Andasol 3 simulation in the SAM. The corresponding correlation coefficients, r, relative differences, ΔE (%), for charge and discharge powers, identity line $y=x$ (given by a red dashed line), and a confidence interval based in the calculated MAE of about 4.31 $MW_e h$, given by two green dashed-dotted lines, are also depicted. The period of study is from July 1st 2017 to June 30th 2018, with the analysis being centred in the EVO station (Évora, southern Portugal).

Regarding E_G daily results obtained for the Andasol 3 simulation, the correlation between measured and forecasted based values increases up to 0.92, with a daily RMSE of ≈119.32 $MW_e h$. In **Fig. 5.9**, E_G daily values based on measured and forecasted data are presented, in which a daily MAE of ≈79.59 $MW_e h$ was found and used to create a confidence interval (similarly to the one established in the previous hourly analysis), where ≈65.2 % of the total number of daily values have an inferior AE in comparison to the

obtained MAE. As it was observed systematically in previous analysis, for lower values of E_G, the predicted base results have a tendency to overestimate the measured based ones due to the misrepresentation of clouds in the IFS, in which the resulting MBE revealed a daily value of -12.33 MW_eh. Moreover, it is during clear sky conditions (i.e. high values of E_G) that both model and measured values have the best correspondence, reaching daily values that go from 800 to 900 MW_eh.

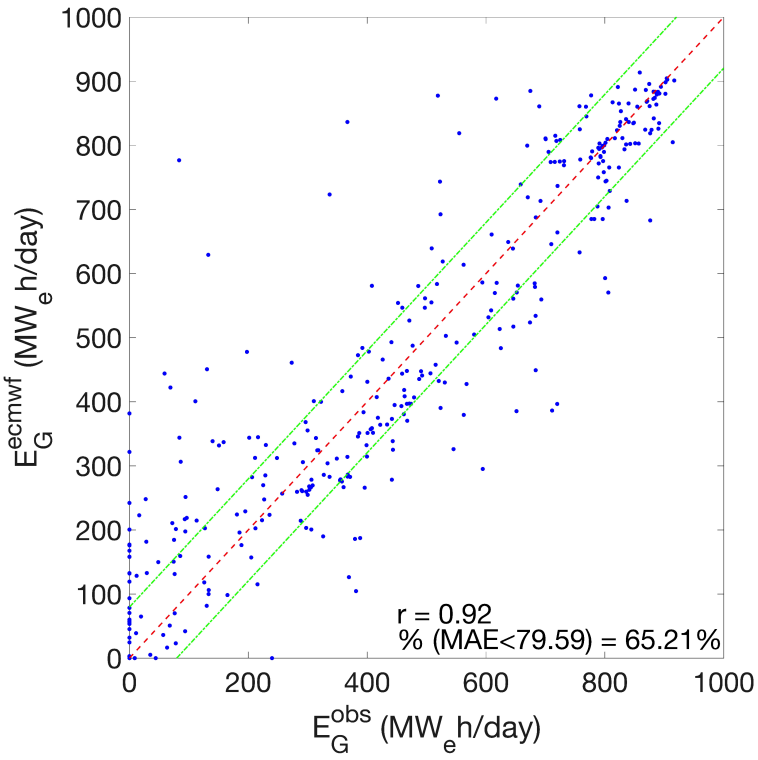

Figure 5.9: Estimated daily values of E_G through the SAM simulation with the use of measurements (obs) and the IFS forecasts (ecmwf) for the Andasol 3 simulation in the SAM. The corresponding correlation coefficient, r, identity line $y=x$ (given by a red dashed line), and a confidence interval based in the calculated MAE of about 79.6 MW_eh, given by two green dashed-dotted lines, are also depicted. The period of study is from July 1st 2017 to June 30th 2018, with the analysis being centred in the EVO station (Évora, southern Portugal).

5.3.4 Parabolic-trough strategies for typical days

Considering the Andasol 3 CSP plant, with a 7.5-hour TES system and no fossil-fuel backup, different strategies can be adopted [134, 135]:

1. Constant load curve during the day with storage of surplus energy and discharge after sunset.
2. Delayed electricity generation for maximum profitability.
3. A growing number of industrial companies are currently considering using cost-effective PV systems to produce electricity during the day, while charging TES with CSP, i.e. hybridization, allowing thermal energy to be discharged after sunset to produce electricity during the night [136].

Other strategies exist when considering a fossil-fuel backup [137], such as minimizing fossil fuel consumption or maximizing profitability, however these scenarios are not included in the present study. The elaboration of appropriate strategies is presented for the simulated PT system accordingly to the predicted DNI and is performed considering two analyses: i) an annual comparison between storage behaviour with predicted and measured irradiances; and ii) a typical day comparison between plant behaviour with predicted and measured irradiances.

Similarly to the Gemasolar proposed strategies, after analyzing the Andasol 3 response for an entire year with predicted and measured DNI data, a more thorough investigation is carried out considering a daily analysis, where four different strategy scenarios depending on four different predictions are defined. For every strategy, a typical day corresponding to a different weather condition has been used as an example.

Strategy I: high irradiance prediction, no clouds

The generated energy from solar, the stored energy and the electricity production during a day (August 2^{nd}) with high irradiance and no clouds, for both simulations, using predicted and measured DNI, are shown in **Fig. 5.10**. In the selected day, electricity production is maintained at a quasi-stationary value throughout the entire day and also after sunset due to discharge operations of the TES system. In both cases, during the afternoon, the energy value is subjected to a drop followed by a plateau, while DNI does not follow the same trend. This behaviour is due to the fact that the TES system is full and is not able to absorb more energy surplus. Consequently, part of the solar field needs to be defocused to avoid overheating. It is possible to conclude that, if the prediction gives a sunny day with high irradiance (typical during the summer), then electricity production should be started as soon as possible, since the total amount of solar energy that can be collected is more important than the total needs of the power plant (50 MW_e production during the entire day, plus full charge of the TES system). This behaviour will be emphasized since predicted DNI values are almost always lower than observations due to the aerosol climatology implemented in the forecast model. For this reason, electricity production should start as soon as possible in order to maximize solar energy utilization. Moreover, a partial charge for safety at the beginning of the day is not required.

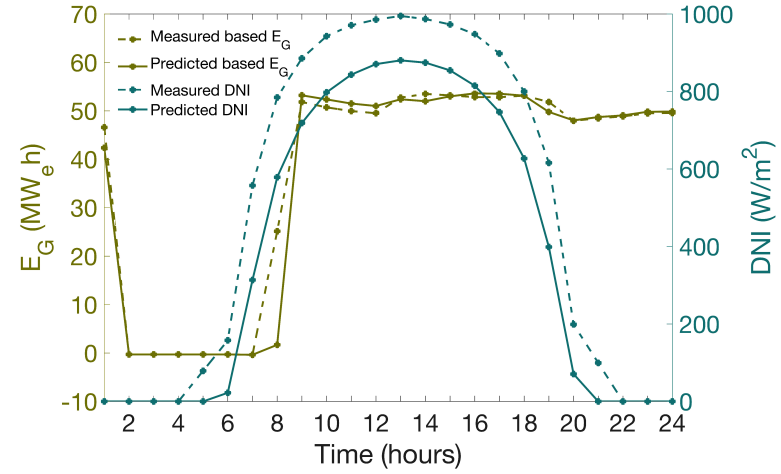

(a)

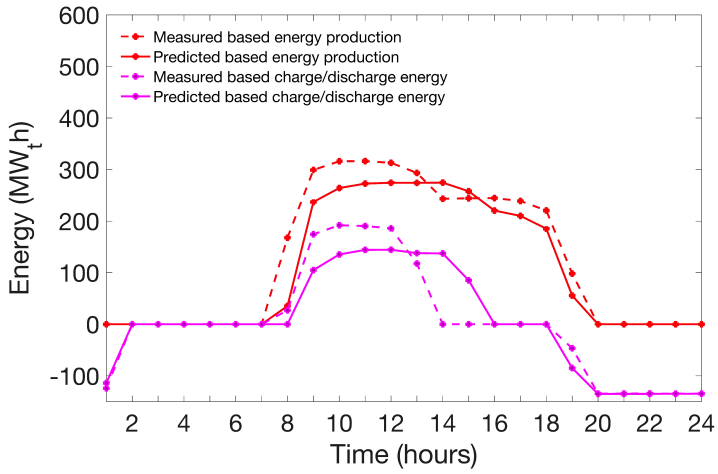

(b)

Figure 5.10: (a) Comparison between the SAM simulation results for August 2nd (prediction of high irradiance without clouds), with predicted and measured hourly mean DNI (W/m^2) and estimated electrical energy, E_G ($MW_e h$), values; (b) estimated thermal energy ($MW_t h$) and charge/discharge values.

Strategy II: high irradiance prediction, with foreseen clouds

Like in the previous case, **Fig. 5.11** shows the estimated solar produced power, stored power and electricity production, but for a day (May 12th) that has high irradiance with a cloud passing over the solar field. The production of electricity is maintained at a quasi-stationary value during the entire day, since sufficient energy surplus has been stored in the TES system before the cloud occurrence (i.e. solar resource intermittency). Although the prediction of a cloud passing by the power plant is accurate, its exact time of appearance and duration are not efficiently forecasted, showing a difference of 1 hour between measured and predicted values of DNI. Consequently, the charge and discharge power curves are different. This means that, if the global day prediction is good (i.e. high irradiance, typically in spring, summer or fall), but a

cloud is foreseen, a partial charge should be performed at the beginning of the day. An early morning partial charge will ensure that a cloud will not stop electricity production, whenever it appears. After a partial charge, electricity production should be started as soon as possible to maximize solar production, while energy surplus (in case of existence) can be sent to the TES system.

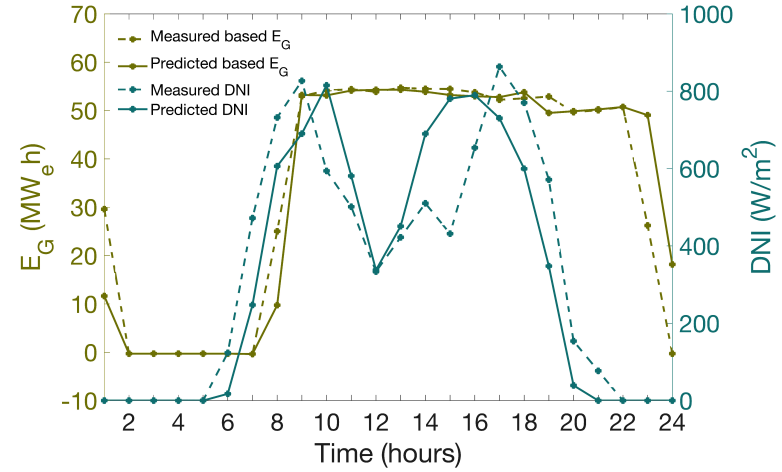

(a)

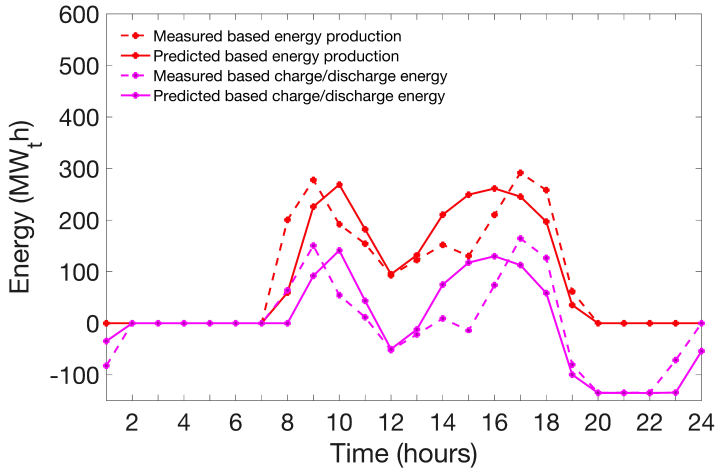

(b)

Figure 5.11: (a) Comparison between the SAM simulation results for May 12th (prediction of high irradiance with a foreseen cloud), with predicted and measured hourly mean DNI (W/m^2) and estimated electrical energy, E_G (MW_eh), values; (b) estimated thermal energy (MW_th) and charge/discharge values.

Strategy III: medium irradiance prediction, with foreseen clouds

In **Fig. 5.12**, the solar produced power, the stored power and the electricity production are shown during a day (February 1st) with medium irradiance and the passing of clouds. In the present case, electricity production has a higher variation due to the clouds and an insufficient charged power before its occurrence.

This means that the adopted production strategy considered by the SAM is not the best choice. Moreover, cloud prediction is not perfectly well represented by the model. Having into account these results, if the global day prediction is medium (i.e. medium irradiance, typically during winter, early spring or late fall) and a cloud is foreseen, then only a charge should be performed. In this case, the available power is not higher than the storage capacity of the TES system, and for that reason, it is relevant to produce electricity after sunset (discharge) and at a constant rate, without suffering from solar resource intermittency.

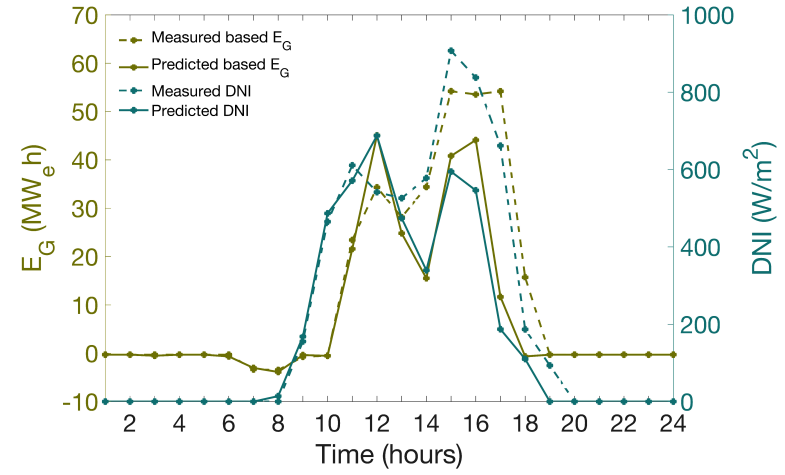

(a)

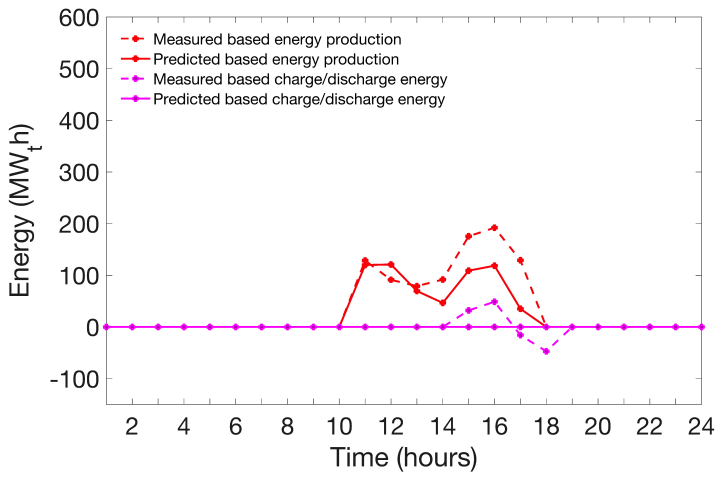

(b)

Figure 5.12: (a) Comparison between the SAM simulation results for February 1st (prediction of medium irradiance with a foreseen cloud), with predicted and measured hourly mean DNI (W/m^2) and estimated electrical energy E_G (MW_eh) values; (b) estimated thermal energy (MW_th) and charge/discharge values.

Strategy IV: low irradiance prediction, with foreseen clouds

The last operational strategy for the PT case study considers the solar produced power, the stored power and the electricity production during a day (January 13^{th}) that has low irradiance values (**Fig. 5.13**). For cloudy days, the SAM output gives a varying electricity production characterized by a very short duration. Knowing the storage capacity of the CSP plant, it should be reasonable to store all available energy. Thus, the subsequent applied strategy will depend on the TES state of charge and on the prediction for the following day:

1. If the model predicts high irradiance for the following day, then production should be started before sunrise thanks to the energy that has been previously stored.
2. If the model predicts high irradiance but with a foreseen cloud, then the previous day partial charge should serve as security margin to overcome poor solar inlet power. Therefore, the production should be started at sunrise.
3. If the model predicts medium irradiance with clouds, then produced energy should be entirely sent to the TES system until reaching a high state of charge (90 %, for instance), and then electricity production should be started.
4. If the next day predicted DNI is very low, then all produced energy should be stored until reaching sufficient state of charge to produce electricity during a reasonable duration.

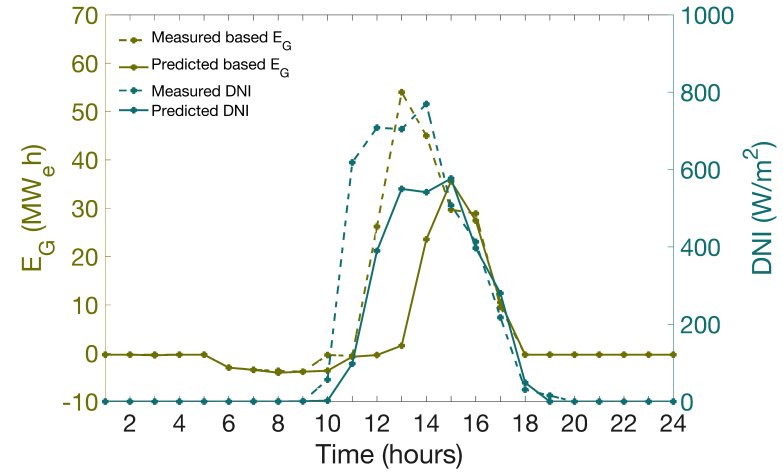

(a)

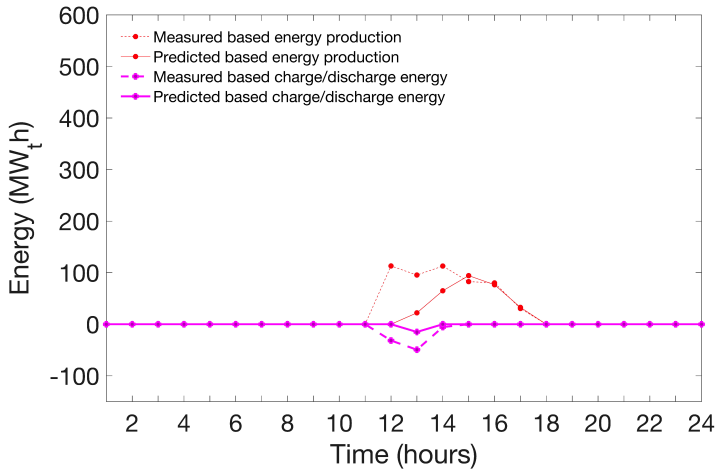

(b)

Figure 5.13: (a) Comparison between the SAM simulation results for January 13th (prediction of low irradiance with or without clouds), with predicted and measured hourly mean DNI (W/m^2) and estimated electrical energy E_G (MW_eh) values; (b) estimated thermal energy (MW_th) and charge/discharge values.

5.3.5 IFS performance in different CSP plants

Since the same dataset (DNI and meteorological variables) from EVO station were used in both CR and PT simulations, the performance of the 24-hour predictions from the IFS in the operation of different CSP systems can be evaluated (**Table 5.6**). The coefficient of variation regarding the RMSE and MAE, i.e. the normalized RMSE and MAE (nRMSE and nMAE, respectively), were obtained for the electricity to grid outputs, from both Gemasolar and Andasol 3 simulations (E_P and E_G, respectively). The calculation of the nRMSE (nMAE) was performed by dividing the RMSE (MAE), obtained between the measured and forecasted based electrical energy values, with the difference between the maximum and minimum values of measured based electrical energy, as given by the following general relations:

$$nRMSE = \frac{RMSE}{(E_{G,Pmax} - E_{G,Pmin})}, \tag{5.3}$$

$$nMAE = \frac{MAE}{(E_{G,Pmax} - E_{G,Pmin})}. \tag{5.4}$$

The obtained hourly values of E_P and E_G show that in the simulation of Gemasolar power plant the forecasted data generates higher deviations from the measured based results than the ones obtained for the Andasol 3 simulation, corresponding to an increase of ≈7.3 % in the nRMSE and ≈2.8 % in the nMAE. Moreover, deviations are lower from hourly to daily values in both simulations, where the Gemasolar shows an increase of ≈2.9 % in the nRMSE and ≈0.7 % in the nMAE. These results indicated that the simulated PT power plant is less sensitive to the DNI prediction than the CR one. However, it should be taken into account that the simulated Andasol 3 has less storage (7.5 hours) than Gemasolar (15 hours), resulting in a larger number of non-production hours (i.e. zero values) for both forecasted and measured simulations, contributing to an apparent reduction of differences between them.

Table 5.6: Hourly and daily values of normalized root mean square error (nRMSE, %) and mean absolute error (nMAE, %) for the estimated total electrical energy to the grid outputs, obtained from the 19.9 MW_e Gemasolar and the 50 MW_e Andasol 3 SAM simulations (E_P and E_G, respectively). The E_P and E_G simulated values are based on the same hourly dataset (DNI and meteorological data) of forecasted (ecRad scheme) and measured input parameters acquired for Évora, for the same period of study (from July 1st 2017 to June 30th 2018).

	nRMSE		nMAE	
Power Plant	**Hourly**	**Daily**	**Hourly**	**Daily**
Gemasolar	28.48	15.88	10.43	9.37
Andasol 3	21.18	13.02	7.65	8.68

5.3.6 Operations with improved forecasts

The use of improved predictions in the daily strategies of a power plant can contribute to a higher level of energy efficiency. Particularly, improved hourly and daily predictions of DNI, as shown in the previous chapter. In this context, having into consideration that PT is currently the most conventional type of CSP technology, this subsection focus the use of corrected predictions of DNI in the simulation of Andasol 3 CSP plant.

With the available data, i.e. measurements, IFS forecasts and corrected forecasts, during a one year period, hourly values of DNI and meteorological variables were used as input parameters. The corresponding produced electrical energy values (E_G, $MW_e h$), generated by each simulation, based on measured and predicted values (IFS, SRM, MRM1 and MRM2), were then compared and discussed accordingly. Like in the previous simulations, the results obtained assume all the plant's power consumption losses, including periods of non-production (i.e. nights and overcast periods) and a constant derating value of 4 %.

The Andasol 3 annual performance results (**Table 5.7**) showed annual energies of ≈166,914 $MW_e h$/year for the measured data, while for the IFS predictions a value of ≈174,086 $MW_e h$/year was obtained. The predicted annual overestimation is a result of the IFS tendency to overestimate measured values during overcast periods, in which the plant efficiency is higher due to lower temperatures. Such conditions occur more frequently than very clean atmospheric periods, in which the IFS has the tendency to underestimate measured values (i.e. when the plant's efficiency is lower). Using the IFS improved DNI predictions, and meteorological predicted data, an annual value of ≈172,339 $MW_e h$/year was found for the SRM, while for the MRM1 ≈169,795 $MW_e h$/year was reached. However, it is with the MRM2 that the best results based on hourly E_G values were attained (highlighted in grey), with ≈167,880 $MW_e eh$/year and a relative difference of ≈0.58 %, being the closest value to the one based on measurements. Moreover, a rough estimation of the economic value of the improved MRM2 predictions can also be performed, considering the average selling price of electricity of 7c€/$kW_e h$ [138] for large industrial customers in Europe. In this context, considering the simulation that run the DNI observations for the considered year, the profit of the plant would be ≈11.68 M€, while the one expected with IFS original forecasted data would be higher, i.e. ≈12.19 M€, corresponding to a difference (Δ_{IFS}) of ≈0.51 M€. On the other hand, if the MRM2 predictions are used instead, such value would be ≈11.75 M€, i.e. an Δ_{MRM2} of ≈0.07 M€ would be attained. This allows to calculate the difference between the two predicted values obtained ($\delta = \Delta_{IFS} - \Delta_{MRM2}$), which can in some way quantify the increased profit with the use of the adjusted predictions. Such value would be around 0.44 M€ (i.e. ≈3.80 % of the total profit). This corresponds to a potential increase of ≈2.6 c€/$kW_e h$ in profits or, from the consumer point of view, a potential reduction in costs. A full range of possible economic improvements can only be accessed with a thorough CSP simulation that allows the implementation of hourly and daily operational strategies, which is out of the scope of this analysis. However, such implementations should be carried out in future studies.

Table 5.7: Hourly produced electrical energy (E_G, $MW_e h$) results through the SAM simulations based on measurements (OBS) and predictions (IFS, SRM, MRM1 and MRM2). One year of data was considered in each run for Évora. SAM simulations were performed with similar configurations to the Andasol 3 CSP. Correlation coefficient (r), coefficient of determination (R^2), root mean square error (RMSE), mean absolute error (MAE), mean bias error (MBE), total E_G, and relative differences (ΔE_G,%), are presented.

	OBS	IFS	SRM	MRM1	MRM2
r	-	0.89	0.89	0.90	0.97
R^2	-	0.79	0.79	0.82	0.93
RMSE ($MW_e h$)	-	11.38	11.25	10.40	6.29
MAE ($MW_e h$)	-	4.11	4.08	3.61	1.85
MBE ($MW_e h$)	-	-0.82	-0.62	-0.33	-0.11
E_G ($MW_e h$/year)	166,914	174,086	172,339	169,795	167,880
ΔE_G (%)	-	4.30	3.25	1.73	0.58

5.4 Conclusions

As demonstrated throughout this chapter, a synergistic use of DNI forecasting and control strategies can help integrating CSP into the electrical grid and improve the local energy distribution performance. Prior to the implementation of a CSP project, information regarding the regional values of solar availability are fundamental for the long-term profit of a CSP plant. Moreover, on the short-term, day-ahead predictions of DNI can help the plant operator to decide better control procedures, allowing to preserve the energy consumption of the power plant (overcast days) or to increase its efficiency (clear sky days). In this context, solar irradiation availability maps of predicted GHI and DNI were created in this study. The predicted values were shown to be consistent with the references ones for the region. Differences stated between predictions and existing references result, first of all, from the fact that reference values comprise a larger set of data than the period of simulations. To specifically use forecasted data in the operations of a CSP plant, two case studies depicting different types of CSP systems were considered. These included the simulation of a central receiver power plant, which possessed comparable configurations to the ones used by the 19.9 MW_e Gemasolar thermosolar power plant, and a linear focus parabolic-trough power plant, with similar configurations as the conventional 50 MW_e Andasol 3. To this end, the SAM (NREL) was used to perform a comparative analysis between measured and predicted based outputs from each CSP system, in which the same DNI and meteorological data were used as input parameters. Regarding the Gemasolar simulation, hourly and daily correlations of $\approx$0.78 and 0.89, respectively, were found for the total produced electrical energy, based on forecasted and measured data. In the case of the Andasol 3 simulation, the estimated total annual energy results showed a relative difference of nearly 2.8 % between forecasted and measured

based values. Produced electrical energy yield correlations of ≈0.87 and 0.92, respectively between hourly and daily energy values of forecasted and measured based values. Since control strategy is deeply tight to the thermal energy storage capacity, different operational strategies were given for a set of typical days that depicted different weather scenarios in order to handle the energy management of a CSP plant during such days. It was recommended the application of charge and discharge operations in accordance to the predicted energy availability for each system, which can respond differently to the intermittency of cloud cover. Although there were still deviations due to cloud and aerosol misrepresentation by the forecast model, the analysis showed that predictions are a valuable tool to be used in the daily energy dispatch operations of CSP plants, particularly in the operation of central receiver units (potentially the main type of CSP system to be used in the future, due to its advantages). The performance of the forecast model in the simulations of Gemasolar and Andasol 3 (imposed with the same datasets), showed that there were higher deviations in the case of Gemasolar than in the Andasol 3. This results from the fact that Andasol 3 has a higher thermal storage capacity than Gemasolar, leading to larger periods of non-production and, consequently, to an apparent reduction of the differences between forecasted and measured based outputs. An increase difference of ≈7.3 % was found, between the Gemasolar and Andasol 3 for the hourly normalized RMSE of the electrical energy generated. Likewise, but considering the normalized MAE, an increase difference of ≈2.8 % was obtained. The differences between the daily results were showed to be lower than the hourly ones, as expected. Additionally, using improved predictions in the simulated Andasol 3 allowed to compare the produced electrical energy (E_G) based on measured, predicted and adjusted data. The results showed that E_G hourly values were best predicted with the MRM2. A simple preliminary economic analysis of the simulated Andasol 3 also showed that MRM2 predicted hourly values of E_G would allow to enhance the plant's profit in ≈0.44 M€, as compared to the use of the original IFS forecasts. This chapter demonstrated that day-ahead forecasts of DNI are suitable to predict the optimum injection of energy into the grid. It was also observed that state-of-the-art NWP models can already be very useful tools for plant operators to apply appropriated strategies for the operational management of CSP systems under different availability scenarios.

The work presented in this chapter resulted from the following publications:

- Francis M. Lopes, Ricardo Conceição, Hugo G. Silva, Rui Salgado, Manuel Collares-Pereira. Improved ECMWF forecasts of direct normal irradiance: a tool for better operational strategies in concentrating solar power plants, Renewable Energy (2020), 163, 755-771.
- Francis M. Lopes, Ricardo Conceição, Thomas Fasquelle, Hugo G. Silva, Rui Salgado, Paulo Canhoto, Manuel Collares-Pereira. Predicted direct solar radiation (ECMWF) for optimized operational strategies of linear focus parabolic-trough systems. Renewable Energy (2019), 151, 378-391.
- Francis M. Lopes, Ricardo Conceição, Thomas Fasquelle, Hugo G. Silva, Rui Salgado, Paulo Canhoto, Manuel Collares-Pereira. Short-term Forecasts of DNI from the Integrated Forecasting System (ECMWF) for Optimized Operational Strategies of a Central Receiver System. Energies 2019, 12, 1368.
- Francis M. Lopes, Hugo G. Silva, Rui Salgado, Afonso Cavaco, Paulo Canhoto, Manuel Collares-Pereira, 2018. Short-term Forecasts of GHI and DNI for Solar Energy Systems Operation: assessment of the ECMWF Integrated Forecasting System in Southern Portugal. Solar Energy (2018), 170, 14-30.

6

Conclusions

Having into consideration the initial proposed milestones for this thesis, this final chapter seeks to address these, including a summary of all the presented subjects, as well as guidelines for future work.

6.1 Main conclusions

This work was set out to evaluate the use of short-term forecasts (i.e. the next 24 hours) of solar radiation in southern Portugal, particularly DNI for operational purposes of CSP systems. At the same time, a contribution for the improvement of DNI forecasts and their use in CSP operations was performed.

The first study (Chapter 3) covered the use of predicted solar radiation in the Alentejo region. Since this is a fundamental first-step when seeking the installation (including siting and sizing decisions) of future solar harvesting systems, the evaluation of the solar resource was carried out by using ground measuring and forecasted data to study GHI and DNI variability in different stations. Although hourly predictions of DNI from the IFS (ECMWF) are hindered by cloud and aerosol misrepresentation, particularly through the former during partly cloudy and overcast periods, it was shown an overall good agreement between measured and forecasted values. Discrepancies between measured and forecasted data were shown to be substantially reduced when using the new and operational IFS radiation scheme, i.e. the ecRad (cycle 43R3), in comparison with its predecessor, i.e. the McRad (cycle 41R2). This study allowed to accomplish the first milestone of the proposed work, as well as to show the potential that DNI forecasts can have for the operational management of CSP systems if implemented in power plant model simulations, becoming the motto for the following work assignments.

Over the course of this work, it was evident that the provided forecasts of DNI were highlighted by deviations characteristic of cloudy periods. This has been one of the main challenges in today's solar forecasting, bringing some limitations to their use. As one of the proposed tasks for this thesis, the correction of hourly forecasts of DNI can be carried out through statistical post-processing techniques, such as MOS, as well as using higher resolution models to downscale the prediction analysis. In the case of the latter, initial efforts were made to use the Meso-NH model as a starting point to improve hourly predictions of DNI. However, at the time, the preliminary analysis was shown (Appendix B) to be conclusive: hourly predictions of DNI produced by the Meso-NH (version 5-3-0) radiation scheme showed errors in overcast situations; and correcting these was outside the scope of this thesis. Despite such results, these findings were a staring point for the improvement of Meso-NH's radiation scheme, a task that would be carried out latter on by the model developers at the *Centre National de Recherches Meteorologiques* (CNRM) of the Météo France. As an alternative, due to the ECMWF's availability in providing the forecasted data, this led to the application of MOS for the predicted DNI from the IFS global model. Following this approach, and using simple post-processing techniques presented in Chapter 4, it was possible to improve hour and day-ahead predictions of DNI using multivariate regression methods. The proposed correction models showed that improvements were best achieved when using a multivariate regression model that considers the previous hour of measured solar radiation data. In this study, it was also demonstrated that day-ahead forecasts of DNI, which originally already exhibit satisfactory results, can be further improved when using the proposed corrected hourly predictions throughout the day. The proposed procedures stand as a contribution to solar forecasting from the plant's operator point of view, providing a simple tool for the improvement of day-ahead

predictions of DNI, and consequently to a more efficient energy management of CSP plants.

The use of predicted data in the simulation of two CSP plants was made possible through the SAM (NREL) in Chapter 5, in which predicted based energy outputs were compared with measured ones. This was the first time that such method had been conducted using IFS hourly forecasts, particularly in the region of study. To fulfill this task, both predicted and measured data centred in Évora were considered for the simulation of a solar tower and a conventional linear focus parabolic-through system, which possessed similar configurations to the currently operational Gemasolar thermosolar and Andasol 3 power plants, respectively installed in Sevilla and Aldeire (Spain). Despite the lack of information regarding actual values for the setup of the power plants, just using improved predictions of DNI from the ecRad, it was possible to observe that operational strategies based on typical days can be implemented for the day-ahead accordingly to the predicted energy availability for each system. This information, if properly managed, can contribute to the improvement of energy dispatch operations of a CSP plant, the selling of electrical energy at premium tariffs in the day-ahead market, and, on the long-term, to a reduction in the final levelized cost of electricity. A final segment of this study consisted in the use of the previous proposed adjusted predictions of DNI through regression analysis (Chapter 4). The simulations results showed that electrical energy values produced by Andasol 3 were best estimated through the use of the MRM2 model, contributing to an overall improvement of the daily operational management of the power plant. As the final milestone of this thesis, this task gave emphasis to a forecast operational system for the Alentejo region, as well as for other similar regions with high solar potential. This study allowed to address a practical application of solar radiation forecasts in the operations of CSP systems.

Aside from the invaluable knowledge gained by the author during his research studies, from an experimental perspective, several other tasks have also been accomplished. These included the maintenance of solar radiation measuring equipment, data pre and post-processing procedures, as well as the participation in the implementation of a nowcasting system using sky cameras near Évora. Although research data from the latter was not used in the author's work, since its installation and data acquisition were outside the time-frame of the proposed thesis, the use of such system can be carried out in the future.

6.2 Future work

The work presented in this thesis can be further developed in future explorations by addressing different topics. To generally improve data analysis between measured and predicted data, a higher number of ground stations should be used, allowing to extend the validation of solar radiation predictions in southern Portugal. This can be accomplished within the DNI-A network (DNI-A project, reference ALT20-03-0145-FEDER-000011), which currently possesses 14 operational ground measuring stations, with more stations being foreseen to be installed in the future. Moreover, the IPMA national network of 89 GHI measuring stations scatter across mainland Portugal can also be used to consolidate the assessment of the solar resource. In addition to the number of stations, the measuring time period is also important, since longer time series

allow to provide a more robust analysis. This aspect should be accomplished with both DNI-A and IPMA networks, in which continuous measurements of DNI and GHI have been carried out during about 5 years within the DNI-A network, while more than 19 years of GHI data is available from IPMA.

Since DNI predictions still demand improvements for CSP applications, several procedures can be performed. At the same time, these should be of easy application to the plant operator in order to facilitate operational procedures, which sometimes can require fast decisions. As a continuation of the proposed correction models (Chapter 4), other important atmospheric parameters that influence DNI at surface can be tested in the MRM2. Future corrections should give more emphasis in correcting hourly values during overcast and partly cloudy (i.e. periods of high energy demand), and clear sky periods (i.e. periods of high energy generation). For instance, for the latter, using aerosol optical depth measured data from the Aerosol Robotic Network (AERONET) will help to further improve DNI hourly predictions, which currently underestimate measured values due to the use of monthly aerosol climatology in NWP models. Another correcting method is the use of higher resolution models to perform dynamic downscale, which can be carried out, for instance, through the current improved version 5.4 of the Meso-NH [122]. This will allow to sub-scale the physical processes that are not accurately represented by the IFS, allowing to obtain better post-processing results. Furthermore, high resolution models can also be used together with a ASI system like the one installed near Évora, as part of a hybrid nowcasting system to correct hourly predictions during cloudy periods. This ASI system is comprised by a cloud tracking system through the use of four cameras [130]. Such systems can also be used to track cloud shadows for DNI predictions [47, 139].

Regarding the simulation of CSP plants and the prediction of energy production values, since the SAM software does not include a high-level strategy algorithm (instead it uses a single strategy, i.e. to produce electricity whenever there is DNI available), more emphasis should be given to a model that makes use of daily operational strategies (e.g. [140]). Particularity, information concerning the solar resource variability and the available energy stored in the previous hour are important for the hour-ahead operational strategy.

Finally, this thesis focused its research towards the implications that DNI predictions can have in operational strategies of CSP systems, however this study is not restricted to such technology. In fact, since there is a higher availability of measured data and more precise predictions of GHI (in comparison to DNI), the application of this research work for PV power plants is possible. This is of particular relevance, especially when PV possesses a higher potential in the electrical market than current CSP. One example of such application would be for prediction of PV electrical energy production maps in southern Portugal.

A

Power plant simulation: configuration tables

In this appendix, a detailed description is given regarding the input parameters used within the SAM software (version 2017.9.5), from NREL, for the simulation of two CSP power plants designed to run a CR (section A.2) and a PT (section A.4) system, as discussed in Chapter 5.

A.1 Introduction

For the Gemasolar CSP power plant case study, the available online information provided by NREL (https://solarpaces.nrel.gov/gemasolar-thermosolar-plant) was complemented with the default SAM inputs designed for the type of power plant, together with T. Fasquelle research contribution regarding several parameters, which were considered (**Table A.1**). Likewise, for the simulation of the Andasol 3 CSP, the input parameters (**Table A.2**) are based on the SAM's default values, online information from NREL (https://solarpaces.nrel.gov/andasol-3), and research-based data. These inputs are presented considering the same database (i.e. DNI and meteorological data) as in the simulated CR system.

A.2 Gemasolar CSP setup

Contrary to the Andasol 3 configuration, a substantial amount of information is missing for the setup of Gemasolar, probably due to privacy reasons. In this context, some assumptions towards the parameters used in this simulation are considered. However, these are fairly close to the Andasol 3 assumptions, in order for a better comparison between the two.

Table A.1: Input parameters for the SAM simulation of the Gemasolar CSP station during one year (from July 1st 2017 to June 30th 2018).

Heliostat Field	Value	Comment
Irradiance at design	700 W/m^2	According to NREL.
Solar Multiple	2.684	According to [113].
Receiver thermal power	120 MW	Auto-generated by SAM.
Heliostat field Multiple	1	Important only if field is larger.
Tower and receiver	Value	Comment
HTF hot temperature	565 °C	According to NREL.
HTF cold temperature	290 °C	According to NREL.
Thermal storage	Value	Comment
Full load hours of storage	15 h	According to NREL.
Solar field hours of storage	5.58867 h	Auto-generated by SAM. Means that if all produced power is stored, at nominal power the storage tank is full after 5.6 hours.

Power cycle	Value	Comment
Design turbine gross output	19.9 MW_e	According to NREL.
Estimated gross to net conversion factor	1	According to NREL.
Estimated net output	19.9 MW_e	Auto-generated by SAM.
Cycle thermal efficiency	0.445	According to NREL.
Cycle thermal power	45 MW	Auto-generated by SAM.
Heliostat field	Value	Comment
Number of Heliostats	2625	Auto-generated by SAM, 2650 according to [141].
Heliostat properties	Value	Comment
Heliostat Width	12.305 m	According to [141].
Heliostat Height	9.752 m	According to [141].
Ratio of reflective area to profile	0.9642	According to [141].
Single heliostat area	115.702 m^2	According to [141].
Image error (slope, single-axis)	1.53 mrad	SAM default parameter.
Reflected image conical error	4.32749 mrad	SAM default parameter.
Number of heliostat facets – X	7	According to [113].
Number of heliostat facets – Y	5	According to [113].
Heliostat focusing method	Ideal	SAM default parameter.
Heliostat canting method	On-axis	SAM default parameter.
Land area	Value	Comment
Non-solar field land area	182 acres	According to NREL.
Solar field land multiplier	1	SAM default parameter.
Base land area	299.624	SAM default parameter.
Total land area	482 acres	According to NREL.
Total heliostat reflective area	303 719 m^2	According to NREL.
Optimization Settings	Value	Comment
Initial optimization step size	0.06	SAM default parameter.
Max. optimization iterations	200	SAM default parameter.
Optimization convergence tolerance	0.001	SAM default parameter.
Heliostat Operation	Value	Comment
Heliostat stow/deploy angle	8°	SAM default parameter.
Wind stow speed	15 m/s	SAM default parameter.
Heliostat start-up energy	0.025 kW_eh	SAM default parameter.
Heliostat tracking power	0.055 kW_e	SAM default parameter.

Design-point-DNI	700 W/m^2	Auto-generated by SAM.
Atmospheric Attenuation	Value	Comment
Polynomial coefficient 0	0.006789	SAM default parameter.
Polynomial coefficient 1	0.1046/km	SAM default parameter.
Polynomial coefficient 2	-0.017/km^2	SAM default parameter.
Polynomial coefficient 3	0.002845/km^3	SAM default parameter.
Average attenuation loss 0	4.8 %	Auto-generated by SAM.
Solar Field Layout Constraints	Value	Comment
Max. heliostat distance to tower height ratio	9.5	SAM default parameter.
Min. heliostat distance to tower height ratio	0.57	According to [141].
Tower Height	140 m	According to NREL.
Max. distance from tower	1330 m	Auto-generated by SAM.
Min. distance from tower	79.8 m	Auto-generated by SAM.
Mirror washing	Value	Comment
Water usage per wash to	0.70 L/m^2	SAM default parameter.
Washes per year to	63	SAM default parameter.
Heliostat field availability	Value	Comment
Mirror reflectance and soiling	0.9	Auto-generated by SAM.
Heliostat availability	0.95	Auto-generated by SAM.
Tower and receiver design parameters	Value	Comment
Solar multiple	2.68	Auto-generated by SAM.
Receiver thermal power	120 MW	Auto-generated by SAM.
HTF hot temperature	565 °C	Auto-generated by SAM.
HTF cold temperature	290 °C	Auto-generated by SAM.
Tower and Receiver Dimensions	Value	Comment
Tower height	140 m	According to NREL.
Receiver height	10 m	According to [141].
Receiver diameter	9 m	According to [141].
Number of panels	14 m	According to NREL.
Receiver heat transfer properties	Value	Comment
Tube outer diameter	40 mm	SAM default parameter.
Tube wall thickness	1.25 mm	SAM default parameter.
Receiver diameter	0.88	SAM default parameter.

Coating absorptance	0.94	SAM default parameter.
Heat loss factor	1	SAM default parameter.
Design and operation	Value	Comment
Min. receiver turndown fraction	0.25	SAM default parameter.
Max. receiver operation fraction	1.2	SAM default parameter.
Receiver start-up delay time	0.25 h	Selected by T.Fasquelle.
Receiver start-up delay energy fraction	0.25	SAM default parameter.
Receiver HTF pump efficiency	0.85	SAM default parameter.
Max. flow rate to receiver	347.778 kg/s	Auto-generated by SAM.
Materials and flow	Value	Comment
HTF type	Solar Salt	Selected by T.Fasquelle.
Property table for user-defined HTF	-	SAM default parameter.
Material Type	Stainless AISI316	Common value used in industry.
Flow pattern	1	SAM default parameter.
Receiver Flux Modelling Parameters	Value	Comment
Max. receiver flux	1000 kW/m^2	SAM default parameter.
Estimated receiver heat loss	30 kW/m^2	See section A.3.1.
Receiver flux map resolution	14	Auto-generated by SAM.
Number of days in flux map lookup	8	SAM default parameter.
Hourly frequency in flux map lookup	2 h	SAM default parameter.
Piping Losses	Value	Comment
Piping heat loss coefficient	1000 W/m	See section A.3.2.
Piping Length constant	80 m	Selected by T.Fasquelle.
Piping length multiplier	2	Selected by T.Fasquelle.
Piping Length	360 m	Auto-generated by SAM.
Total piping loss	3672 kW_t	Auto-generated by SAM.
General design parameters	Value	Comment
Pumping power for HTF through power block	0.55 kW/kg.s	SAM default parameter.
Fraction of thermal power needed for standby	0.2	SAM default parameter.
Power blocks start-up time	0.5 h	Selected by T.Fasquelle.
Fraction of thermal power needed for startup	0.2	Selected by T.Fasquelle.
Min. turbine operation	0.2	SAM default parameter.
Max. turbine overdesign operation	1.05	SAM default parameter.

Cycle design HTF mass flow rate	108 kg/s	Auto-generated by SAM.
Rankine cycle parameters	Value	Comment
Boiler operating pressure	105 bars	Common value used in industry.
Steam cycle blowdown fraction	0.016	According to NREL.
Turbine inlet pressure control	Fixed pressure	SAM default parameter.
Condenser type	Air cooled	SAM default parameter.
Ambient temperature at design	42 °C	SAM default parameter.
ITD at design	16 °C	SAM default parameter.
Reference condenser water ΔT	10 °C	SAM default parameter.
Approach temperature	5 °C	SAM default parameter.
Condenser pressure ratio	1.0028	SAM default parameter.
Min. condenser pressure	2 inHg	SAM default parameter.
Cooling system part levels	8	SAM default parameter.
Thermal storage design parameters	Value	Comment
Cycle thermal power	44.7 MW	Auto-generated by SAM.
Hours of storage at power cycle full load	15 h	According to NREL.
HTF hot temperature	565 °C	Auto-generated by SAM.
HTF cold temperature	290 °C	Auto-generated by SAM.
Storage type	Two tanks	According to NREL.
TES thermal capacity	670.8 MWh	Auto-generated by SAM.
Available HTF volume	3219 m^3	Auto-generated by SAM.
Tank Height	10.5 m	According to [113].
Tank minimum fluid height	1 m	Common value used in industry.
Storage tank volume	3558 m^3	Auto-generated by SAM.
Parallel tank pairs	1	SAM default parameter.
Tank diameter	20.8 m	Auto-generated by SAM.
Wetted loss coefficient	0.4 $W/m^2.K$	SAM default parameter.
Estimated heat loss	0.3 MW	Auto-generated by SAM.
Initial hot HTF percent	20 %	Selected by T.Fasquelle.
Cold tank heater temperature set point	280 °C	Selected by T.Fasquelle.
Cold tank heater capacity	13 MW_e	Selected by T.Fasquelle.
Hot tank heater temperature set point	500 °C	Selected by T.Fasquelle.
Hot tank heater capacity	26 MW	Selected by T.Fasquelle.
Tank heater efficiency	0.98	SAM default parameter.
HTF density	1811.42 kg/m^3	Auto-generated by SAM.

It should be noted that other configurations such as dispatch control, scheduling, system costs, Lifetime, financial parameters, incentives, electricity rates and electricity load, are outside the scope of this thesis. For that matter, all these parameters were set to the SAM default values for the simulation of a CR system.

A.3 Gemasolar CSP calculations

A.3.1 Receiver Heat Losses

Heat losses from the receivers are a consequence of radiation to the environment and convection. The equation of heat losses per square meter for a receiver is therefore given by the following relation:

$$P_{\text{rec}} = \epsilon \times \sigma \times \left(T_{\text{rec}}^4 - T_{\text{ext}}^4\right) + h_{\text{conv,ext}} \times \left(T_{\text{rec}} - T_{\text{ext}}\right), \tag{A.1}$$

Considering a receiver temperature, T_{rec}, of ≈565 °C (or ≈838.15 K), an external temperature, T_{ext} of ≈20 °C (or ≈293.15 K), a receiver emittance, ϵ, of ≈0.88 (input for SAM),a receiver absorptance, σ, of $\approx 5.67 \times 10^{-8}$ W.m^{-2}.K^{-4} (input for SAM), and a convection coefficient, $h_{\text{conv,ext}}$, of ≈10 W.m^{-2}.K^{-1}, the previous equation writes:

$$P_{\text{rec}} = 0.88 \times 5.67 \times 10^{-8} \times \left(838.15^4 - 293.15^4\right) + 10 \times \left(838.15 - 293.15\right), \tag{A.2}$$

$$\Leftrightarrow P_{\text{rec}} = 24255 + 5450 \approx 29705 \quad \text{W.m}^{-2}. \tag{A.3}$$

A.3.2 Heat losses from the pipes

Heat losses from the pipes, $P_{\text{loss,pipes}}$, are closely related to the conductivity of the insulation material, $R_{\text{cond}}^{\text{ins}}$, and the pipe convection, $R_{\text{conv}}^{\text{pipe}}$. The two terms, together with the temperature differential between fluid and exterior temperatures, ΔT, lead to the following relation [111, 31]:

$$P_{\text{loss,pipes}} = \frac{\Delta T}{R_{cond}^{\text{ins}} + R_{conv}^{\text{pipe}}}, \tag{A.4}$$

$$\Leftrightarrow P_{\text{loss,pipes}} = \frac{T_{\text{f}} - T_{\text{ext}}}{\frac{\ln\left(\frac{r_{\text{ext,p}}+e_{\text{ins}}}{r_{\text{ext,p}}}\right)}{2\times\pi\times k_{\text{ins}}} + \frac{1}{h_{\text{ext}}\times 2\times\pi\times r_{\text{ext,p}}}}. \tag{A.5}$$

A 3 inch pipe, typical in solar thermal applications, corresponds to a an internal diameter of ≈80.0 mm and an external diameter of ≈81.28 mm, i.e. $r_{\text{ext,p}}$ ≈40.64 mm. Considering a convection coefficient, h_{ext}, of ≈15 W.m^{-2}.K^{-1}, an insulation thickness, ϵ_{ins}, of ≈150 mm, a thermal conductivity, k_{ins}, of ≈0.08 W.m^{-1}.K^{-1} (typical value for rockwool material at the average temperature considered here), a fluid temperature, T_{f}, of ≈565 °C (typical for molten salt processes) and an external temperature, T_{ext}, of ≈20 °C, the previous equation can be resolve as follows:

$$P_{\text{loss,pipes}} = \frac{565 - 20}{\frac{\ln\left(\frac{0.04064+0.15}{0.04064}\right)}{2\times\pi\times 0.08} + \frac{1}{15\times 2\times\pi\times 0.04064}}, \tag{A.6}$$

$$\Leftrightarrow P_{\text{loss,pipes}} \approx 163 \quad \text{W.m}^{-1}. \tag{A.7}$$

The obtained value is substantially lower than SAM's default value. For such reason, this result was rounded to 1000 W.m^{-1}. It should be noted that, in order to increase the heat loss coefficient, a higher k_{ins} would be required.

A.4 Andasol 3 CSP setup

Table A.2: Input parameters for the SAM simulation of the Andasol 3 CSP station during one year (from July 1st 2017 to June 30th 2018).

Solar Field	Value	Comment
Field gross aperture area	510120 m^2	According to NREL. This value accounts only for reflective area.
Row spacing	17 m	According to Google maps.
Stow angle	170°	SAM default parameter.
Deploy angle	10°	SAM default parameter.
Number of field subsections	4	According to NREL.
Header pipe roughness	4.57×10^{-5} m	SAM default parameter.
HTF pump efficiency	0.85	SAM default parameter.
Freeze protection temperature	150 °C	SAM default parameter.

Irradiance at design	700 W/m^2	According to NREL.
Allow partial defocusing	Yes, simultaneous	SAM default parameter. Common strategy in PT plants to avoid HTF overheating while producing maximum allowed power.

Heat transfer fluid (HTF)	Value	Comment
HTF	Downtherm A	According to NREL.
Design loop inlet temperature	293 °C	According to NREL.
Design loop outlet temperature	393 °C	According to NREL.
Max. single loop flow rate	11 kg/s	See section A.5.1.
Min. single loop flow rate	1 kg/s	See section A.5.2.

Collector orientation	Value	Comment
Collector tilt	0°	SAM default parameter. Plant perfectly horizontal.
Collector azimuth	0°	SAM default parameter. North-South axis.

Mirror washing	Value	Comment
Water usage per wash	0.7 L/m^2	SAM default parameter.
Washes per year	63	SAM default parameter.

Plant heat capacity	Value	Comment
Hot piping thermal inertia	0.2 $kW_{th}h/MW_e.K$	SAM default parameter.
Cold piping thermal inertia	0.2 $kW_{th}h/MW_e.K$	SAM default parameter.
Field loop piping thermal inertia	4.5 $W_{th}h/m.K$	SAM default parameter.

Land area	Value	Comment
Non-solar field land area multiplier	1.558	SAM default parameter.

Single loop configuration	Value	Comment
Number of SCA per loop	4	According to NREL.
Types of SCAs	All 1	According to NREL.
Types of HCEs	All 1	According to NREL.

Collector geometry	Value	Comment
Reflective aperture area	817 m^2	According to NREL.
Total aperture width	5.77 m	For conventional collectors.
Length of collector assembly	150 m	According to NREL.
Number of modules per assembly	12	According to NREL.
Average surface-to-focus path length	2.116 m	See section A.5.3.

Piping distance between assemblies	2 m	According to Google maps.
Optical parameters	Value	Comment
Incidence angle modifier	$1–0.040107 \times \theta/cos(\theta)$ $-0.00206265 \times \theta^2/cos(\theta)$	According to [142]. θ is in radians.
Tracking error	0.988	SAM default parameter.
General optical error	1	SAM default parameter.
Geometry effect	0.952	SAM default parameter.
Mirror reflectance	0.93	SAM default parameter.
Dirt on mirror	0.97	SAM default parameter.
Receiver geometry	Value	Comment
Absorber tube inner diameter	0.066 m	SAM default parameter (Schott PTR70).
Absorber tube outer diameter	0.070 m	SAM default parameter (Schott PTR70).
Glass envelope inner diameter	0.119 m	SAM default parameter (Schott PTR70).
Glass envelope outer diameter	0.125 m	SAM default parameter (Schott PTR70).
Absorber flow plug diameter	0 m	SAM default parameter (Schott PTR70).
Internal surface roughness	4.5×10^{-5}	SAM default parameter (Schott PTR70).
Absorber flow pattern	Tube flow	SAM default parameter (Schott PTR70).
Absorber material type	304 L	SAM default parameter (Schott PTR70).
Variations (Normal data)	Value	Comment
Variant weighting fraction	1	SAM default parameter By selecting 1, all receivers are identical.
Absorber absorptance	0.94	Common value used in industry.
Envelope absorptance	0.0225	Common value used in industry.
Envelope emittance	0.9	Common value used in industry.
Envelope transmittance	0.955	Common value used in industry.
Annulus gas type	Hydrogen	SAM default parameter.
Annulus pressure	0.0001 torr	SAM default parameter.
Estimated average heat loss	374 W/m	See section A.5.4.

Bellow shadowing	0.935	SAM default parameter.
Dirt on receiver	0.98	SAM default parameter.

Plant capacity	Value	Comment
Design gross output	55 MW_e	Net power provided by NREL is 50 MWe. However, due to parasitic losses, the gross power is set to 55 MWe.
Estimated gross to net conversion factor	0.9	Parasitic losses are considered.

Power block design point	Value	Comment
Rated cycle conversion efficiency	0.381	SAM default parameter.
Fossil backup efficiency	0.9	SAM default parameter.
Aux. heater outlet temperature	393 °C	SAM default parameter.
Fossil dispatch mode	Min. backup	According to NREL.

Plant control	Value	Comment
Low resource standby period	2 h	SAM default parameter.
Fraction of thermal power for standby	0.2	SAM default parameter.
Power block start-up time	0.5 h	SAM default parameter.
Fraction of thermal power for start-up	0.2	SAM default parameter.
Min. required start-up temperature	320 °C	To produce steam at 100 bars, 320 °C is the minimum to vaporize water (T_{vap} = 311 °C).
Max. turbine over design operation	1.05	SAM default parameter.
Min. turbine over design operation	0.2	SAM default parameter.

Rankine cycle parameters	Value	Comment
Boiler operating pressure	100 bars	SAM default parameter.
Steam cycle blowdown fraction	0.016	SAM default parameter.
Turbine inlet pressure control	Fixed-pressure	SAM default parameter.
Condenser-type	Air-cooler	SAM default parameter.
Ambient temperature at design	42 °C	SAM default parameter.
Initial temperature difference at design point	16 °C	SAM default parameter.
Condenser pressure ratio	1.0028	SAM default parameter.

Min. condenser pressure	2 inHg	SAM default parameter.
Cooling system part load levels	8	SAM default parameter.
Thermal Storage	Value	Comment
Full load hours of TES	7.5 h	According to NREL.
Parallel tank pairs	1	SAM default parameter.
Parallel tank pairs	1	SAM default parameter.
Tank height	14 m	SAM default parameter.
Tank fluid min. height	1 m	SAM default parameter.
Tank loss coefficient	0.4 $W/m^2.K$	See section A.5.5.
Cold tank heater set point	250 °C	SAM default parameter. Since freezing temperature is 220 °C, 250°C is selected to leave margin.
Hot tank heater set point	365 °C	SAM default parameter.
Tank heater capacity	25 MW_e	SAM default parameter.
Tank heater efficiency	0.98	SAM default parameter.
Hot side HX approach temperature	300 °C	SAM default parameter.
Storage HTF fluid	Solar Salt	According to NREL.
Parasitics	Value	Comment
Piping thermal loss coefficient	0.45 $W/m^2.K$	See section A.5.6.
Tracking power	125 W/SCA	SAM default parameter.
Required pumping power for HTF through power block	0.55 kJ/kg	SAM default parameter.
Required pumping power for HTF through storage	0.15 kJ/kg	SAM default parameter.
Fraction of rated gross power consumed at all time	0.005	SAM default parameter.
Balance of plant parasitic value	0 MW_e/MW_{cap}	SAM default parameter.
Aux. heater parasitic value	0.02273 MW_e/MW_{cap}	SAM default parameter.
Factor	1	SAM default parameter.
Coefficients 0,1,2	0.483, 0.517, 0	SAM default parameter.

Following the adopted procedure of the Gemasolar setup, for the simulation of a PT system dispatch control, scheduling, system costs, Lifetime, financial parameters, incentives, electricity rates and electricity load, were set to the SAM default values.

A.5 Andasol 3 CSP calculations

A.5.1 Nominal mass flow of one loop

The nominal mass flow, $\dot{m}_{\mathrm{nom}}$, can be calculated with the following equation [143]:

$$\dot{m}_{\mathrm{nom,loop}} = \frac{P_{\mathrm{nom,loop}}}{C_{\mathrm{m}} \times (T_{\mathrm{H}} - T_{\mathrm{L}})}, \tag{A.8}$$

where the inlet power, $P_{\mathrm{nom,loop}}$, can be found, considering the collectors field aperture area, A_{col}, of ≈510120 m^2, the total number of loops, N_{loop}, of 157, the conversion energy efficiency, η_{g}, of ≈0.7, and a nominal DNI of ≈1000 W.m^{-2}, as follows:

$$P_{\mathrm{nom,loop}} = \eta_{\mathrm{g}} \times \frac{DNI \times A_{\mathrm{col}}}{N_{\mathrm{loop}}}, \tag{A.9}$$

$$\Leftrightarrow P_{\mathrm{nom,loop}} = 0.7 \times \frac{1000 \times 510120}{157} \approx 2.27 \quad \mathrm{MW_t}. \tag{A.10}$$

Assuming that the specific heat, C_{m}, has a linear behaviour with temperature, the average value between hot and cold temperatures (in K), T_{H} and T_{L} (respectively), can be used. Thus, the following value is attained for the nominal mass flow:

$$C_{\mathrm{m}} = \frac{C\,(T = T_{\mathrm{L}}) + C\,(T = T_{\mathrm{H}})}{2}, \tag{A.11}$$

$$\Leftrightarrow C_{\mathrm{m}} = \frac{2300 + 2574}{2} \approx 2437 \quad \mathrm{J.kg^{-1}.K^{-1}} \tag{A.12}$$

Thus, the nominal mass flow is given by:

$$\dot{m}_{\mathrm{nom}} = \frac{2.29 \times 10^6}{2437 \times (393 - 293)} \approx 9.4 \quad \mathrm{kg.s^{-1}}. \tag{A.13}$$

In nominal regime, a mass flow of 9.4 kg.s^{-1} can be calculated. However, assuming some safety margin to the pump, in case of too high inlet temperatures or a unusual DNI, 11 kg.s^{-1} is selected for the maximum single loop flow rate parameter.

A.5.2 Reynolds number with respect to mass flow and temperature

According to the receivers manufacturer, e.g. Rioglass Solar (https://www.rioglass.com/), the Reynolds number, R_{e}, in PT systems needs to be higher than 20,000 in order to maintain a turbulent regime and sufficient heat transfer between the HTF and the absorber tube. In this case, Reynolds number depends on the pipe internal radius ,r_{int}, the fluid mass flow, $\dot{m}$, and viscosity, μ, with the latter depending on temperature:

$$R_{\mathrm{e}} = \frac{2 \times \dot{m}}{\mu \times \pi \times r_{\mathrm{int}}}. \tag{A.14}$$

The following 2D plot (**Fig. A.1**) can therefore be pictured between Reynolds number, mass flow and fluid temperature. It can be seen that for the temperature range of Andasol 3 (i.e. 290-390 °C), a mass flow of 0.5 kg.s^{-1} is insufficient. For lower temperatures (i.e. preheating mode), down to 100 °C, 1 kg.s^{-1} is assumed for the minimum single loop flow rate parameter.

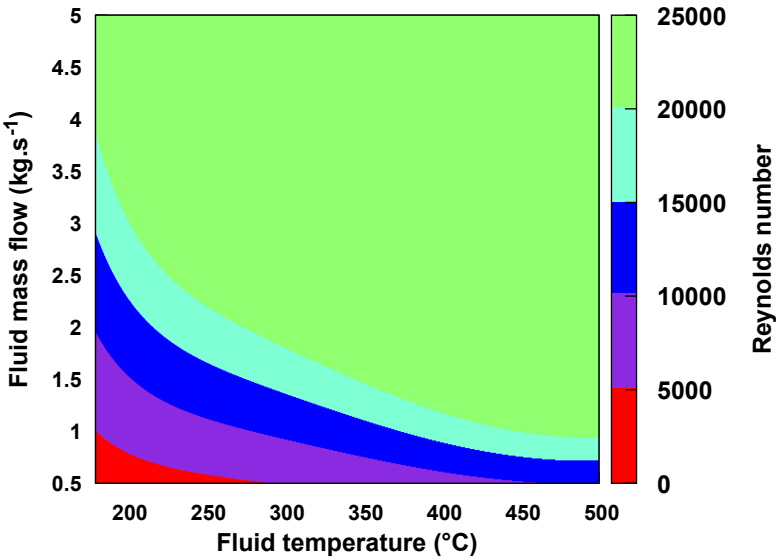

Figure A.1: Figure created and kindly shared by T. Fasquelle.

A.5.3 Average surface-to-focus path length

The average surface-to-focus path length, F_{avg}, is given by the following relation [144]:

$$F_{\mathrm{avg}} = W \times \sqrt{\frac{\left[4 \times a^2 + \left(\frac{W}{2}\right)^2\right]^2}{a^2}} \times \frac{12 \times a^2 + (\frac{W}{2})^2}{12 \times W \times \left[4 \times a^2 + (\frac{W}{2})^2\right]}, \tag{A.15}$$

where, according to NREL manual, *W* is the collector aperture (5.77 m) and *a* the focal length (1.71 m).

Thus, attributing these values to the previous equation:

$$F_{\text{avg}} = 5.77 \times \sqrt{\frac{\left[4 \times 1.71^2 + \left(\frac{5.77}{2}\right)^2\right]^2}{1.71^2}} \times \frac{12 \times 1.71^2 + \left(\frac{5.77}{2}\right)^2}{12 \times 5.77 \times \left[4 \times 1.71^2 + \left(\frac{5.77}{2}\right)^2\right]}, \tag{A.16}$$

$$\Leftrightarrow F_{\text{avg}} \approx 2.116 \quad \text{m}. \tag{A.17}$$

A.5.4 Estimated average heat loss

Two research works estimated heat losses of PTR70 receivers: [145] used an electrical resistance around the absorber tube, then measured the tube temperature and estimated heat losses from the electrical consumption to maintain a certain temperature; [142] performed thermal qualification tests directly in the solar field, consisting in sending fluid at a given temperature and with a constant mass flow until reaching steady-state (in the absence of sunlight). Heat losses were estimated by measuring the inlet and outlet temperatures, and mass flow (power calculation). The former method has the advantage of knowing the absorber outer temperature, which is directly related to heat losses. For that matter, it should be more accurate. However, it seems that heat losses were underestimated by [145], perhaps due testing performance inside a building, lowering heat losses (i.e. no wind, no radiation to the sky). The latter method assumes that the fluid and the absorber tube have the same temperature. However, during the test, the absorber tube will have a lower temperature, although in on-sun tests absorber tube has a higher temperature than the fluid. When a specific value for heat losses is calculated for a specific fluid temperature, it actually corresponds to a lower absorber temperature. As a consequence, theoretically, heat losses should be underestimated with this method. Nonetheless, they are higher than with [145]. The equation of heat losses (P, W.m^{-1}) obtained by Burkholder is given below:

$$P = 0.141 \times T_{\text{a}} + 6.48 \times 10^{-9} \times {T^4}_{\text{a}}, \tag{A.18}$$

with T_{a} being the absorber temperature, which can be considered equal to the fluid one. The equation obtained by Valenzuela is given below:

$$P = 0.36111 \times \Delta T_{\text{f}\leftrightarrow\text{amb}} + 1.1805 \times 10^{-8} \times {\Delta T^4}_{\text{f}\leftrightarrow\text{amb}}, \tag{A.19}$$

where $\Delta T_{\text{f}\leftrightarrow\text{amb}}$ is the average temperature difference between the fluid and the ambient temperatures:

$$\Delta T_{\text{f}\leftrightarrow\text{amb}} = \frac{T_{\text{f,out}} + T_{\text{f,in}}}{2} - T_{\text{amb}}. \tag{A.20}$$

The obtained results using both methods are given in **Table A.3**, considering an ambient temperature of 20 °C. Based on these results, the average value found (≈374 W.m^{-1}) with the Valenzuela et al. method

was selected.

Table A.3: Different output results for heat loss based on [140] and [143] relations.

Temperature (°C)	Valenzuela et al.	Burkholder et al.
293	239 W.m^{-1}	89 W.m^{-1}
393	572 W.m^{-1}	210 W.m^{-1}
343 (medium)	374 W.m^{-1}	138 W.m^{-1}
500	1309 W.m^{-1}	476 W.m^{-1}

A.5.5 Heat losses from the tanks to the environment

The tanks are ≈14 m high and have ≈34 m in diameter (i.e. a tank external radius, $r_{\mathrm{ext,t}}$, of 17 m), being considered to be perfect cylinders with convection all around (even at the bottom, for simplification reasons). These are insulated with ≈500 mm of rockwool. The global heat loss coefficient (U, W.m^{-2}.K^{-1}) is given by the following equation:

$$U = \frac{1}{\frac{\ln\left(\frac{r_{\mathrm{ext,t}}+e_{\mathrm{ins}}}{r_{\mathrm{ext,t}}}\right)\times(r_{\mathrm{ext,t}}+e_{\mathrm{ins}})}{k_{\mathrm{ins}}} + \frac{1}{h_{\mathrm{ext}}}} + \frac{2}{\frac{e_{\mathrm{ins}}}{k_{\mathrm{ins}}} + \frac{1}{h_{\mathrm{ext}}}}. \tag{A.21}$$

Assuming a heat transfer coefficient, h_{ext}, of ≈15 W.m^{-1}.K^{-1} and a thermal conductivity, k_{ins}, of ≈0.06 W.m^{-1}.K^{-1} for the insulating material, the previous equation is solved as:

$$U_{\mathrm{tank}} = \frac{1}{\frac{\ln\left(\frac{17+0.5}{17}\right)\times(17+0.5)}{0.06} + \frac{1}{15}} + \frac{2}{\frac{0.5}{0.06} + \frac{1}{15}}. \tag{A.22}$$

$$\Leftrightarrow U_{\mathrm{tank}} \approx 0.36 \quad \mathrm{W.m^{-2}.K^{-1}}. \tag{A.23}$$

A.5.6 Heat losses from the pipes

Considering 2 inch pipes with ≈15 cm of insulation thickness, e_{ins} , the heat loss coefficient for the pipes, U_{pipes} (W.m^{-2}.K^{-1}), is given as:

$$U_{\mathrm{pipes}} = \frac{1}{\frac{ln\left(\frac{r_{\mathrm{ext,p}}+e_{\mathrm{ins}}}{r_{\mathrm{ext,p}}}\right)\times r_{\mathrm{ext,p}}}{k_{\mathrm{ins}}} + \frac{1}{h_{\mathrm{ext}}}}. \tag{A.24}$$

With a 2 inch pipe (i.e. an external radius, $r_{\mathrm{ext,p}}$, of ≈0.0508 m), an external convection coefficient, h_{ext}, of ≈15 W/m^2.K, and a thermal conductivity k_{ins} of ≈0.06 W.m^{-1}.K^{-1}, the following relation can be

obtained:

$$U_{\text{pipes}} = \frac{1}{\frac{ln\left(\frac{0.0508+0.15}{0.0508}\right)\times 0.0508}{0.06} + \frac{1}{15}}, \tag{A.25}$$

$$\Leftrightarrow U_{\text{pipes}} \approx 0.21 \quad \text{W.m}^{-2}\text{.K}^{-1}. \tag{A.26}$$

This value is different than the SAM default parameter, since all thermal bridges (e.g. supports, valves and probes) and the pipes that are different (e.g. flexible hose) are not being taken into account. For this reason, the SAM value (0.45 $\text{W.m}^{-2}\text{.K}^{-1}$) should be considered.

B

DNI predictions using the Meso-NH atmospheric model

This appendix includes a preliminary analysis carried out before the writing of this thesis, as part of a research work developed during the Atmospheric Modelling Class from the doctoral programme at the University of Évora. The results identified problems in the prediction of the DNI by the Meso-NH model. Since the development of the model was outside the scope of this thesis, errors were reported and discussed with the Meso-NH development team (at Centre National de Recherches Meteorologiques/Météo-France), which later led to the correction of bugs and finally by the introduction of a new radiation scheme [122].

B.1 Introduction

DNI is an essential component in the context of solar irradiance and is defined as the direct irradiance that is received on a plane normal to the position of the sun in the sky over the total solar spectrum [24]. Under clear sky conditions, DNI is the foremost important solar resource that can be used for an efficiency usage and management of electricity grids and solar energy distribution. The two main solar energy conversion technologies that use DNI as solar resource are CSP and CPV systems. The former demands a high DNI forecast accuracy, especially in cloudless periods, whilst the latter requires more global irradiance forecasts [22].

Short (24 hours) and medium-term (2 days to 2 weeks ahead) forecasts are particularly important to CSP efficient operations and for that reason, the use of NWP models is an essential tool in understanding the spatial-temporal variation of available DNI, as well as in performing solar radiation predictions. Currently, these type of forecasts through NWP models are still very recent and their quality should be accessed and improved. There are several available NWP models which include global and mesoscale high resolution models for DNI simulation and prediction that allow a detailed physical description of atmospheric processes. For instance, the IFS global model from the ECMWF, which is known to provide a general good performance in predicting solar radiation. In the context of high resolution NWP modelling, the Weather Research and Forecasting (WRF) model, the limited area model (AROME) and the non-hydrostatic model (Meso-NH), respectively [146] and [123] are all currently in operation. In particular, the AROME model is used by the Portuguese meteorological service (IPMA), whilst the Meso-NH (Météo-France) has been more used for research purposes, such as for atmospheric circulations modelling in southern Portugal [147, 87].

The study location is in the Alentejo region (southern Portugal), having exceptional conditions for solar radiation and atmospheric transparency, it holds one of the highest DNI potentials measured at surface in Europe. Mean daily values (24-hour integration) of DNI in the order of 300 W/m^2, with a daily maximum of $\approx$950 W/m^2, are usually observed during the summer months. For these reasons, the area of study, in which we focus our DNI simulations and compare with local observations, offers an ideal setup for future installations of CSP projects and for solar radiation forecasting prospects.

B.2 Methodology

B.2.1 The mesoscale non-hydrostatic model (Meso-NH)

The non-hydrostatic model Meso-NH (developed as from 1994) was built under an anelastic approach, which allows less computational time than others mesoscale models. The model can perform simulations ranging from synoptic scale (hundreds of kilometres) to microscale (tens of meters), while calculating budgets simultaneously, as well as performing multi-scale methods through grid-nesting techniques. The model version used in this study is the MNH-V5-3-0 and has surface schemes that allow to enhance the

modelling in the lower levels of the atmosphere, giving more realistic lower boundary conditions. For that matter, the surface model scheme SURFEX (SURFace EXternalized) is used here, allowing to modulate the exchanges of flux between surface and atmosphere at each time step having in consideration different types of surface (e.g. vegetation, ocean, lakes and city). Moreover, a chemistry (gas-phase, aerosol and aqua-phase components) and a lighting module are also coupled to the model. Other model characteristics are the simple formulations implemented for the interactions that occur between the dynamical and physical processes. For instance, condensation of water and the possibility to express the equations in a Boussinesq form [148].

The radiation code used for the DNI calculations in the Meso-NH is shared with the ECMWF, which only provides DNI forecasts from 2014. The code takes into account interactions between microphysics, dynamics and radiation, including radiative fluxes (surface shortwave and longwave), while at the same time considers absorption-emission of long wave radiation and reflection, as well as the scattering and absorption of solar radiation in the Earth's surface and atmosphere.

The radiation variables provided by the model to simulate the direct normal and the diffuse radiation on a flat surface contain 6 spectral bands: 185-250, 250-440, 440-690, 690-1190, 1190-2380 and 2380-4000 nm. All the radiation and meteorological variables outputted by the model that were taken into account here are listed below in **Table B.1**.

Table B.1: Atmospheric variables provided by the Meso-NH.

Variable	Designation	Units
Direct normal irradiance on flat surface	DIRFLASWD	W/m^2
Diffuse irradiance on flat surface	SCAFLASWD	W/m^2
Shortwave downward radiative flux	SWD	W/m^2
Zenith angle	ZENITH	°
Air temperature at 2 m height	T2M	°C
Relative humidity at 2 m height	HU2M	%
Horizontal wind at 10 m height	UM10	m/s
Vertical wind at 10 m height	VM10	m/s

B.2.2 Experiemental setup

The Meso-NH simulations were performed on a horizontal resolution grid of 3 x 3 km^2, with a vertical resolution of 20 m, chosen to represent the domain of interest (southern Portugal: 36.5-40° N; 9.8-6.4° W). The selected time period (21^{st}-24^{th} July) comprises 72 hours of simulation, with spatial-temporal averages calculated by the model for each hourly instant. The model was setup to initialize the simulation 6 hours before the start of the observational period due to the computational time adjustment. The period of simulation coincides with the intensive observational period (IOP), which took place in the Alqueva region

during the ALqueva hydro-meteorological EXperiment 2014 (ALEX2014) campaign. The IOP provides data that includes vertical profiles of the planetary boundary layer through the release of air balloons under clear sky conditions, as well as other important measurements in the context of DNI under such conditions. The observational data used for the Meso-NH validation can be consulted online in the ALEX2014 data base (https://www.alex2014.cge.uevora.pt).

Physical schemes are important components to be considered for the parameterizations during simulation of DNI at surface, as they are part of the model that deals with diabatic processes (water state changes, sub grid processes and surface interaction), including microphysics, convection, turbulence, radiation, surface and chemistry. In particular, the ECOCLIMAP data base is used to generate the Meso-NH physiography [8], including a detailed representation of the Alqueva reservoir ($\approx$250 km^2) since 2003. As part of the SURFEX platform, the ISBA (Interaction Soil-Biosphere-Atmosphere) is also implemented. Amongst others, there is the turbulence scheme with turbulent kinetic energy (TKE) and the scheme of shallow convection Eddy-Diffusivity-Kain-Fritsch (EDKF) for the parameterization of dry and cloudy convective boundary layers.

B.2.3 Intercomparison methods

Six observational stations were considered to assess the model performance, all of them are located in the southern region of Portugal. The 1-minute radiation data was measured in Parque Solar near the shore of the Alqueva reservoir (38.197583°N, 7.486139°W), 1-minute meteorological data was obtained from the ICT station in Mitra (38.530522°N, 8.011221°W) and the 10-minute meteorological data gathered from the IPMA stations placed in Estremoz (38.862133°N, 7.512756°W), Elvas (38.889600°N, 7.140833°W), Portel (38.317594°N, 7.860753°W) and Mora (38.940683°N, 8.164058°W). Likewise the Meso-NH, all the observational data is in universal time (0 UTC). Moreover, the respective geographic coordinates of each in-situ station were used to find the nearest point for each one in the model grid.

The DIRFLASWD and SCAFLASWD variables have 6 separated spectral bands (comprising the solar spectrum), therefore the sum of all modeled bands was performed in order to compare with the observed radiation. The global radiation (GFLASWD) can be simply calculated by:

$$\mathrm{GFLASWD_{meso}} = \mathrm{DNI_{meso}} + \mathrm{SCAFLASWD}, \tag{B.1}$$

$$\mathrm{DNI_{meso}} = \frac{\mathrm{DIRFLASWD}}{\cos(\mathrm{ZENITH})}. \tag{B.2}$$

B.3 Results

B.3.1 Model validation

As a first approach in assessing the Meso-NH, comparison with in-situ atmospheric variables profiles (air temperature and air relative humidity at 2 m and the wind speed at 10 m) were carried out in 5 meteorological stations: Mitra (MT), Estremoz (EM), Elvas (EV), Portel (PT) and Mora (MR). Since the model provides hourly values for a specific instant during the time period analysed, an hourly centred mean was applied in the measured data. **Table B.2** summarizes the correlations between observations and model outputs for the three meteorological parameters.

Table B.2: Correlations between meteorological observations and Meso-NH. Meteorological stations: Mitra (MT), Estremoz (EM), Elvas (EV), Portel (PT) and Mora (MR).

Variable	MT	EM	EV	PT	MR
Air temperature at 2 m	0.94	0.95	0.95	0.95	0.93
Relative humidity at 2 m	0.83	-	-	-	0.91
Wind speed at 10 m	0.50	0.80	0.61	0.47	0.51

Temperature profiles in MT station (**Fig. B.1a**) show that there is a good correspondence between curves, with a very similar behaviour throughout the rest of the period. Of all stations, EV and PT seem to be the ones in which the model shows better results, while in MR there are deviations of almost 6 °C on the second day (not shown here). The Meso-NH humidity in MT (**Fig. B.1b**) highly overestimates measurements during the first day (≈20 %), having a very similar correspondence with the observation thereafter. Only other station had humidity profile available (MR), where the result show similar behaviour as in MT. The wind speed has a high variability, which depends on several local factors, and is expected to show strong deviations when comparing with the measured one. This can be easily seen in **Table B.2**, where all the correlations between the measured and predicted wind speed depict low values. Nevertheless, the Meso-NH wind speed curves appear to show a similar tendency of the observed in MT, with a general increase during the entire period (**Fig. B.1c**). This was also the case in all the wind profiles between the other stations (not shown here).

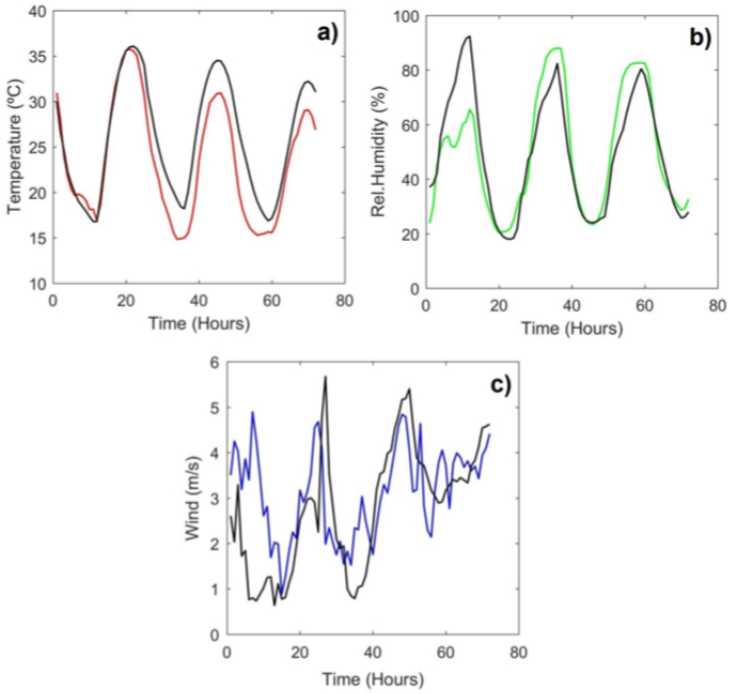

Figure B.1: Meteorological profiles in Mitra: a) Air Temperature (°C), b) Air Relative Humidity (%) and c) Wind Speed (m/s). Colour palletes: measured temperature (in red), measured relative humidity (in green), measured wind speed (in blue), Meso-NH simulations (in black).

B.3.2 DNI modelling

To compare Meso-NH global, direct and diffuse radiations with measurements, only data from Parque Solar (PS) station with a SOLYS2 Sun Tracker (Kipp & Zonen) was used.

Under clear sky conditions (i.e. the first two days), the simulated global radiation GFLASWD in **Fig. B.2**, from **Eq. B.1**, is in good agreement with the observed global mean (in red). A small deviation occurs during the first hours each day (≈7 UTC) due to a shadow casted by the presence of trees in the surrounding area. There is also a slight overestimation by the model at the hour of maximum radiation (12 UTC) reaching ≈1050 W/m^2 (i.e. ≈20 W/m^2 more than the observation). In the third day, which is characterized by the presence of passing clouds, the model curves do not behave as expect from the observation. Instead, the curve continues to depict the same daily variation as in the two previous days. Moreover, in clear days the model overestimation is due to the absence of diffuse radiation that would result from local aerosols produced in land and lake and would contribute to a small decrease of the curve peak. On a cloudy day, the model seems to consider the diffuse radiation that results entirely from clouds.

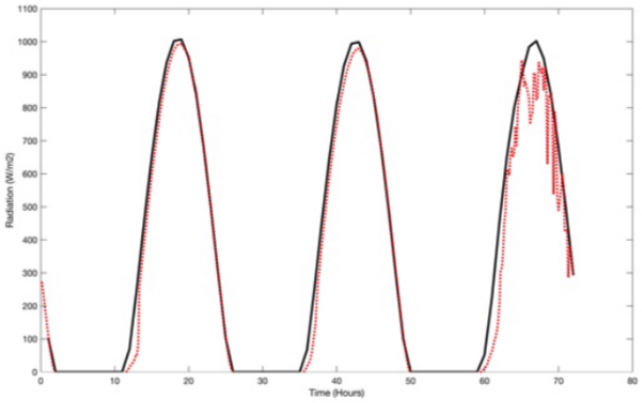

Figure B.2: Global solar radiation in Parque Solar. DIRFLASWD + SCAFLASWD (filled black line) and the observed mean (red line). Period of observation: 21st to 24th July 2014. Spectral bands used: 185-4000 nm. Units: W/m^2.

In **Fig. B.3**, the Meso-NH simulated DNI, through **Eq. B.2**, and the observed mean DNI show a close behaviour with each other, reaching values close to 950 W/m^2 at mid-day. The fact that shadow is influencing the initial values of observed DNI leads to a small deviation at the begin of each day. A slight underestimation by the model occurs in the first day while in the last day due to the presence of clouds the model seems to consider their presence although with less effect on the DNI recorded by measurements. In **Fig. B.4**, during the first two days, the diffuse radiation from the model overestimates the observations, depicting values of about 100 W/m^2, while on the third day it shows a behaviour similar to the observed, although with smaller increases during cloudy periods.

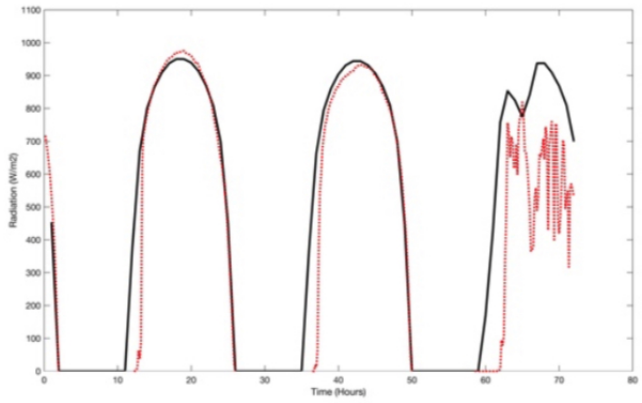

Figure B.3: Direct normal radiation in Parque Solar. DIRFLASWD/cos(ZENITH) (filled black line) and the observed mean (red line). Period of observation: 21st to 24th July 2014. Spectral bands used: 185-4000 nm. Units: W/m^2.

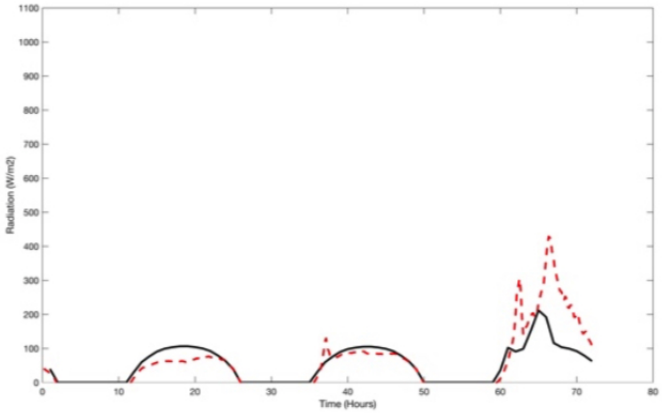

Figure B.4: Diffuse radiation in Parque Solar. SCAFLASWD (filled black line) and the observed mean (red-dashed line). Period of observation: 21st to 24th July 2014. Spectral bands used: 185-4000 nm. Units: W/m^2.

A representation of the daily available solar energy from the simulated DNI is depicted over the region of study for a cloudless day (**Fig. B.5**), i.e. 21-22 July. This day is characterized to have an inland uniform distribution of values reaching a maximum of 4 x 10^7 J/m^2, as expected during this period of the year. The highest values obtained are located over the sea, particularly in the south due to the Mediterranean proximity. The lower values that occur near the western coast are due to the presence of clouds in the area.

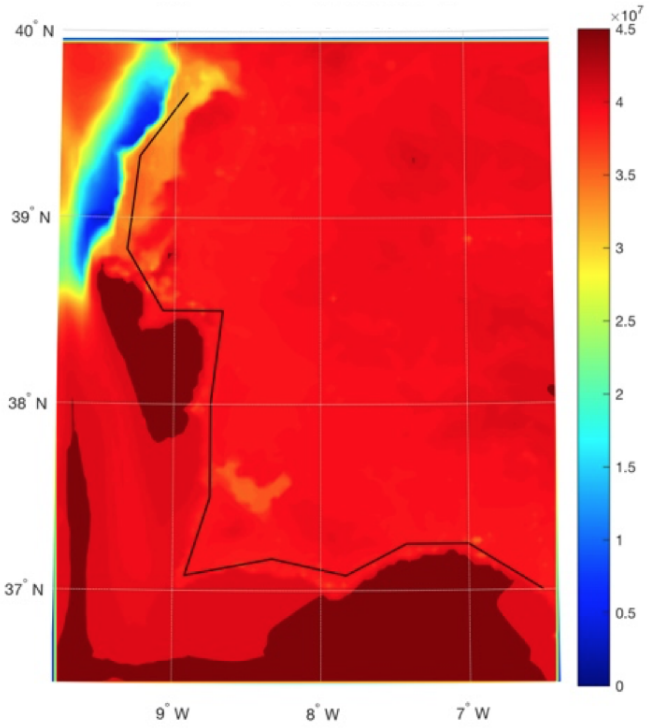

Figure B.5: Direct normal radiation in southern Portugal. Period of observation 21st to 22th July 2014. Units: J/m^2.

B.4 Conclusions

In this work, an assessment of the Meso-NH mesoscale atmospheric model was carried out for a three-day simulation of meteorological variables and solar radiation. The comparison of the model outputs was conducted by using 6 in-situ stations in the southern region of Portugal for 21st-24th July 2014, during the ALEX2014 campaign. Hourly predictions in a 3 x 3 km^2 horizontal grid was analysed. Results show that simulated profiles of meteorological components are close to the measured data. In particular, air temperature, although with small deviations which can be due to local sub-grid factors. The radiation results have shown that the current radiation scheme of the Meso-NH model, version V5-3-0, does not represent with precision the hourly variation of solar radiation when clouds are present. The issues found are linked to the implemented radiation scheme and should be addressed in future works. Such developments will allow the use of longer time series and other observational stations to perform a more thorough analysis. Moreover, the use of the model in a nowcasting system that comprises four all sky imaging cameras near Évora is also foreseen. This will allow an efficient use the modelled radiation for the operationalization of CSP systems in the region.

C

Multivariate regression tables

In this appendix, the results obtained from multivariate regression analysis carried out in Chapter 4 (Improvement of DNI Forecasts: Implications for CSP), considering two years of measured and predicted data in Évora, are shown.

C.1 Introduction

In tables **C.1**, **C.2**, **C.3** and **C.4**, all significant and possible relations between predictors and predictand (Terms), the weight (Estimates) that each relation has in the respective adjustment, the standard error (SE) obtained, the t-statistics (tStat) and the p-value (pValue) for both MRM1 and MRM2 hourly and daily adjustments are presented. The following set of predictors were considered for the hourly adjustments: $x_1(DNI_i^{IFS})$, $x_2(GHI_i^{IFS})$, $x_3(GHI_i^{TOA})$, $x_4(DNI_i^{TOA})$, $x_5(T_i^{IFS})$, $x_6(RH_i^{IFS})$, $x_7(W_i^{IFS})$, $x_8(Pr_i^{IFS})$, $x_9(Tcc_i^{IFS})$, $x_{10}(DNI_{i-1}^{OBS})$ and $x_{11}(GHI_{i-1}^{OBS})$, with DNI_i^{OBS} as the predictand. In the case of the daily adjustments, predictors x_1, x_2, x_5, x_6 and x_9 were considered.

C.2 Regression tables

Table C.1: Hourly multivariate regression metrics obtained through the use of the stepwise function considering a second-degree polynomial adjustment of DNI (MRM1) during one year (from July 1st 2018 to June 30th 2019).

MRM1				
Terms	**Estimates**	**SE**	**tStat**	**pValue**
'(Intercept)'	-3.59 x 10^4	1.27 x 10^4	-2.83	4.65 x 10^{-3}
'x_1'	8.18	2.10	3.90	9.84 x 10^{-5}
'x_2'	1.30	3.20	0.41	0.68
'x_3'	-3.56	1.40	-2.54	0.01
'x_4'	47.51	17.80	2.67	7.64 x 10^{-3}
'x_5'	174.09	65.97	2.64	8.35 x 10^{-3}
'x_6'	29.45	17.65	1.67	0.10
'x_7'	327.68	130.22	2.52	0.01
'x_8'	-1.35 x 10^4	4.18 x 10^3	-3.22	1.29 x 10^{-3}
'x_9'	3.54 x 10^3	850.58	4.16	3.25 x 10^{-5}
'$x_1 \cdot x_3$'	-8.65 x 10^{-4}	1.90 x 10^{-4}	-4.55	5.56 x 10^{-6}
'$x_1 \cdot x_4$'	-5.04 x 10^{-3}	1.45 x 10^{-3}	-3.48	5.07 x 10^{-4}
'$x_1 \cdot x_5$'	-0.03	7.20 x 10^{-3}	-3.90	9.68 x 10^{-5}
'$x_1 \cdot x_6$'	-4.43 x 10^{-3}	2.33 x 10^{-3}	-1.90	0.06
'$x_1 \cdot x_8$'	-16.42	10.71	-1.53	0.13
'$x_1 \cdot x_9$'	-0.06	0.11	-0.50	0.62
'$x_2 \cdot x_4$'	-1.88 x 10^{-3}	2.24 x 10^{-3}	-0.84	0.40
'$x_2 \cdot x_5$'	0.02	6.65 x 10^{-3}	2.26	0.02
'$x_2 \cdot x_6$'	2.70 x 10^{-3}	3.50 x 10^{-3}	0.77	0.44
'$x_2 \cdot x_7$'	-0.01	9.54 x 10^{-3}	-1.39	0.16

'$x_2 \cdot x_8$'	-5.94	18.78	-0.32	0.75
'$x_2 \cdot x_9$'	0.99	0.21	4.78	1.83×10^{-6}
'$x_3 \cdot x_4$'	3.57×10^{-3}	1.02×10^{-3}	3.52	4.44×10^{-4}
'$x_3 \cdot x_6$'	-4.27×10^{-3}	1.64×10^{-3}	-2.60	9.42×10^{-3}
'$x_3 \cdot x_8$'	15.35	7.20	2.13	0.03
'$x_3 \cdot x_9$'	-0.84	0.16	-5.13	3.02×10^{-7}
'$x_4 \cdot x_5$'	-0.11	0.04	-2.49	0.01
'$x_4 \cdot x_6$'	-0.02	0.01	-1.40	0.16
'$x_4 \cdot x_7$'	-0.22	0.09	-2.52	0.01
'$x_4 \cdot x_9$'	-2.50	0.59	-4.24	2.33×10^{-5}
'$x_5 \cdot x_6$'	-0.15	0.08	-1.97	0.05
'$x_5 \cdot x_7$'	-0.85	0.47	-1.80	0.07
'$x_5 \cdot x_9$'	-6.39	3.07	-2.08	0.04
'$x_6 \cdot x_7$'	0.20	0.15	1.39	0.16
'$x_6 \cdot x_9$'	-2.81	1.00	-2.80	5.06×10^{-3}
'$x_7 \cdot x_9$'	-23.55	5.83	-4.04	5.49×10^{-5}
'x_1^2'	7.81×10^{-4}	1.42×10^{-4}	5.51	3.83×10^{-8}
'x_2^2'	4.24×10^{-4}	1.49×10^{-4}	2.85	4.44×10^{-3}
'x_3^2'	-1.69×10^{-4}	5.91×10^{-5}	-2.85	4.35×10^{-3}
'x_4^2'	-0.02	6.30×10^{-3}	-2.51	0.01
'x_5^2'	-0.35	0.15	-2.38	0.02
'x_6^2'	-0.04	0.02	-2.52	0.01
'x_8^2'	4.68×10^{5}	1.20×10^{5}	2.34	0.02
'x_9^2'	246.04	52.12	4.72	2.42×10^{-6}

Table C.2: Daily availabilities multivariate regression metrics obtained through the use of the stepwise function considering a second-degree polynomial adjustment of DNI (MRM1) during one year (from July 1st 2018 to June 30th 2019).

MRM1				
Terms	**Estimates**	**SE**	**tStat**	**pValue**
'(Intercept)'	-5.98	4.06	-1.47	0.14
'x_1'	1.27	0.50	2.53	0.01
'x_2'	0.40	0.22	1.78	0.08
'x_5'	0.05	0.08	0.69	0.49
'x_6'	0.21	0.09	2.41	0.02
'x_9'	3.878	1.53	2.53	0.01
'$x_1 \cdot x_6$'	-0.02	6.16×10^{-3}	-2.97	3.16×10^{-3}

'$x_2 \cdot x_5$'	-0.01	0.01	-1.13	0.26
'$x_6 \cdot x_9$'	-0.11	0.03	-3.63	3.29×10^{-4}
'x_1^2'	0.05	0.02	2.46	0.01
'x_5^2'	-2.21×10^{-3}	2.88×10^{-3}	-0.77	0.44
'x_6^2'	-9.48×10^{-4}	4.81×10^{-4}	-1.97	0.05

Table C.3: Hourly multivariate regression metrics obtained through the use of the stepwise function considering a second-degree polynomial adjustment of DNI (MRM2) during one year (from July 1st 2018 to June 30th 2019).

MRM2				
Terms	**Estimates**	**SE**	**tStat**	**pValue**
'(Intercept)'	-2.18×10^4	7.11×10^3	-3.06	2.21×10^{-3}
'x_1'	7.48	1.74	4.30	1.74×10^{-5}
'x_2'	-4.45	2.12	-2.10	0.04
'x_3'	0.39	0.18	2.21	0.03
'x_4'	33.55	10.60	3.16	1.57×10^{-3}
'x_5'	-10.92	2.74	-3.98	6.96×10^{-5}
'x_6'	-18.20	9.64	-1.89	0.06
'x_7'	103.16	72.98	1.41	0.16
'x_9'	-257.21	647.21	-0.40	0.69
'x_{10}'	-2.82	1.00	-2.81	4.96×10^{-3}
'x_{11}'	0.46	1.77	0.26	0.80
'$x_1 \cdot x_2$'	1.20×10^{-3}	3.48×10^{-04}	3.46	5.53×10^{-4}
'$x_1 \cdot x_3$'	-1.02×10^{-3}	2.56×10^{-4}	-3.97	7.25×10^{-5}
'$x_1 \cdot x_4$'	-4.25×10^{-3}	1.24×10^{-3}	-3.43	6.07×10^{-4}
'$x_1 \cdot x_5$'	-0.03	5.73×10^{-3}	-6.04	1.70×10^{-9}
'$x_1 \cdot x_6$'	-3.49×10^{-3}	1.81×10^{-3}	-1.93	0.05
'$x_1 \cdot x_9$'	-0.43	0.11	-3.95	7.90×10^{-5}
'$x_1 \cdot x_{10}$'	7.82×10^{-4}	1.58×10^{-4}	4.96	7.44×10^{-7}
'$x_1 \cdot x_{11}$'	-7.67×10^{-4}	3.00×10^{-4}	-2.55	0.01
'$x_2 \cdot x_3$'	-5.72×10^{-4}	2.38×10^{-4}	-2.41	0.02
'$x_2 \cdot x_4$'	2.84×10^{-3}	1.47×10^{-3}	1.94	0.05
'$x_2 \cdot x_5$'	0.02	9.13×10^{-3}	2.53	0.01
'$x_2 \cdot x_6$'	1.26×10^{-3}	2.49×10^{-3}	0.50	0.61
'$x_2 \cdot x_9$'	0.66	0.22	2.98	2.93×10^{-3}

'$x_2 \cdot x_{10}$'	-1.57×10^{-3}	2.99×10^{-4}	-5.27	1.47×10^{-7}
'$x_2 \cdot x_{11}$'	1.34×10^{-3}	4.32×10^{-4}	3.10	1.96×10^{-3}
'$x_3 \cdot x_5$'	5.03×10^{-3}	4.73×10^{-3}	1.06	0.29
'$x_3 \cdot x_9$'	-0.30	0.15	-1.99	0.05
'$x_3 \cdot x_{10}$'	8.13×10^{-4}	1.70×10^{-4}	4.78	1.85×10^{-6}
'$x_3 \cdot x_{11}$'	5.20×10^{-4}	2.24×10^{-4}	2.33	0.02
'$x_4 \cdot x_6$'	0.01	6.87×10^{-3}	1.80	0.07
'$x_4 \cdot x_7$'	-0.07	0.05	-1.26	0.21
'$x_4 \cdot x_9$'	0.15	0.48	0.31	0.75
'$x_4 \cdot x_{10}$'	1.70×10^{-3}	6.91×10^{-4}	2.45	0.01
'$x_4 \cdot x_{11}$'	-3.11×10^{-4}	1.23×10^{-3}	-0.25	0.80
'$x_5 \cdot x_6$'	0.04	0.03	1.51	0.13
'$x_5 \cdot x_9$'	2.97	1.79	1.66	0.098
'$x_5 \cdot x_{10}$'	0.03	3.88×10^{-3}	7.06	1.96×10^{-12}
'$x_5 \cdot x_{11}$'	-0.01	6.50×10^{-3}	-1.97	0.05
'$x_6 \cdot x_{10}$'	4.06×10^{-3}	1.34×10^{-3}	3.03	2.44×10^{-3}
'$x_6 \cdot x_{11}$'	-1.97×10^{-3}	2.24×10^{-3}	-0.88	0.38
'$x_7 \cdot x_{10}$'	-6.48×10^{-3}	4.54×10^{-3}	-1.43	0.15
'$x_9 \cdot x_{10}$'	0.35	0.06	5.71	1.24×10^{-8}
'$x_9 \cdot x_{11}$'	-0.27	0.11	-2.40	0.02
'$x_{10} \cdot x_1$'	2.31×10^{-4}	1.30×10^{-4}	1.78	0.08
'x_1^2'	-2.48×10^{-4}	1.82×10^{-4}	-1.37	0.17
'x_3^2'	-1.37×10^{-4}	9.07×10^{-5}	-1.51	0.13
'x_4^2'	-0.01	3.97×10^{-3}	-3.23	1.27×10^{-3}
'x_7^2'	-0.64	0.61	-1.04	0.30
'x_9^2'	50.03	42.74	1.17	0.24
'x_{11}^2'	-6.98×10^{-4}	1.62×10^{-04}	-4.31	1.67×10^{-5}

Table C.4: Daily availabilities multivariate regression metrics obtained through the use of the stepwise function considering a second-degree polynomial adjustment of DNI (MRM2) during one year (from July 1st 2018 to June 30th 2019).

MRM2				
Terms	**Estimates**	**SE**	**tStat**	**pValue**
'(Intercept)'	-2.79	5.97	-0.47	0.64
'x_1'	0.61	1.13	0.54	0.59
'x_2'	-0.81	0.56	-1.44	0.15
'x_5'	0.31	0.15	2.07	0.039
'x_6'	0.25	0.09	2.68	7.81×10^{-3}
'x_9'	-4.84	5.57	-0.87	0.39
'x_{10}'	-0.47	0.18	-2.66	8.09×10^{-3}
'x_{11}'	1.18	0.75	1.59	0.11
'$x_1 \cdot x_2$'	0.08	0.05	1.50	0.13
'$x_1 \cdot x_5$'	-0.07	0.03	-2.62	9.24×10^{-3}
'$x_1 \cdot x_6$'	-0.03	8.80×10^{-3}	-3.14	1.82×10^{-3}
'$x_1 \cdot x_9$'	2.03	0.60	3.37	8.30×10^{-4}
'$x_1 \cdot x_{11}$'	-0.08	0.05	-1.77	0.08
'$x_2 \cdot x_5$'	0.07	0.03	2.06	0.04
'$x_5 \cdot x_9$'	-0.22	0.12	-1.83	0.07
'$x_5 \cdot x_{10}$'	0.04	9.72×10^{-3}	3.88	1.25×10^{-4}
'$x_5 \cdot x_{11}$'	-0.07	0.03	-2.48	0.01
'$x_6 \cdot x_9$'	-0.17	0.05	-3.46	6.06×10^{-4}
'$x_6 \cdot x_{11}$'	6.51×10^{-3}	5.43×10^{-3}	1.20	0.23
'$x_9 \cdot x_{11}$'	-0.74	0.31	-2.38	0.02
'x_1^2'	0.14	0.07	2.07	0.04
'x_5^2'	-3.53×10^{-3}	2.99×10^{-3}	-1.18	0.24
'x_6^2'	-9.45×10^{-4}	4.93×10^{-4}	-1.9	0.06
'x_9^2'	7.39	2.07	3.56	4.17×10^{-4}

Bibliography

[1] National Aeronautics and Space Administration, "Our Solar System," 2013.

[2] M. Diagne, M. David, J. Boland, N. Schmutz, and P. Lauret, "Post-processing of solar irradiance forecasts from WRF model at Reunion Island," *Solar Energy*, vol. 105, pp. 99–108, 2014.

[3] R. B. Stull, "An introduction to boundary layer meteorology," *Atmospheric Science Programme, Department of Geography, University of British Columbia, vancouver, Canada. Kluwer Academic Publishers*, 1994.

[4] S. E. Haupt, P. A. Jiménez, J. A. Lee, and B. Kosović, "Principles of meteorology and numerical weather prediction," *Renewable Energy Forecasting: From Models to Applications*, pp. 3–28, 2017.

[5] P. Bauer, A. Thorpe, and G. Brunet, "The quiet revolution of numerical weather prediction," *Nature*, vol. 525, no. 7567, pp. 47–55, 2015.

[6] V. Bjerknes, E. Volken, and S. Brönnimann, "The problem of weather prediction, considered from the viewpoints of mechanics and physics," *Meteorologische Zeitschrift*, vol. 18, no. 6, pp. 663–667, 2009.

[7] C.-G. Rossby and R. B. Montgomery, "The layer of frictional influence in wind and ocean currents," *The layer of frictional influence in wind and ocean currents*, no. 71, 1935.

[8] V. Ekman, "On the Influence of the Earth's Rotation on Ocean-Currents," *Arkiv för Matematik, Astronomi och Fysik*, vol. 2, pp. 1–52, 1905.

[9] M. L. Weisman and J. B. Klemp, "Characteristics of Isolated Convective Storms," *Mesoscale Meteorology and Forecasting*, pp. 331–358, 1986.

[10] P. A. Jiménez, J. A. Lee, B. Kosovic, and S. E. Haupt, "Solar Resource Mapping - Fundamentals and Applications," 2019.

[11] C. M. Fernández-Peruchena, M. Gastón, M. Schroedter-Homscheidt, I. M. Marco, J. L. Casado-Rubio, and J. A. García-Moya, "Increasing the temporal resolution of direct normal solar irradiance forecasted series," *AIP Conference Proceedings*, vol. 1850, 2017.

[12] S. G. Benjamin, J. M. Brown, G. Brunet, P. Lynch, K. Saito, and T. W. Schlatter, "100 Years of Progress in Forecasting and NWP Applications," *Meteorological Monographs*, vol. 59, pp. 13.1–13.67, 2019.

[13] T. K. Ghosh and M. A. Prelas, *Energy Resources and Systems*, vol. 2. 2011.

[14] Y. Goswami, "Advances in Solar Energy: an Annual Review of Research and Development," *EarthScan from Routledge, American Solar Energy Society, Inc, Boulder, Colorado*, vol. 16, 2005.

[15] P. Wolfe, "Solar Photovoltaic projects in the Mainstream Power Market," *EarthScan from Routledge, Taylor & Francis Group, New York, US.*, 2013.

[16] E. Kalnay, "Atmospheric Modeling, Data Assimilation, and Predictability," *Paperbound, Cambridge University Press,*, pp. 1–5, 2002.

[17] M. Schroedter-Homscheidt, A. Benedetti, and N. Killius, "Verification of ECMWF and ECMWF/MACC's global and direct irradiance forecasts with respect to solar electricity production forecasts," *Meteorologische Zeitschrift*, vol. 26, no. 1, pp. 1–19, 2017.

[18] S. Pereira, P. Canhoto, R. Salgado, and M. J. Costa, "Development of an ANN based corrective algorithm of the operational ECMWF global horizontal irradiation forecasts," *Solar Energy*, vol. 185, pp. 387–405, 2019.

[19] L. Ramírez and J. M. Vindel, *Forecasting and nowcasting of DNI for concentrating solar thermal systems*. Elsevier Ltd, 2016.

[20] J. A. Ruiz-Arias, C. A. Gueymard, F. J. Santos-Alamillos, and D. Pozo-Vázquez, "Worldwide impact of aerosol's time scale on the predicted long-term concentrating solar power potential," *Scientific Reports*, vol. 6, pp. 1–10, 2016.

[21] A. Troccoli and J. J. Morcrette, "Skill of direct solar radiation predicted by the ECMWF global atmospheric model over Australia," *Journal of Applied Meteorology and Climatology*, vol. 53, no. 11, pp. 2571–2588, 2014.

[22] M. Schroedter-Homscheidt, A. Oumbe, A. Benedetti, and J. J. Morcrette, "Aerosols for concentrating solar electricity production forecasts: Requirement quantification and ECMWF/MACC aerosol forecast assessment," *Bulletin of the American Meteorological Society*, vol. 94, no. 6, pp. 903–914, 2013.

[23] M. Collares-Pereira and A. Rabl, "Simple procedure for predicting long term average performance of nonconcentrating and of concentrating solar collectors," *Solar Energy*, vol. 23, no. 3, pp. 235–253, 1979.

[24] P. Blanc, B. Espinar, N. Geuder, C. Gueymard, R. Meyer, and R. Pitz-Paal et al, "Direct normal irradiance related definitions and applications: The circumsolar issue," *Solar Energy*, vol. 110, pp. 561–577, 2014.

[25] World Meteorological Organization (WMO), *Guide to Instruments and Methods of Observation*, vol. I. 2018.

[26] J. Pascual, J. Barricarte, P. Sanchis, and L. Marroyo, "Energy management strategy for a renewable-based residential microgrid with generation and demand forecasting," *Applied Energy*, vol. 158, pp. 12–25, 2015.

[27] J. Forrester, "The value of CSP with thermal energy storage in providing grid stability," *Energy Procedia*, vol. 49, pp. 1632–1641, 2014.

[28] E. W. Law, A. A. Prasad, M. Kay, and R. A. Taylor, "Direct normal irradiance forecasting and its application to concentrated solar thermal output forecasting - A review," *Solar Energy*, vol. 108, pp. 287–307, 2014.

[29] International Energy Agency (IEA), *Annual Report 2017*.

[30] Renewables 2017, *Global Status Report 2017*.

[31] S. A. Kalogirou, *Solar Energy Engineering: Processes and Systems: Second Edition*. 2014.

[32] S. C. Müller and J. Remund, "Shortest Term Forecasting of Dni for Concentrated Solar Technologies," *Pvsec 2016*, pp. 0–5, 2016.

[33] L. Nonnenmacher, A. Kaur, and C. F. Coimbra, "Day-ahead resource forecasting for concentrated solar power integration," *Renewable Energy*, vol. 86, pp. 866–876, 2016.

[34] H. A. Shah and A. U. Ahmad, "Solar Energy and Duck Curve," vol. 8, no. 4, pp. 373–379, 2019.

[35] C. Brancucci Martinez-Anido, B. Botor, A. R. Florita, C. Draxl, S. Lu, H. F. Hamann, and B. M. Hodge, "The value of day-ahead solar power forecasting improvement," *Solar Energy*, vol. 129, pp. 192–203, 2016.

[36] C. F. Coimbra, J. Kleissl, and R. Marquez, *Overview of Solar-Forecasting Methods and a Metric for Accuracy Evaluation*. Elsevier, 2013.

[37] V. Lara-Fanego, J. A. Ruiz-Arias, A. D. Pozo-Vázquez, C. A. Gueymard, and J. Tovar-Pescador, "Evaluation of DNI forecast based on the WRF mesoscale atmospheric model for CPV applications," *AIP Conference Proceedings*, vol. 1477, pp. 317–322, 2012.

[38] J. P. Mulcahy, D. N. Walters, N. Bellouin, and S. F. Milton, "Impacts of increasing the aerosol complexity in the Met Office global numerical weather prediction model," *Atmospheric Chemistry and Physics*, vol. 14, no. 9, pp. 4749–4778, 2014.

[39] J. Fan, Y. Wang, D. Rosenfeld, and X. Liu, "Review of aerosol-cloud interactions: Mechanisms, significance, and challenges," *Journal of the Atmospheric Sciences*, vol. 73, no. 11, pp. 4221–4252, 2016.

[40] P. G. Kosmopoulos, S. Kazadzis, M. Taylor, E. Athanasopoulou, O. Speyer, and P. I. Raptis et al, "Dust impact on surface solar irradiance assessed with model simulations, satellite observations and ground-based measurements," *Atmospheric Measurement Techniques*, vol. 10, no. 7, pp. 2435–2453, 2017.

[41] S. K. Mukkavilli, A. A. Prasad, R. A. Taylor, A. Troccoli, and M. J. Kay, "Mesoscale simulations of Australian direct normal irradiance, featuring an extreme dust event," *Journal of Applied Meteorology and Climatology*, vol. 57, no. 3, pp. 493–515, 2018.

[42] P. A. Jimenez, J. P. Hacker, J. Dudhia, S. E. Haupt, J. A. Ruiz-Arias, and C. A. Gueymard et al, "WRF-SOLAR: Description and clear-sky assessment of an augmented NWP model for solar power prediction," *Bulletin of the American Meteorological Society*, vol. 97, no. 7, pp. 1249–1264, 2016.

[43] A. Bozzo, S. Remy, A. Benedetti, J. Flemming, P. Bechtold, M. J. Rodwell, and J.-J. Morcrette, "Implementation of a CAMS-based aerosol climatology in the IFS," pp. 1–35, 2017.

[44] C. Voyant and G. Notton, "Solar irradiation nowcasting by stochastic persistence: A new parsimonious, simple and efficient forecasting tool," *Renewable and Sustainable Energy Reviews*, vol. 92, pp. 343–352, 2018.

[45] Y. Chu and C. F. Coimbra, "Short-term probabilistic forecasts for Direct Normal Irradiance," *Renewable Energy*, vol. 101, pp. 526–536, 2017.

[46] G. Lefebvre, E. Jiménez, and B. Cabañas, *Environment, Energy and Climate Change II - Energies from New Resources and the Climate Change*, vol. 34. 2016.

[47] B. Nouri, K. Noureldin, T. Schlichting, S. Wilbert, T. Hirsch, and M. Schroedter-Homscheidt et al, "Optimization of parabolic trough power plant operations in variable irradiance conditions using all sky imagers," *Solar Energy*, vol. 198, pp. 434–453, 2020.

[48] J. Nou, R. Chauvin, J. Eynard, S. Thil, and S. Grieu, "Towards the intrahour forecasting of direct normal irradiance using sky-imaging data," *Heliyon*, vol. 4, no. 4, 2018.

[49] S. Quesada-Ruiz, Y. Chu, J. Tovar-Pescador, H. T. Pedro, and C. F. Coimbra, "Cloud-tracking methodology for intra-hour DNI forecasting," *Solar Energy*, vol. 102, pp. 267–275, 2014.

[50] R. Marquez and C. F. Coimbra, "Intra-hour DNI forecasting based on cloud tracking image analysis," *Solar Energy*, vol. 91, pp. 327–336, 2013.

[51] G. Reikard and C. Hansen, "Forecasting solar irradiance at short horizons: Frequency and time domain models," *Renewable Energy*, pp. 1270–1290, 2019.

[52] I. Belhaj, O. E. Fatni, S. Barhmi, and E. H. Saidi, "A direct normal irradiation forecasting model based on artificial neural networks," vol. 19, pp. 21–28, 2016.

[53] C. Renno, F. Petito, and A. Gatto, "Artificial neural network models for predicting the solar radiation as input of a concentrating photovoltaic system," *Energy Conversion and Management*, vol. 106, pp. 999–1012, 2015.

[54] R. Marquez and C. F. Coimbra, "Forecasting of global and direct solar irradiance using stochastic learning methods, ground experiments and the NWS database," *Solar Energy*, vol. 85, no. 5, pp. 746–756, 2011.

[55] M. J. Blanco, "Using Learning Machines To Create Solar Radiation Maps From Numerical Weather Prediction Models , Ground Measurements and Satellite Images," *SolarPaces Conference*, 2012.

[56] T. Cebecauer and M. Suri, "Site-adaptation of satellite-based DNI and GHI time series: Overview and SolarGIS approach," *AIP Conference Proceedings*, vol. 1734, 2016.

[57] D. P. Larson, L. Nonnenmacher, and C. F. Coimbra, "Day-ahead forecasting of solar power output from photovoltaic plants in the American Southwest," *Renewable Energy*, vol. 91, pp. 11–20, 2016.

[58] G. Marshall, *Statistical methods in the atmospheric sciences, second edition D. S. Wilks. 1995. International Geophysics Series, Vol 59, Academic Press, ISBN-10: 0127519653. ISBN-13: 978-0127519654.* No. 2.

[59] M. Rummukainen, "Methods for statistical downscaling of GCM simulations.," *SMHI Rapporter. Meteorologi och Klimatologi (Sweden). no. 80.*, 1997.

[60] W. H. Klein, B. M. Lewis, and I. Enger, "Objective Prediction of Five-Day Mean Temperatures During Winter," 1959.

[61] H. R. Glahn and D. A. Lowry, "The Use of Model Output Statistics (MOS) in Objective Weather Forecasting," 1972.

[62] W. Y. Cheng and W. J. Steenburgh, "Strengths and weaknesses of MOS, running-mean bias removal, and Kalman filter techniques for improving model forecasts over the western United States," *Weather and Forecasting*, vol. 22, no. 6, pp. 1304–1318, 2007.

[63] A. Pérez-Burgos, J. Bilbao, A. De Miguel, and R. Román, "Analysis of solar direct irradiance in Spain," *Energy Procedia*, vol. 57, pp. 1070–1076, 2014.

[64] T. N. Krishnamurti, C. M. Kishtawal, T. E. LaRow, D. R. Bachiochi, Z. Zhang, and C. E. Williford et al, "Improved Weather and Seasonal Climate Forecasts from," *Science*, vol. 285, no. 1548, pp. 1–4, 1999.

[65] P. L. Houtekamer and H. L. Mitchell, "Data assimilation using an ensemble Kalman filter technique," *Monthly Weather Review*, vol. 126, no. 3, pp. 796–811, 1998.

[66] J. W. B. Lin and J. David Neelin, "Toward stochastic deep convective parameterization in general circulation models," *Geophysical Research Letters*, vol. 30, no. 4, pp. 1–4, 2003.

[67] J. M. Murphy, D. M. H. Sexton, D. N. Barnett, G. S. Jones, M. J. Webb, M. Collins, and D. A. Stainforth, "Quantification of modelling uncertainties in a large ensemble of climate change simulations," *Nature*, vol. 430, no. Letters to Nature, 2004.

[68] J. Berner, G. J. Shutts, M. Leutbecher, and T. N. Palmer, "A spectral stochastic kinetic energy backscatter scheme and its impact on flow-dependent predictability in the ECMWF ensemble prediction system," *Journal of the Atmospheric Sciences*, vol. 66, no. 3, pp. 603–626, 2009.

[69] W. I. Hameed, B. A. Sawadi, S. J. Al-Kamil, M. S. Al-Radhi, Y. I. Al-Yasir, A. L. Saleh, and R. A. Abd-Alhameed, "Prediction of solar irradiance based on artificial neural networks," *Inventions*, vol. 4, no. 3, pp. 1–10, 2019.

[70] G. Reikard, S. E. Haupt, and T. Jensen, "Forecasting ground-level irradiance over short horizons: Time series, meteorological, and time-varying parameter models," *Renewable Energy*, vol. 112, pp. 474–485, 2017.

[71] D. Yang, "Ensemble model output statistics as a probabilistic site-adaptation tool for satellite-derived and reanalysis solar irradiance," *Journal of Renewable and Sustainable Energy*, vol. 12, no. 1, 2020.

[72] E. Díez, C. Primo, J. García-Moya, J. Gutiérrez, and B. Orfila, "Statistical and dynamical downscaling of precipitation over Spain from DEMETER seasonal forecasts," *Tellus A: Dynamic Meteorology and Oceanography*, vol. 57, no. 3, pp. 409–423, 2005.

[73] M. Wittmann, H. Breitkreuz, M. Schroedter-Homscheidt, and M. Eck, "Case studies on the use of solar irradiance forecast for optimized operation strategies of solar thermal power plants," *IEEE Journal of Selected Topics in Applied Earth Observations and Remote Sensing*, vol. 1, no. 1, pp. 18–27, 2008.

[74] N. Blair, A. P. Dobos, J. Freeman, T. Neises, M. Wagner, and T. Ferguson et al, "System advisor model, sam 2014.1. 14: General description," *NREL Report No. TP-6A20-61019, National Renewable Energy Laboratory, Golden, CO*, p. 13, 2014.

[75] E. F. Abreu, P. Canhoto, V. Prior, and R. Melicio, "Solar resource assessment through long-term statistical analysis and typical data generation with different time resolutions using GHI measurements," *Renewable Energy*, vol. 127, pp. 398–411, 2018.

[76] United Nations Department of Economic and Social Affairs Population Division, *World Population Prospects 2019: Demographic Profiles*, vol. II. 2019.

[77] PNEC, "Plano Nacional Energia E Clima 2021-2030,"

[78] G. Seiz, E. P. Baltsavias, and A. Gruen, "Cloud mapping from the ground: Use of photogrammetric methods," *Photogrammetric Engineering and Remote Sensing*, vol. 68, no. 9, pp. 941–951, 2002.

[79] H. Y. Cheng, "Cloud tracking using clusters of feature points for accurate solar irradiance nowcasting," *Renewable Energy*, vol. 104, pp. 281–289, 2017.

[80] C. W. Chow, B. Urquhart, M. Lave, A. Dominguez, J. Kleissl, J. Shields, and B. Washom, "Intra-hour forecasting with a total sky imager at the UC San Diego solar energy testbed," *Solar Energy*, vol. 85, no. 11, pp. 2881–2893, 2011.

[81] F. M. Lopes, H. G. Silva, A. J. Bennett, and A. H. Reis, "Global Electric Circuit research at Graciosa Island (ENA-ARM facility): First year of measurements and ENSO influences," *Journal of Electrostatics*, vol. 87, pp. 203–211, 2017.

[82] F. M. Lopes, H. G. Silva, R. Salgado, M. Potes, K. A. Nicoll, and R. G. Harrison, "Atmospheric electrical field measurements near a fresh water reservoir and the formation of the lake breeze," *Tellus, Series A: Dynamic Meteorology and Oceanography*, vol. 68, pp. 1–12, 2016.

[83] F. M. Lopes, H. G. Silva, R. Salgado, A. Cavaco, P. Canhoto, and M. Collares-Pereira, "Short-term forecasts of GHI and DNI for solar energy systems operation: assessment of the ECMWF integrated forecasting system in southern Portugal," *Solar Energy*, vol. 170, 2018.

[84] F. M. Lopes, R. Conceição, T. Fasquelle, H. G. Silva, R. Salgado, P. Canhoto, and M. Collares-Pereira, "Predicted direct solar radiation (ECMWF) for optimized operational strategies of linear focus parabolic-trough systems," *Renewable Energy*, vol. 151, pp. 378–391, 2020.

[85] F. M. Lopes, R. Conceição, H. G. Silva, R. Salgado, and M. Collares-Pereira, "Improved ECMWF forecasts of direct normal irradiance : A tool for better operational strategies in concentrating solar power plants," vol. 163, pp. 755–771, 2020.

[86] F. M. Lopes, R. Conceição, H. G. Silva, T. Fasquelle, R. Salgado, P. Canhoto, and M. Collares-Pereira, "Short-Term Forecasts of DNI from an Integrated Forecasting System (ECMWF) for Optimized Operational Strategies of a Central Receiver System," *Energies*, vol. 1, no. 8, p. 7, 2019.

[87] R. Salgado, P. M. Miranda, P. Lacarrère, and J. Noilhan, "Boundary layer development and summer circulation in Southern Portugal," *Tethys*, vol. 12, pp. 33–44, 2015.

[88] H. G. Silva, E. F. Abreu, F. M. Lopes, A. Cavaco, P. Canhoto, J. Neto, and M. Collares-Pereira, "Solar Irradiation Data Processing using estimator MatriceS (SIMS) validated for Portugal (southern Europe)," *Renewable Energy*, vol. 147, pp. 515–528, 2020.

[89] A. Cavaco, H. G. Silva, P. Canhoto, T. Osório, and M. Collares-Pereira, "Progresses in DNI measurements in Southern Portugal," *AIP Conference Proceedings*, vol. 2033, 2018.

[90] R. Conceição, H. G. Silva, J. Mirão, M. Gostein, L. Fialho, L. Narvarte, and M. Collares-Pereira, "Saharan dust transport to Europe and its impact on photovoltaic performance: A case study of soiling in Portugal," *Solar Energy*, vol. 160, pp. 94–102, 2018.

[91] M. Diagne, M. David, P. Lauret, J. Boland, and N. Schmutz, "Review of solar irradiance forecasting methods and a proposition for small-scale insular grids," *Renewable and Sustainable Energy Reviews*, vol. 27, pp. 65–76, 2013.

[92] T. R. Ayodele and A. S. Ogunjuyigbe, "Prediction of monthly average global solar radiation based on statistical distribution of clearness index," *Energy*, vol. 90, pp. 1733–1742, 2015.

[93] C. M. Fernández-Peruchena and A. Bernardos, "A comparison of one-minute probability density distributions of global horizontal solar irradiance conditioned to the optical air mass and hourly averages in different climate zones," *Solar Energy*, vol. 112, pp. 425–436, 2015.

[94] M. Lefèvre, A. Oumbe, P. Blanc, B. Espinar, B. Gschwind, and Z. Qu et al, "McClear: A new model estimating downwelling solar radiation at ground level in clear-sky conditions," *Atmospheric Measurement Techniques*, vol. 6, no. 9, pp. 2403–2418, 2013.

[95] S. K. Solanki, N. A. Krivova, and J. D. Haigh, "Solar irradiance variability and climate," *Annual Review of Astronomy and Astrophysics*, vol. 51, pp. 311–351, 2013.

[96] C. A. Gueymard and J. A. Ruiz-Arias, "Extensive worldwide validation and climate sensitivity analysis of direct irradiance predictions from 1-min global irradiance," *Solar Energy*, vol. 128, pp. 1–30, 2016.

[97] A. J. Gutiérrez-Trashorras, E. Villicaña-Ortiz, E. Álvarez-Álvarez, J. M. González-Caballín, J. Xiberta-Bernat, and M. J. Suarez-López, "Attenuation processes of solar radiation. Application to the quantification of direct and diffuse solar irradiances on horizontal surfaces in Mexico by means of an overall atmospheric transmittance," *Renewable and Sustainable Energy Reviews*, vol. 81, pp. 93–106, 2018.

[98] C. N. Long and E. G. Dutton, "BSRN Global Network recommended QC tests, V2," *Journal of Climate*, vol. 25, no. 24, pp. 8542–8567, 2010.

[99] T. Haiden, M. Janousek, J. R. Bidlot, R. Buizza, L. Ferranti, F. Prates, and F. Vitart, "Evaluation of ECMWF forecasts, including the 2018 upgrade," p. 52 pp, 2018.

[100] R. Hogan, M. Ahlgrimm, G. Balsamo, A. Beljaars, P. Berrisford, and A. Bozzo et al, "Radiation in numerical weather prediction," *ECMWF Technical Memoranda*, pp. 9–11, 2017.

[101] R. J. Hogan and A. Bozzo, "A Flexible and Efficient Radiation Scheme for the ECMWF Model," *Journal of Advances in Modeling Earth Systems*, vol. 10, no. 8, pp. 1990–2008, 2018.

[102] E. J. Mlawer and S. A. Clough, "Shortwave and longwave enhancements in the rapid radiative transfer model," *Proceedings of the Seventh Atmospheric Radiation Measurement (ARM) Science Team Meeting*, no. 1992, pp. 409–413, 1998.

[103] J. J. Morcrette, H. W. Barker, J. N. Cole, M. J. Iacono, and R. Pincus, "Impact of a new radiation package, McRad, in the ECMWF integrated forecasting system," *Monthly Weather Review*, vol. 136, no. 12, pp. 4773–4798, 2008.

[104] I. Tegen, P. Hollrig, M. Chin, I. Fung, D. Jacob, and J. Penner, "Contribution of different aerosol species to the global aerosol extinction optical thickness: Estimates from model results," *Journal of Geophysical Research Atmospheres*, vol. 102, no. 20, pp. 23895–23915, 1997.

[105] M. G. Lawrence, "The relationship between relative humidity and the dewpoint temperature in moist air: A simple conversion and applications," *Bulletin of the American Meteorological Society*, vol. 86, no. 2, pp. 225–233, 2005.

[106] S. Pelland, G. Galanis, and G. Kallos, "Solar and photovoltaic forecasting through post-processing of the Global Environmental Multiscale numerical weather prediction model," *Progress in Photovoltaics: Research and Applications*, vol. 21, no. 3, pp. 284–296, 2013.

[107] R. Perez, E. Lorenz, S. Pelland, M. Beauharnois, G. Van Knowe, and K. Hemker et al, "Comparison of numerical weather prediction solar irradiance forecasts in the US, Canada and Europe," *Solar Energy*, vol. 94, pp. 305–326, 2013.

[108] W. Fuqiang, C. Ziming, T. Jianyu, Y. Yuan, S. Yong, and L. Linhua, "Progress in concentrated solar power technology with parabolic trough collector system: A comprehensive review," *Renewable and Sustainable Energy Reviews*, vol. 79, pp. 1314–1328, 2017.

[109] International Energy Agency (IEA), *Annual Report 2014*.

[110] M. I. R. Serrano, "Concentrating Solar Thermal Technologies: Analysis and Optimisation by CFD Modelling," *Green Energy and Technology. Springer, Switzerland.*, 2017.

[111] T. Lopes, T. Fasquelle, H. G. Silva, and K. Schmitz, "HPS2 - Demonstration of Molten-Salt in Parabolic Trough Plants - Simulation Results from System Advisor Model," *Renewable Energy*, 2020.

[112] T. Lopes, T. Fasquelle, and H. G. Silva, "Pressure drops , heat transfer coefficient , costs and power block design for direct storage parabolic trough power plants running molten salts," *Renewable Energy*, 2020.

[113] J. I. Burgaleta, S. Arias, and D. Ramirez, "Gemasolar, the first tower thermosolar commercial plant with molten salt storage," *Solarpaces*, pp. 1–8, 2011.

[114] F. Dinter and D. M. Gonzalez, "Operability, reliability and economic benefits of CSP with thermal energy storage: First year of operation of ANDASOL 3," *Energy Procedia*, vol. 49, pp. 2472–2481, 2014.

[115] C. A. Gueymard, "Temporal variability in direct and global irradiance at various time scales as affected by aerosols," *Solar Energy*, vol. 86, no. 12, pp. 3544–3553, 2012.

[116] A. Roesch, M. Wild, A. Ohmura, E. G. Dutton, C. N. Long, and T. Zhang, "Assessment of BSRN radiation records for the computation of monthly means," *Atmospheric Measurement Techniques*, vol. 4, no. 2, pp. 339–354, 2011.

[117] R. Conceição, H. G. Silva, J. Mirão, and M. Collares-Pereira, "Organic soiling: The role of pollen in PV module performance degradation," *Energies*, vol. 11, no. 2, pp. 1–13, 2018.

[118] S. Marques, J. G. Borges, J. Garcia-Gonzalo, F. Moreira, J. M. Carreiras, and M. M. Oliveira et al, "Characterization of wildfires in Portugal," *European Journal of Forest Research*, vol. 130, no. 5, pp. 775–784, 2011.

[119] H. G. Silva, F. M. Lopes, S. Pereira, K. Nicoll, S. M. Barbosa, and R. Conceição et al, "Saharan dust electrification perceived by a triangle of atmospheric electricity stations in Southern Portugal," *Journal of Electrostatics*, vol. 84, pp. 106–120, 2016.

[120] T. Sirch, L. Bugliaro, T. Zinner, M. Möhrlein, and M. Vazquez-Navarro, "Cloud and DNI nowcasting with MSG/SEVIRI for the optimized operation of concentrating solar power plants," *Atmospheric Measurement Techniques*, vol. 10, no. 2, pp. 409–429, 2017.

[121] R. G. Harrison, N. Chalmers, and R. J. Hogan, "Retrospective cloud determinations from surface solar radiation measurements," *Atmospheric Research*, vol. 90, no. 1, pp. 54–62, 2008.

[122] C. Lac, J. P. Chaboureau, V. Masson, J. P. Pinty, P. Tulet, and J. Escobar et al, "Overview of the Meso-NH model version 5.4 and its applications," *Geoscientific Model Development*, 2018.

[123] J. P. Lafore, J. Stein, N. Asencio, P. Bougeault, V. Ducrocq, and J. Duron et al, "The Meso-NH Atmospheric Simulation System. Part I: Adiabatic formulation and control simulations," *Annales Geophysicae*, 1998.

[124] M. Iakunin, R. Salgado, and M. Potes, "Breeze effects at a large artificial lake: Summer case study," *Hydrology and Earth System Sciences*, vol. 22, no. 10, pp. 5191–5210, 2018.

[125] M. Potes, R. Salgado, M. J. Costa, M. Morais, D. Bortoli, I. Kostadinov, and I. Mammarella, "Lake-atmosphere interactions at Alqueva reservoir: A case study in the summer of 2014," *Tellus, Series A: Dynamic Meteorology and Oceanography*, vol. 69, no. 1, p. 1272787, 2017.

[126] J. L. Casado-Rubio, M. A. Revuelta, M. Postigo, I. Martínez-Marco, and C. Yagüe, "A postprocessing methodology for direct normal irradiance forecasting using cloud information and aerosol load forecasts," *Journal of Applied Meteorology and Climatology*, vol. 56, no. 6, pp. 1595–1608, 2017.

[127] S. Kinne, D. O'Donnel, P. Stier, S. Kloster, K. Zhang, and H. Schmidt et al, "MAC-v1: A new global aerosol climatology for climate studies," *Journal of Advances in Modeling Earth Systems*, vol. 5, no. 4, pp. 704–740, 2013.

[128] H. Liu, R. T. Pinker, and B. N. Holben, "A global view of aerosols from merged transport models, satellite, and ground observations," *Journal of Geophysical Research D: Atmospheres*, vol. 110, no. 10, pp. 1–16, 2005.

[129] I. T. Jollife and D. B. Stephenson, "Forecast Verification, A Practitioner's Guide in Atmospheric Science," *Second Edition, Wiley-Blackwell.*, 2012.

[130] B. Nouri, S. Wilbert, N. Blum, P. Kuhn, T. Schmidt, and Z. Yasser et al, "Evaluation of an All Sky Imager Based Nowcasting System for Distinct Conditions and Five Sites," *AIP Proceedings, SolarPACES 2020*.

[131] F. M. Lopes, R. Conceição, H. G. Silva, R. Salgado, P. Canhoto, and M. Collares-Pereira, "Predictive value of short-term forecasts of DNI for solar energy systems operation," *AIP Conference Proceedings*, vol. 2126, no. July, 2019.

[132] R. J. Ramorakane and F. Dinter, "Evaluation of parasitic consumption for a CSP plant," *AIP Conference Proceedings*, vol. 1734, pp. 1–9, 2016.

[133] R. P. V. Salgado, *Interacção solo - atmosfera em clima semi-árido*. PhD thesis, University of Évora, 2005.

[134] P. H. Wagner and M. Wittmann, "Influence of different operation strategies on transient solar thermal power plant simulation models with molten salt as heat transfer fluid," *Energy Procedia*, vol. 49, pp. 1652–1663, 2014.

[135] K. M. Powell and T. F. Edgar, "Modeling and control of a solar thermal power plant with thermal energy storage," *Chemical Engineering Science*, vol. 71, pp. 138–145, 2012.

[136] X. Ju, C. Xu, X. Han, H. Zhang, G. Wei, and L. Chen, "Recent advances in the PV-CSP hybrid solar power technology," *AIP Conference Proceedings*, vol. 1850, 2017.

[137] J. García-Barberena, P. Garcia, M. Sanchez, M. J. Blanco, C. Lasheras, A. Padrós, and J. Arraiza, "Analysis of the influence of operational strategies in plant performance using SimulCET, simulation software for parabolic trough power plants," *Solar Energy*, vol. 86, no. 1, pp. 53–63, 2012.

[138] B. F. Towler, "The Future of Energy," *The Future of Energy*, pp. 1–376, 2014.

[139] P. Kuhn, D. Garsche, S. Wilbert, B. Nouri, N. Hanrieder, and C. Prahl et al, "Shadow-camera based solar nowcasting system for shortest-term forecasts," *Meteorologische Zeitschrift*, vol. 28, no. 3, pp. 255–270, 2019.

[140] T. Fasquelle, Q. Falcoz, P. Neveu, F. Lecat, and G. Flamant, "A thermal model to predict the dynamic performances of parabolic trough lines," *Energy*, vol. 141, pp. 1187–1203, 2017.

[141] F. J. Collado and J. Guallar, "Two-stages optimised design of the collector field of solar power tower plants," *Solar Energy*, vol. 135, pp. 884–896, 2016.

[142] L. Valenzuela, R. López-Martín, and E. Zarza, "Optical and thermal performance of large-size parabolic-trough solar collectors from outdoor experiments: A test method and a case study," *Energy*, vol. 70, pp. 456–464, 2014.

[143] M. J. Wagner and P. Gilman, "Technical manual for the SAM physical trough model, by National Renewable Energy Laboratory (NREL, U.S. Department of Energy)," *National Renewable Energy Laboratory*, vol. 303, pp. 275–3000, 2011.

[144] E. K. Ezeanya, G. H. Massiha, W. E. Simon, J. R. Raush, and T. L. Chambers, "System advisor model (SAM) simulation modelling of a concentrating solar thermal power plant with comparison to actual performance data," *Cogent Engineering*, vol. 5, no. 1, pp. 1–26, 2018.

[145] F. Burkholder and C. Kutscher, "Heat loss testing of Schott's 2008 PTR70 parabolic trough receiver," *NREL Technical Report*, p. 58, 2009.

[146] W. C. Skamarock, J. B. Klemp, J. Dudhi, D. O. Gill, D. M. Barker, and M. G. Duda et al, "A Description of the Advanced Research WRF Version 3," *Technical Report*, p. 113, 2008.

[147] C. Policarpo, R. Salgado, and M. J. Costa, "Numerical Simulations of Fog Events in Southern Portugal," *Advances in Meteorology*, vol. 2017, no. 1989, 2017.

[148] R. Honnert, "Representation of the grey zone of turbulence in the atmospheric boundary layer," *Advances in Science and Research*, vol. 13, pp. 63–67, 2016.

UNIVERSIDADE DE ÉVORA
INSTITUTO DE INVESTIGAÇÃO
E FORMAÇÃO AVANÇADA

Contactos:

Universidade de Évora

Instituto de Investigação e Formação Avançada — IIFA

Palácio do Vimioso | Largo Marquês de Marialva, Apart. 94

7002 - 554 Évora | Portugal

Tel: (+351) 266 740 800

Fax: (+351) 266 744 677

email: geral@iifa.uevora.pt